

UC Davis

UC Davis Electronic Theses and Dissertations

Title

Nitrogen-Heterocycles in the Interstellar Medium: Experimental and Computational Approaches to an Astrochemical Mystery

Permalink

<https://escholarship.org/uc/item/6428j6w0>

Author

Johansen, Sommer Lynn

Publication Date

2021

Peer reviewed|Thesis/dissertation

Nitrogen-Heterocycles in the Interstellar Medium: Experimental and Computational
Approaches to an Astrochemical Mystery

By

SOMMER LYNN JOHANSEN
DISSERTATION

Submitted in partial satisfaction of the requirements for the degree of

DOCTOR OF PHILOSOPHY

in

Chemistry

in the

OFFICE OF GRADUATE STUDIES

of the

UNIVERSITY OF CALIFORNIA

DAVIS

Approved:

Kyle N. Crabtree, Chair

Matthew Augustine

Lee-Ping Wang

Committee in Charge

2021

Acknowledgements

Six years ago, I made a very spontaneous and potentially risky decision to abandon my original plan for grad school, which was to join a very respected and well-established group doing work for which I was highly qualified, and instead joined a brand-new lab, with a new assistant professor about whom I knew nothing, doing work for which I was absolutely not qualified. It was one of the best decisions I have ever made for many reasons; the most significant of which has been the opportunity to work with said new professor. Kyle, I know that people saying nice things about you makes you deeply uncomfortable, but bear with me. From the very beginning, you've made it clear that you were fundamentally on my side and cared about my growth and well-being as a scientist and as a human. You gave me the space to develop my own ideas and the support to actually turn those ideas into reality. You pushed me to try difficult things (just the fact that I'm writing this with LaTeX on a Linux machine is proof of that) but also to take breaks and to be kind to myself. I really like the person that you have helped me become, and I cannot thank you enough for that. The last six years have sometimes felt like an endless series of challenges coming at our lab from every direction (often literally), but I have never regretted my decision to join this group. I'm going to take this opportunity to offer you some advice, though; your non-runner group members probably don't care how your run this morning went, but they'll suppress the eye-roll and pretend to because you're the PI. Don't make them do this.

Since the start of covid, one of the things I've missed the most in my daily life is being in the lab and the office, surrounded by my labmates. I miss talking through research problems and laughing (or crying) at life's absurdities together. To Zach and Zhongxing, I'm so glad you also made the potentially stupid decision to join a brand new lab. I've learned so much from both of you, and really enjoyed those early years when we were all working on building the kinetics experiment together. Zach, I forgive you for abandoning me to go to France. Sorry I abandoned you this last year. And to get married, and go on my honeymoon. Clearly I'm the worse friend. Kelly, it has been so fun to work with someone else with a similar overlapping interest in art and science. I'm excited to continue working with you on the SCInema podcast! Wes, thank you for teaching me what an acceptable cup of coffee truly tastes like and giving me an appreciation for the intricacies of large amplitude motion; you're right, it is objectively beautiful. Sorry Kelly. Anna, thank you for the Paula Poundstone books and for challenging me to be a better teacher. Our group is lucky to have you. To Adam and Sophie, I wish we could have worked together more. Thank you for fighting the good fight (aka the kinetics experiment). I wish you the best of luck and can't wait to cheer on your successes.

To those I've had the honor of mentoring over the years— Hannah, Haley, Anna, Sonja, Sofia, and Anahut—

you have all inspired me to no end, and nothing is more satisfying than seeing you all go on to do amazing things. Hannah, especially, thank you for supporting me from afar in literally every way you possibly could have; despite whatever you were going through (which, um, has been a lot), you still have always reached out to make sure I was okay. You're simultaneously one of the most wholesome and fight-ready people I know and deserve to have an amazingly fulfilling graduate experience at MIT.

There are lots of other people who have gone above and beyond to help me with scientific and technical problems. Paul Stucky and Scott Berg especially have dropped everything to come help innumerable times. Alan Hicklin did the same during my first year. Many thanks to the three of you for dealing with my incessant questions, but especially for teaching me to do things myself so I didn't have to keep asking you for help. Thanks also to the administrators who have helped me navigate all the various non-science aspects of graduate life, most notably Brad Wolf, Emily Atkinson, and Laura Troutner.

To my committee members, Professors Lee-Ping Wang and Matthew Augustine, thank you all of your useful comments on this dissertation. Lee-Ping, thank you for being game to take on this nanoreactor collaboration and for your excitement about the scientific results. I really appreciate all the time you've taken to work with me over the years; despite not being your student, you've always gone out of your way to thoroughly answer my questions. Additional thanks goes to Professor Bill McCurdy for the many hours of educational conversations while I was your TA, and for helping me to develop my ideas for a postdoc proposal last fall.

The experimental work presented in Chapter 2 was all done at the Harvard-Smithsonian Center for Astrophysics. Many thanks to Michael McCarthy and his group at the time, Kelvin Lee, Jessie Porterfield, and Brandon Carroll, for the use of their cavity FTMW spectrometer and helpful discussions during experiments and preparation of the published work. Thank you to Kelvin for also providing invaluable help with the theoretical work. John F. Stanton has also been immensely helpful for all of our CFOUR related problems, and helped steer us in the right direction both the theoretical part of Chapter 2 and all of Chapter 3. Further thanks goes to Kirill Prozument, who provided a copy of Ref. 1, and Harshal Gupta for taking the time to chat with Kyle and I at Firehaus (RIP) about how to best confirm that we were indeed looking at cyanovinyll spectra.

All of the work present within this dissertation was supported at least partially by NASA Headquarters under the NASA Earth and Space Science Fellowship Program- Grant 80NSSC18K1110.

There are also many people from my academic career before UC Davis to whom I owe thanks. At the University of Vermont, I was welcomed as a first year undergraduate into Professor Matthew Liptak's lab.

Thank you so much for introducing me to spectroscopy and giving me challenging research projects to work on throughout my years in your group. To Amanda Graves, you were the graduate student mentor that I aspired to be. Also an A+ karaoke partner. Ariel Schuelke-Sanchez, I'm so glad we overlapped my last year. Thank you for being a really good friend when I desperately needed one. Many other professors were incredibly supportive, and since leaving UVM I am sometimes shocked to remember truly how wonderful the entire academic community was. In particular, Professors Rory Waterman, Chris Danforth, John Forbes, Paul Besaw, Clare Byrne, Theresia Höck, and Joanna Rankin. Professor Rankin played more of a role than she realized at the time in my future graduate work; she encouraged me to write a term paper on astrochemistry for her astrophysics course. I just reread that paper, and am pleased to report that my understanding of astrochemistry has significantly improved since then. Lastly, there were many teachers I had in high school who encouraged me to dream big, but Suzanne Andrews more than anyone else inspired my interest in scientific research; thank you.

To Dan, Marshall, Shannon, and the Zachs; I'm really not certain that I would have gotten through my first quarter of grad school without you all. Thank you for every quantum pun, helping me figure out how to code, running the Python workshops once we thought we'd figured it out enough to teach other people, adventure runs, and just generally being the group of super nerds I always hoped I'd get to be friends with someday. Our collective Physical Kids wavefunction has been delocalized far more than I'd like, but I can't wait for us to get together again (solar eclipse 2024 at Zachary's?).

Grad school can make it difficult to keep up with other friends, and that's particularly the case when grad school is 3000 miles away. Thank you to Ethan, Mary, Aron, Katie, Toria, Tracy, Alex, and Jackson for not only not forgetting about me, but continuing to be really great friends from (mostly) the other side of the continent. Extra special thank you to Alex and Jackson for hosting me while I was doing experiments at the CfA.

To Jisoo and Conor (and Robin, and sure also Aeri), thank you for everything you've done for Marcus and I. You have been an integral part of our support system while we've lived in Davis, and particularly this summer, with all the times you've helped take care of Ollie so I could write. Jisoo, it's been really great to have someone else who understands the PhD/mom struggle. Thank you for being my role model in that.

Maya; I've been going back and forth on whether or not you count as a friend or as family in how I've organized these acknowledgements, but I guess that's a little ridiculous because you're absolutely both. I am constantly thankful that our lives have intersected the way that they have, and especially thankful that you ended up in Davis this summer. Even if our next steps in life don't result in us being in the same town,

you'll always be my sister, and Ollie's Aunt Yaya.

To my family-in-law, Lisa, Dean, Paul, Alex, Jackie, Dominic, Nick, and Tomas, who have defied every existing stereotype about in-laws to be people I adore spending time with, thank you so much for welcoming me into the family ten (!) years ago. To my stepsister, Jess, and brother, Leif, giving up spending time with you guys has been one of the hardest things about living so far away. I'm so happy that both of you have found wonderful partners (hi, Josh and Emma!) and are doing great things in life. To Leif especially, thank you for all the long-distance check-ins and late night conversations. I can't wait for you two to meet your nephew. Thank you to my grandparents, who have shown such interest and excitement in everything I've done and who have always asked meaningful questions about my work. To my dad, mom, and stepmom, thank you for your ceaseless enthusiasm for my research, even though it has kept me busy and far away. Mom and Dad, thank you so much for teaching me to both be curious and care deeply about the world around me. I love you all so, so much and hope life eventually brings me a little closer to home.

I owe so much to my own little family, the more human ones and the less human ones. Maggie, Chena, Mikey, and Georgie, thank you for keeping me grounded and teaching me to always have a sense of humor (especially when it comes to bodily fluids, which has turned out to be quite important recently). To Ollie, who slept on my lap while I wrote large chunks of this dissertation; watching you grow and start to figure out the world has made me see with new eyes. You have brought context to my life and given me renewed purpose and I feel so lucky to have been able to spend the first six months of your life at home with you. You've also allowed me to master typing with one hand, as I'm doing now while you sit on my lap and pull my hair and smudge my glasses and giggle nonstop. Ich liebe dich, Ollie. Thanks for choosing me to be your mom.

And to Marcus; it's hard to know where to begin, because you have made every single aspect of my life better since the day we met ten years ago. You are more brilliant and a harder worker than you give yourself credit for, and you have taught me how to be kind to myself and to not worry about things that don't matter. Thank you for taking on all of the housework and Ollie time that you possibly could while I wrote this, and for still taking time every single day to make sure that I was doing okay (and doing everything you could to help when I wasn't). Getting to spend everyday with you has been the light in the darkness of these last 18 months, including watching you so naturally ease into the role of father. Ollie has no idea how lucky he is to have you, and I'm going to go ahead and speak for him too when I say we both love you so much. Thank you for everything. You are my favorite.

Abstract

Astrochemistry, while a relatively new field, has seen an explosion of growth and scientific interest in the last several decades. Currently, roughly 250 molecules have been identified in space, with the pace of new discoveries increasing each year. The variety of new laboratory techniques, telescopes, and computational technology that have recently become available have helped to fuel this rapid pace of exploration. However, for all we have learned about the chemical environments of the interstellar medium, there remain many unanswered questions. One of these mysteries pertains to nitrogen-containing heterocycles, cyclic hydrocarbons that contain at least one nitrogen within the ring. These species are of fundamental interest to a wide variety of scientific disciplines, due mainly to their critical role in biology as DNA and RNA nucleobases, amino acid side chains, components of vitamins, and building blocks of porphyrins. They have been detected on meteorites with non-terrestrial isotopic abundances, suggesting an interstellar origin. Furthermore, observations of the unidentified infrared bands that are thought to arise from polycyclic aromatic hydrocarbons include one transition with a shift attributed to the presence of a nitrogen atom within the aromatic structure. However, despite the evidence that nitrogen-containing heterocycles are produced in astrochemical environments, not one has been detected in space despite numerous astronomical searches, and they are not included at present in reaction paths within predictive chemical kinetics models. The work presented here serves as the foundation for a broad research program with the goal of drastically increasing our understanding of astrophysical N-heterocycles. This is achieved through spectroscopic characterization of N-heterocycles and their precursors and reaction path discovery with *ab initio* molecular dynamics. Future work will include kinetics experiments to determine rate constants and branching ratios of formation and destruction pathways, as well as astronomical searches for N-heterocycles in a variety of interstellar and circumstellar environments. Beyond the importance for astrochemistry, the study of gas-phase nitrogen-containing species is particularly relevant for attempts to understand the chemistry within Titan's atmosphere, as well as the terrestrial combustion of biomass.

Contents

1	Introduction	1
1.1	Astrophysical nitrogen-containing heterocycles	1
1.1.1	From biology to outer space	1
1.1.2	The stellar life cycle	3
1.1.3	Top-down vs. bottom-up chemistry	4
1.1.4	Solving the N-heterocycle mystery	4
1.2	Literature Review	5
1.2.1	Astronomical searches	5
1.2.2	Reaction discovery and characterization	16
1.3	Significance of this work	28
1.3.1	Spectroscopic Characterization	28
1.3.2	<i>ab initio</i> Molecular Dynamics	29
1.3.3	Future Work	30
1.3.4	Relevance to Planetary Science and Combustion Chemistry	30
2	Rotational Spectrum of the β-Cyanovinyl Radical: A Possible Astrophysical N-Heterocycle Precursor	32
2.1	Introduction	33
2.2	Theoretical Methods	34
2.3	Experimental Methods	36
2.4	Results and Discussion	37
2.5	Conclusion	45
2.6	Supporting Information	46

3	Coupled Cluster Characterization of 1-, 2-, and 3-Pyrrolyl: Parameters for Vibrational and Rotational Spectroscopy	47
3.1	Introduction	48
3.2	Methods	50
3.3	Results & Discussion	50
3.4	Implications for Laboratory Spectroscopy and Astronomy	60
3.5	Conclusions	64
4	Reaction Discovery Part I: Search for Novel Gas-Phase N-heterocycle Formation Pathways with an <i>ab initio</i> Nanoreactor	67
4.1	Introduction	68
4.2	Methods	71
4.3	Results and Discussion	74
4.3.1	Pyridine	74
4.3.2	Pyrrole	77
4.4	Conclusion	84
5	Reaction Discovery Part II: Gas-Phase N-heterocycle Formation Pathways From Acyclic Precursors	86
5.1	Introduction	87
5.2	Methods	89
5.3	Results and Discussion	91
5.4	Implications for N-heterocycle Formation in the ISM and Planetary Atmospheres	95
5.5	Conclusion	96
6	Reaction Discovery Part III: Low-Temperature Gas-Phase Ring Insertion Reactions	97
6.1	Introduction	97
6.2	Methods	99
6.3	Results and Discussion	99
6.3.1	H ₂ CCN + Azete	99
6.3.2	HCCN + 1-Pyrrolyl	101
6.4	Implications for Astrochemistry, Planetary Science, and Combustion Chemistry	102
6.5	Conclusion	103

7	Conclusion and Future Work	105
7.1	Spectroscopic characterization	105
7.2	Reaction path discovery	106
7.3	Experimental determination of rate constants and branching ratios	107
7.4	Astronomical searches	108

Chapter 1

Introduction

Nitrogen-containing molecules make up more than a third of the roughly 250 molecules that have been identified in space,^a but none of these species are nitrogen-containing heterocycles, cyclic hydrocarbons that contain at least one nitrogen within the ring. This is particularly interesting because these species have been detected on meteorites with non-terrestrial isotopic abundances, and there is evidence for incorporation of nitrogen with the large polycyclic aromatic hydrocarbon structures that are ubiquitous throughout interstellar space. This peculiar absence of N-heterocycles within astronomical surveys is the focus of this dissertation. In this chapter, the mystery is introduced and a thorough literature review covering previous astronomical searches and experimental work is presented, with a focus on why N-heterocycles have not been detected and what information is lacking. The research presented in later chapters is placed within the context of the broader astrophysical N-heterocycle problem.

1.1 Astrophysical nitrogen-containing heterocycles

1.1.1 From biology to outer space

Nitrogen-containing heterocycles (henceforth, N-heterocycles) are critical biological moieties. DNA and RNA contain nucleobases adenine, guanine, cytosine, thymine, and uracil that have either a purine ($C_5H_4N_4$) or pyrimidine ($C_4H_4N_2$) backbone. Of the twenty biological amino acids, histidine, tryptophan, and proline have sidechains that include the N-heterocycles imidazole ($C_3H_4N_2$), indole (C_8H_7N), and pyrrolidine (C_4H_9N), respectively. The structures of thiamine, riboflavin, nicotinic acid, pyridoxine, biotin, folic acid, and cobal-

^aSee <https://cdms.astro.uni-koeln.de/classic/molecules> for most up to date list.

amin, which collectively make up all but one of the B vitamins, include a wide variety of N-heterocyclic species in their structures, from a simple pyridine ring (C_5H_5N) in pyridoxine and nicotinic acid to the large conjugated system of the porphyrin ($C_{20}H_{14}N_4$) in cobalamin. The porphyrin moiety, made of four conjoined pyrrole (C_4H_5N) rings, plays many other roles in biology, including in heme, the iron-containing structure in hemoglobin.

The ubiquity of N-heterocycles in biology is likely due to the intricate relationship between their structure and function. The nucleobases, for example, form specific hydrogen bonds between base pairs, which is intrinsic to the ability of these structures to store information.² Rings with different numbers of nitrogen atoms or different patterns of conjugation show significantly different properties. As common organometallic ligands, pyridine is a Lewis base and a good hydrogen bond acceptor, while pyrrole is nonbasic and a good hydrogen bond donor.³ Derivatives of the porphyrin moiety are used in cyanobacteria to absorb a wide range of visible wavelengths by slightly altering their coplanarity.⁴ This wide range of properties does not arise from the purely carbon-based cyclic species; the incorporation of nitrogen within these hydrocarbon rings is a key step towards life as we know it.

Therefore, studying N-heterocycles is very attractive from an astrochemical and astrobiological perspective. N-heterocycles, as well as other biological and prebiotic molecules, have been detected on carbonaceous chondrite type meteorites.⁵⁻⁷ The soluble organic species were found to have $^{12}C/^{13}C$ ratios indicative of non-terrestrial origins.⁶ This provides a potential connection between chemistry in space and the origin of life on Earth, and the hypothesis of exogenous delivery of the ingredients for early life has long fascinated astrobiologists.⁸ The significance of meteoritic N-heterocycles for the investigations presented in this dissertation is the strong evidence that N-heterocycles can, somehow, be produced in space; an important conclusion in light of the fact that no N-heterocycle has been definitely detected in interstellar or circumstellar environments.

Another strong piece of evidence for astrophysical N-heterocycles arises from the unidentified infrared (UIR) bands, interstellar emission features are seen throughout the observable universe and are attributed to fluorescence in polycyclic aromatic hydrocarbons (PAHs).⁹ The $6.2 \mu m$ UIR band, however, cannot be replicated purely through C-C stretching vibrational modes in PAHs, but is modeled well by the incorporation of a nitrogen within the central rings of PAH structures.¹⁰ Computational simulations found that incorporation of O and Si into aromatic rings could not reproduce the $6.2 \mu m$ feature, nor did complexation of pure PAH species with the metal cations Fe^+ , Mg^+ , and Mg^{2+} . The addition of one or more N atoms within the carbon rings shifts the C - C stretching mode by redistributing the electron density within the ring; the $6.2 \mu m$ line does not arise from a C - N stretch. More recent work has extended observations of

the 6.2 μm emission to numerous extragalactic sources and suggests that a significant portion of the PAHs in these galaxies also contain nitrogen.

For the sake of this discussion, the term N-heterocycle will refer to mono- or bi-cyclic nitrogen-containing hydrocarbon rings, similar to the structures detected on meteorites. Polycyclic aromatic nitrogen-containing hydrocarbon (PANH) will be used to refer to tri-cyclic or larger PAHs that have a nitrogen incorporated into the ring structure.

1.1.2 The stellar life cycle

The relevant astrophysical regions to PANHs and meteoritic N-heterocycles are closely associated with the stellar life cycle. Aging stars begin to release massive amounts of material into their surroundings, developing dense and dusty shells known as circumstellar envelopes (CEs). CEs have temperatures as high as 1000 K with a number density around 10^{10} cm^{-3} , although the material expands and cools rapidly as it flows outward from the accretion envelope.¹¹ This material expands outward into the interstellar medium (ISM) where it is eventually incorporated into a diffuse interstellar cloud, and then a dense molecular cloud (DMC) as gravitational collapse begins. Within this DMC, pockets of higher mass begin to collapse further, eventually forming what is known as a hot molecular core (HMC). As expected, densities increase as gravitational collapse proceeds, with the number density of diffuse clouds of order 10^2 cm^{-3} ,¹² increasing to $10^3 - 10^5 \text{ cm}^{-3}$ for DMCs,¹³ and then further to $\leq 10^8 \text{ cm}^{-3}$ for HMCs.¹⁴ Temperature does not follow this trend, however, due to the increase in visual extinction in DMCs that make them colder than diffuse clouds; diffuse cloud temperatures are typically 30 – 100 K,¹² while DMCs have temperatures between 10 – 20 K.¹³ HMCs are warmer, as the name implies, with temperatures $\leq 300 \text{ K}$.¹⁴ Further gravitational collapse eventually results in a protostar surrounded by a protoplanetary disk (PPD), formed due to the angular momentum of the collapse. The material in this disk eventually gives rise to planets and other rocky bodies. Meteorite parent bodies form within the outer envelopes of these disks, where temperatures are as low as 14 K and densities of order 10^5 cm^{-3} .¹⁵

The most well-studied regions of space from an astrochemical perspective are known as star-forming regions, where all of the stages of the stellar life-cycle can be observed. Sagittarius B2 (Sgr B2), located at the center of our galaxy, and the Taurus Molecular Cloud (TMC), located only 140 pc away within the constellation Taurus,¹⁶ are common targets for astronomical searches for complex organic species. For a broader discussion of the role of astrochemistry within star-forming regions and at each stage of the stellar life cycle, see the review by van Dishoeck¹⁷.

1.1.3 Top-down vs. bottom-up chemistry

Astrophysical N-heterocycle formation lies at the intersection of the two general classes of astrochemical pathways; top-down and bottom-up chemistry. Both pathways hypothesize potential formation mechanisms of the complex organic molecules (COMs) within DMCs. Top-down pathways begin with PAH formation in CEs.¹⁸ Upon the transition to the bare or diffuse ISM, PAHs are fragmented by bombardment with UV radiation.^{9,19} After incorporation into a DMC, PAHs and their fragments are shielded from further destruction due to extinction of UV wavelengths. Alternatively, bottom-up pathways suggest COMs in DMCs, even ones as complex as large icosahedral PAH structures,²⁰ are formed from the association reactions of smaller species. The UV shielding allows for long lifetimes of molecules that have a high susceptibility to UV photolysis and thus would rapidly be destroyed within the bare or diffuse ISM, as is the case for N-heterocycles.²¹

Recently detected cyclic species including benzonitrile,²² cyanonaphthalene,²³ and indene^{24,25} within TMC-1 are the closest confirmed interstellar species to N-heterocycles and also lie at the nexus of top-down and bottom-up chemistry. Extending general formation schemes of these newly detected molecules proposed by Burkhardt et al.²⁵ to N-heterocycles leads to three possibilities: N-heterocycles were either (1) built up from smaller species within DMCs, HMCs, or outer envelopes of protoplanetary disks, (2) formed from PANH fragmentation in the bare and diffuse ISM, or (3) formed from PANH fragmentation within a DMC. The first hypothesis could apply to either meteoritic N-heterocycles or larger PANHs, while the second two assume PANHs were formed within CEs.

Our current level of understanding does not permit the elimination of any of these hypotheses. This is due to both the lack of detections and that the main databases that contain kinetics information about astrochemical pathways, specifically KIDA²⁶ and UMIST²⁷, do not include any N-heterocycles, limiting their potential inclusion in chemical models. Therefore, both top-down and bottom-up pathways should be taken into consideration in studies of N-heterocycle formation.

1.1.4 Solving the N-heterocycle mystery

Astrochemistry is an inherently interdisciplinary field, requiring a combination of astronomical observations, laboratory experiments, computational and theoretical chemistry, and predictive chemical kinetics models. The results of the first three are used in order to build more robust models, from which we can gain an understanding of the chemical nature of a certain area of space. Ultimately, the incorporation of reactions with known astronomical abundances of precursors, rate constants, and branching ratios into chemical models

will provide us with the most valuable insight into the question of N-heterocycle formation in space. The rest of this chapter will discuss what has already been done towards this goal and the significance of the research presented in this dissertation. The discussion of prior work has been broken up into two general categories; astronomical searches and reaction discovery. Trends and limitations of this body of work is discussed, followed by how the original work presented in later chapters addresses these shortcomings.

1.2 Literature Review

After many decades of investigations related to astrophysical N-heterocycles, a high-level analysis is worthwhile to determine if the combined efforts have produced some collective insight into either the mystery itself or as to why we have not yet been able to solve it. The areas of prior work can be distilled down to astronomical searches and characterization of reaction pathways. Astronomical searches have relied on complementary laboratory spectroscopy and theoretical chemistry. Despite none of the observations reporting definitive detections, several saw tentative transitions in their surveys, and many derived upper limits to column densities. Reaction path discovery and characterization can be done purely with computational chemistry, or with combined experimental and theoretical techniques. These studies includes gas-phase chemistry, ice-surface photochemistry, and aqueous processing of meteorite parent bodies. Currently, there is not enough information to reliably include these pathways within chemical kinetics models, severely limiting our understanding of astrophysical N-heterocycles.

1.2.1 Astronomical searches

Finding molecules in space

Radio astronomy The vast majority of molecules that have been detected in space have been identified by their rotational spectra. These transitions are in the frequency range accessible by radio telescopes and include wavelengths between the centimeter and submillimeter range. Emission features are typically observed in regions with high gas temperatures, like circumstellar shells or hot cores. Even in regions with low excitation temperatures, absorption features can be seen against a continuum of blackbody radiation from warmer dust. This presents a significant advantage over optical and infrared astronomy, which require a sightline towards a star in order to detect electronic or vibrational transitions. However, radio observations do require that molecules be in the gas phase so that they can freely rotate, which is not a limitation of vibrational or electronic transitions.

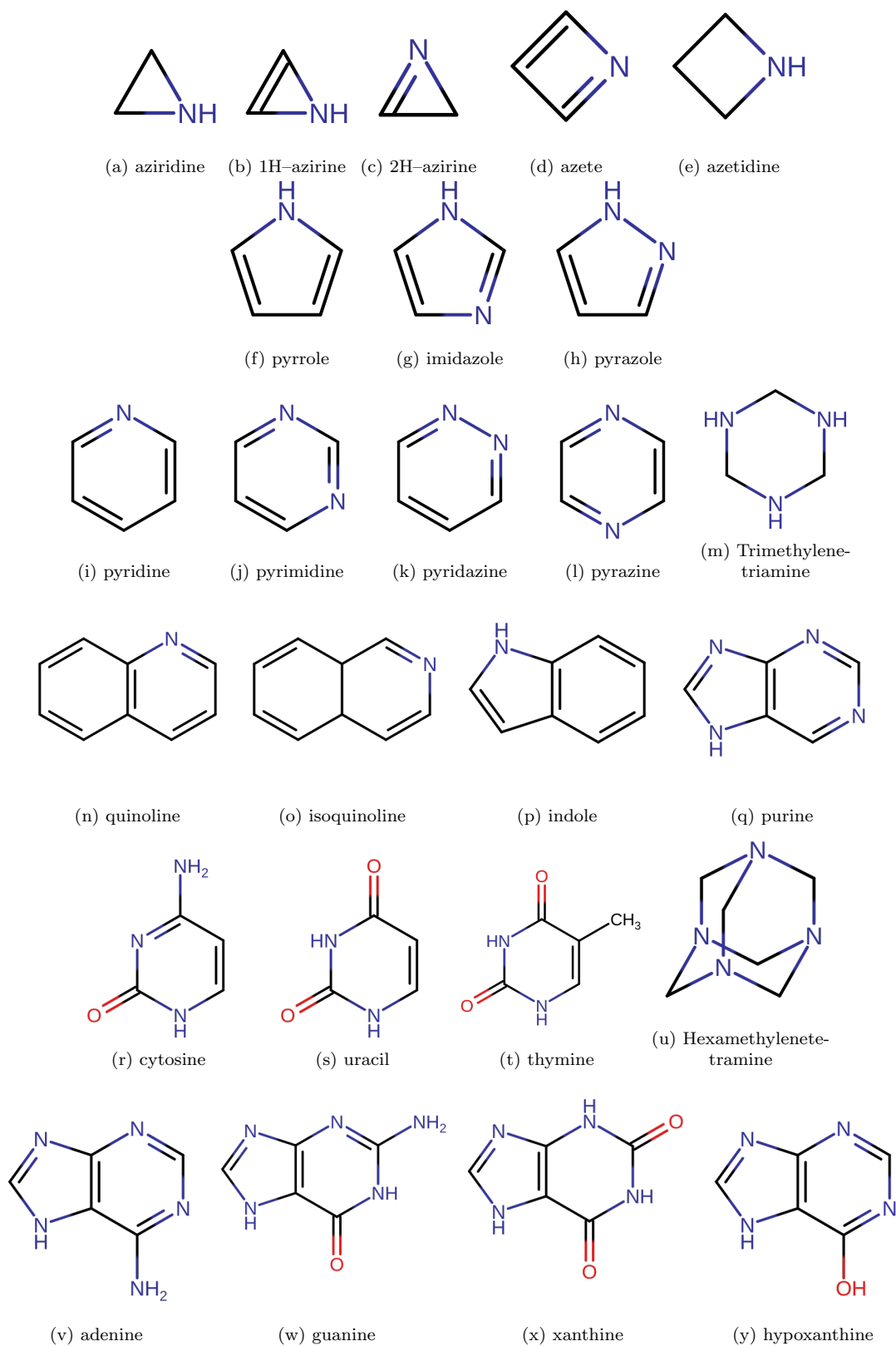


Figure 1.1: Structures of N-heterocycles discussed in the text.

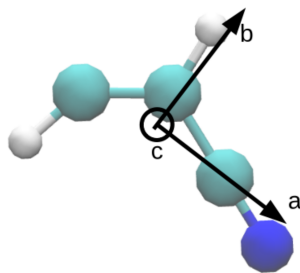


Figure 1.2: Principal molecular axes a , b , and c , where a and b are in the plane of the text and c is orthogonal.

As illustrated below, rotational energy levels are dependent on the mass and position of each atom, so even slight variations in structure produce different energy levels, and consequently the rotational spectrum of each molecule is unique. This molecular “fingerprint” is exploited in radio astronomy in order to unambiguously identify different species in space. For a linear rigid rotor, the Hamiltonian is

$$\hat{H} = \frac{\hat{J}^2}{2I} \quad (1.1)$$

where \hat{J} is the combined rotational, orbital, and electron spin angular momentum, and I is the moment of inertia, defined as

$$I = \sum_{j=1}^n m_j r_j^2 \quad (1.2)$$

where m_j is the mass of each atom j and r_j is the equilibrium distance between atom j and the center of mass. The associated energy eigenvalues are

$$E = BJ(J + 1) \quad (1.3)$$

B is known as a rotational constant, and is also dependent on a molecule’s inertia. In units of Hz,

$$B = \frac{h}{8\pi^2 I} \quad (1.4)$$

This is substantially more complicated for non-linear molecules, for which a single rotational constant is no longer sufficient. Instead, there are three rotational constants A , B , and C that are inversely proportional to the moment of inertia along the three principal molecular axes, with an example shown in Figure 1.2.

The general rigid rotor (RR) Hamiltonian for a nonlinear molecule is

$$\hbar^2 \hat{H} = X \hat{J}_x^2 + Y \hat{J}_y^2 + Z \hat{J}_z^2 \quad (1.5)$$

where \hat{J}_x is an operator corresponding to the projection of the angular momentum \hat{J} onto the x principal axis, and likewise for \hat{J}_y and \hat{J}_z . The \hbar^2 term on the left is a convention for expressing energies in units of rotational constants. Each operator \hat{J}_x , \hat{J}_y , and \hat{J}_z commutes with \hat{J}^2 , but not with each other, such that $[\hat{J}_x, \hat{J}_y] = \varepsilon_{xyz} i \hbar \hat{J}_z$.

In the symmetric top case, a molecule is either prolate ($A > B = C$) or oblate ($A = B > C$) and \hat{H} can be rewritten in a diagonal form:

$$\hbar^2 \hat{H} = \frac{X+Y}{2} \hat{J}^2 + \left(Z - \frac{X+Y}{2} \right) \hat{J}_z^2 \quad (1.6)$$

In the prolate case, $\{x, y, z\} \rightarrow \{b, c, a\}$ as a Type I^r representation, while in the oblate case $\{x, y, z\} \rightarrow \{a, b, c\}$ as a Type III^r representation. The eigenfunctions are $|J, K\rangle$, where J is again the angular momentum quantum number, and K is the projection of J onto the molecular symmetry (z) axis with allowed values $\{J, J-1, \dots, -J+1, -J\}$. Given the matrix elements,

$$\langle J'K' | \hat{J}^2 | JK \rangle = \hbar^2 J(J+1) \delta_{J'J} \delta_{K'K} \quad (1.7)$$

$$\langle JK | \hat{J}_z^2 | JK \rangle = \hbar^2 K^2 \delta_{J'J} \delta_{K'K} \quad (1.8)$$

the symmetric top energies are

$$E_{\text{prolate}} = BJ(J+1) + (A-B)K^2 \quad (1.9)$$

$$E_{\text{oblate}} = BJ(J+1) + (C-B)K^2 \quad (1.10)$$

The vast majority of the molecules mentioned within this work are the more complicated asymmetric tops, defined by rotational constants $A > B > C$. There is no generalized closed-form expression for rotational energy levels of asymmetric tops as there are for linear and symmetric tops. The Hamiltonian is generally written as

$$\hbar^2 \hat{H} = \left(\frac{X+Y}{2} \right) \hat{J}^2 + \left(Z - \frac{X+Y}{2} \right) \hat{J}_z^2 + \left(\frac{X-Y}{4} \right) ((\hat{J}^+)^2 + (\hat{J}^-)^2) \quad (1.11)$$

where $\hat{J}^+ = \hat{J}_x + i\hat{J}_y$ is a lowering operator and $\hat{J}^- = \hat{J}_x - i\hat{J}_y$ is a raising operator.

Using a basis set of symmetric top wavefunctions, the raising and lowering operators can be expressed within matrix elements as

$$\langle JK + 2 | (\hat{J}^-)^2 | JK \rangle = \hbar^2 \sqrt{(J - K)(J + K + 1)(J - K - 1)(J + K + 2)} \delta_{J',J} \delta_{K',K+2} \quad (1.12)$$

$$\langle JK - 2 | (\hat{J}^+)^2 | JK \rangle = \hbar^2 \sqrt{(J + K)(J - K + 1)(J + K - 1)(J - K + 2)} \delta_{J',J} \delta_{K',K-2} \quad (1.13)$$

This Hamiltonian has off-diagonal matrix elements in K , so it must be solved by explicit diagonalization. From the form of the matrix elements, the total matrix can be factored into series of $2J + 1$ dimensional blocks for each J , which are diagonalized separately. For the $J = 0$ energy level, all matrix elements are zero. For the $J = 1$ level, in the III^r representation, one block of the Hamiltonian matrix is:

$$\hat{H} = \begin{bmatrix} C + \frac{A+B}{2} & 0 & \frac{A-B}{2} \\ 0 & A+B & 0 \\ \frac{A-B}{2} & 0 & C + \frac{A+B}{2} \end{bmatrix} \left(\text{basis vector} \rightarrow \begin{bmatrix} \langle 1, -1 | \\ \langle 1, 0 | \\ \langle 1, 1 | \end{bmatrix} \right) \quad (1.14)$$

with the relevant basis vector shown on the right.

Diagonalization and solving the eigenvalue problem gives the three solutions $E_1 = A + B$, $B + C$, or $A + C$. Asymmetric top energy levels denoted $J_{K_a K_c}$, where “near” quantum numbers K_a and K_c describe the value of K for $A + B = A + C$, the prolate case, and $A + B = 2A$, the oblate case, respectively. For $J = 1$ in the III^r representation, $E(1_{10}) = A + B$, $E(1_{11}) = A + C$, and $E(1_{01}) = B + C$. For asymmetric tops under the rigid rotor approximation, this method of diagonalization and solving for eigenvalues provides analytical expressions for the rotational energy levels. A correlation diagram used to associate the asymmetric top energy level with the corresponding symmetric top energy levels is presented in Figure 6.33 of Ref 28. If a species has a non-zero electron spin angular momentum, the quantum number N is used instead of J ; N accounts for rotational and orbital angular momentum.

Transitions between rotational energy levels are related to the projection of the dipole moment along the principal axes (μ_a , μ_b , μ_c). Each non-zero dipole moment projection leads to a unique set of transitions: a -type transitions are associated with μ_a , b -type with μ_b , and c -type with μ_c . All transitions follow selection rule $\Delta J = 0, \pm 1$ and have the following ΔK selection rules:

$$\Delta K_a = \begin{cases} 0(\pm 2, \pm 4\dots), & a\text{-type} \\ \pm 1(\pm 3, \pm 5\dots), & b\text{-type} \\ \pm 1(\pm 3, \pm 5\dots), & c\text{-type} \end{cases}$$

$$\Delta K_c = \begin{cases} \pm 1(\pm 3, \pm 5\dots), & a\text{-type} \\ \pm 1(\pm 3, \pm 5\dots), & b\text{-type} \\ 0(\pm 2, \pm 4\dots), & c\text{-type} \end{cases}$$

The intensity of a rotational transition is dependent on both the magnitude of the electronic dipole moment and the population difference between the energy levels. This presents two limitations. The first is that totally symmetric molecules with no dipole moment are invisible within the applicable frequency range to radio telescopes, and molecules with weak dipole moments are also quite difficult to observe unless they are in high abundance. The second is that because rotational constants are inversely proportional to a molecule's moments of inertia, larger molecules have smaller rotational constants, leading to more closely spaced rotational energy levels. In this case, the rotational partition function is such that population is more evenly distributed between states, negatively impacting the intensities of individual rotational transitions. Despite these limitations, modern radio astronomy has been successful at identifying larger species with relatively weak dipole moments, most notably the recent detection of indene (C_9H_8), a bicyclic PAH with a total dipole moment of 0.62 D by both McGuire et al.²³ and Cernicharo et al.²⁴

The intensity of a particular transition is related to the total number of molecules along a given sight line, called the column density, given in units of m^{-2} or cm^{-2} . Assuming local thermodynamic equilibrium and an absorption feature, the column density is related to the observed optical depth by:²⁹

$$N_{\text{tot}} = \frac{3h}{8\pi^3|\mu_{lu}|^2} \frac{Q_{\text{rot}}}{g_u} \exp\left(\frac{E_u}{kT_{ex}}\right) \left[\exp\left(\frac{h\nu}{kT_{ex}}\right) - 1\right]^{-1} \int \tau_\nu d\nu \quad (1.15)$$

where N_{tot} is the total molecular column density, μ_{lu} is the transition dipole moment, Q_{rot} is the rotational partition function, g_u is the degeneracy of the upper level, E_u is the energy of the upper level, and ν is the frequency of the transition. Here, $\int \tau_\nu d\nu$ is the integrated optical depth with respect to frequency, and by definition has units of $[D^2/(Js)]cm^{-2}$. T_{ex} is the excitation temperature, defined as

$$T_{ex} = \frac{h\nu/k}{\ln\left(\frac{n_l g_u}{n_u g_l}\right)} \quad (1.16)$$

where n_l and n_u are the number densities in the lower and upper levels of the transition, respectively. For emission features, the integrated optical depth is replaced by an integral over source radiation temperature, $\int T_R dv$.

This definition shows the relationship between the observed rotational transition and the column density derived from it. Many other approximations are possible, for example, to take into account environments that are not in local dynamic equilibrium or for optically thin or thick lines of sight. For more details, see the 2015 review by Mangum and Shirley²⁹. When no molecular feature is detected, an upper limit on the column density can be derived by using a measure of the spectral noise (often a multiple of its standard deviation) over the frequency range of the line as the value of the optical depth.

The success of radio astronomy for astrochemistry is due in large part to the excellent radio telescopes that have been developed in the last 50 years. Particularly noteworthy for the field today are the Robert C. Byrd Green Bank Telescope (GBT) in West Virginia^b and the Atacama Large Millimeter/submillimeter Array (ALMA) in Chile's Atacama Desert.^c The GBT is the largest steerable single-dish telescope in the world at 100 m in diameter and covers a frequency range of 0.1 to 116 GHz. ALMA is an array of 66 separate antennas that uses interferometry for observations and currently operates from 84 to 950 GHz, although will be extended down to 35 GHz in the near future.

Laboratory spectroscopy and theoretical chemistry The complex chemical mixture within astronomical sources relevant to N-heterocycles results in a high density of lines, necessitating that rest frequencies for rotational transitions are known as accurately as possible. In reality, this cannot be done simply by solving the equations given above for energy levels because real molecules are not rigid rotors, and therefore energy level expressions are further complicated by centrifugal distortion (CD). CD terms add to the rigid rotor energy expressions as a power series in terms of J and K . This makes the accurate prediction of energy levels challenging, particularly for higher J (or N). The frequency range of most telescopes covers transitions between higher energy levels, so molecular detections in these regions are predicated on experimental measurements. A combination of laboratory spectroscopy and theoretical chemistry is therefore a prerequisite to observational radio astronomy for all but the simplest of molecules that can be identified by their astronomical spectra alone.

Stable, commercially available molecules are the easiest to target with laboratory spectroscopy from a practical standpoint. Most neutral N-heterocycles fall into this category, and therefore have known rotational

^b<https://greenbankobservatory.org/science/telescopes/gbt/>

^c<https://www.almaobservatory.org/>

spectra. In these cases, the compound of interest is the only carrier of rotational transitions within the instrument, and the theoretical need is a molecular structure that can be used to predict the rotational spectrum and aid in quantum number assignment. Low-level electronic structure methods like density functional theory (DFT) or second order Møller Plesset perturbation theory (MP2) are generally sufficient.

However, the conditions of space allow for long lifetimes of unstable molecules that are not easy to synthesize under terrestrial conditions. Potential precursors to N-heterocycles include radicals and ions, so characterizing the rotational spectra of these reactive species is necessary in order to determine astronomical abundances and eventual inclusion in chemical models. Reactive species are typically produced by subjecting one or more stable precursor molecules to harsh conditions, such as a plasma discharge, laser ablation, or pyrolysis (see, for example, Chapter 2 and Refs 30–32). However, such methods produce a wide array of products; this is well-illustrated in the recent exhaustive product analysis of three different benzene discharges;³⁰ at the time of publication 3300 spectral features had been identified and assigned to 152 different species.

When measuring the spectrum of a species produced in such a complex mixture, minimizing uncertainty of predicted rest frequencies is essential. The “gold standard” for such predictions are high-level *ab initio* electronic structure calculations at the coupled-cluster level of theory³³ with single and double excitations and perturbative treatment of triples [CCSD(T)],³⁴ employing a basis set that is at least triple zeta, such as the correlation-consistent polarized valence (cc-pVTZ)³⁵ or core-valence (cc-pCVTZ)³⁶ basis sets from Dunning. These calculations result in optimized geometries, from which equilibrium rotational constants are determined, and zero-point vibrational corrections, generally calculated with second order vibrational perturbation theory.³⁷ This level of theory generally produces extremely accurate rotational constants, often within 0.1% of experimental values, but is quite computationally expensive and scales up with the number of electrons as N^7 . The experimental complexity and computational cost associated with laboratory spectroscopy of reactive species has left a large number of potential N-heterocycle precursors without known rotational spectra; fulfilling this need is a key goal of this dissertation, as discussed in section 1.3.1.

Before proceeding with a discussion of astronomical searches for N-heterocycles, it is worth pointing out that not all molecules in space exist in the gas phase. Molecules are also known to be present on icy grain surfaces,^{38,39} particularly in low temperature regions like DMCs and outer envelopes of PPDs. Observations of these species are more difficult; rotational transitions cannot occur in the condensed phase, so observations are reliant on sightlines towards stars or protostars where vibrational and electronic absorption is possible. For this reason, only six species have been definitely detected: H₂O,⁴⁰ CO,⁴¹ CO₂,⁴² CH₄,⁴³ CH₃OH,⁴⁴ and

NH_3 ⁴⁵. Rather, our understanding of chemistry on icy grains has been developed by theoretical simulations, experiments on analogs of interstellar ice, and chemical models.

Previous observational attempts and discussion

There have been a large number of astronomical searches over the past four decades for a variety of N-heterocycles, none of which have resulted in a definitive detection. These are summarized in Table 1.1. Of the targeted sources, Sgr B2 and TMC-1 are DMCs, IRC + 10216, CRL 2688, and CRL 618 are CEs, and all other sources listed in Table 1.1 are HMCs.

Several of the searches did return tentative detections. These are listed in bold in Table 1.1. Observations of aziridine (Figure 1.1a) and 2H-azirine (Figure 1.1c), both 3-membered N-heterocycles, were reported by two different groups in 2001 towards five different HMCs in total. The survey done jointly with the Swedish ESO Submillimetre 15 m telescope, the Arizona Radio Observatory 12 m telescope, and the NASA Deep Space Network 70 m telescope (SEST/ARO/DESN)⁴⁶ covered non-contiguous frequency bands between 18 and 260 GHz included two tentative aziridine lines at 226.233 and 86.312 GHz, corresponding to $N_{K_a K_c} = 5_{50} - 4_{41}$ and $2_{11} - 1_{01}$, respectively, which were predicted to be some of the strongest aziridine transitions in the observed frequency range. These were seen towards HMCs G237.3-0.6 and G10.47+0.03. However, other aziridine transitions within the range covered were absent. The $9_{09} - 8_{18}/9_{19} - 8_{08}$ doublet at 249.420 GHz, predicted to be of similar intensity to the observed frequencies, was not observable due to overlap with a prominent methanol emission feature. The $5_{05} - 4_{14}/5_{15} - 4_{04}$ doublet at 142.375 GHz was also absent, potentially due to blending with a nearby OC^{34}S transition. The $3_{03} - 2_{12}$ and $3_{13} - 2_{02}$ lines at 88.740 and 88.964 GHz, respectively, were also not observed, suggesting the abundance inferred from the 226.233 and 86.312 GHz lines could actually be 2 – 5 times lower. Beam dilution towards the small hot core sources is also offered as a reason for the absence of these lines.

The National Radio Astronomy Observatory (NRAO) 12 m survey⁴⁷ resulted in single-line detections of both aziridine and 2H-azirine. A feature at 236.0 GHz was assigned to the blended $6_{15} - 5_{25}$ and $6_{25} - 5_{15}$ aziridine transitions toward Orion KL and W51 e1/e2. Orion KL was also included in the SEST/ARO/DSN survey, with no reported aziridine lines. A second line seen toward Orion KL and Sgr B2(N) was assigned to the 2H-azirine $6_{25} - 5_{14}$ transition at 226.2 GHz (the proximity to the aziridine line in the SEST/ARO/DSN survey is likely coincidence). Raw survey data are not publicly available for more detailed analysis, and no further details on other transitions were provided.

A tentative pyrimidine detection was also reported in survey performed with the James Clerk Maxwell

Table 1.1: Astronomical searches for N-heterocycles with their source, telescope, upper limit to the column density (N_T), year work was published, and the corresponding reference. In references where multiple lines were used for the column density calculations, the average is provided here. Tentative detections are listed in bold with the corresponding tentatively assigned column density.

Molecule	N_T (10^{13} cm $^{-2}$)	Source	Telescope	Year	Ref.
Aziridine	–	TMC-1(CP)	SEST 15 m, ARO 12 m, DSN 70 m	2001	46
		Orion KL	SEST 15 m, ARO 12 m, DSN 70 m	2001	46
		Orion 3'N	SEST 15 m, ARO 12 m, DSN 70 m	2001	46
	15.	G327.3-0.6	SEST 15 m, ARO 12 m, DSN 70m	2001	46
		L134N(C)	SEST 15 m, ARO 12 m, DSN 70 m	2001	46
		IRS 16293	SEST 15 m, ARO 12 m, DSN 70 m	2001	46
	3.– 6.	NGC 6334F	SEST 15 m, ARO 12 m, DSN 70 m	2001	46
	30.– 60.	Sgr B2(N)	SEST 15 m, ARO 12 m, DSN 70 m	2001	46
	5.	G10.47+0.03	SEST 15 m, ARO 12 m, DSN 70 m	2001	46
		W33A	SEST 15 m, ARO 12 m, DSN 70 m	2001	46
	3.– 6.	G31.41+0.31	SEST 15 m, ARO 12 m, DSN 70 m	2001	46
	3.– 6.	G34.3+0.2	SEST 15 m, ARO 12 m, DSN 70 m	2001	46
	1.7	Orion KL	NRAO 12 m	2004	47
	2.5	W51 e1/e2	NRAO 12 m	2004	47
2H-azirine	0.91	Sgr B2(N)	NRAO 12 m	2004	47
	0.82	Orion KL	NRAO 12 m	2004	47
Pyrrole	0.4	TMC-1	NRAO 36 ft	1980	48
	6.	Sgr B2	NRAO 36 ft	1980	48
	3.– 10.	Sgr B2	Bell 7 m, NRAO 140 ft	1980	49
	0.040	TMC-1	DSN 70 m	2001	50
		TMC-1	GBT	2018	22
	0.029	TMC-1	GBT	2020	51
Pyridine		Sgr B2	NRAO 36 ft	1973	52
		Orion KL	NRAO 36 ft	1973	52
	2.3	CRL 618	ARO 12 m	2005	53 ^d
	0.73	IRC + 10216	ARO 12 m	2005	53
		CRL 2688	ARO 12 m	2005	53
		TMC-1	GBT	2018	22
	0.59	TMC-1	GBT	2020	51
Pyrimidine		Sgr B2	NRAO 36 ft	1973	52
		Orion KL	NRAO 36 ft	1973	52
	36.6	Orion KL	JCMT	2003	54
	16.8	Sgr B2	JCMT	2003	54
	33.7	W51 e1/e2	JCMT	2003	54
		CRL 618	ARO 12 m	2005	53
		IRC + 10216	ARO 12 m	2005	53
4.2	TMC-1	GBT	2017	55	
Imidazole	0.6	TMC-1	Onsala 20 m	1981	56
	0.6	L 134 N	Onsala 20 m	1981	56
	13.	Ori A	Onsala 20 m	1981	56
	8.	DR 21 (OH)	Onsala 20 m	1981	56
	100.	IRC + 10216	Onsala 20 m	1981	56

Molecule	N_T (10^{13} cm $^{-2}$)	Source	Telescope	Year	Ref.
Quinoline	2.2	IRC + 10216	ARO 12 m, IRAM 30 m, GBT	2005	53
	8.7	CRL 618	ARO 12 m, IRAM 30 m, GBT	2005	53
	3.6	CRL 2688	ARO 12 m, IRAM 30 m, GBT	2005	53
	6.2	TMC-1	GBT	2017	55
Isoquinoline	2.3	IRC + 10216	ARO 12 m, IRAM 30 m, GBT	2005	53
	27.	CRL 618	ARO 12 m, IRAM 30 m, GBT	2005	53
	11.	CRL 2688	ARO 12 m, IRAM 30 m, GBT	2005	53
	0.094	TMC-1	GBT	2017	55
Uracil	6.0	Sgr B2	ARO 12 m, IRAM 30 m	2006	57

15 m telescope (JCMT) toward HMC W51 e1/e2 at 342.3 GHz,^{47,53,54} corresponding to a $J \leq 55$ band-head between 342.2899 and 342.2974 GHz that contains 32 separate transitions. The nearby $J \leq 54$ band-head at 336.1 GHz was absent in the observations, as was the $27_{27,1} - 26_{26,0}$ and $27_{27,0} - 26_{26,1}$ blended transition at 338 GHz. The other $J \leq 55$ band-head at 348.4 GHz was reported to be “smeared out by a nearby interloper”⁴⁷ so it is not clear if a line is also present here. They suggest that a low rotational temperature would make the 342.3 GHz line more intense than the 348.4 GHz transition.

Speaking purely to the feasibility of observing N-heterocycles, and not to their potential to exist in a particular environment, there are a two main points that can be drawn from this set of attempted observations.

- There has been no observing campaign dedicated specifically to the search for N-heterocycles, and past searches have not been particularly systematic. For example, the tentative detections of aziridine and 2H-azirine were never followed up with deeper searches in other environments and with better radio telescopes; these species have never been searched for outside of hot cores, despite being the simplest N-heterocycles and the detections of three-membered oxygen-containing heterocycles toward both HMCs^{58,59} and DMCs.⁶⁰
- As discussed in the description of the SEST/ARO/DSN survey,⁴⁶ the angular resolution required for observations of small hot core regions is higher than what was achievable by any of the facilities used for their survey. This is the case for all of the telescopes listed in Table 1.1. The low angular resolution compared to the size of the HMC sources causes the intensity of molecules that are only in the hot core and not the surrounding cloud to be washed out. This effect becomes more severe at lower frequency, which can complicate confirmation of tentative detections made at higher frequency. Future observations of hot cores with ALMA, which can achieve a much higher angular resolution than any single dish facility, are highly desirable.

As to the first point, there are other species that should be targeted, particularly in light of the recent detections of aromatics in TMC-1 and other DMCs. Benzonitrile has now been shown to be abundant in multiple DMCs,⁶¹ and other cyano-aromatics have also been observed, including 5-membered cyanocyclopentadiene⁶² and bicyclic cyano-naphthalene.²³ Rotational spectra of cyano-pyridine^{63–65} and cyano-pyrrole^{66,67} are available in the literature, although the resolution of the cyanopyrrole lines may not be sufficient for modern astronomical methods, such as line-stacking.⁶⁸ An extensive literature search did not reveal any experimental rotational spectroscopy of other cyano-functionalized N-heterocycles, including cyano-quinoline, cyano-pyrimidine, cyano-indole, or cyano-purine, preventing astronomical searches for these species. The pure hydrocarbon indene has also recently been detected in TMC-1,^{24,25} so future observations should include indole (Figure 1.1p), for which a rotational spectrum has been published.^{69,70} It is also interesting that neither pyrrole, quinoline, nor isoquinoline has been included in any of the searches towards HMCs; this should be remedied in future ALMA surveys.

1.2.2 Reaction discovery and characterization

Even if a N-heterocycle is eventually detected in space, knowing its current abundance would not actually tell us how that species formed or how long its lifetime might be. Knowledge of both formation and destruction pathways is essential to understand how individual molecules influence their local chemical network, as well as the interplay between chemistry and the astrophysical environment. To this end, the study of these reaction paths is another necessary aspect of astrochemistry. There are essentially two parts to the study of reaction paths; finding new reactions, and then studying their kinetics to determining rate constants and branching ratios.

The discussion below reviews the N-heterocycle formation mechanisms that have been proposed within the literature. It begins with an overview of these methods and some fundamental principles, and then is followed by details on N-heterocycle forming reactions in the gas phase, on icy grain surfaces, and finally within meteorite parent bodies. Few have known rate constants or branching ratios, either measured experimentally or calculated with theory, but those will be provided where applicable.

Characterizing astrochemical pathways

Compared to the conditions of terrestrial chemistry, it might seem unrealistic for chemistry in cold regions of astrochemical interest to occur at all. However, the astronomical observations of DMCs demonstrate a rich chemical environment that cannot be explained by inheritance from chemistry occurring in higher

temperature regions like CEs. This is due to the intense UV radiation present in the bare ISM, which destroys almost all molecules before they could be incorporated into a DMC, with large PAHs being the main exception.⁹ For the case of N-heterocycles, their lifetime in the bare or diffuse ISM has been predicted to be on order hours.^{21,71} High dust concentrations within a DMC prevent substantial penetration of UV radiation.¹³ Because molecules from DMCs are known to be incorporated into rocky bodies within PPDs,⁷² the study of low temperature chemistry is vital to unraveling the chemical networks of DMCs and the chemical inventory present for early planet formation.

With temperatures as low as 10 – 20 K in these regions, operative chemical pathways are kinetically, rather than thermodynamically, controlled; the heights of the energetic barriers are more important than the relative energy of the products, as long as the reaction overall is exothermic. This can be illustrated with the Arrhenius equation, $k = Ae^{(\frac{E_a}{k_B T})}$, where k is the rate constant, A is an experimentally-determined pre-exponential factor, E_a is the barrier energy, k_B is Boltzmann’s constant and T is temperature. At 15 K, the exponential factor for a reaction with a 1 kJ/mol barrier is three orders of magnitude lower than at room temperature (298 K); for a reaction with a 10 kJ/mol barrier, the 15 K exponential factor is 33 orders of magnitude lower than at room temperature. Pathways that are effectively barrierless, where the reactant energy is greater than that of any transition state or barrier, are therefore very important in these environments, as are those where quantum-mechanical tunneling through barriers is possible. The Arrhenius equation is no longer valid in these scenarios; rate constants generally have no temperature dependence for barrierless pathways and have been shown to increase dramatically at low temperatures if tunneling is possible (as described in detail in reviews 73 and 74). This leads to a reliance on detailed, accurate knowledge of the potential energy surface for prediction of rate constants. While there are theoretical approximations available to do this, such as with microcanonical transition state theory,⁷⁵ experimental quantification of temperature-dependent kinetic parameters is of the utmost importance due to the sensitivity of the rate constants to the absolute energies along the potential energy surface. Small errors in calculated structures lead to inaccurate energies, which can result in large errors in computed rate constants.

For bimolecular reactions (termolecular processes are virtually impossible in DMCs) of the form $A + B \longrightarrow C + D$, the relevant rate law is

$$-\frac{d[A]}{dt} = -\frac{d[B]}{dt} = k[A][B] \tag{1.17}$$

where k , the rate constant, is essentially a proportionality constant that describes how the rate of change of

the reactants relates to the concentration of the reactants. This rate constant is dependent on temperature, and often written as $k(T)$. Inclusion of accurate low-temperature rate constants in models makes the connection between current molecular abundances observed in clouds and their rate of change. This allows for the study of chemical evolution over time, instead of limiting our understanding to this particular moment in astrochemical history. However, the rate constant of the depletion of reactants alone is not sufficient, since many reactions have multiple channels. Therefore, if $A + B$ leads also to $E + F$, two separate rate constants are required to describe this reaction, one for the formation of $C + D$ and the other for $E + F$. The branching ratios that describe the relative product concentrations are related to these product-specific rate constants through

$$\frac{k_{C,D}}{k_{E,F}} = \frac{[C] + [D]}{[E] + [F]} \quad (1.18)$$

When it comes to finding new pathways and determining their rate constants and branching ratios, the interplay of theory and experiment is crucial. Theoretical and computational chemistry provide the tools to develop approximations of potential energy surfaces (PESs) that describe all the reaction channels starting from certain precursors. This can be done manually by systematically changing which atoms are bonded, or with more automated techniques such as *ab initio* molecular dynamics. Rice-Ramsberger-Kassel-Marcus (RRKM) calculations offer statistical approximations to determine unimolecular rate constants, which is used to study unimolecular reaction events within a complex mechanism.⁷⁶ Experimental methods, such as the CRESU technique⁷⁷, can provide accurate kinetics data over a range of temperatures for gas-phase reactions. Other experimental methods provide useful information on chemical dynamics, such as the crossed molecular beams technique,^{78,79} which is excellent for reaction discovery but not kinetics. Experimental work on ice-surface chemistry can also provide the kinetics of product formation,⁸⁰ generally by measuring the formation of species over time with infrared spectroscopy, but the accuracy and astrophysical relevance is very dependent on the composition of the ice, making these experiments more difficult than pure gas phase ones.

Gas-phase N-heterocycle formation

Besides the requirement that a gas-phase low-temperature reaction pathway be exothermic and either barrierless or amenable to tunneling mechanisms through any barriers, it is also advantageous if the reaction results in two products. This is because excess energy can be converted into kinetic energy in the dissociation process, whereas in single product reactions, collisional relaxation or radiative relaxation in the form of spontaneous emission is required to prevent the reverse reaction from occurring. Collisional relaxation in

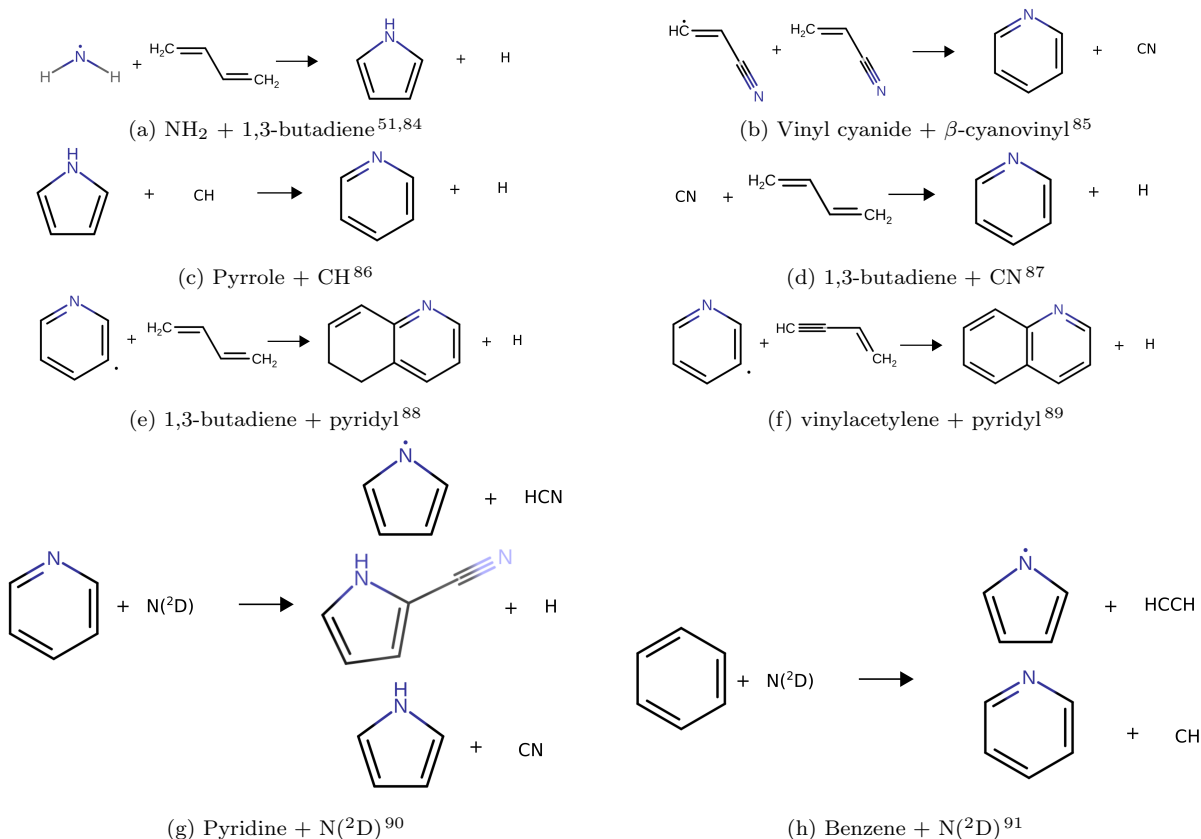


Figure 1.3: Gas-phase, neutral-neutral N-heterocycle formation pathways.

these low density regions is too slow for this to be a means of stabilizing a single product. Radiative association reactions occur when a single product is formed and then stabilized by the release of a photon. In reactions that result in species of ~ 10 atoms or more, the rate of radiative relaxation is competitive with the rate of dissociation back to reactants,⁸¹ therefore a barrierless bimolecular N-heterocycle forming reaction could potentially lead to a stabilized single product. While several of the ion-neutral reactions discussed in the second section below do fall into the radiative association classification, the majority of products are stabilized through the dissociation of a small byproduct. All the reactions are effectively barrierless, with the exception of several that do not currently have calculated PESs but are likely barrierless due to the nature of the reactants. This discussion is mostly limited to the formation of the pure N-heterocycles; there have been other formation mechanisms proposed that solely form nucleobases (see, for example Gupta et al.⁸² and Majumdar et al.⁸³), but analyzing reactions that only form specific biological molecules is not so useful for this systematic overview.

Neutral-neutral Schematics of the gas-phase, neutral-neutral N-heterocycle forming pathways are shown in Figure 1.3. The reactions are arranged such that 1.3a to 1.3e scale up in product size from pyrrole to quinoline, while the last two reactions involve a ring extraction or replacement reaction.

$\text{NH}_2 + 1,3\text{-butadiene (C}_4\text{H}_6)$, Figure 1.3a, is believed to form pyrrole and an H atom.^{51,84} Pyrrole was identified in a plasma discharge source beginning with NH_3 and 1,3-butadiene. The exact formation mechanism and PES have not been further studied, so it is only speculated that $\text{NH}_2 + 1,3\text{-butadiene}$ are indeed the reactants that lead to the detection of pyrrole. Collisional relaxation is definitely possible within the plasma discharge, so NH could have been the other reactant, or NH_2 could have reacted with a 1,3-butadienyl radical after it underwent an H abstraction.

In Figure 1.3b, neutral vinyl cyanide $\text{C}_2\text{H}_3\text{CN}$ combines with its radical derivative, β -cyanovinyl $\text{C}_3\text{H}_2\text{CN}$, and forms pyridine and the cyano radical, CN.⁸⁵ Pyridine was detected in a pyrolytic reactor where vinyl cyanide and nitrosobenzene were mixed. Nitrosobenzene likely was pyrolyzed to the phenyl radical, which then abstracted a H from vinyl cyanide to produce the β -cyanovinyl species. Kinetics information or height of reaction barriers could not be determined directly from the experiment, but accompanying DFT calculations at the B3LYP/cc-pVTZ level of theory with single point energies calculated CCSD(T)/cc-pVTZ (B3LYP/cc-pVTZ//CCSD(T)/cc-pVTZ) showed a barrierless pathway to pyridine. Further kinetics experiments or calculations have not been performed on this reaction.

The reaction of pyrrole with the methyldyne radical, CH, (Figure 1.3c) was explored with the PIMS technique.⁸⁶ Isotopic substitution showed no H rearrangement upon CH insertion. H elimination from the nitrogen follows the ring expansion. This work does not include a calculated PES or kinetics, but points to several other studies of CH reacting with hydrocarbons in a barrierless, highly exothermic pathway.^{92,93}

Figure 1.3d shows the pyridine forming reaction between CN and 1,3-butadiene.⁸⁷ This was investigated with the crossed molecular beam technique and supplemented with electronic structure (B3LYP/cc-pVTZ//CCSD(T)/cc-pVTZ) and RRKM calculations, which allowed for predictions of unimolecular rate constants and branching ratios. Between their experimental detections of pyridine and their calculations, they suggest that the branching fraction of the pyridine forming channel is 3-6%, while the main product is 1-cyano-1,3-butadiene.

Both 1,4-dihydroquinoline and 1,4-dihydro(iso)quinoline were detected under single-collision conditions in a crossed-molecular beams experiment from the reaction of 1,3-butadiene and the pyridyl radicals (Figure 1.5g to 1.5i).⁹⁴ Complementary calculations at B3LYP/6-311+G*//CCSD(T)/6-311+G(2d,2p) were performed to characterize the pathways. The entrance channel for each reaction was calculated at $\omega\text{B97X}/6\text{-}$

311+G**//CCSD(T)/6-311+G(2d,2p) to better capture the long range interactions. RRKM theory was again employed to calculate unimolecular rate constants and branching ratios over collision energies from 0 to 30 kJ/mol. For the ortho- and meta-pyridyl reactions, the main product is predicted to be 1,4-dihydroquinoline. For the para-pyridyl reaction, though, 1,4-dihydro(iso)quinoline is predicted to be dominant at low collision energies and decreases as collision energy increases.

Very recently, quinoline and isoquinoline were detected after the reaction of the three pyridyl radicals and vinylacetylene (H_2CCHCCH),⁸⁹ using the same pyrolytic reactor setup as the vinyl cyanide + cyanovinyl work.⁸⁵ PESs were developed at the B3LYP/6-311G(d,p) level with additional energy corrections at CCSD(T)/6-311G(d,p) and MP2/6-311G(d,p) within the G3(MP2,CC) model. RRKM calculations were done to predict unimolecular rate constants and branching ratios. Ortho-pyridyl was shown to form solely quinoline, meta-pyridyl to form both quinoline and isoquinoline, and para-pyridyl only formed isoquinoline.

Pyrrole, 2-cyanopyrrole, and 1-pyrrolyl were found to form in the reaction of pyridine with $\text{N}(^2\text{D})$, which was studied with the crossed molecular beam technique and theoretical calculations at the B3LYP/aug-cc-pVTZ//CCSD(T)/aug-cc-pVTZ level of theory.⁹⁰ This is a rather unique reaction compared to the ones previously discussed, as pyrrole derivatives are formed after eliminating a carbon from a pyridine ring, in almost a reverse reaction of the one shown in 1.3c. Besides the three most abundant N-heterocyclic products are shown in Figure 1.3g, minor channels were thought to form diazo-1,3-cyclopentadiene, 1H-imidazole radical, 1H-pyrazole radical, meta-pyridinyl nitrene, and pyrimidine. H-elimination channels were also observed and were shown to account for 65% of the total reactions, with almost the full 35% remaining leading to 1-pyrrolyl + HCN.

Interpretation of the above reaction was helped in part by a similar system, benzene + $\text{N}(^2\text{D})$, that has been studied purely with theory.⁹¹ All structures were calculated with B3LYP, CAM-B3LYP, MO6-2X, and $\omega\text{B97X-D}$ and the 6-311+G(d,p) basis set. Energy calculations were also performed at CCSD(T)/CBS, where cc-pVDZ, cc-pVTZ, and cc-pVQZ were used to estimate the complete basis set limit. RRKM calculations were used to calculate unimolecular rate constants and branching ratios. The reaction paths are split between one that first adds nitrogen within the ring to form a seven-membered ring intermediate and one which proceeds through a NH-benzene intermediate. The only N-heterocycle products to form are 1-pyrrolyl (with HCCH) and pyridine (with CH). The dominant channel ends with the formation of cyclopentadienyl radical and HCN, accounting for a branching fraction of 88.9% – 91.5%. 1-pyrrolyl and HCCH accounted for 5.8%–7.5%, while the branching fraction for pyridine was less than 0.5%.

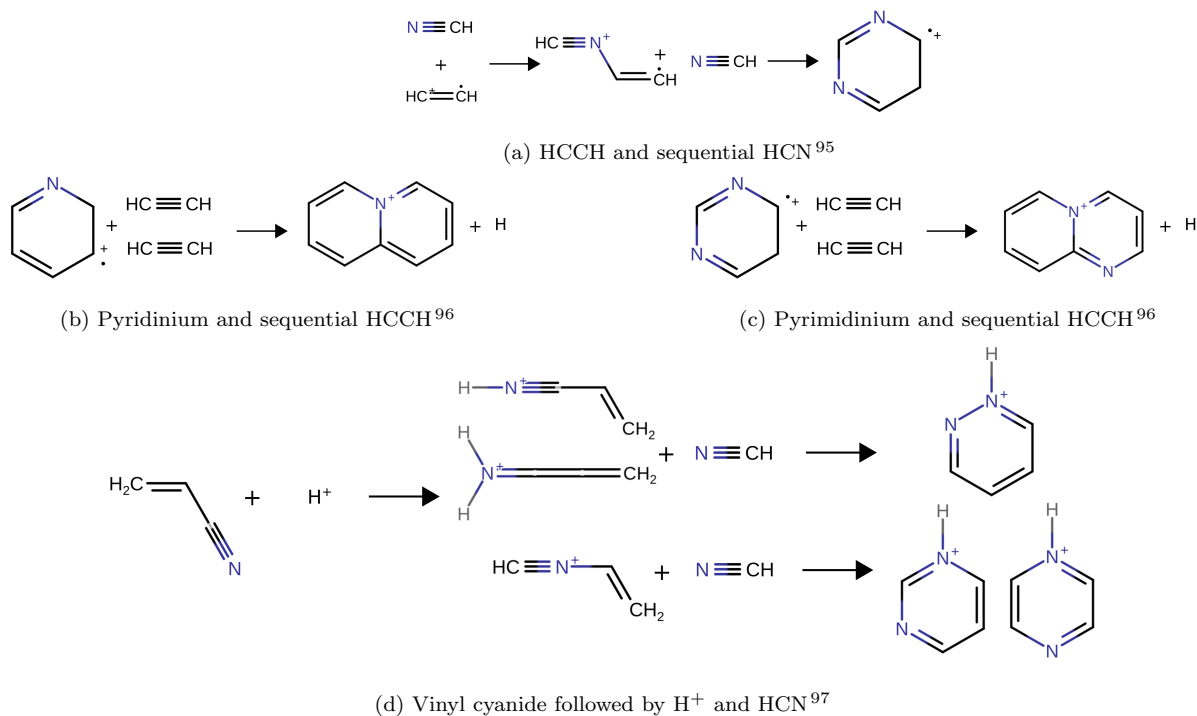


Figure 1.4: Gas-phase, ion-neutral N-heterocycle formation or destruction pathways.

Ion-neutral Many studies, both experimental and theoretical, have included N-heterocycle ions or reactions between neutral N-heterocycles and ions. Among these, comparatively few have yielded pathways that are good candidates for astrophysical relevance; these are shown in Figure 1.4. Nevertheless, the details of these pathways give useful information regarding gas-phase reactivity of N-heterocycles and their derivatives, including fragmentation pathways^{98–100}, reactivity with atoms and small interstellar molecules,^{101–106}, determination of C–H bond strength,¹⁰⁷ and cyclization pathways within van der Waals clusters.¹⁰⁸ Such studies should be taken into consideration when incorporating N-heterocycles into astrochemical networks, but the following discussion will focus on astrophysically feasible formation pathways.

The first reaction shown in Figure 1.4a was explored experimentally with mass-selected ion mobility mass spectrometry by Hamid et al.⁹⁵. Their results showed the formation of the C₄H₄N₂ radical cation, which they confirmed to be pyrimidine radical cation through comparison of thermochemical equilibrium measurements of the detected C₄H₄N₂ association with HCN, to the association of HCN with the actual pyrimidine radical cation, measured separately. The proposed formation mechanism involves sequential addition of HCN to HCCH, first forming the HCNCHCH⁺ radical cation, followed by addition of a second HCN and the formation of the pyrimidine radical cation. A PES surface calculated at B3LYP/cc-pVTZ//CCSD(T)/cc-pVTZ from

the HCNCHCH^+ intermediate to the products is shown, with two barrierless paths to pyrimidine and one to pyrazine. Pyrimidine is suggested to be the favored product, although calculations of rate constants and branching ratios were not performed. Experimentally, this product was stabilized by third body collisions with the helium buffer gas, but in the ISM, the authors point out that radiative relaxation or the loss of a hydrogen or proton would be needed for stability. The size of the pyrimidine radical cation may allow radiative relaxation to be competitive with dissociation.⁸¹

The sequential addition of two HCCH molecules to both pyridine and pyrimidine radical cations was explored by Soliman et al.⁹⁶, shown in Figures 1.4b and 1.4c. These reactions were also studied with mass-selected ion mobility mass spectrometry, both as single reaction events in the gas phase and within pyridine-acetylene binary clusters and compared to the reactivity of the benzene radical cation. At room temperature, acetylene and benzene radical cation are unreactive, while covalent addition to pyridinium and pyrimidinium ions occurs with 6% and 100% efficiency with rate constants measured at 9.0×10^{-11} and $1.4 \times 10^{-9} \text{ cm}^3\text{s}^{-1}$, respectively. This trend suggests that cation rings with more nitrogen atoms are more likely to promote growth of additional rings, and that the addition to the pyridinium radical cation is barrierless. Further additions of HCCH are shown to be exothermic, but it is unclear if these steps include a barrier.

The final reaction shown in Figure 1.4d involves the protonation of vinyl cyanide followed by HCN addition to form pyrimidine (Figure 1.1j), pyridazine (Figure 1.1k), and pyrazine (Figure 1.1l). The protonated vinyl cyanide intermediate isomerizes to form either protonated vinyl isocyanide or the H_2NCCCH_2 chain. This chain, as well as protonated vinyl cyanide, lead to pyridazine cation after HCN addition, while protonated vinyl isocyanide and HCN can form either pyrimidine or pyrazine cation. This reaction was studied experimentally with an ion trap and liquid chromatography mass spectrometry and theoretically at B3LYP/6-311++G(d,p). The MEPs for the formation of these three N-heterocycle isomers were effectively barrierless, although the same considerations as mentioned for the reaction in 1.4a are relevant for the stabilization of the products.

Ice chemistry

DMCs are referred to as “dark” because they contain dust grains that scatter and absorb background starlight, making these clouds appear as amorphous dark clouds against the starry sky.¹³ These dust grains are another source of chemical complexity, and the interplay between gas and grain chemistry is one of the main concerns for many astrochemical models. In fact, the formation of H_2 , one of the most fundamental processes in all of astrochemistry, is known to occur mainly on grain surfaces.¹⁰⁹ Generally, it is known that

small species (H_2O ,⁴⁰ CO ,⁴¹ CO_2 ,⁴² CH_4 ,⁴³ CH_3OH ,⁴⁴ and NH_3 ⁴⁵, as mentioned above) are present within icy surfaces coating these grains, and it is likely that larger molecules condense rapidly onto grain surfaces at low temperatures.^{17,39} Photoprocessing of these ices by cosmic rays or as star formation begins is thought to form radicals, which are able to diffuse across the surface and react in succession to form complex organics. These are then sublimated into the gas phase as warming occurs with the formation of a HMC.³⁹

Perhaps the most intriguing study of ice surface chemistry in the context of N-heterocycles is the recent experimental work that demonstrated formation of a variety of N-heterocycles from only small precursors known to be present in icy grains. Beginning with the vapor deposition of H_2O , CO , NH_3 , and CH_3OH in a 5:2:2:2 ratio on an aluminum substrate that was cooled to 10 K, deuterium discharge lamps were then used to irradiate the ice surface with a photon flux that replicates the astrophysical irradiation over 10^{7-8} years. The sample was then analyzed with both FTIR during irradiation and mass spectrometry after, following temperature-programmed desorption (TPD) of the ices. The goal of this experiment was not to form N-heterocycles, but rather to replicate previous experiments with improved analytical methods and at colder temperatures. Despite this unbiased approach, they detected a wide variety of N-heterocycles, including imidazole (Figure 1.1g), pyrimidine (1.1j), purine (1.1q), and the biological nucleobases cytosine (1.1r), uracil (1.1s), thymine (1.1t), and adenine (1.1v). This marks the first time N-heterocycles were detected in astrophysical ice analogues from only the small precursors known to exist in interstellar ices. The authors suggest that because both pyrimidine and purine were found in much lower abundance than their nucleobase derivatives, the formation pathways of these nucleobases is unlikely to proceed through a pyrimidine or purine intermediate, but also highlight the need for additional studies to verify this. The potential for nucleobases to form through alternative means then addition to one of the prototypical N-heterocycles is especially interesting in light of the extensive body of work to show that if pyrimidine or purine is present within an astrophysical ice analogue, nucleobases can form after irradiation.¹¹⁰⁻¹¹⁵

Another study¹¹⁶ has demonstrated that both N- and O-heterocycles can be produced in a H_2O and NH_3 astrophysical ice analog that contains benzene and naphthalene. In this experimental setup, H_2O , NH_3 , and either benzene or naphthalene were deposited on a 15-25 K aluminum foil substrate before being irradiated, undergoing TPD, and finally analysis with gas chromatography mass spectrometry. Pyridine, quinoline, and isoquinoline were all detected, suggesting that ring scission followed by replacement of a carbon atom with a nitrogen from NH_3 is possible; however, like the work discussed above,¹¹⁷ specific mechanisms were not able to be determined in this setup.

Most recently, the multidentate N-heterocycle hexamethylenetetramine (HMT, Figure 1.1u) and sat-

urated six-membered ring trimethylenetriamine (TMT, Figure 1.1m) were formed by the irradiation of CH_3NH_2 and H_2O ice.¹¹⁸ Vapor deposition on a MgF_2/KBr substrate was followed by irradiation with a F-type microwave discharged hydrogen lamp. The ice samples were monitored with FTIR, followed by TPD and detection of products with mass spectrometry. While CH_3NH_2 is not definitely known to be present in icy grains, the authors argue that it is quite likely to be present based on how widely it has been detected in astrophysical environments and its similarity to CH_3OH , which is known to be present in ices. Similar to the study by Materese et al.¹¹⁶, the intention of this investigation was to produce N-heterocycles, so it is not particularly surprising that TMT and HMT were formed, particularly because these heterocycles are condensates of CH_3NH_2 . Neither of these species are among the N-heterocycles that have been detected on meteorites.⁷

Aqueous processing in meteorite parent bodies

While the vast majority of the work done to study astrophysical N-heterocycle formation has been in either the gas phase or on icy grains, it has also been suggested that meteoritic N-heterocycles could form via aqueous processing in the meteorite parent body. Naraoka et al.¹¹⁹ revealed the diversity of N-heterocycles on the Murchison carbonaceous chondrite by high-performance liquid chromatography/ultrahigh-resolution mass spectrometry of methanol-extracts from the meteoritic interior. They also found a wealth of aldehydes and ketones and suggested that aldol condensation, such as the Chichibabin synthetic route to pyridines¹²⁰ or the Radzisevski route to imidazoles¹²¹, could be responsible for the N-heterocycles.

Another potential route to meteoritic N-heterocycles is through the degradation of HMT. Vinogradoff et al.¹²² simulated aqueous processing of HMT by submitting it to temperatures up to 150° for multiple days (up to 31) under alkaline pH. HMT powder mixed with water at $\text{pH} = 10.0$ was used as the sample. A variety of functionalized pyrazines, pyrroles, pyridines, imadazoles, and pyrazoles were detected with GCMS, IR spectroscopy and X-ray absorption near edge structure spectroscopy using synchrotron radiation. While HMT it is unclear if HMT actually forms on icy grains or within a meteorite parent body itself, it has been shown to be a precursor worth further study for both ice chemistry and aqueous processing.

Discussion

There are a number of key points and trends that jump out in this examination of proposed reaction paths. Discussion of these also allows for general conclusions to be drawn pertaining to the search for astrophysical N-heterocycles.

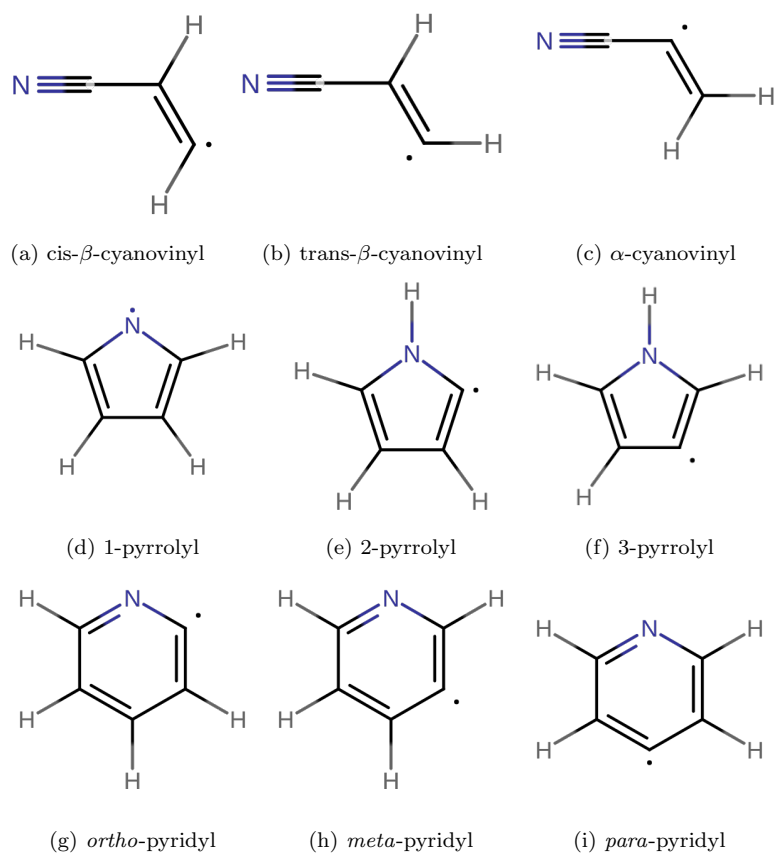


Figure 1.5: Structures of radicals discussed in the text.

- Perhaps most importantly, as was the case for astronomical searches, there lacks a systematic approach to studying astrophysical N-heterocycle formation. Most of the gas-phase work has focused on the formation of mono- or bicyclic six-membered rings, such as pyridine and pyrimidine, with pyrrole included in several neutral-neutral reactions but not among the ion-neutral products. The ion-neutral reactions are very limited in scope, with all pathways relying on HCN and/or HCCH addition. The products of these gas-phase reactions are not representative of the wide variety of simple N-heterocycles found on meteorites, without even consideration of various patterns of functionalization.

For ice surface and meteorite analogue chemistry, studies of HMT make up a large portion of the small body of work, despite the broader lack of evidence of its astrophysical relevance. Other potential complex N-containing species that could result in a similar variety of breakdown products should be explored.

Lastly, the detection of a variety of N-heterocycles formed within H₂O, CO, NH₃, and CH₃OH ice,¹¹⁷ while promising, was still limited to one ice composition. It is also unclear if the 5:2:2:2 ratio between the precursors is a good representation of actual icy grain surfaces. Therefore, directly connecting this result to astrophysical ices is impractical until it is shown that this wealth of N-heterocyclic species forms readily on multiple other, more astrophysically relevant ice analogues.

- Rate constants and branching ratios, which are essential for incorporation within chemical models, have been determined experimentally in only a single study of N-heterocycle formation (Soliman et al.⁹⁶, 1.4b, 1.4c). While theoretical methods are used to predict unimolecular rate constants for 1.3d, 1.3e, and 1.3f, these cannot take the place of an overall, experimentally measured bimolecular rate constant.
- Following from the previous point, the strong reliance on the B3LYP functional to calculate PESs introduces uncertainty about the accuracy of the structures and energies, particularly the transition states. This then propagates to uncertainties of the unimolecular rate constants and branching ratios. Benchmarking of density functionals has shown that B3LYP is actually one of the least accurate hybrid functionals when it comes to calculating reaction energies.¹²³ Some of these reactions are only calculated to be effectively barrierless by a small amount (just 1 kJ/mol in the Parker et al.⁸⁵ vinyl cyanide + cyanovinyl reaction, for example) so a high level of accuracy is important. The calculation of CCSD(T) energies of the B3LYP structures, which is almost universal amongst PESs, will not improve the overall accuracy if the structure itself is wrong. Other functionals have demonstrated much better performance for calculating structures and barrier heights; for instance, dispersion-corrected ω B97X

and M08HX.¹²³

Reflecting on the question of why N-heterocycles have not been detected in space, one distinct possibility is that they simply are not present in the gas phase, or at least not present in high enough amounts at any given time for detection to be possible. Perhaps they are unable to desorb from icy grains as temperatures rise in HMCs after either rapidly condensing onto icy grains after gas-phase formation in the low temperature DMCs, or after forming directly on the ice surface. It has recently been shown theoretically that N-heterocycles have higher binding energies within these ices than pure hydrocarbons.¹²⁴ It is also possible that the meteoritic N-heterocycles formed due almost exclusively to aqueous processing of HMT or a similar compound. When it comes to PANHs, the other evidence for astrophysical N-heterocycles, perhaps their formation only occurs if nitrogen is incorporated as PAHs grow within CEs, and not seeded from monocyclic N-heterocycles. This might then be followed by photolysis of the nitrogen-containing portion of the PANH within the unshielded diffuse ISM such that N-heterocycles are never included within PANH fragments in a DMC.

1.3 Significance of this work

The main goal of the work presented within this dissertation is to build the foundation for a systematic research program designed to gather as much information as possible about astrophysical N-heterocycles. Completion of this program requires significantly more time and effort in the future, but this is most likely necessary in order to detect N-heterocycles in space or have enough information to improve the accuracy of predictive chemical models through their inclusion.

This work is broken up into four components. The first, spectroscopic characterization, is covered in Chapters 2 and 3. AIMD simulations, the second component, are covered in Chapters 4 through 6. The others, kinetics experiments and astronomical searches, will be undertaken in the future and are discussed more in Chapter 7.

1.3.1 Spectroscopic Characterization

The first element of this approach is the spectroscopic characterization of important precursors, intermediates, and N-heterocycles that have no known rotational spectra. The need for this is twofold. As discussed in section 1.2.1, the majority of molecules detected in space have been identified by their unique rotational spectra. All the non-functionalized, closed-shell N-heterocycles shown in Figure 1.1 have been spectroscopically characterized (by vibrational spectroscopy for the molecules with no total electronic dipole moment).

However, there is very limited spectroscopic work on radical precursors or open-shell N-heterocyclic radicals. This is likely due to the fact that N-containing radicals are both difficult to produce in the laboratory and have complicated rotational spectra due to multiple sources of angular momentum coupling.

Measuring the spectra of these species will allow for them to be included in astronomical searches. Determining astronomical abundances of potential N-heterocycle precursors is a key aspect of incorporation within chemical models. Additionally, rotational spectra enable kinetics studies of reactive species with recently-developed instruments that combine microwave/millimeter wave spectroscopy with low-temperature uniform molecular beams.⁷⁴

The rotational spectroscopy of the β -cyanovinyl radical is discussed in Chapter 2. This radical was implicated in the formation of pyridine⁸⁵ (Figure 1.3b). While the α -cyanovinyl radical (Figure 1.5c) had been studied previously with rotational spectroscopy,¹ this was not only the first measured rotational spectra of the *cis*- (1.5a) and *trans*- β -cyanovinyl (1.5b) radicals, but also the first time they were ever detected experimentally. Theoretical structures of all three isomers were also calculated at the CCSD(T)/ANO1 level of theory for the first time.

Chapter 3 details the theoretical prediction of molecular structures and spectroscopic constants of the three pyrrolyl radical isomers (Figures 1.5d, 1.5e, 1.5f). The pyrrolyl radicals are photodissociation products of pyrrole, and 1-pyrrolyl was the main N-heterocyclic product formed in the reactions of both pyridine and benzene with N(²D) (Figures 1.3g, 1.3h). 1-pyrrolyl has previously been studied as a photodissociation product of pyrrole, but none of the isomers have been the subject of high resolution spectroscopy. Harmonic and anharmonic frequencies, rovibrational corrections, rotational constants, spin-rotation terms, and other hyperfine parameters were all calculated at the CCSD(T) level of theory in order enable experimental spectroscopy and eventually astronomical searches and kinetics experiments.

1.3.2 *ab initio* Molecular Dynamics

The second pillar of this project involves using an *ab initio* nanoreactor¹²⁵ in order to explore novel N-heterocycle formation and destruction pathways. This computational tool allows for the discovery of new chemical reactions without the limitations of human chemical intuition; this is ideal for the unearthy chemistry of the ISM and star-forming regions. The nanoreactor allows for the identification of a large number of potential N-heterocycle precursors and pathways, which will direct future spectroscopic characterization as well as kinetics experiments and astronomical searches.

Chapter 4 details AIMD simulations aimed at generating a large number of potential radical-neutral

precursors to pyrrole and pyridine. These simulations started with either pyridine or pyrrole, a CN radical, and He atoms as a buffer gas. The N-heterocycles were then broken down during the AIMD trajectories in order to search for formation pathways in reverse. 249 simulations with pyridine and 156 simulations with pyrrole were run in total. Future work is also discussed, including other types of N-heterocycles to study in this way.

Chapter 5 explores a pyrrole forming pathway inspired by a set of particularly astrophysically relevant acyclic precursors seen in a nanoreactor simulation. One precursor, ketenimine (H_2CCNH) is a higher energy isomer of the well-studied astrophysical molecule methyl cyanide (CH_3CN). H_2CCNH has been observed towards hot cores in Sgr B2.¹²⁶ The other precursor is β -cyanovinyl, discussed above as a precursor to pyridine, as well.

Two ring-insertion reactions are detailed in Chapter 6 that suggest a trend of building up larger rings from smaller ones. The first reaction starts with the 4-membered N-heterocycle, azete ($\text{C}_3\text{H}_3\text{N}$). In a reaction with the cyanomethyl radical (H_2CCN), pyrrole and CN are formed. In the second reaction, pyridine and CN are formed from the reaction of 1-pyrrolyl with cyanomethylene (HCCN).

1.3.3 Future Work

Chapter 7 discusses future goals, including experimental determination of rate constants and branching ratios and astronomical searches. The necessary prerequisites for both are discussed. Additionally, specific goals for the next steps with all four components of this project are laid out.

1.3.4 Relevance to Planetary Science and Combustion Chemistry

The significance of this project extends beyond its main purpose of solving the puzzle of astrophysical N-heterocycles. Gas-phase chemistry of N-heterocycles is also quite pertinent to planetary atmospheres, especially that of Titan, as well as terrestrial atmospheric and combustion chemistry.

Atmospheric Chemistry of Titan

Titan, one of the moons of Saturn, is perhaps one of the most chemically fascinating places in our solar system, and its atmosphere is particularly rich in nitrogen-containing species,¹²⁷ which have been identified via radio astronomy^{128,129} and Cassini's Ion Neutral Mass Spectrometer (INMS).^{130,131} The vast majority of Titan's atmosphere is made up of N_2 and CH_4 .¹³² Other N-containing species form after photodissociation or ionization of N_2 in the upper atmosphere, the products of which then react with CH_4 and other organics.

A large amount of the scientific interest in Titan has been as a proxy for early Earth,^{133,134} as one of the most promising places in the solar system to search for life,¹³⁵ and as a model for how prebiotic molecules could have formed on early Earth.¹³⁶ This last point has been one of the main drivers in the exploration of N-heterocycles on Titan. The INMS detected m/z ratios that match those of pyrrolyl, protonated pyridine, and protonated pyrimidine.¹³⁰ In laboratory investigations of the formation of tholins, the haze particles that give Titan its distinct orange glow, the INMS detected species with mass to charge ratios were found to match those of N-heterocycles and N-heterocycle radicals within the tholin analogues.^{136–140} Pyridine and pyrimidine were recently unsuccessfully searched for with ALMA as part of a successful search for cyclopropenylidene.¹⁴¹ Of relevance to the overall goals of this work, the authors note that the uncertainty over N-heterocycle formation pathways is preventing their incorporation in chemical models, and therefore our overall understanding of the role of N-heterocycles in Titan’s atmosphere.

Combustion of Biomass

Combustion processes occur when organic molecules are heated in the presence of oxygen. Since N-heterocycles are components of all biomaterial, they are present in the combustion of biomass or material derived from biomass, including coal, biofuels, and wildfires. Because combustion of N-heterocycles leads to the NO_x family of pollutants (NO , NO_2 , and N_2O), the oxidation pathways of the prototypical pyridine and pyrrole rings are of considerable interest (for example, see 142–145). Incomplete combustion of N-heterocycles is also known to lead to PANHs.¹⁴⁶ Radical intermediates are important in both of these processes, and kinetic modeling suggests both β -cyanovinyl and 1-pyrrolyl are formed in combustion of pyridine.¹⁴⁴ At present, combustion pathways of other N-heterocycles have not been investigated, so nanoreactor simulations of radical-neutral reactions of additional species will help to shed light on some of these combustion mechanisms.

Chapter 2

Rotational Spectrum of the β -Cyanovinyl Radical: A Possible Astrophysical N-Heterocycle Precursor

This chapter has been adapted from: Johansen SL, Martin-Drumel M-A, Crabtree KN. Rotational Spectrum of the β -Cyanovinyl Radical: A Possible Astrophysical N-Heterocycle Precursor. *J Phys Chem A*. 2019;123(24):5171-5177. doi:10.1021/acs.jpca.9b03798 © 2019 American Chemical Society

A fundamental question in the field of astrochemistry is whether the molecules essential to life originated in the interstellar medium (ISM) and, if so, how they were formed. Nitrogen-containing heterocycles are of particular interest because of their role in biology, but to date no N-heterocycle has been detected in the ISM and it is unclear how and where such species might form. Recently, the β -cyanovinyl radical (HCCHCN) was implicated in the low temperature gas-phase formation of pyridine. While neutral vinyl cyanide (H₂CCHCN) has been rotationally characterized and detected in the ISM, HCCHCN has not. Here we present the first theoretical study of all three cyanovinyl isomers at the CCSD(T)/ANO1 level of theory and the experimental rotational spectra of *cis*- and *trans*-HCCHCN, as well as those of their ¹⁵N isotopologues, from 5 to 75 GHz. The observed spectra are in good agreement with calculations, and provide a basis for further laboratory

and astronomical investigations of these radicals.

2.1 Introduction

The discovery of biological molecules such as amino acids,¹⁴⁷ nucleobases,^{5,6} and vitamins¹¹⁵ on meteorites with non-terrestrial isotopic abundances raises the possibility that such species are formed in space. Aromatic, nitrogen-containing heterocycles are a key building block for many of these molecules; however, while many N-containing species have been identified in space, to date N-heterocycles have not.

Potential astrochemical formation pathways of N-heterocycles include processing of icy grain mantles by UV radiation or cosmic rays¹¹⁶ and gas-phase pathways involving polymerization of hydrogen cyanide and acetylene.¹⁴⁸ These gas-phase mechanisms are unlikely to explain the abundance of N-heterocycles on meteorites, because this and similar polymerization mechanisms possess large activation barriers and therefore are unlikely to be operative in cold environments that are shielded from UV radiation. If not shielded, lifetimes are proposed to be only hours, as N-heterocycles are highly susceptible to UV photolysis.²¹

Searches for N-heterocycles in a variety of interstellar environments have been unsuccessful: pyridine, quinoline, and isoquinoline have been searched for in circumstellar shells,⁵³ pyrimidine in hot molecular cores,^{53,54} malonitrile, quinoline, isoquinoline, and pyrimidine in the molecular cloud TMC-1,⁵⁵ and uracil in molecular cloud Sgr B2(N).⁵⁷ These non-detections suggest that if N-heterocycles are produced in these regions, they are depleted rapidly by deposition or further chemical processing. However, benzonitrile, an aromatic molecule containing a nitrogen atom, was recently observed in TMC-1,²² marking the first interstellar detection of a species comparable to an N-heterocycle. The formation pathway of benzonitrile is unknown, but thought to be driven by low temperature radical-neutral reactions in the gas-phase. If so, similar pathways might exist for N-heterocycle formation.

Recently, pyridine was observed as a product of the pyrolysis of vinyl cyanide (C_2H_3CN , VyCN) and nitrosobenzene.⁸⁸ While the experiment was done at 1000 K, calculations suggest that pyridine was formed through the barrierless reaction of vinyl cyanide and the β -cyanovinyl radical ($HCCHCN$, β -CV), which may be feasible at the low temperatures of dense clouds. These environments are shielded from UV radiation and N-heterocycles could have lifetimes long enough to be incorporated into larger species, such as nitrogen containing polycyclic aromatic hydrocarbons, or deposited onto icy grain surfaces.

Radical-neutral formation pathways of 1,4-dihydroquinoline and 1,4-dihydroisoquinoline have also recently been proposed. These N-heterocycles were observed as products in the low temperature reaction of

1,3-butadiene and the pyridyl radical, which was calculated to be barrierless.⁹⁴ The authors suggest that pyridine, in the form of the pyridyl radical, is central to forming more complex nitrogen containing polycyclic aromatic hydrocarbons. These studies motivate further work to determine if such mechanisms are indeed operative in dense clouds. However, β -CV, one of the proposed pyridine precursors, has not only never been detected in space, but, to the best of our knowledge, has not been spectroscopically characterized at all.

VyCN has been studied extensively; the first rotational spectrum was published in 1959,¹⁴⁹ and it has been detected in molecular clouds such as Sgr B2(N) and TMC-1.^{150,151} Of its three radical derivatives, α , *cis*- β , and *trans*- β , (Figure 2.1) only the α -cyanovinyl radical (H_2CCCN , α -CV) has been characterized experimentally. Its rotational spectrum in the centimeter and millimeter bands has been reported,^{1,152} as well as its FTIR emission spectrum.^{153,154} The β -CV radical isomers have been considered in experimental and theoretical studies of VyCN UV photodissociation¹⁵⁵ and in the theoretical study of the gas phase reaction of VyCN and OH,¹⁵⁶ but no clear observation of these species exists.

Beyond their potential role in interstellar chemistry, CV radicals are likely involved in other chemical processes. Recently, ALMA was used to confirm the presence of VyCN in Titan’s atmosphere,¹²⁸ where radical-neutral reactions have been proposed to be significant.¹⁵⁷ VyCN is also a thermal decomposition product of a variety of plastics,¹⁵⁸ and there is ongoing research into the most environmentally safe catalytic combustion mechanisms of VyCN.¹⁵⁹ Both of these processes likely involve radical intermediates.

Here, we present the first *ab initio* theoretical structures of α , *cis*- β -, and *trans*- β -CV calculated at the same level of theory and the first experimental study of the rotational structure of the β -CV isomers. We have measured the previously unknown rotational spectra of the *cis*- and *trans*- β -CV radicals and their nitrogen-15 isotopologues using a combination of cavity Fourier-transform microwave (FTMW) spectroscopy and double resonance techniques. Using these experimental frequencies, interstellar searches for both *cis*- and *trans*- β -CV can now be undertaken. These results also enable further spectroscopic investigations, as well as kinetics and dynamics experiments.

2.2 Theoretical Methods

Quantum chemical calculations were performed using the CFOUR package¹⁶⁰ on the α -, *cis*- β - and *trans*- β -CV species. Starting geometries for the α and *trans*- β isomers were set to previously published DFT structures.¹⁵⁶ To the best of our knowledge, the geometry of the *cis*- β -CV isomer has not been previously calculated, so its initial geometry was set identical to *trans*- β -CV, except the HCCH dihedral angle was ro-

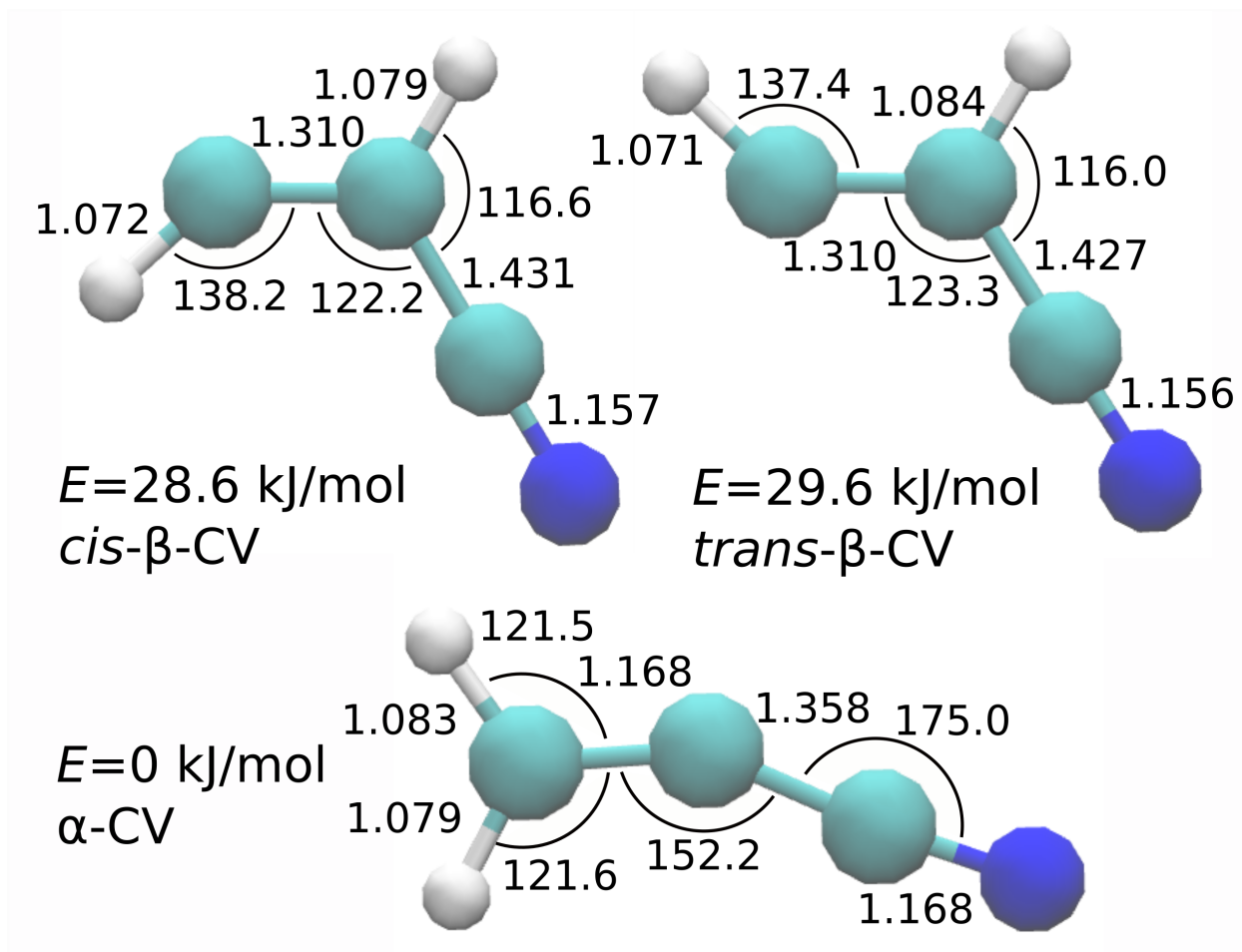


Figure 2.1: The CCSD(T)/ANO1 equilibrium structures of *cis*- β -CV (top left), *trans*- β -CV (top right), and α -CV (bottom). Bond lengths are in Å and angles in degrees. Here we define the α carbon as the carbon closest to the highest priority functional group (CN). The *cis* and *trans* isomers are defined by the relative positions of the terminal H and CN.

tated by 180° . Calculations were performed at the coupled cluster level of theory³³ with iterative inclusion of single and double excitations and perturbative inclusion of triple excitations [CCSD(T)]³⁴ using atomic natural orbitals (ANO) basis sets.¹⁶¹ Equilibrium geometries were first determined at the CCSD/ANO0 level, followed by CCSD(T)/ANO0, and finally at CCSD(T)/ANO1. While T_1 diagnostics,¹⁶² a measure of multireference character in the electronic wavefunction, were higher than is ideal for open-shell coupled cluster calculations, multireference configuration interaction (MRCI) calculations yielded similar results (see Supplemental Information for further detail). Anharmonic vibrational frequencies, zero-point vibrational corrections to the rotational constants, and centrifugal distortion terms were calculated at the CCSD(T)/ANO0 level by second order vibrational perturbation theory³⁷ with cubic force fields. Spin-rotation tensor elements (e.g., ϵ_{aa} , ϵ_{bb} , ϵ_{cc}) were calculated at the CCSD(T)/ANO0 level. First order properties, calculated at the CCSD(T)/ANO1 level, included spin-spin coupling and Fermi contact terms (e.g., T_{aa} , T_{bb} , a_F) for both H nuclei and the N nucleus, as well as N-quadrupole coupling terms (e.g., χ_{aa} , χ_{bb}). All coupled cluster calculations used unrestricted Hartree-Fock as a reference.

2.3 Experimental Methods

VyCN (99% purity) was purchased from Sigma Aldrich (CAS#: 107-13-1) and ^{15}N -substituted VyCN (98% purity) was purchased from Cambridge Isotope Laboratories. The following methods were performed using both normal and isotopically substituted VyCN. Samples were prepared by introducing 1 g of liquid VyCN into an evacuated 7 L gas cylinder which was filled to 200 psi with Ne, yielding 2% VyCN by pressure before being further diluted with Ne in a 1:2 ratio in a gas delivery manifold.

This sample was then expanded through a pulsed discharge nozzle^{31,163,164} operating at 6 Hz, yielding a total flow rate of 15 – 50 standard cubic centimeters per minute. The optimal voltage of the discharge source required to produce the CV species was approximately 1.5 kV. From the nozzle, the gas underwent an adiabatic supersonic expansion into a vacuum chamber. This expansion is collision-free and typical rotational temperatures of $\sim 1 - 2$ K are obtained by the time the sample reaches center of the chamber.³¹

Rotational spectra were measured with a 5 – 43 GHz Fabry-Perot cavity Fourier Transform microwave (FTMW) spectrometer,¹⁶⁵ which consists of two 14 in. diameter mirrors that surround the expanding gas coaxially. Species with rotational transitions near the resonance frequency of the cavity are polarized with a near-resonant microwave pulse, and resultant free induction decays are digitized and processed with a Fourier transform to yield the frequency spectrum.¹⁶⁶

The program SPCAT¹⁶⁷ was used to predict the rotational spectra of *cis*- and *trans*- β -CV using our calculated structures and spectroscopic parameters. For each species, a survey was undertaken over a range of $\pm 1\%$ around the predicted frequency of the fundamental *a*-type transition ($N_{K_a K_c} = 1_{01} - 0_{00}$). Unknown lines detected in this survey were remeasured without the discharge to verify that they disappeared without the plasma, and then with the application of a magnetic field to determine if the carrier was open-shell, as the line profile of transitions of open-shell molecules are significantly altered by the Zeeman effect. The same process was repeated to find the $2_{02} - 1_{01}$, $3_{03} - 2_{02}$, and $4_{04} - 3_{03}$ transitions, all of which were in the range of the cavity spectrometer.

Double resonance (DR) techniques, depicted in Figure 2.3, were used to verify our assignments of the *a*-type transitions and to find *b*-type transitions out of the range of the spectrometer. In a DR experiment, one line is monitored in the cavity while the sample is irradiated perpendicular to the cavity axis by a second (probe) microwave frequency. When the probe frequency matches that of a transition sharing a quantum state with the monitor line, the intensity of the monitor line is depleted. This technique is described in more detail elsewhere.¹⁶⁸ The use of various multiplier chains coupled with a DC to 40 GHz microwave synthesizer enabled searches for transitions up to 210 GHz.

2.4 Results and Discussion

Of the three CV isomers, α -CV was calculated to be the lowest in energy, with *cis*- and *trans*- β -CV 28.6 kJ/mol and 29.6 kJ/mol higher, respectively (Figure 2.1). The calculated barrier between *cis*- and *trans*- β -CV is 22.2 kJ/mol (Figure 2.4). CCSD(T) and MRCI calculations predict all species to be planar with C_s symmetry, although the previous α -CV results¹ suggest that there should be two non-planar geometries with the terminal hydrogens bent out of plane. Computational searches for a non-planar equilibrium structure of α -CV with both CCSD(T) and MRCI methods were unsuccessful. All CV isomers are near-prolate asymmetric tops with μ_a greater than μ_b ($\mu_a = 3.72, 3.18, 4.91$ D and $\mu_b = 0.18, 0.40, 1.47$ D for α -, *cis*- β -, and *trans*- β -CV, respectively).

The calculated geometries yield equilibrium rotational constants A_e , B_e , and C_e , and we obtained predictions for the ground state rotational constants A_0 , B_0 , and C_0 by including vibration-rotation interaction terms calculated from the anharmonic force fields. Together with calculated quartic centrifugal distortion constants, we simulated the $N_{K_a K_c}$ rotational levels for all CV isomers. Each of these levels is expected to be split by spin-rotation and other hyperfine interactions, as will be discussed in more detail later. Full lists

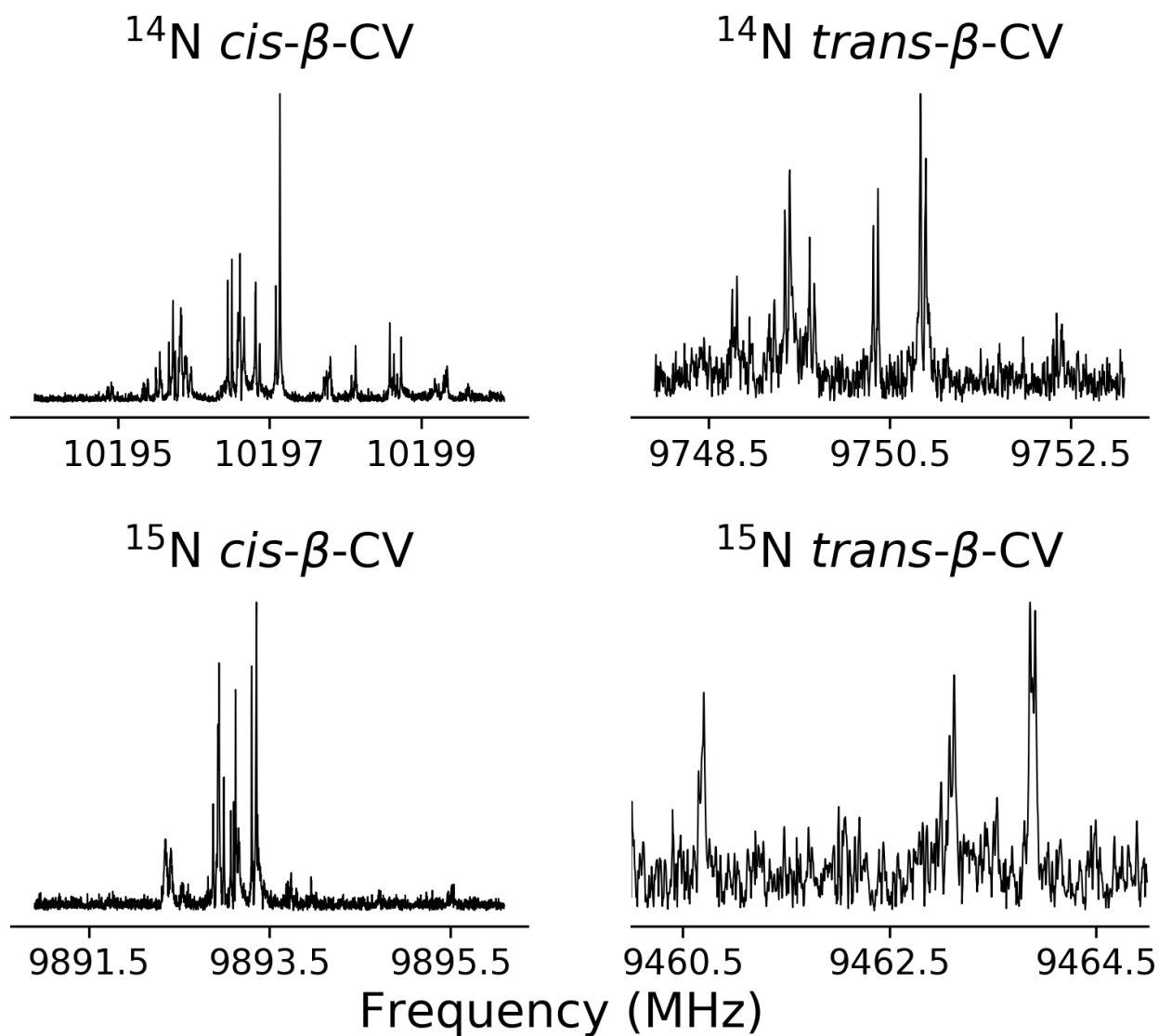


Figure 2.2: Fundamental α -type transition ($N_{K_a K_c} = 1_{01} - 0_{00}$) of each isomer and isotopologue of β -CV. The $trans$ - β -CV transitions are weaker than those of the cis - β -CV by about an order of magnitude. Only the strongest $trans$ - β -CV spin-rotation component is shown.

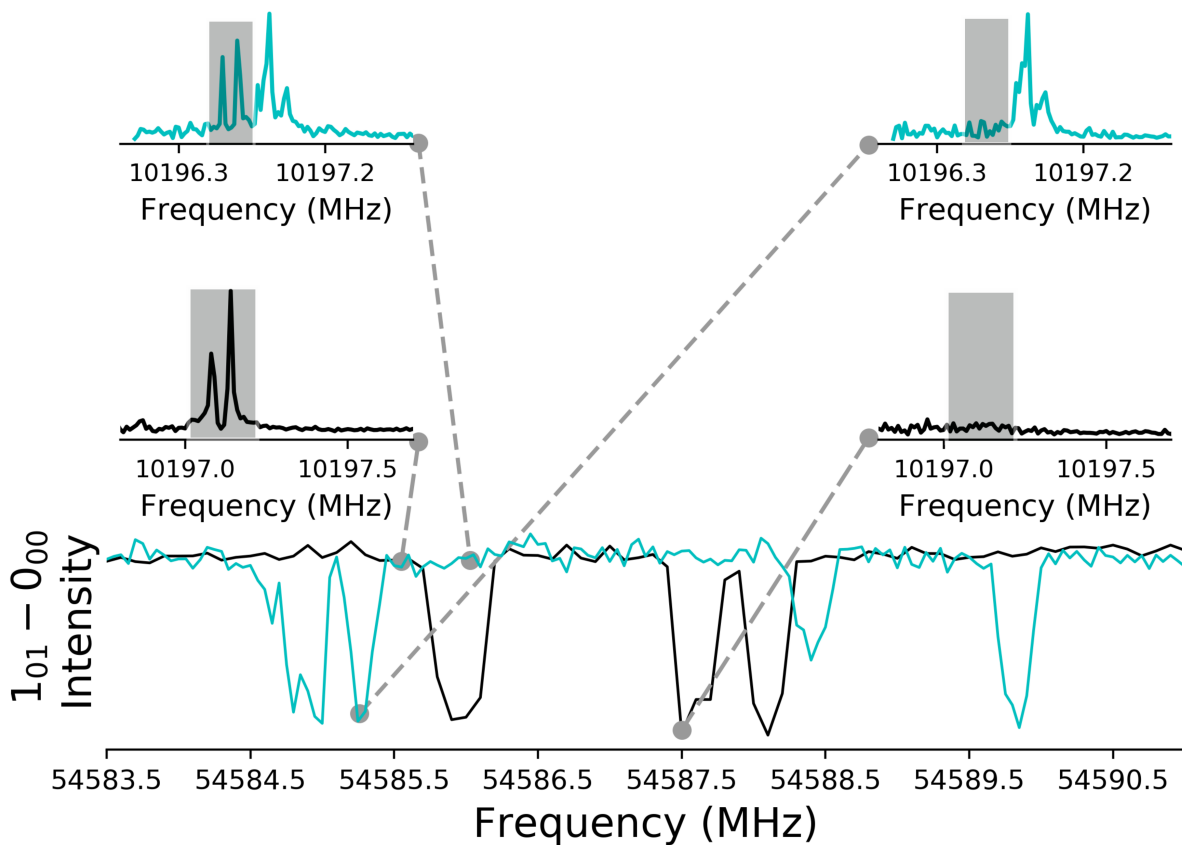


Figure 2.3: Hyperfine components of the $1_{11} - 0_{00}$ *b*-type transition of *cis*- β -CV recorded using the DR technique. Insets show the 10196.5 and 10197.1 MHz monitor components of the $1_{01} - 0_{00}$ line when the probe frequency was non-resonant (left) and resonant (right). Substantially more lines were detected in the $1_{11} - 0_{00}$ transition; here only the lines linked to two of the $1_{01} - 0_{00}$ lines are shown.

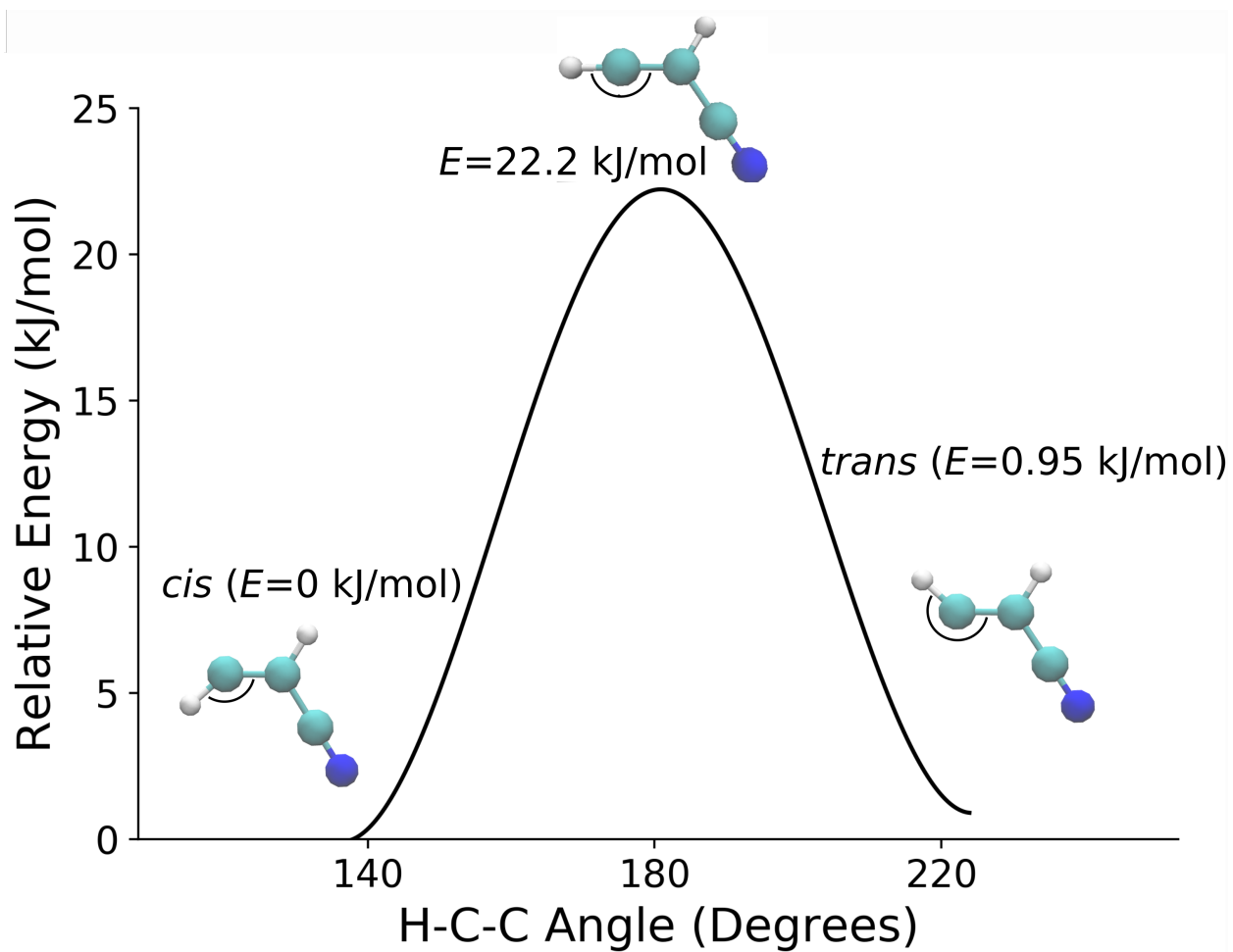


Figure 2.4: CCSD(T)/ANO0 minimum energy path between *cis*- and *trans*- β -CV. Equilibrium geometries along the path were calculated with the terminal H-C-C bond angle frozen. All structures are planar, and the transition state H-C-C bond angle is 180° . The barrier height is 22.2 kJ/mol, and *trans*- β -CV is 0.95 kJ/mol higher in energy than *cis*- β -CV. Here, *cis*- β -CV is used as a zero energy reference.

of all calculated spectroscopic constants are available in the supplemental information (Table S8).

As a benchmark for our computational work, we compared our calculated α -CV structure with the previously published experimental rotational spectrum.¹ The authors of that study detected a series of a -type transitions within the $K_a = 0$ ladder for α -CV and its doubly-deuterated isotopologue (d2- α -CV), and reportedly observed inversion doubling. Because of the lack of any b -type transitions or transitions involving $K_a \neq 0$ levels, only the rotational constant combination $(B_0 + C_0)/2$ was determined for each component of the inversion doublet. As mentioned above, our calculations did not find a nonplanar geometry consistent with the inversion motion, so for comparison we averaged the reported $(B_0 + C_0)/2$ values of the two inversion doublet components to compare with our ground-state rotational constants for the planar structure. Their value of 4365.6 MHz for α -CV differs from our *ab initio* calculations by only 0.1% [$(B_0 + C_0)/2 = 4359.9$ MHz]. For d2- α -CV, the reported $(B_0 + C_0)/2$ value is 3953.93 MHz, which differs from our calculations by 0.2% [$(B_0 + C_0)/2 = 3944.63$ MHz]

Given the satisfactory agreement of our calculations of α -CV with experiment, we began a search for *cis*- and *trans*- β -CV guided by our *ab initio* structures. We optimized our experimental conditions, such as discharge voltage and flow rates, by maximizing the intensities of the known α -CV transitions. In our initial experimental searches, we found putative *cis*- and *trans*- β -CV $N_{K_a K_c} = 1_{01} - 0_{00}$ transitions within 1% of the frequencies predicted from our quantum chemical calculations. These rotational transitions displayed a complex structure and were affected by the presence of a magnetic field, as expected for open-shell molecules. The cluster of peaks associated with the *cis*- β -CV $1_{01} - 0_{00}$ transition was of comparable intensity to the corresponding transition of α -CV, while the *trans*- β -CV transitions were nearly an order of magnitude weaker. Higher N a -type transitions for the *cis* isomer were readily identified at near-harmonic frequencies, while longer integrations were required to find similar transitions for *trans*- β -CV. The $2_{02} - 1_{01}$ transitions of *trans*- β -CV, found clustered around 19,500.0 MHz, were very close to the $2_{11} - 1_{10}$ transitions of vibrationally excited VyCN ($\nu_{11} = 1$), which are centered around 19,495.0 MHz.

The fundamental b -type transitions ($1_{11} - 0_{00}$) for both β radicals were predicted to lie outside the range of the cavity, requiring searches using DR. These searches covered a large frequency range because the calculated A rotational constant is highly sensitive to inaccuracies in the H atom positions. Ultimately, the $1_{11} - 0_{00}$ transitions were found within 2.3% of the predictions. Once these lines were assigned, further searches quickly revealed more lines using both FTMW and DR techniques. A total of 84 *cis*- β -CV lines were measured among 7 rotational transitions. Owing to the lower SNR, we observed 23 *trans*- β -CV lines among 6 rotational transitions.

The complex structure observed in the spectra arises from the angular momentum coupling within these radicals; rotational transitions are split by spin-rotation coupling between the spin of the unpaired electron and the rotational angular momentum, by quadrupole effects from the ^{14}N nucleus, and by spin-spin coupling and Fermi-contact interactions due to the three $I > 0$ nuclei. Simulations of the rotational spectra, including all calculated coupling terms, show that the $1_{01} - 0_{00}$ and $1_{11} - 0_{00}$ transitions are split into approximately 100 lines each. The number of lines increases significantly with N ; the $2_{02} - 1_{01}$ transitions contain approximately 250 lines. For each rotational transition, there were predicted to be ~ 30 lines with intensities within an order of magnitude of the most intense peak. As N increases, the most intense peaks collapse into smaller groups; for instance, in the $9_{09} - 8_{08}$ transition of *cis*- β -CV near 91 GHz, the most intense peaks are all predicted to fall within about a 1.5 MHz range.

In the experimental *cis*- β -CV spectrum, the most intense lines are in a cluster ~ 5 MHz wide around the rigid-rotor frequencies for all N levels within the range of the cavity. The peaks in the cluster arise from different combinations of angular momenta; however, the splittings induced by each source of angular momentum coupling are comparable in magnitude. In the *a*-type spectrum, this is reflected in the sums of the diagonal elements of the coupling tensors (e.g., $\epsilon_{bb} + \epsilon_{cc} = 1.05$ MHz, $T_{bb}(\text{H1}) + T_{cc}(\text{H1}) = 0.54$ MHz, and $\chi_{bb} + \chi_{cc} = 3.88$ MHz for *a*-type transitions, etc.). As a result, assigning a full set of angular momentum quantum numbers to each individual transition is challenging, as no dominant source of splitting is obvious. Further discussion about our efforts to assign these quantum numbers and fit the associated spectroscopic constants is provided in the supplemental information. We have therefore only assigned N , K_a , and K_c quantum numbers to the observed transitions of *cis*- β -CV.

For *trans*- β -CV, the value of $\epsilon_{aa} + \epsilon_{cc}$ (97.38 MHz) is calculated to be much larger than the analogous terms in the other coupling tensors (e.g., $T_{aa}(\text{N}) + T_{cc}(\text{N}) = 1.45$ MHz, $T_{aa}(\text{H1}) + T_{cc}(\text{H1}) = 6.24$ MHz, and $\chi_{aa} + \chi_{cc} = -1.87$ MHz). Consequently, the complex structure for the fundamental *b*-type transition is predicted to contain two distinct clusters of peaks associated with different spin-rotation components. Like *cis*- β -CV, these clusters are also spread over a range of ~ 5 MHz or less, but they are spaced by about 150 MHz for the $1_{11} - 0_{00}$ transition, which is about a factor of 2 larger than predicted from the calculated spin-rotation tensor elements. The *a*-type spectrum is more complicated. Our spectrum shows two clusters of lines spaced by about 10 MHz, also a bit larger than, but consistent with, the predicted splitting arising from value of $\epsilon_{bb} + \epsilon_{cc}$ (7.57 MHz). However, the spin-spin coupling tensor for the terminal hydrogen (H2) has $T_{bb} + T_{cc} = -40.86$ MHz, which is expected to produce a ~ 30 MHz splitting. We have not detected a second component in the $1_{01} - 0_{00}$ transition toward either lower or higher frequency, but the SNR of the

Table 2.1: Rotational transitions of *cis*- β -CV, in MHz. Frequencies were derived by approximating the centers of the observed clusters of lines (see text). Estimated uncertainties in parentheses are given in units of the last digit.

$N'_{K'_a, K'_c} - N''_{K''_a, K''_c}$	Frequency	Obs. – Calc.
$1_{01} - 0_{00}$	10196.67(230)	-0.163
$2_{12} - 1_{11}$	19862.50(230)	0.740
$2_{02} - 1_{01}$	20389.18(230)	0.336
$3_{03} - 2_{02}$	30571.41(230)	0.192
$4_{04} - 3_{03}$	40738.86(230)	-0.298
$1_{10} - 1_{01}$	44922.22(400)	0.058
$1_{11} - 0_{00}$	54586.15(400)	-1.179
$2_{12} - 1_{01}$	64253.18(400)	0.257

lines we did observe is low so we cannot rule out that this component is present below the noise level. We have therefore tentatively assigned N , K_a , K_c , and J quantum numbers to all *trans*- β -CV lines. Complete lists of the frequencies of all observed spectroscopic transitions and their estimated uncertainties for both isomers are available in the supplemental information.

In light of the difficulty in assigning the full complex structure, to determine experimental spectroscopic parameters we simplified the rotational spectrum by approximating the frequency at the center of each assigned cluster of lines, thereby averaging over the hyperfine structure. The uncertainties assigned to these frequencies, of order $\sim 2 - 3$ MHz, are estimated based on the observed frequency spread of each cluster, and are therefore substantially larger than the uncertainties on any one peak (of order a few kHz for lines measured in the cavity, and a few tens of kHz for DR measurements). These frequencies, shown in Tables 2.1 and 2.2, were used along with a standard Watson A -reduced effective Hamiltonian¹⁶⁹ to fit the ground-state rotational constants A_0 , B_0 , and C_0 for both isomers, along with $\epsilon_{aa} + \epsilon_{cc}$ and $\epsilon_{bb} + \epsilon_{cc}$ for *trans*- β -CV, using quartic CD constants held at their theoretical values owing to the low N and K quantum numbers in our data set.

Table 2.3 shows a comparison of the calculated and experimental values for both β -CV species. As expected, the largest deviations arise in the A_0 values, as these are sensitive to the light atom positions and the anharmonicities associated with their vibrational motion. The *cis*- β -CV B_0 and C_0 calculated and experimental values agree to within 0.25%, implying that the structure of the heavy atom backbone is calculated quite accurately, while the analogous values calculated for *trans*- β -CV larger than the experimental values by almost 1%. This may provide evidence that a second undetected hyperfine component exists at higher frequency than the clusters we observed for each a -type rotational transition, which would cause our current fit to underestimate the true values of the B_0 and C_0 rotational constants. Alternatively the

Table 2.2: Rotational transitions of *trans*- β -CV, in MHz. Frequencies of each spin-rotation component were derived by approximating the centers of the observed clusters of lines (see text). Estimated uncertainties in parentheses are given in units of the last digit.

$N'_{K'_a, K'_c} - N''_{K''_a, K''_c}$	$J' - J''$	Frequency	Obs. – Calc.
$1_{01} - 0_{00}$	$3/2 - 1/2$	9750.23(200)	0.745
$1_{01} - 0_{00}$	$1/2 - 1/2$	9760.10(200)	-0.067
$2_{02} - 1_{01}$	$5/2 - 3/2$	19500.00(145)	-0.696
$2_{02} - 1_{01}$	$3/2 - 1/2$	19507.00(145)	-0.742
$3_{03} - 2_{02}$	$7/2 - 5/2$	29248.95(200)	0.737
$1_{10} - 1_{01}$	$3/2 - 1/2$	61161.95(200)	-0.706
$1_{11} - 0_{00}$	$3/2 - 1/2$	70545.39(200)	1.348
$1_{11} - 0_{00}$	$1/2 - 1/2$	70699.63(200)	0.081
$2_{12} - 1_{01}$	$5/2 - 3/2$	79932.63(200)	-0.723

calculations may be underestimating the C=C-C bond angle or some of the bond lengths along the molecular backbone. Spectroscopy involving ^{13}C isotopic substitution would provide further insight. The experimental spin-rotation tensor elements for *trans*- β -CV are larger than the theoretical values by about a factor of 2; however, owing to the low SNR, we were not able to observe enough transitions to fit all three diagonal elements simultaneously. Therefore, we constrained the ratio $\epsilon_{bb}/\epsilon_{cc}$ to maintain the *ab initio* value. Other choices of constraints are possible and would yield different numerical values, so definitive conclusions about the exact magnitudes of the tensor elements cannot be made at present. Nevertheless, the good agreement between the calculated and experimental rotational constants strongly supports the assignments of the detected lines to *cis*- and *trans*- β -CV.

To further verify the identification of these radicals, the spectra of their ^{15}N isotopologues were obtained. Because the equilibrium geometry of a molecule is unchanged by isotopic substitution (under the Born-Oppenheimer approximation), we used the equilibrium rotational constants (Table 2.4) to predict the frequencies of the fundamental *a*- and *b*-type transitions of the ^{15}N species by scaling the observed frequencies of the parent species in the following manner. For the $1_{01} - 0_{00}$ transition, we divided the experimental frequency by the calculated $B_e + C_e$ to obtain a scaling factor, then multiplied the calculated $B_e + C_e$ value for the ^{15}N species by that same factor to produce a prediction for its $1_{01} - 0_{00}$ frequency. A similar procedure involving $A_e + C_e$ was used for the $1_{11} - 0_{00}$ transition. For *trans*- β -CV, only the lower spin-rotation component of each transition was used in this procedure, as we assume the spin-rotation tensor elements are not significantly changed upon isotopic substitution. In all cases, ^{15}N transitions were located within 0.02% of the predicted values, and the $2_{02} - 1_{01}$ transitions were also detected (Table 2.5). The ^{15}N transitions also showed complex structure that could not be fully assigned, as substituting the $I = 1/2$ ^{15}N nucleus for the

Table 2.3: Experimental and calculated Parameters of *cis*- and *trans*- β -CV, in MHz. Uncertainties in parentheses are given in units of the last digit.

Parameter	<i>cis</i>			<i>trans</i>		
	Calc.	Exp.	% Diff. ^a	Calc.	Exp.	% Diff. ^a
A_0	51001.38	49757.42(27)	-2.50	65143.77	65918.10(53)	1.17
B_0	5363.23	5364.31(16)	0.02	5107.83	5067.06(59)	-0.80
C_0	4844.05	4832.54(13)	-0.24	4728.75	4685.71(57)	-0.92
$10^3 \Delta_N$	3.13	3.13 ^b	-	2.15	2.15 ^b	-
$10^1 \Delta_{NK}$	-1.10	-1.10 ^b	-	-1.56	-1.56 ^b	-
Δ_K	3.03	3.03 ^b	-	7.08	7.08 ^b	-
$10^4 \delta_N$	6.86	6.86 ^b	-	4.19	4.19 ^b	-
$10^2 \delta_K$	3.03	3.03 ^b	-	2.17	2.17 ^b	-
ϵ_{aa}	4.86	-	-	-99.04	-208.15(124)	52.42
ϵ_{bb}	5.82	-	-	-9.23	-16.89(111)	45.35
ϵ_{cc}	-4.77	-	-	1.66	3.04 ^c	-
RMS		0.445			0.398	

^a(Exp. - Calc.)/Exp. $\times 100$

^bHeld at theoretical values

^cRatio of ϵ_{bb} and ϵ_{cc} held constant

Table 2.4: Calculated equilibrium rotational constants of the ^{14}N and ^{15}N *cis*- and *trans*- β -CV radicals.

Parameter	<i>cis</i>		<i>trans</i>	
	^{14}N	^{15}N	^{14}N	^{15}N
A_e	50602.68	50387.46	65002.95	64690.40
B_e	5387.26	5220.35	5118.28	4963.20
C_e	4868.91	4730.27	4744.68	4609.55

$I = 1$ ^{14}N nucleus only eliminates the quadrupole coupling tensor, still preserving the spin-spin splitting.

Complete line lists for the ^{15}N isotopologues are given in the supplemental information.

2.5 Conclusion

Here, we report new quantum chemical calculations of the α -, *cis*- β -, and *trans*- β cyanovinyl radicals at the CCSD(T) level of theory, and provide the first experimental characterization of the two β -CV radicals by means of their pure rotational spectra. The rotational transitions feature complex structure that is consistent with theoretical predictions, but which cannot be fully assigned at present. Nevertheless, the excellent agreement between the calculated and experimental rotational constants provides strong support for the identifications of these radicals, and the assignments are further confirmed by ^{15}N isotopic substitution experiments.

Table 2.5: Experimental and predicted transition frequencies for the ^{15}N *cis*- and *trans*- β -CV, in MHz.

Species	$N'_{K'_a, K'_c} - N''_{K''_a, K''_c}$	Calc.	Scaled ^a	Exp.	% Diff. ^b
^{15}N <i>cis</i> - β -CV	$1_{01} - 0_{00}$	9901.72	9891.82	9893.39	0.02
	$2_{02} - 1_{01}$	19799.42	19779.62	19782.12	0.01
	$1_{11} - 0_{00}$	55488.82	54240.32	54242.73	0.004
^{15}N <i>trans</i> - β -CV	$1_{01} - 0_{00}$	9462.05	9463.25	9546.35	0.02
	$2_{02} - 1_{01}$	18926.02	18924.99	19191.04	0.004
	$1_{11} - 0_{00}$	70122.53	70116.62	69418.09	0.01

^a See text for explanation of scaling.

^b $(\text{Exp.} - \text{Scaled})/\text{Exp.} \times 100$

The derived rotational constants provide a basis for future spectroscopic studies in the millimeter wave region, where the hyperfine structure is expected to collapse while the spin-rotation splitting increases. Such measurements may ultimately assist with interpreting the low- N hyperfine structure observed in the present study. Moreover, our results pave the way for deep astronomical searches for the CV radicals in cold interstellar clouds, where they may participate in barrierless reactions leading to the formation of pyridine, one of the most fundamental N-heterocycles.

2.6 Supporting Information

Discussion and illustrations of attempts to fit the complex rotational structure of *cis*- β -CV, discussion of T_1 diagnostics, comparison of MRCI and CCSD(T) calculations, full experimental linelists of both *cis*- and *trans*- β -CV rotational spectra, calculated harmonic and anharmonic frequencies of vibrational modes for *cis*- β , *trans*- β , and α -CV, lists of all calculated parameters for *cis*- and *trans*- β -CV, and input files for SPFIT/SPCAT for both β -CV isomers.

Chapter 3

Coupled Cluster Characterization of 1-, 2-, and 3-Pyrrolyl: Parameters for Vibrational and Rotational Spectroscopy

This chapter has been adapted from: Johansen SL, Xu Z, Westerfield JH, Wannemacher AC, Crabtree KN. Coupled Cluster Characterization of 1-, 2-, and 3-Pyrrolyl: Parameters for Vibrational and Rotational Spectroscopy. *J Phys Chem A*. 2021;125(5):1257-1268. doi:10.1021/acs.jpca.0c09833 © 2021 American Chemical Society

Pyrrolyl (C_4H_4N) is a nitrogen-containing aromatic radical that is a derivative of pyrrole (C_4H_5N) and is an important intermediate in the combustion of biomass. It is also relevant for chemistry in Titan's atmosphere, and may be present in the interstellar medium. The lowest-energy isomer, 1-pyrrolyl, has been involved in many experimental and theoretical studies of the N–H photodissociation of pyrrole, yet it has only been directly spectroscopically detected via electron paramagnetic resonance and through the photoelectron spectrum of the pyrrolide anion, yielding three vibrational frequencies. No direct measurements of 2- or 3-pyrrolyl have been made, and little information is known from theoretical calculations beyond their relative energies. Here, we present an ab initio quantum chemical characterization of the three pyrrolyl

isomers at the CCSD(T) level of theory in their ground electronic states, with an emphasis on spectroscopic parameters relevant for vibrational and rotational spectroscopy. Equilibrium geometries were optimized at the CCSD(T)/cc-pwCVTZ level of theory and the quadratic, cubic, and partial quartic force constants were evaluated at CCSD(T)/ANO0 for analysis using second-order vibrational perturbation theory to obtain harmonic and anharmonic vibrational frequencies. In addition, zero-point-corrected rotational constants, electronic spin-rotation tensors, and nuclear hyperfine tensors are calculated for rotational spectroscopy. Our computed structures and energies agree well with earlier density functional theory calculations, and spectroscopic parameters for 1-pyrrolyl are compared with the limited existing experimental data. Finally, we discuss strategies for detecting these radicals using rotational and vibrational spectroscopy on the basis of the calculated spectroscopic constants.

3.1 Introduction

The study of nitrogen-containing heterocycles in the gas phase is important for combustion chemistry, astrochemistry, and the study of planetary atmospheres. Pyrrole (C_4H_5N), a five-membered aromatic ring with one nitrogen, is present in fuels derived from biomass, including coal and biofuels^{170,171}. Pyrrole combustion leads to the formation of NO_x species and potentially nitrogen-containing polycyclic aromatic hydrocarbons (PANHs), both presenting health hazards^{146,172–174}. N-heterocycles, including pyrrole derivatives, have also been identified on meteorites with non-terrestrial isotopic abundances⁷, and although no such molecule has been detected in space to date^{48,49,175}, numerous experimental studies of interstellar ice analogues under irradiation have produced these compounds^{80,110,111,116}. In Titan’s atmosphere, nitrogen-containing hydrocarbons have been detected by radioastronomy¹²⁸ and the Cassini Ion Neutral Mass Spectrometer (INMS)^{130,131,176}, with a tentative INMS detection of pyrrole.

In each of these environments, radical intermediates play key roles in driving important chemical pathways. In interstellar clouds, for example, the barrierless reaction of the CN radical with benzene has been suggested to explain the recent detection of benzonitrile^{22,177}, and the aforementioned ice studies are strongly suspected to involve radical intermediates⁸⁰. Radical-mediated chemistry is also widely used in models of Titan’s atmosphere¹⁷⁸, and the potential for the presence of pyrrolyl (C_4H_4N), the radical derivative of pyrrole, has recently been explored¹⁷⁹. Finally, models of biofuel combustion explicitly depend on reactions involving the 1-pyrrolyl radical^{142–145,180–182}. Pyrrolyl has three isomeric forms: the 1-pyrrolyl radical that arises from N–H bond fission in pyrrole, and the 2- and 3-pyrrolyl radicals that come from the two possible

C–H bond fission sites.

As the product of N–H photodissociation, 1-pyrrolyl has the subject of several experimental^{183–188} and theoretical studies^{189–194} owing to its complex dynamics. The potential energy surface shows that along the N–H dissociation coordinate, pyrrole in its 1A_1 ground electronic state correlates to the 2A_1 second excited electronic state of 1-pyrrolyl, while the 2A_2 ground state of 1-pyrrolyl correlates to the 1A_2 excited electronic state of pyrrole. During photodissociation, population between these states is redistributed on the femtosecond time scale via a conical intersection^{186,190}. Photoexcitation of pyrrole to its 1B_2 electronic excited state has also been found to yield 2- and/or 3-pyrrolyl via C–H bond fission following relaxation to vibrationally excited levels in the 1A_1 ground state, albeit on a slower time scale than N-H bond dissociation^{183,186}.

Despite numerous photochemistry experiments, direct spectroscopic observations of the pyrrolyl radicals are limited to only a few observations of 1-pyrrolyl. Three vibrational frequencies of 1-pyrrolyl were experimentally measured in the photoelectron spectrum of the pyrrolide anion¹⁹⁵. Several vibrational transitions were also attributed to 1-pyrrolyl in H Rydberg photofragmentation studies of pyrrole on the basis of DFT calculations,¹⁸⁴ but there is some ambiguity in the assignments. An electron spin resonance study of 1-pyrrolyl suggests that its unpaired electron is delocalized amongst the aromatic π bonds¹⁹⁶. Information on 2- and 3-pyrrolyl is even more scarce. Two recent computational studies show that, unlike 1-pyrrolyl, they are σ -type radicals, with the unpaired electron localized to the respective carbon^{179,197}. These studies also included equilibrium geometries and the relative electronic energies of the three isomers.

Here, we present the first coupled-cluster study of all three pyrrolyl isomers with a focus on providing spectroscopic constants needed for supporting experimental spectroscopy in the infrared and microwave regions. For each isomer we compute equilibrium geometries, harmonic and anharmonic vibrational frequencies and intensities, equilibrium and ground-state rotational constants, dipole moment projections, and spin-rotation and hyperfine coupling parameters. These are, to the best of our knowledge, the first reported vibrational frequencies for 2- and 3-pyrrolyl, as well as the first complete set of rotational spectroscopic parameters for any of the three isomers. Where data are available, we compare the results of our calculations with earlier experimental and theoretical calculations. Prospects for the spectroscopic detection of these radicals in different spectral regions are discussed. It is hoped that the results presented here will enable new experimental studies of pyrrolyl kinetics and dynamics and potentially enable its detection in astrophysical environments.

3.2 Methods

Calculations were performed with the CFOUR quantum chemistry package¹⁹⁸. Unless indicated otherwise, all calculations were performed using an Unrestricted Hartree-Fock (UHF) reference. Structures previously calculated at the (U)B3LYP/cc-pVTZ¹⁹⁷ level were optimized with the coupled cluster method³³ with iterative inclusion of single and double excitations and up to perturbative inclusion of triple excitations [CCSD(T)]³⁴ and the Dunning polarized weighted core-valence basis sets (cc-pwCVXZ).³⁶ Initial geometry optimizations were done at the ae-CCSD/cc-pwCVDZ level of theory (all electrons correlated), followed by ae-CCSD(T)/cc-pwCVDZ, and finally at ae-CCSD(T)/cc-pwCVTZ.

To evaluate vibrational terms, the quadratic, cubic, and partial quartic force constants were evaluated via finite differences of electronic energies under the frozen-core (fc) approximation. Restricted open-shell Hartree-Fock (ROHF) was used as a reference for 1-pyrrolyl. These calculations were performed at fc-CCSD(T)/ANO0 from a reference geometry optimized using the same level of theory. The force constants and displacements were used to evaluate the harmonic vibrational frequencies and intensities, centrifugal distortion coefficients, and vibration-rotation interaction terms, and anharmonic vibrational frequencies were evaluated using second-order vibrational perturbation theory (VPT2)³⁷.

Electronic spin-rotation and g-tensors¹⁹⁹ were calculated at the final optimized geometry using multiple levels of theory: selected combinations of fc-CCSD, ae-CCSD, ae-CCSD(T) with the Ames Atomic Natural Orbital basis ANO0¹⁶¹ as well as the Dunning cc-pVXZ ($X = D, T$)²⁰⁰, cc-pwCVXZ ($X = D, T$), and aug-cc-pVDZ³⁵ basis sets. Electric dipole moments, nitrogen quadrupole tensors, spin-spin coupling tensors, and Fermi contact terms were calculated at ae-CCSD(T)/cc-pwCVTZ.

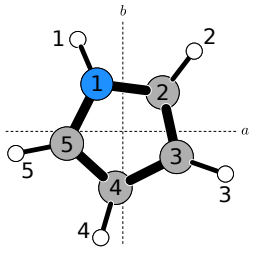
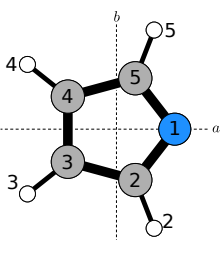
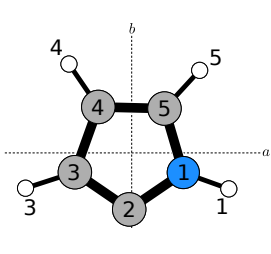
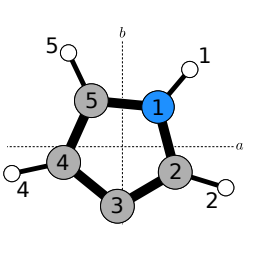
Additional discussion of the choice of methods is provided in the next section.

3.3 Results & Discussion

Energies and Geometries

The Born-Oppenheimer equilibrium structures and electronic energies of 1-, 2-, and 3-pyrrolyl calculated at the ae-CCSD(T)/cc-pwCVTZ level are shown in Table 3.1, along with the experimentally derived structure of pyrrole for comparison²⁰¹. Previous ae-CCSD(T) calculations with a core-valence basis set (cc-pCV n Z) for treating core correlation have been shown to provide accurate molecular properties and spectroscopic constants for the phenyl radical²⁰². A benchmarking study of the cc-pCVXZ and cc-pwCVXZ basis sets

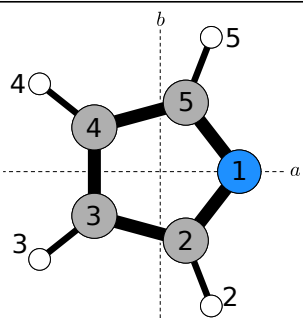
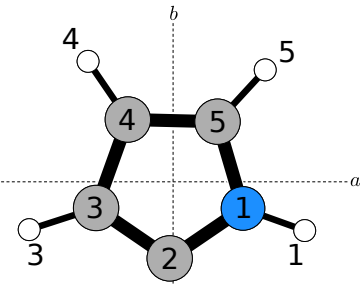
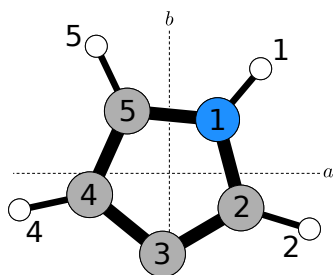
Table 3.1: Equilibrium geometries (in Ångstrom and degrees) and relative energies^a (in kJ/mol) calculated at CCSD(T)/cc-pwCVTZ.

	Pyrrole ^b	1-Pyrrolyl	2-Pyrrolyl	3-Pyrrolyl
				
N1-C2	1.370	1.345	1.356	1.379
C2-C3	1.382	1.458	1.363	1.364
C3-C4	1.417	1.360	1.436	1.412
C4-C5	1.382	1.458	1.371	1.379
C5-N1	1.370	1.345	1.382	1.368
N1-H1	0.996	–	1.001	1.003
C2-H2	1.076	1.080	–	1.074
C3-H3	1.077	1.077	1.074	–
C4-H4	1.077	1.077	1.077	1.075
C5-H5	1.076	1.080	1.076	1.076
∠C2-N1-C5	109.8	104.4	107.9	110.1
∠N1-C2-C3	107.7	112.6	111.3	105.5
∠N1-C5-C4	107.7	112.6	107.8	108.7
∠C2-C3-C4	107.9	105.2	104.6	110.8
∠C5-C4-C3	107.9	105.2	108.4	104.9
∠C2-N1-H1	125.1	–	126.0	125.0
∠N1-C2-H2	121.5	120.9	–	122.0
∠N1-C5-H5	121.5	120.9	121.0	121.0
∠C2-C3-H3	127.1	126.3	127.7	–
∠C5-C4-H4	127.1	126.3	125.7	126.4
		Rel. Energy 0.00	Rel. Energy +106.35	Rel. Energy +105.08

^aRelative energies include anharmonic zero-point vibrational energies calculated at fc-CCSD(T)/ANO0.

^bExperimental values measured by²⁰¹ Uncertainties are ± 0.005 Å for bond length measurements and $\pm 0.5^\circ$ for bond angles.

Table 3.2: Mulliken analysis of ae-CCSD(T)/cc-pwCVTZ spin densities.

	1-Pyrrolyl		2-Pyrrolyl		3-Pyrrolyl	
						
Atom	This Work	Ref. ^{179a}	This Work	Ref. ^{179a}	This Work	Ref. ^{179a}
N1	-0.14	-0.13	-0.02	-0.01	0.01	-0.02
C2	0.52	0.48	0.95	1.02	-0.02	-0.08
C3	0.08	0.09	0.00	-0.09	0.96	1.08
C4	0.08	0.09	0.00	0.05	0.02	-0.09
C5	0.52	0.48	0.05	0.02	-0.01	0.04
H1	-		0.00		0.01	
H2	-0.03		-		0.00	
H3	-0.01		0.00		-	
H4	-0.01		0.01		0.00	
H5	-0.03		0.00		0.01	

^a Calculated at ω B97X-V/cc-pVTZ.

demonstrated that cc-pwCVXZ shows a better convergence rate for molecular properties, notably equilibrium bond length, with increasing X^{36} , and so the weighted core-valence basis sets were used in the present calculations.

Pyrrole is an aromatic molecule with 6 π electrons delocalized among the C and N $2p_z$ orbitals. In the ground 2A_2 state of 1-pyrrolyl, the N–H bond from pyrrole is replaced by a lone electron pair, and the unpaired electron nominally resides in the N $2p_z$ orbital, leaving 5 delocalized π electrons. The coupled cluster wavefunction for 1-pyrrolyl is well-described as a doublet electronic state with minimal spin contamination ($\langle S^2 \rangle = 0.747$). The spin densities, shown in Table 3.2, show that the unpaired electron is delocalized significantly among the N and two adjacent C atoms, and to a lesser extent the remaining C atoms. Relative to pyrrole, the partial loss in aromaticity results in the lengthening of the (equivalent) C2–C3 and C4–C5 bonds from 1.382 Å to 1.458 Å and the shortening of the C3–C4 bond from 1.417 Å to 1.360 Å in 1-pyrrolyl. Similar trends were obtained from unrestricted DFT and QCISD calculations. For ω B97X-V/cc-pVTZ¹⁷⁹, bond lengths and angles agree within 0.006 Å and 0.2°; for (U)B3LYP/cc-pVTZ¹⁹⁷, within 0.004 Å and 0.2°; for (U)M06-2X/cc-pVTZ¹⁹⁷, within 0.008 Å and 0.2°; for QCISD/6-311G(d,p)²⁰³, within 0.011 Å (bond angles were not provided). The spin densities match those calculated at ω B97X-V/cc-pVTZ¹⁷⁹ within a few hundredths at each atom. Despite the significant distortion of the ring structure, 1-pyrrolyl is nevertheless the most stable isomer.

2- and 3-pyrrolyl are nearly equal in energy; including the fc-CCSD(T)/ANO0 zero-point corrections, they lie 106.35 and 105.08 kJ/mol higher than 1-pyrrole, respectively. These are well matched with the relative energies provided in the literature, all of which are calculated with unrestricted DFT methods (108.32 and 106.48¹⁷⁹, 103.34 and 101.67¹⁹⁷, and 91.63 and 89.96¹⁹⁷ kJ/mol). The $\langle S^2 \rangle$ values for both species are 0.746 at ae-CCSD(T)/cc-pwCVTZ. In both 2- and 3-pyrrolyl, the spin density calculations (Table 3.2) show that the unpaired electron remains localized to the respective C atom, suggesting these species are more reactive than 1-pyrrolyl. While the bond lengths of 2- and 3-pyrrolyl are not significantly different than those of pyrrole, the bond angles are widened around the radical centers from 107.7° to 111.3° for 2-pyrrolyl and from 107.4° to 110.75° for 3-pyrrolyl. The trend in 1-pyrrolyl is the opposite; relative to pyrrole the C–N–C bond angle is reduced from 109.8° to 104.39°.

Like 1-pyrrolyl, these trends agree well with those in the literature. For 2-pyrrolyl, the ω B97X-V/cc-pVTZ¹⁷⁹ bond lengths and angles agree within 0.004 Å and 0.3°; for (U)B3LYP/cc-pVTZ¹⁹⁷, within 0.003 Å and 0.1°; for (U)M06-2X/cc-pVTZ¹⁹⁷, within 0.005 Å and 0.1°; for QCISD/6-311G(d,p)²⁰³, within 0.008 Å. For 3-pyrrolyl, the ω B97X-V/cc-pVTZ¹⁷⁹ bond lengths and angles agree within 0.006 Å and 0.2°; for

Table 3.3: fc-CCSD(T)/ANO0 harmonic (ω) and anharmonic frequencies (ν), in cm^{-1} , and harmonic and anharmonic intensities (Int.), in km/mol .

Mode ^a	1-Pyrrolyl				2-Pyrrolyl				3-Pyrrolyl						
	Mode ^b	ω	Int.	ν	Int.	Mode ^b	ω	Int.	ν	Int.	Mode ^b	ω	Int.	ν	Int.
7	ν_{11}, A_2	488.7	0.00	478.7	0.00	ν_{21}, A''	325.8	45.85	362.7	43.85	ν_{21}, A''	403.0	71.40	408.0	69.43
8	ν_{21}, B_1	541.0	17.35	532.1	17.99	ν_{20}, A''	499.3	13.03	492.1	15.37	ν_{20}, A''	543.4	6.97	535.7	7.69
9	ν_{18}, B_2	668.3	8.78	558.6	7.89	ν_{19}, A''	610.6	0.76	600.9	1.02	ν_{19}, A''	632.9	2.13	620.7	1.69
10	ν_{20}, B_1	700.9	59.40	683.1	57.09	ν_{18}, A''	695.7	55.35	691.0	58.72	ν_{18}, A''	665.0	12.31	662.2	10.65
11	ν_{10}, A_2	815.0	0.32	801.8	0.16	ν_{17}, A''	750.0	72.00	738.0	59.94	ν_{17}, A''	747.3	87.43	736.4	84.57
12	ν_{19}, B_1	815.6	0.00	791.5	0.00	ν_{16}, A''	842.0	0.07	829.4	0.05	ν_{16}, A''	828.3	0.65	816.6	0.25
13	ν_8, A_1	869.5	11.00	847.7	7.94	ν_{15}, A'	846.0	3.10	849.0	1.25	ν_{15}, A'	852.8	2.68	840.4	2.36
14	ν_9, A_2	885.3	0.00	856.9	0.00	ν_{14}, A'	878.9	1.20	867.8	3.96	ν_{14}, A'	877.9	2.05	866.8	1.72
15	ν_{17}, B_2	924.6	0.01	902.6	0.01	ν_{13}, A'	1020.7	16.30	1001.2	2.17	ν_{13}, A'	1032.5	34.02	1003.1	2.55
16	ν_7, A_1	1039.1	0.05	1010.6	2.34	ν_{12}, A'	1060.2	18.87	1037.6	18.11	ν_{12}, A'	1065.8	14.23	1035.8	8.53
17	ν_{16}, B_2	1069.4	2.17	957.0	3.12	ν_{11}, A'	1103.8	10.65	1081.9	6.03	ν_{11}, A'	1149.4	3.18	1111.3	325.11
18	ν_6, A_1	1084.2	32.12	1066.0	49.78	ν_{10}, A'	1166.8	8.81	1143.5	7.51	ν_{10}, A'	1168.2	0.29	1143.4	0.09
19	ν_5, A_1	1188.6	1.53	1133.6	4.20	ν_9, A'	1245.7	2.48	1216.5	2.78	ν_9, A'	1232.0	6.19	1211.9	33.27
20	ν_{15}, B_2	1284.3	0.02	1250.9	2.27	ν_8, A'	1373.8	2.07	1342.9	1.39	ν_8, A'	1386.2	1.11	1355.3	0.21
21	ν_{14}, B_2	1349.0	38.69	1309.4	19.24	ν_7, A'	1412.6	18.66	1364.3	16.50	ν_7, A'	1441.0	8.15	1393.2	9.53
22	ν_4, A_1	1447.3	18.81	1426.8	2.39	ν_6, A'	1460.8	22.92	1428.8	16.08	ν_6, A'	1489.4	17.17	1446.7	14.78
23	ν_3, A_1	1549.1	0.28	1478.8	0.08	ν_5, A'	1562.9	0.96	1529.1	0.50	ν_5, A'	1537.2	2.99	1505.5	1.91
24	ν_{13}, B_2	3226.2	14.98	3086.7	3.23	ν_4, A'	3259.1	1.92	3123.0	2.48	ν_4, A'	3269.9	0.41	3133.5	0.94
25	ν_2, A_1	3230.7	2.81	3094.2	3.49	ν_3, A'	3286.9	1.37	3151.3	2.67	ν_3, A'	3291.8	1.45	3155.6	2.38
26	ν_{12}, B_2	3254.2	5.64	3113.1	0.85	ν_2, A'	3295.3	0.15	3159.6	0.29	ν_2, A'	3299.6	0.19	3163.7	0.19
27	ν_1, A_1	3275.1	1.35	3139.3	2.36	ν_1, A'	3695.4	101.88	3522.2	79.13	ν_1, A'	3676.3	74.61	3504.6	57.14

^a Normal modes ordered by Hessian eigenvalue.

^b Normal modes as numbered in the Herzberg convention.

(U)B3LYP/cc-pVTZ¹⁹⁷, within 0.006 Å and 0.3°; for (U)M06-2X/cc-pVTZ¹⁹⁷, within 0.008 Å and 0.9°; for QCISD/6-311G(d,p)²⁰³, within 0.009 Å. The ae-CCSD(T)/cc-pwCVTZ spin densities of 2- and 3-pyrrolyl show more variation relative to the ω B97V/cc-pVTZ values¹⁷⁹; most notably that the spin density is less localized on the radical centers compared with the DFT values.

Vibrational Modes

The fc-CCSD(T)/ANO0 vibrational frequencies and intensities are shown in Table 3.3 for all isomers. Harmonic values and the VPT2 anharmonic values are shown. The combination of frozen-core CCSD(T) calculations with the ANO family of basis sets has been shown to provide good estimates of properties that depend on force constants, including vibrational frequencies, rotational centrifugal distortion terms, and vibration-rotation interaction corrections to rotational constants, even for open-shell molecules^{204–207}. For 1-pyrrolyl, UHF instabilities at some displacements yielded nonphysical force constants, a known issue for some open-shell systems²⁰⁸. For this reason a ROHF reference was used for this isomer. Similar behavior was not observed for 2- and 3-pyrrolyl, potentially due to their lower symmetry, and the UHF reference was used for these calculations.

A comparison between the fc-CCSD(T)/ANO0 harmonic vibrational frequencies calculated in this work and those calculated previously for 1-pyrrolyl^{179,184,192,209} is shown in Table 3.4. Three experimental fre-

Table 3.4: Comparison of fc-CCSD(T)/ANO0 1-pyrrolyl harmonic and anharmonic frequencies with literature values, in cm^{-1} .

Mode	Harmonic					Anharmonic		Experimental
	This work	Ref. ^{184a}	Ref. ^{209b}	Ref. ^{179c}	Ref. ^{192d}	This Work	Ref. ^{184a}	Ref. ^{195e}
ν_1, A_1	3275.1	3245.8	3245.7	3270.28	3396	3139.3	3118.4	–
ν_2, A_1	3230.7	3198.1	3198.0	3220.19	3369	3094.2	3056.5	–
ν_3, A_1	1549.1	1560.5	1560.7	1595.90	1655	1478.8	1486.3	–
ν_4, A_1	1447.3	1434.1	1434.2	1474.31	1558	1426.8	1414.8	1464(20)
ν_5, A_1	1188.6	1204.4	1204.3	1222.06	1268	1133.6	1140.8	–
ν_6, A_1	1084.2	1091.3	1091.4	1106.20	1163	1066.0	1061.9	–
ν_7, A_1	1039.1	1042.7	1043.0	1056.39	1106	1010.6	1012.2	1012(25)
ν_8, A_1	869.5	883.0	883.1	887.04	932	847.7	857.4	925(65)
ν_9, A_2	885.3	912.8	913.1	946.32	932	856.9	896.9	–
ν_{10}, A_2	815.0	823.3	823.5	853.67	861	801.8	800.1	–
ν_{11}, A_2	488.7	491.9	492.1	504.23	533	478.7	485.4	–
ν_{12}, B_2	3254.2	3226.0	3225.8	3249.43	3376	3113.1	3096.3	–
ν_{13}, B_2	3226.2	3193.9	3193.8	3215.39	3362	3086.7	3051.4	–
ν_{14}, B_2	1349.0	1355.8	1355.8	1379.09	1474	1309.4	1329.6	–
ν_{15}, B_2	1284.3	1291.6	1291.8	1303.57	1408	1250.9	1260.7	–
ν_{16}, B_2	1069.4	1075.9	1075.3	1092.51	1156	957.9	1052.7	–
ν_{17}, B_2	924.6	933.6	934.0	954.05	997	902.6	920.3	–
ν_{18}, B_2	668.3	656.1	655.6	669.03	710	558.6	664.1	–
ν_{19}, B_1	815.6	839.6	840.0	865.44	867	791.5	821.9	–
ν_{20}, B_1	700.9	714.8	714.6	728.16	757	683.1	700.3	–
ν_{21}, B_1	541.0	544.2	544.3	548.04	586	532.1	534.0	–

^{a,b} B3LYP/6-311G(d,p).

^c ω B97X-V/cc-pVTZ. Mode labels are estimated from frequencies and intensities.

^d SA-CASSCF(8,7)/CASPT2/aug-cc-pVTZ+.

^e Threshold photoelectron spectroscopy.

quencies, measured with threshold photoelectron spectroscopy of the pyrrolide anion¹⁹⁵, are also included. 1-pyrrolyl has C_{2v} symmetry: the A_2 and B_1 modes correspond to in-plane bending motions but the A_2 modes are IR inactive. The A_1 modes correspond to symmetric in-plane stretching and out-of-plane bending motions, while the B_2 modes are asymmetric in-plane stretching and out-of-plane bending motions. The four highest frequencies, all over 3000 cm^{-1} , are the C–H stretching modes.

Our harmonic frequencies agree most closely with those calculated at B3LYP/6-311G(d,p)^{184,209}, giving a root mean square deviation (RMSD) of 17.7 cm^{-1} . The RMSD between the present values and those calculated at ω B97X-V/cc-pVTZ¹⁷⁹ is 28.3 cm^{-1} , with the greatest discrepancies between the ν_9 A_2 and ν_{19} B_1 modes. The CASPT2/aug-cc-pVTZ+ frequencies¹⁹² give a rather large RMSD of 90.2 cm^{-1} , which is expected given the lower-level treatment of electron correlation together with the state-averaged reference space employed in the calculation to treat electronically excited states.

A comprehensive literature search only turned up a single set of anharmonic frequencies calculated at

B3LYP/6-311G(d,p) by¹⁸⁴ The *fc*-CCSD(T)/ANO0 anharmonic frequencies generally match these well, but the B_2 modes ν_9 and ν_{17} are notably different; the RMSD is 36.2 cm^{-1} with these modes included, but drops to 19.8 cm^{-1} when they are removed. These two modes also have the largest deviations between the calculated harmonic and anharmonic frequencies, so it is possible that effects of symmetry breaking are still giving anomalously large higher-order force constants for these motions. For the experimental frequencies¹⁹⁵, our calculated anharmonic values are lower, especially for the ν_8 mode measured at $925 \pm 65\text{ cm}^{-1}$. The experimental bands were assigned on the basis of B3LYP/6-311++G(d,p) harmonic frequencies and Franck-Condon simulations from the pyrrolide anion to the 1-pyrrolyl radical. Further calculations involving vibronic coupling may shed more light on the nature of the experimental spectrum.

To the best of our knowledge, no vibrational frequencies have been previously reported for 2- or 3-pyrrolyl, both of which have C_s symmetry. The six lowest frequencies are all A'' out-of-plane bending modes, and all other modes are A' in-plane bending and stretching modes. Both isomers show a bright N–H stretching mode near 3500 cm^{-1} as well as three C–H stretching modes around 3150 cm^{-1} . In addition, the ν_{21} mode shows a negative anharmonicity in both isomers, and this mode participates in several combination band transitions as discussed more below. Of particular note, the 3-pyrrolyl ν_{11} mode in Table 3.3 shows a suspiciously large anharmonic intensity contribution, which should be viewed with caution.

Rotational Constants and Vibration-Rotation Interaction

The equilibrium rotational constants, vibration-rotation corrections, and centrifugal distortion constants in Watson’s A -reduction²¹⁰ are shown in Table 7.8, along with the projections of the dipole moment along the principal axes. The magnitudes of the vibration-rotation corrections are $\sim 1\%$ or less in all cases, and no individual vibration-rotation interaction constant for any mode or axis exceeds 60 MHz. After inclusion of these corrections, the inertial defects are all very small in magnitude (0.063 , -0.003 , and 0.014 amu \AA^2), giving confidence in the reliability of the vibration-rotation terms.

All pyrrolyl isomers have a stronger total dipole moment than pyrrole (1.74 D^{201}), making them good candidates for rotational spectroscopy. By symmetry, 1-pyrrolyl has only a -type rotational transitions ($\mu_a = 2.02\text{ D}$), while 2- and 3-pyrrolyl have both a - and b -type transitions. The b -type transitions in 2-pyrrolyl are predicted to be significantly weaker than the a -type, as $\mu_a = 1.78\text{ D}$ while $\mu_b = 0.22\text{ D}$. In 3-pyrrolyl, the b -type transitions are predicted to be the strongest, with $\mu_b = 2.29\text{ D}$ and $\mu_a = 1.22\text{ D}$.

Table 3.5: ae-CCSD(T)/cc-pwCVTZ equilibrium rotational constants of 1-, 2-, and 3- pyrrolyl with fc-CCSD(T)/ANO0 vibration-rotation and centrifugal distortion terms, in MHz unless otherwise noted.

Parameter	1-	2-	3-
A_e	10020.21	10289.08	10307.28
B_e	8821.32	8935.88	8990.49
C_e	4691.31	4782.43	4801.98
$A_e - A_0^a$	103.86	82.09	71.24
$B_e - B_0^a$	38.89	64.37	71.45
$C_e - C_0^a$	36.51	36.02	36.47
$10^3 \Delta_N^a$	1.67	1.44	1.53
$10^3 \Delta_{NK}^a$	2.93	0.57	0.07
$10^3 \Delta_K^a$	-1.39	2.12	2.52
$10^4 \delta_N^a$	6.64	5.56	5.99
$10^3 \delta_K^a$	3.08	1.54	1.42
μ_a (D)	2.02	1.78	1.22
μ_b (D)	-	0.22	2.29
Δ_e^b (amu \AA^2)	0.000	0.000	0.000
Δ_0^b (amu \AA^2)	0.063	-0.003	0.014

^a Calculated at fc-CCSD(T)/ANO0.

^b Inertial defect: $I_c - I_a - I_b$.

Electronic Spin-Rotation Coupling

For open-shell molecules, coupling between the electronic spin angular momentum and the rotational angular momentum leads to splittings of the rotational energy levels. Electronic spin-rotation coupling terms have not previously been calculated for any of the pyrrolyl isomers. Table 3.6 shows the diagonal elements of spin-rotation tensor for each isomer at the ae-CCSD(T)/ANO0 level of theory. Complete spin-rotation tensors computed with a variety of methods and basis sets are reported in the Supplemental Information. The ae-CCSD(T)/ANO0 method has been shown to accurately predict experimentally-measured spin-rotation coefficients for 2-furanyloxy, another open-shell 5-member heterocycle²⁰⁶. However, it has been shown that spin-rotation tensor calculations at the same level of theory on different molecules do not necessarily result in the same degree of accuracy¹⁹⁹. Our additional calculations all give consistent values for the tensor elements.

The diagonal tensor elements are quite similar for 2- and 3-pyrrolyl; the ϵ_{aa} term is nearly an order of magnitude larger than ϵ_{bb} and ϵ_{cc} , which are within ~ 1 MHz of each other in magnitude but are opposite in sign, with a negative ϵ_{cc} value. For the 1-pyrrolyl isomer, ϵ_{aa} is the largest in magnitude and negative, ϵ_{cc} is one order of magnitude smaller and is also negative, and ϵ_{bb} is an order of magnitude smaller still and is positive. These trends arise because the natures of the electronic wavefunctions are similar as discussed previously: 2- and 3-pyrrolyl are both σ -type radicals while 1-pyrrolyl is better described as a π -type radical. The remaining differences are primarily associated with the different orientations of the principal axes. For

Table 3.6: CCSD(T)/cc-pwCVTZ ground-state rotational constants and hyperfine parameters for 1-, 2-, and 3-pyrrolyl, in MHz.

Parameter ^a	1-	2-	3-
A_0^b	9916.35	10207.00	10236.04
B_0^b	8782.43	8871.51	8919.04
C_0^b	4654.80	4746.41	4765.51
ϵ_{aa}^c	-9.31	16.96	9.56
ϵ_{bb}^c	0.10	3.85	3.16
ϵ_{cc}^c	-1.05	-2.71	-3.37
χ_{aa}	-4.05	1.47	1.35
χ_{bb}	1.78	1.58	1.56
χ_{cc}	2.28	-3.05	-2.91
$a_F(\text{N})$	-8.24 (-8.16) ^d	16.05	23.60
$T_{aa}(\text{N})$	4.01	1.11	-0.59
$T_{bb}(\text{N})$	4.04	2.40	2.96
$T_{cc}(\text{N})$	-8.05	-3.51	-2.37
$a_F(\text{H1})$	-	12.92	14.93
$T_{aa}(\text{H1})$	-	12.67	0.50
$T_{bb}(\text{H1})$	-	-4.95	2.88
$T_{cc}(\text{H1})$	-	-7.71	-3.38
$a_F(\text{H2})$	-36.20 (-37.18) ^d	-	6.96
$T_{aa}(\text{H2})$	-14.31	-	9.69
$T_{bb}(\text{H2})$	14.45	-	-3.87
$T_{cc}(\text{H2})$	-0.14	-	-5.82
$a_F(\text{H3})$	-9.10 (-9.95) ^d	8.24	-
$T_{aa}(\text{H3})$	6.61	11.32	-
$T_{bb}(\text{H3})$	-4.13	-4.25	-
$T_{cc}(\text{H3})$	-2.49	-7.07	-
$a_F(\text{H4})$	-9.10 (-9.95) ^d	18.91	10.82
$T_{aa}(\text{H4})$	6.61	0.63	10.53
$T_{bb}(\text{H4})$	-4.13	2.64	-4.43
$T_{cc}(\text{H4})$	-2.49	-3.27	-6.10
$a_F(\text{H5})$	-36.20 (-37.18) ^d	6.04	18.14
$T_{aa}(\text{H5})$	-14.31	0.31	0.28
$T_{bb}(\text{H5})$	14.45	3.01	2.84
$T_{cc}(\text{H5})$	-0.14	-3.33	-3.12

^a Hydrogen labels match those in Tables 3.1 and 3.2. ^b Calculated from parameters in Table 7.8, $A_e - (A_e - A_0)$. ^c Calculated at ae-CCSD(T)/ANO0. ^d Measured with electron spin resonance spectroscopy¹⁹⁶ with uncertainty of ± 0.085 MHz.

Table 3.7: Calculated Fermi contact coupling constants for carbon-13, in MHz.

Parameter ^a	1-	2-	3-
$a_F(\text{C2})$	34.14	506.76	69.30
$a_F(\text{C3})$	–	43.00	39.65
$a_F(\text{C4})$	–10.56	50.93	460.05
$a_F(\text{C5})$	–	39.33	37.92

^aAtom labels match those in Tables 3.1 and 3.2.

2- and 3- pyrrolyl, the spin density is oriented along the b molecular axis, while for 1-pyrrolyl it is more delocalized.

Hyperfine Interactions and Nuclear Spin Statistics

In addition to the electronic spin-rotation interaction, several other sources of angular momentum in the pyrrolyl radical split the rotational energy levels. The spin-1 ^{14}N nucleus has coupling of its electric quadrupole moment with the electric field gradient at the nucleus as well as dipolar electron spin-nuclear spin coupling. Spin-spin coupling also arises from the spin-1/2 H nuclei, which possess magnetic moments. Additionally, each $I > 0$ nucleus has a Fermi contact interaction arising from spin density within the volume of the nucleus. All of these coupling terms have been calculated at the ae-CCSD(T)/cc-pwCVTZ for each pyrrolyl isomer. The Fermi contact a_F terms, the diagonal elements of the nitrogen quadrupole coupling tensor (χ_{aa} , etc.), and the diagonal elements of the dipolar spin-spin coupling tensors (T_{aa} , etc.) are listed in Table 3.6. Complete tensors are provided in the Supplemental Information.

The ^{14}N -quadrupole coupling tensors follow a similar trend to the electron spin-rotation coupling tensors. The diagonal elements of the 2- and 3-pyrrolyl χ tensors are quite similar to those for pyrrole (in MHz, $\chi_{aa} = 1.40475(181)$, $\chi_{bb} = 1.29577(203)$, $\chi_{cc} = -2.70052(272)$)³⁰, while those of 1-pyrrolyl resemble those of pyridine (in MHz, $\chi_{aa} = -4.91224(147)$, $\chi_{bb} = 1.43083(151)$, $\chi_{cc} = -3.48141(211)$)³⁰. This suggests that the electronic structure local to the nitrogen is not much altered by the dissociation of either C–H bond, as the unpaired electron remains localized to the respective carbon in 2- and 3-pyrrolyl. The electronic environment near the nitrogen in 1-pyrrolyl, however, is more consistent with a π -aromatic system combined with a lone pair in a σ -type molecular orbital in the molecular plane.

The electronic structure trends are also reflected in the Fermi contact terms, particularly those for ^{13}C shown in Table 3.7. The magnitudes of the Fermi contact terms are proportional to the spin density at the nuclear center: positive terms correspond to excess α density and negative terms to excess β density. In 1-pyrrolyl, all values are either negative or weakly positive because the unpaired electron is primarily

delocalized among π orbitals above and below the nuclear plane. Meanwhile, 2- and 3-pyrrolyl have large positive values on the radical center where the unpaired electron lies in a σ -type orbital and weakly positive values elsewhere.

Finally, 1-pyrrolyl has two sets of equivalent hydrogen atoms, and therefore rotational transition intensities are affected by nuclear spin statistics. In C_{2v} , the nuclear spin wavefunction symmetry is $10A_1 \oplus 6B_1$, the former of which combine with even K_a rotational wavefunctions and the latter combine with odd K_a wavefunctions owing to the A_2 symmetry of the ground electronic state^{211,212}. As a result, there is a 5:3 ratio of statistical weights for the even:odd K_a rotational energy levels.

3.4 Implications for Laboratory Spectroscopy and Astronomy

Vibrational, Rovibrational, and Vibronic Spectroscopy

To date, three vibrational transitions have been measured and assigned to 1-pyrrolyl using threshold photoelectron spectroscopy¹⁹⁵. No experimental measurements have been reported for 2- or 3-pyrrolyl, and prior to this work, no theoretical predictions of harmonic frequencies were available. Since the photoelectron measurements in 2004, developments in vibrational spectroscopy make the pyrrolyl radicals attractive targets. Vibrational transitions of the pyridyl radical have been recently measured by cryogenically cooled slow photoelectron velocity map imaging (cryo-SEVI)²¹³ and matrix isolation infrared spectroscopy²¹⁴. Stable 5-membered heterocycles have been studied with rotational resolution using Fourier transform infrared spectroscopy with synchrotron sources (e.g., including pyrrole²¹⁵, furan²¹⁶, thiophene²¹⁷), and with an appropriate plasma source or F-abstraction technique²¹⁸, the pyrrolyl radicals may be amenable to detection using these methods.

Simulated anharmonic spectra for the pyrrolyl radicals, evaluated using fc-CCSD(T)/ANO0 force constants with VPT2, are shown in Figure 3.1. A complete list of the transition frequencies and intensities for the non-fundamental modes are provided in the Supporting Information. No additional treatments of Fermi or Coriolis resonances have been performed. For 1-pyrrolyl, the strongest transition is, surprisingly, calculated to be the $2\nu_{21}$ overtone at 1054 cm^{-1} . As this involves an out-of-plane bending vibrational mode, symmetry-breaking effects may induce significant changes in the electronic wavefunction at displaced geometries even without a noticeable error in energy²⁰⁸, so this intensity should be viewed with caution. Other bright modes include the ν_{20} fundamental transition at 683 cm^{-1} and the ν_6 fundamental at 1066 cm^{-1} . The C–H stretching modes near 3100 cm^{-1} are comparable in intensity to several combination band transitions:

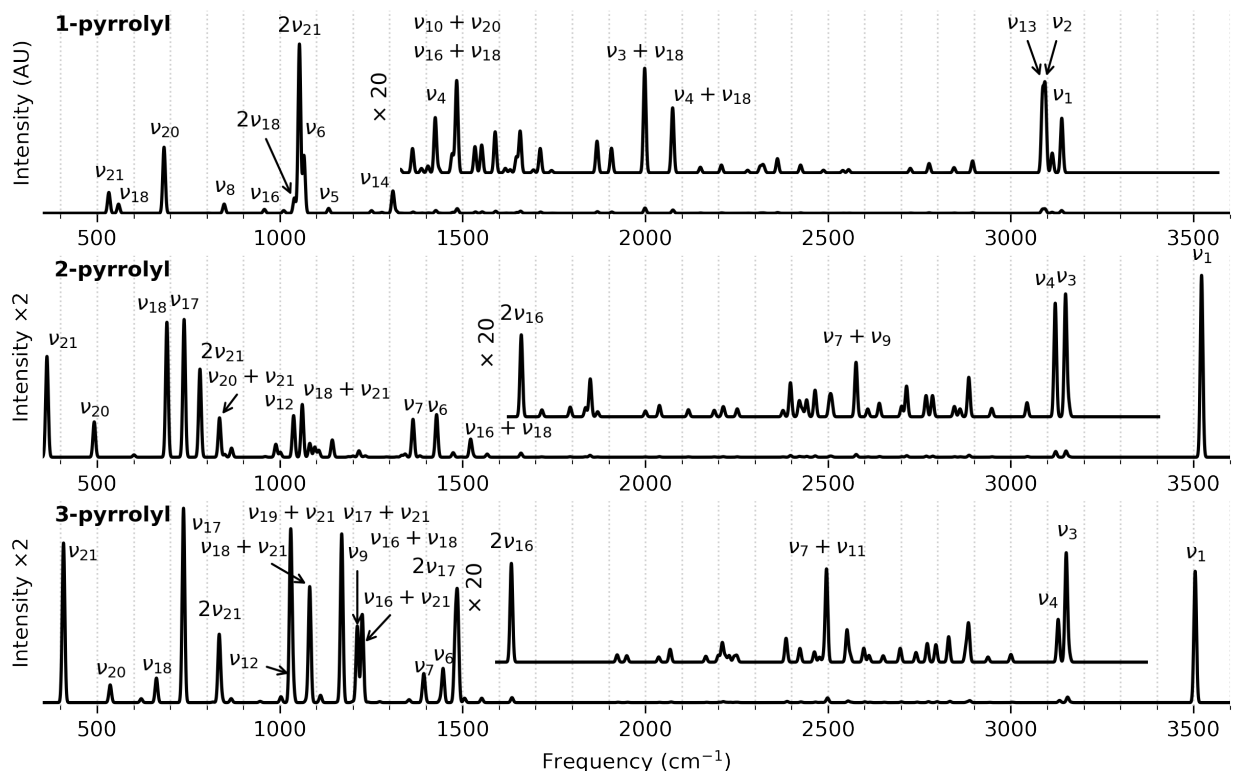


Figure 3.1: Simulated VPT2 anharmonic vibrational spectra of pyrrolyl radical isomers calculated at *fc*-CCSD(T)/ANO1 and convolved to a linewidth of 3 cm^{-1} . Insets show the spectrum magnified by a factor of 20. Labels indicate several of the strongest modes; a complete list of frequencies and intensities is provided in the Supporting Information. For 3-pyrrolyl, the intensity for the ν_{11} mode at 1100 cm^{-1} (not labeled) is plotted using the harmonic value; all other modes in all three plots use anharmonic intensities.

$\nu_{10} + \nu_{20}$ and $\nu_{16} + \nu_{18}$ at 1485 cm^{-1} , $\nu_3 + \nu_{18}$ at 1999 cm^{-1} and $\nu_4 + \nu_{18}$ at 2075 cm^{-1} . These combination band transitions are particularly attractive targets as they lie in a region free from any pyrrole transitions of significant intensity²¹⁹.

Spectra of 2- and 3-pyrrolyl can be readily distinguished by the presence of the bright N–H stretching mode (ν_1) near 3500 cm^{-1} , as well as three A'' modes below 900 cm^{-1} that correspond to IR-inactive A_2 modes in 1-pyrrolyl. The ν_1 mode of 3-pyrrolyl is calculated to lie 18 cm^{-1} below that of 2-pyrrolyl, which in turn is 8 cm^{-1} below the ν_1 mode of pyrrole²¹⁹. Assuming both isomers are present in the same environment, the $700\text{--}1200\text{ cm}^{-1}$ region features several transitions that readily distinguish the two. In particular, two combination bands involving ν_{21} near 1200 cm^{-1} ($\nu_{17} + \nu_{21}$ at 1169 cm^{-1} and $\nu_{16} + \nu_{21}$ at 1226 cm^{-1}) are especially bright in 3-pyrrolyl, while $\nu_{20} + \nu_{21}$ mode at 835 cm^{-1} is more distinct in 2-pyrrolyl.

A peak with $m/z = 66$, the nominal mass of $\text{C}_4\text{H}_4\text{N}$, was detected in Titan’s atmosphere by the Cassini Ion-Neutral Mass Spectrometer¹³¹. Radicals are thought to play an important role in Titan’s atmospheric

chemistry¹⁷⁸, and the cyclic reactive molecule cyclopropenylidene (*c*-C₃H₂) was recently detected at high altitudes with the Atacama Large Millimeter Array. Infrared observations with the James Webb Space Telescope (JWST) may provide a means for detecting additional reactive species. The Mid Infrared Instrument aboard JWST will have its greatest signal-to-noise ratio and spectral resolution in the 800–2000 cm⁻¹ range²²⁰. The large CH₄ concentration in Titan’s atmosphere will dominate the spectrum near 1300 cm⁻¹, but each pyrrolyl isomer has at least one bright mode in the 800–1200 cm⁻¹ range that can be targeted. 3-pyrrolyl also has a strong overtone transition 2ν₁₇ at 1480 cm⁻¹ and a combination band ν₁₆ + ν₁₈ at 1486 cm⁻¹ that may be observable.

Rotational Spectroscopy

Pure rotational spectroscopy has proven to be a powerful method for detecting transient molecular species, and the pyrrolyl radicals would appear to be excellent targets. Pulsed discharge nozzle expansions coupled with chirped-pulse and/or cavity Fourier Transform microwave (FTMW) spectroscopy has led to the identification of a number of radicals in the 2–90 GHz range, including C₆H₅²²¹, HOCO²²², and H₂C₃N among many others. Pyrolysis nozzles are also used in conjunction with FTMW spectroscopy to effectively generate radicals such as C₆H₅O²²³ and C₄H₃O₂²⁰⁶. In addition, the recent use of buffer gas cooling cells with chirped-pulse FTMW spectroscopy^{224,225} has enabled new high-sensitivity measurements owing to their large duty cycles, and addition of a pyrolysis or discharge source would make production of pyrrolyl from pyrrole a possibility in these instruments as well. Toward higher frequencies, long-pass millimeter-wave frequency modulation spectroscopy is routinely employed with discharge or F-abstraction cells similar to those used with synchrotron sources to detect radicals^{202,226–228}.

To guide potential searches using molecular beam or buffer gas methods, simulated 4 K rotational spectra in the centimeter band are shown for all three isomers in Figure 3.2. All isomers are asymmetric tops, with $\kappa \approx 0.6$ for 1-pyrrolyl and 0.5 for 2- and 3-pyrrolyl. Each features a prominent *a*-type progressions with a large harmonic defect owing to the significant asymmetry: though $B_0 + C_0$ is ~ 13.5 GHz for each, these progressions are spaced by ~ 10 GHz. Changes in the orientation of the principal axes relative to the ring structure cause each rotational constant to follow the trend (1-pyrrolyl) < (2-pyrrolyl) < (3-pyrrolyl), making isomer discrimination especially simple in the pure rotational spectrum. The spectrum of 3-pyrrolyl additionally contains *b*-type transitions of appreciable intensity. Analogous transitions are present in the spectrum of 2-pyrrolyl but are much weaker owing to its small μ_b value, and they are not apparent in Figure 3.2.

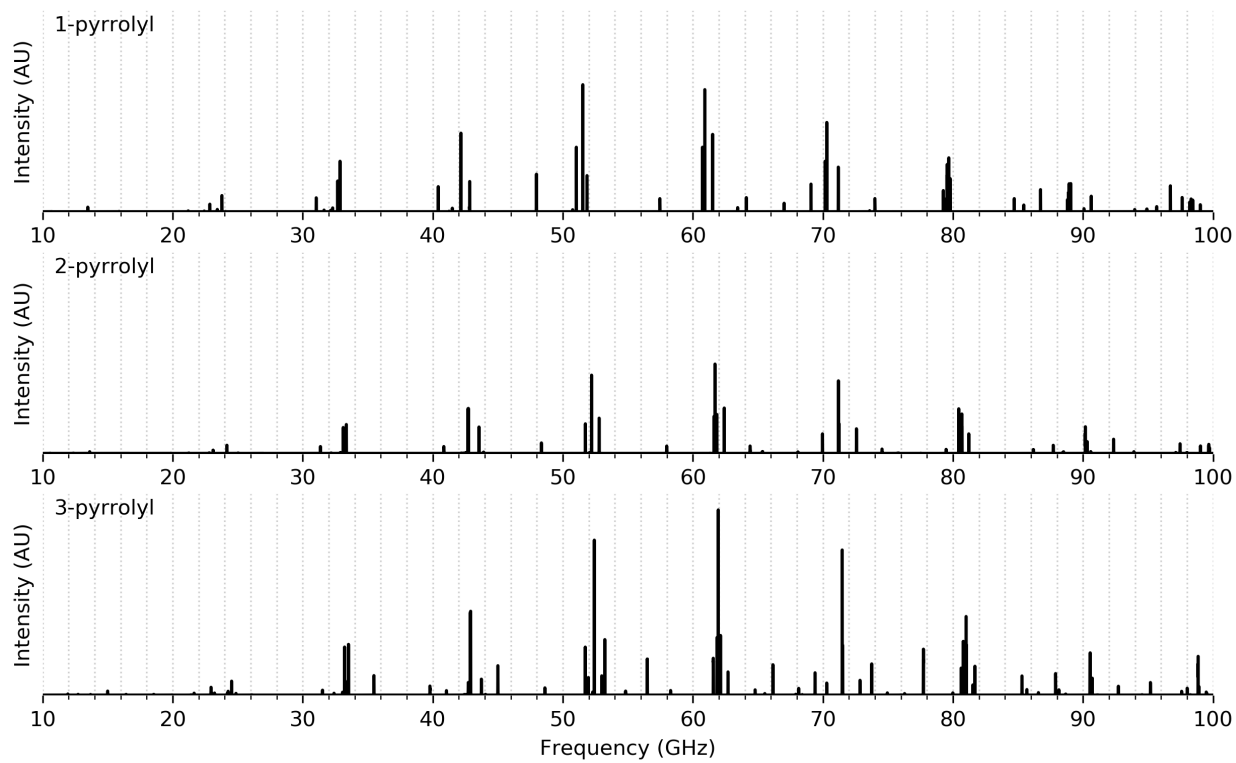


Figure 3.2: Simulated rotational spectra of pyrrolyl isomers in the 10–100 GHz frequency range at a temperature of 4 K. All panels use the same vertical scale for intensity comparisons. Rotational transitions are convolved to a linewidth of 3 MHz.

The low- N transitions of all three radicals show complex structure arising from spin-rotation and hyperfine splitting, as shown in Figure 3.3. As N increases, the structure associated with nuclear spin collapses. The majority of the intensity in the hyperfine structure associated with the fundamental a -type ($N_{K_a K_c} = 1_{01} - 0_{00}$) rotational transition spans 20–30 MHz for all three radicals, and that of the fundamental b -type ($1_{11} - 0_{00}$) transition for 2- and 3-pyrrolyl. The $9_{09} - 8_{08}$ a -type rotational transition, which is heavily mixed with $9_{19} - 8_{18}$ and the b -type transitions $9_{19} - 8_{08}$ and $9_{09} - 8_{18}$ (2- and 3-pyrrolyl only) shows a much more compact structure spanning only 1–2 MHz. For 2- and 3-pyrrolyl, the two prominent clusters of peaks have clearly resolved into a spin-rotation doublet typical of a radical with a doublet electronic state, as shown with lower resolution in Figure 3.4. Similar collapse is observed in higher- N b -type transitions like the $9_{46} - 8_{35}$ transition shown in Figure 3.3. The spin-rotation doublet is beginning to become resolved in 2-pyrrolyl, and becomes more apparent at still greater N . This limited structure within higher N transitions makes both spectroscopy and radioastronomy in the mm-wave region particularly promising; however, the transition frequencies predicted from the spectroscopic constants presented here are expected to be less accurate than those toward low frequencies.

3.5 Conclusions

In this work, we have characterized the 1-, 2-, and 3-pyrrolyl radicals in their ground electronic states at the CCSD(T) level of theory with an emphasis on computing spectroscopic parameters for rotational and vibrational spectroscopy. Pyrrolyl radicals are important combustion intermediates and have been proposed to be able to form under the conditions of Titan’s atmosphere, but to date little spectroscopic information is available. Our CCSD(T) optimized equilibrium geometries, computed with full electron correlation, are in general agreement with previous DFT structures and obtain the same relative energy ordering: 1-pyrrolyl is the most stable, with 3-pyrrolyl lying 105 kJ/mol higher and 2-pyrrolyl 106 kJ/mol higher.

To evaluate parameters sensitive to the local potential energy surface, quadratic, cubic, and a subset of quartic force constants were derived from finite differences at displaced molecular geometries under the frozen core approximation at CCSD(T)/ANO0. These force constants were used to derive harmonic vibrational frequencies and intensities, vibration-rotation interaction coefficients, and centrifugal distortion constants. In addition, tensor elements were computed for the electron spin-rotation interaction, the dipolar electron spin-nuclear spin interactions for $I > 0$ nuclei, and the ^{14}N quadrupole interaction, as well as Fermi contact interactions for each $I > 0$ nucleus, which are in excellent agreement with isotropic coupling terms measured

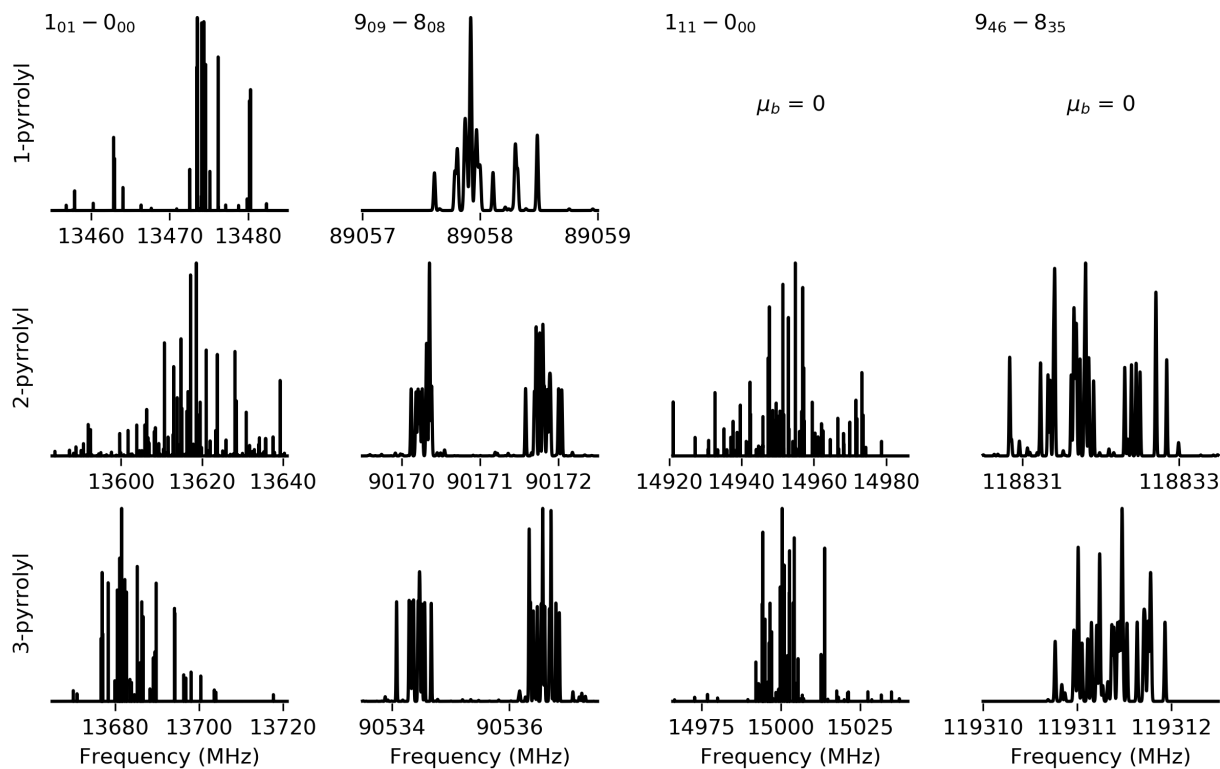


Figure 3.3: Simulated hyperfine splitting in selected *a*- and *b*-type rotational transitions of pyrrolyl radicals. Transitions are convolved to a linewidth of 10 kHz, and the vertical axis scale for each plot is different; relative intensities between plots are not to scale.

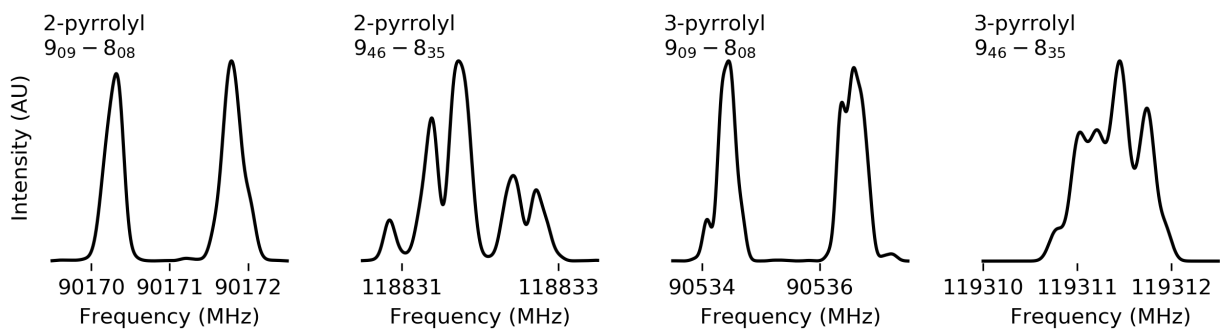


Figure 3.4: As Figure 3.3, but transitions are convolved to 100 kHz to show the collapse of hyperfine structure.

previously with electron spin resonance for 1-pyrrolyl.

Simulated anharmonic vibrational spectra were shown in Figure 3.1 in the 400–4000 cm^{-1} range covering all of the fundamental modes. In particular, several combination bands involving low-frequency bending modes for each isomer are calculated to carry significant intensity, providing distinctive infrared spectral signatures that distinguish each isomer from the others and from pyrrole. These isomers are amenable to detection by high-resolution photoelectron methods such as cryo-SEVI or by matrix isolation infrared spectroscopy. The pure rotational spectra are simulated using ground-state rotational constants and all diagonal hyperfine tensor elements in Figures 3.2, 3.3, and 3.4. Each isomer has at least one dipole moment projection exceeding 1 D, and should be readily observable by FTMW methods if sufficient quantities of the radicals can be produced. At low frequencies, each rotational transition is split into many tens of lines due to angular momentum coupling, but most of this structure collapses by $N = 9$ near 100 GHz, so the prospects for detection in the millimeter-wave band (both in the laboratory and in space using ALMA) are promising, especially if initial observations in the centimeter band are made to refine the rotational constants.

Given their importance in N-containing pollution from biomass combustion, in situ spectroscopic measurements of the pyrrolyl radicals may yield fundamental mechanistic data needed help guide mitigation efforts. Laboratory spectroscopy is also a necessary precursor to astronomical observations seeking to identify these radicals in Titan’s atmosphere and in the interstellar medium. Our goal with this work is to enable these new laboratory spectroscopic investigations of the pyrrolyl radicals to be undertaken.

Chapter 4

Reaction Discovery Part I: Search for Novel Gas-Phase N-heterocycle Formation Pathways with an *ab initio* Nanoreactor

Nitrogen-containing heterocycles pose an intriguing astrochemical mystery. 45 different varieties have been detected on meteorites with non-terrestrial isotopic abundances, but none have been detected in space, despite numerous search attempts. It is unclear if these species are more likely to form through low-temperature gas-phase chemistry, photoprocessing of icy grains, or a combination thereof. Further exploration of this question requires a broader catalog of potential N-heterocycle precursors, particularly for low temperature gas-phase chemistry. N-heterocycles are also believed to be present in Titan's atmosphere, where their chemistry might have implications for the formation of prebiotic molecules in the atmosphere of early Earth. Here, results of *ab initio* molecular dynamics simulations of gas-phase N-heterocycle forming reactions will be discussed. These simulations were performed with an *ab initio* nanoreactor, a computational tool developed for chemical reaction discovery. Multiple novel gas-phase N-heterocycle formation pathways have been revealed that are likely feasible at low temperatures and warrant further experimental and astronomical study.

4.1 Introduction

The potential interstellar formation of N-heterocycles has long been of interest to astronomers and astrobiologists due in large part to their importance in biology, and therefore their relevance to origin of life questions. A wide variety of species that contain this motif have been identified on meteorites with non-terrestrial isotopic abundances,⁷ and there is evidence that the 6.2 μm unidentified infrared (UIR) band can only arise from the presence of a nitrogen atom in a polycyclic aromatic hydrocarbon (PAH) structure.¹⁰ However, despite the 94 nitrogen containing species identified in space (per the Cologne Database of Molecular Spectroscopy at the time of this writing^a), all astronomical searches for N-heterocycles have been unsuccessful.^{22,229}

Historically, it was thought that meteoritic N-heterocycles could only form through photochemistry on the surfaces of icy grains in cold molecular clouds or the outer envelopes of protoplanetary disks. Isotopic ratios from these regions match those in meteorites, suggesting that interstellar material, including icy grains, is accreted to meteorite parent bodies.⁷² Irradiation of H_2O and NH_3 ices that contain benzene and naphthalene have been shown to produce N- and O-heterocycles,¹¹⁶ and other experiments have shown that simple N-heterocycles can be functionalized to form nucleobases and vitamins.^{111,230–232} Although it is unclear how well these experiments reproduce astrophysical conditions, they were still thought to be more promising than gas-phase mechanisms; the only ones described in the literature either contained energetic barriers to the incorporation of nitrogen into aromatic rings¹⁴⁸ or relied on other N-heterocycles as precursors.⁸⁶ Energetic barriers prevent a reaction from happening efficiently at the extremely low temperatures and densities of the regions of interest, and with no N-heterocycle detections, chemistry relying on these species is shrouded in uncertainty. The survivability of N-heterocycles in the bare ISM is a matter of hours due to their susceptibility to UV radiation,²³³ so it is highly unlikely that the abundance of meteoritic N-heterocycles can be explained by formation in higher temperature environments followed by travel to the low temperature environments of interest.

However, within the last decade there have been a large number of chemical reactions that have been shown to be efficient at cold temperatures due to effectively barrierless reaction coordinates, where all intermediates and transition states are lower in energy than the reactants. Several of these reactions form N-heterocycles. Perhaps most interesting to N-heterocycle formation is the reaction of vinyl cyanide (H_2CCHCN) with the β -cyanovinyl radical (HCCHCN) to form pyridine,⁸⁵ suggesting that ring closing reactions between acyclic precursors is indeed possible in these cold environments, even between neutral

^aSee <https://cdms.astro.uni-koeln.de/classic/molecules> for the most current list of molecules detected in space.

species.

Recently, the GOTHAM survey of the Taurus Molecular Cloud 1 (TMC-1) has identified five never-before-detected cyclic carbon rings, all functionalized with a cyano (CN) group.⁶² This cold molecular cloud has temperatures near 10 K and number density of order 10^3 cm^{-3} . Despite these conditions, the reaction of aromatics and has also been shown to proceed rapidly due to a barrierless reaction coordinate.¹⁷⁷ The derived abundances of recently detected aromatic and cyclic molecules greatly exceed the values predicted by chemical models, despite their accurate predictions of acyclic carbon chain abundances. This survey included a search for N-heterocycles pyrrole (c-C₄H₅N) and pyridine (c-C₅H₅N), but they were not found. This suggests that the gas-phase formation pathways of homocyclic carbon rings and N-heterocycles in such a low-temperature environment proceed through different classes of reactions or require precursors that exist in abundance for the homocyclic but not heterocyclic pathways. Overall, this indicates that there is a wealth of low-temperature astrochemistry that we currently do not understand.

Similar questions exist about the formation of the ubiquitous interstellar polycyclic aromatic hydrocarbons (PAHs) form through top-down or bottom-up chemistry. The top-down approach suggests that large PAHs are formed in the outflows of massive stars, and are subsequently broken-down through exposure to cosmic rays and UV radiation in the bare ISM and diffuse clouds.¹⁹ The bottom-up approach suggests that PAHs and other complex organic molecules are formed from association reactions of smaller species.²⁰ With the limited knowledge about the incorporation of nitrogen within aromatic rings, it is currently unclear through which pathway nitrogen-containing PAHs (PANHs) might be formed. If the 6.2 μm UIR band does indeed arise from PANHs, the lack of observed smaller N-heterocycles could be evidence of a top-down formation mechanism. However, the paucity of information about N-heterocycle reaction networks, especially in the gas phase, prevents such a conclusion from being drawn at this point.

It is also possible that the prototypical, non-functionalized N-heterocycles that have been the subjects of astronomical searches are quickly depleted or deposited. Many of the aforementioned experimental ice surface studies show that N-heterocycles, when deposited on surfaces analogous to icy grains found in cold molecular clouds and outer envelopes of protoplanetary disks, can be functionalized to form the same biological molecules, such as nucleobases and vitamins, that have been identified in meteorites.^{111,230–232} Little is known about functionalization reactions of N-heterocycles in the gas phase at low temperature, so it is unclear if any such pathways may be operative.

N-heterocycles are also of significant interest in the study of Titan's atmosphere. Several tentative detections of single-ringed species, along with a wealth of other N-containing complex organic molecules that

could be potential N-heterocycle precursors, were made by the Cassini/Huygens mission.^{128,141,176} Titan is considered an analog for early Earth,^{133,134,136} so understanding the role N-heterocycles play in this environment could provide insight into potential terrestrial formation of such prebiotic species.

Ultimately, an understanding of how N-heterocycles participate in meteoritic chemistry, PANH formation, and Titan’s atmosphere requires inclusion of appropriate formation and destruction pathways into chemical kinetics models. These models seek to replicate the chemistry of a particular environment, and when done comprehensively, can offer accurate predictions of molecular abundances. However, as detailed in Chapter 1, very few low-temperature pathways that include N-heterocycles are available in the current literature, and KIDA, a database of chemical reactions relevant for astrochemistry, does not include any.²⁶ More reactions must be identified in order to accurately incorporate N-heterocycles within these models.

Modern computational chemistry offers an array of tools to search for new chemical reactions. The *ab initio* nanoreactor,¹²⁵ an *ab initio* molecular dynamics (AIMD) simulation, is unique in that it explores potential energy surfaces without the need for predetermined reaction coordinates. This makes it excellent for chemical discovery; its usefulness has been demonstrated in the search for multiple pathways to organic molecules, including biomolecules urea and glycine.¹²⁵ In these computational experiments, both novel pathways and ones previously identified with experiment were found by the nanoreactor. However, in this previous work, the main scientific question was in what potential products might form from a certain set of reactants. Here, the desired products, N-heterocycles, are already known, while the exploration of potential precursors is the goal. Therefore, instead of starting with potential reactants to search for products, these simulations began with either pyrrole or pyridine, plus CN, in order to search for non-intuitive bimolecular breakdown products that could be present in the interstellar and planetary environments of interest to this work.

This chapter and the two following detail this search for pyridine and pyrrole formation mechanisms. In this chapter (Part I), the nanoreactor simulations and the wide range of N-heterocycle breakdown pathways are described. The next two chapters discuss novel reactions found by expanding upon pathways identified in the nanoreactor simulations. Part II explores a pyrrole forming pathway with β -cyanovinyl (HCCHCN) and ketenimine (H₂CCNH) precursors. Part III details two reaction schemes whereby an n -membered ring is formed through an insertion reaction into an $(n - 1)$ -membered ring; specifically, the formation of pyrrole from azete (*c*-C₃H₄N) and cyanomethyl (H₂CCN), and the formation of pyridine from 1-pyrrolyl (*c*-C₄H₄N) and cyanomethylene (HCCN). This work will hopefully enable and inspire future searches for astrophysical formation mechanisms of complex organic molecules using the nanoreactor, as well as theoretical and

experimental kinetics and dynamics studies that further our understanding of the newly identified reactions.

4.2 Methods

Two computational approaches have been employed in this search for barrierless N-heterocycle forming pathways. The first, discussed here, is the use of the nanoreactor to identify interesting N-heterocycle precursors. The second, detailed in parts II and III, involves both searching for minimum energy paths (MEPs) for the reactions discovered in the nanoreactor and expanding the potential energy surfaces (PESs) that contain these MEPs to search for other routes to N-heterocycle formation.

The details of the nanoreactor simulation have been previously described.^{105,125} Briefly, the Born-Oppenheimer potential energy surface for these AIMD calculations was calculated with B3LYP with an unrestricted wavefunction and a 6-31G* basis set, hereafter referred to as uB3LYP/6-31G*, using the TeraChem quantum chemistry program (development version).²³⁴ TeraChem is unique in that it uses GPUs to evaluate two-electron integrals in parallel, which has been shown to be two orders of magnitude faster than programs that rely on CPUs. Each frame of the simulation corresponds to a 0.5 fs timestep, and Langevin dynamics are used to maintain a simulation temperature with a ~ 6 fs time constant.

The simulation takes place within a sphere containing a certain number of N-heterocycle molecules, CN radicals, and He atoms with a potential

$$U(r) = mk(r - r_0)^2\theta(r - r_0)$$

where m is atomic mass, k is the force constant, and θ is the Heaviside step function. This potential is harmonic at radii greater than r_0 and zero at values smaller than r_0 .

The initial configurations of molecules were made using the program PACKMOL,²³⁵ which populates molecules and atoms of interest within spheres of certain radii in such a way that there are no overlapping atoms. Spheres containing pyridine and CN and pyrrole and CN with multiple unique starting configurations were produced. The number of each species used in these initial spheres are given in Table 4.1. Each starting configuration was minimized at uB3LYP/6-31G* to prevent the inclusion of any high energy arrangements that would significantly impact the molecular dynamics trajectories.

The simulation is split into two different temporal components. In the first (t_1), the contents of the sphere are allowed to expand out to radius $r_0 = r_1$. In the second (t_2), the radius is decreased to $r_0 = r_2$, forcing the contents of the sphere into the center and promoting collisions and chemical reactions. The radius then

Table 4.1: Starting spheres for nanoreactor simulations. For each sphere, numbers of each species, the number of different starting configurations, and the total number of simulations are listed.

Label	Type	N-heterocycle	CN	He	Configurations	Total Simulations
P1	pyridine	1	1	50	4	76
P2a	pyridine	2	1	10	2	72
P2b	pyridine	2	1	20	4	52
P3	pyridine	3	3	20	4	25
P5	pyridine	5	5	20	4	24
R1	pyrrole	1	1	50	6	60
R2	pyrrole	2	2	30	4	96

Table 4.2: Ranges of parameters explored for each sphere (by label in Table 4.1).

Sphere	T (K)	r_1 (Å)	r_2 (Å)	t_1 (0.5 fs)	t_2 (0.5 fs)	k_1 ($\frac{\text{kcal}}{\text{mol}^{-1}\text{Å}^{-2}}$)	k_2 ($\frac{\text{kcal}}{\text{mol}^{-1}\text{Å}^{-2}}$)
P1	1500 - 2500	8.0 - 12.0	3.0 - 5.0	2000	200 - 1000	1.0	0.5 - 0.75
P2a	2000	8.0 - 12.0	3.0 - 5.0	1000 - 2000	200 - 800	1.0	0.5
P2b	1000 - 3500	12.0	3.0 - 5.0	2000	1000	1.0	0.5
P3	1000 - 3000	12.0	4.5 - 5.0	2000	1000	1.0	0.5
P5	1000 - 3000	12.0	5.0	2000	1000	1.0	0.5
R1	1500 - 3500	12.0	3.0	1500	200 - 1000	1.0	0.5 - 1.0
R2	1500 - 2500	8.0 - 12.0	3.0 - 4.0	1500	300 - 600	1.0	0.5

reverts to r_1 after time t_2 to prevent further chemical reactions from occurring. This is described by

$$V(r, t) = f(t)U(r; r_1, k_1) + (1 - f(t))U(r; r_2, k_2), \text{ where } f(t) = \theta\left(\left\lfloor \frac{t}{T} \right\rfloor - \frac{t}{T} + \frac{t_1}{T}\right)$$

Here, $f(t)$ describes a rectangular wave. T is equivalent to $t_1 + t_2$, such that $f(t) = 1$ for duration t_1 and $f(t) = 0$ for duration $T - t_1$. The bracket indicates a floor function. A visual example of this process is shown in Figure 4.1.

All parameters were varied between simulations. Table 4.2 details the range of parameters explored for each starting configuration. Each simulation was allowed to run for 24 hours of computation time, yielding several picoseconds of simulation time. The completed simulations were visualized with the Visual Molecular Dynamics program.²³⁶ Most of the resulting products were identified visually. Products for P1 and R1 simulations are listed in Tables 4.3 through 4.10. The products listed here are the first stable products formed in the simulations; in many trajectories these products reacted further, generally leading to significant fragmentation that is not scientifically interesting for this investigation. In cases where visual identification of the first products formed was not possible, the trajectories were extracted from the full simulation by analyzing the species present for changes in connectivity, determined with a combination of

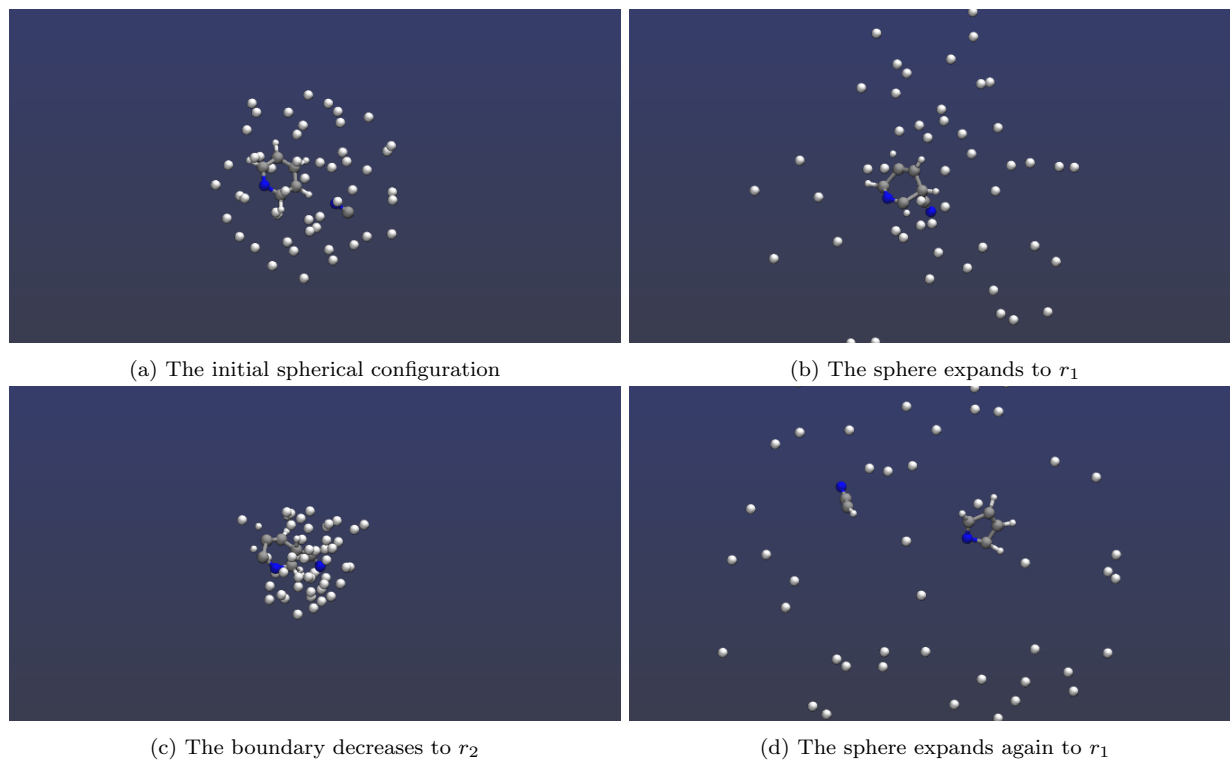


Figure 4.1: The chronology of the nanoreactor simulations proceeds from 4.1a to 4.1d. The simulation begins in a He-filled sphere that is allowed to expand to fill a space with radius r_1 for amount of time t_1 . Then the radius shrinks to r_2 for amount of time t_2 , forcing the contents into the center and causing chemical reactions to occur. After t_2 , the sphere expands back to r_1 , preventing chemical reactions from continuing. In this example, it can be seen that the pyridine and CN react to produce 1-pyrrolyl and HCCN, visible in the last image. The white spheres are He atoms.

graph theory and machine learning.¹⁰⁵ This analysis then produced a trajectory of each individual reaction that occurred within the nanoreactor simulation.

4.3 Results and Discussion

There were two main aims of this investigation: to demonstrate the usefulness of the *ab initio* nanoreactor in the search for low-temperature formation pathways and to identify novel N-heterocycle formation pathways for inclusion in astrochemical networks. The results of the simulations as they pertain to these goals are discussed below. Tables with the specific outcomes for the sets of simulations containing 1 pyridine and 1 pyrrole are also provided. Simulations with other numbers of reactants were run and are listed in Tables 4.1 and 4.2, but they produced mostly reactions that were not relevant to the search for bimolecular N-heterocycle forming pathways. Due to the extremely low densities in the regions of space of interest to this investigation, three body reactions are not feasible. Unimolecular rearrangements occur in these conditions mainly as intermediates along a bimolecular pathway; spontaneous rearrangement of a stable precursor is not favorable at these low temperatures. For these reasons, this discussion includes only the scientific relevance of the trajectories that result in two products.

All simulations are available for download from the associated GitHub repository.^b

4.3.1 Pyridine

Simulation Outcomes

In total, 249 simulations of pyridine and CN were run. In simulations P3 and P5, polymerization of the CN radicals was very common and appeared to be more rapid than a reaction between CN and the ring. Often in the initial minimization, the CN would polymerize or bind to pyridine. The P2a and P2b simulations avoided the CN polymerization, but three body reactions were promoted by the presence of the other pyridine. For these reasons, these simulations will not be discussed further.

For the P1 simulations, four different initial configurations of the pyridine, CN, and helium atoms were used. After the minimization of these configurations, the pyridine and CN remained separated. These simulations produced 30 trajectories where three or more products were formed, listed in Table 4.3, 19 trajectories where two products formed, listed in Table 4.4, 12 trajectories where one product formed, listed in Table 4.5, and 15 trajectories in which no reaction occurred, listed in Table 4.6. There are useful trends

^bhttps://github.com/sljohansen793/Nanoreactor_data

that arise from these results, despite the relatively small sample size and the fact that not every parameter value was used for the same number of simulations (for example, 44 simulations were run with $r_1 = 12.0 \text{ \AA}$, and only 16 for both $r_1 = 8.0 \text{ \AA}$ and $r_1 = 10.0 \text{ \AA}$).

Each initial configuration did result in multiple pathways of each type in all cases, suggesting that the starting arrangement of pyridine, CN, and He in the sphere did not heavily bias the outcome towards a particular type of reaction. The r_1 and k_2 parameters influenced the type of trajectory most significantly. 50% of all simulations with $r_1 = 8.0 \text{ \AA}$ had zero reaction events, while only 25% with $r_1 = 10.0 \text{ \AA}$ and less than 7% with $r_1 = 12.0 \text{ \AA}$ had zero reaction events. Likewise, 0% of $r_1 = 8.0 \text{ \AA}$ trajectories were fragmentation pathways, while 12.5% of $r_1 = 10.0 \text{ \AA}$ and 63.6% of $r_1 = 12.0 \text{ \AA}$ pathways lead to three or more products. This trend is likely because a greater expansion correlates with collisions with greater kinetic energy after the sphere collapses.

The k_2 parameter controls the force constant of the harmonic potential around the sphere during the t_2 interval of the simulation, when the molecules are forced into the center. The difference between 0.5 and 0.75 kcal mol⁻¹ Å⁻² is substantial. At 0.5 kcal mol⁻¹ Å⁻², only 14.6% of trajectories fragmented into three or more products, while 70.8% of simulations run with 0.75 kcal mol⁻¹ Å⁻² did. There were no non-reactive 0.75 kcal mol⁻¹ Å⁻² trajectories, while 31.7% of the 0.5 kcal mol⁻¹ Å⁻² trajectories had zero reactions. Like r_1 , a greater k_2 value imparts greater kinetic energy to the contents of the sphere as it moves towards the center.

The trend regarding equilibrium temperature seems to point to lower temperatures leading to more reaction events, but the differences between 2500 K and 1500 K trajectories are not as substantial as they were for r_1 and k_2 . There is a higher percentage of 2500 K simulations that lead to no reaction events (37.5%) compared to 1500 K (13.6%), and a higher percentage of 1500 K simulations that lead to fragmentation into three or more products (40.9%) than in the 2500 K simulations (25%). Simulations run with a broader range of temperatures while all other variables are held constant would help to elucidate whether or not this trend is real.

The variable r_2 also hints at a trend, but requires more data to confirm if this is the case. The only values used were 3.0 and 5.0 Å, and 5.0 Å was only used for 16 of the 76 simulations. This larger radius in the second time step might have discouraged fragmentation, as none of the trajectories with an r_2 value of 5.0 Å resulted in three or more products, and only three resulted in two product trajectories. For 3.0 Å, 50% of the trajectories resulted in three or more products, and 26.7% resulted in two. As is the case with equilibrium temperature, though, more simulations would need to be run to evaluate this potential trend.

The only other parameter that was varied, t_2 , does not show any observable trend between simulations.

Bimolecular Pathways

The trajectories that results in two products are listed in Table 4.4. Table 7.13 includes descriptions of the mechanisms seen in these trajectories.

Two of these reactions involve the formation of pyrrolyl and HCCN. In both these simulations, CN bonded to the ortho carbon, then extracted that carbon from the ring. This also occurred in one of the single product trajectories, but the final product was HCCN bonded to the pyrrolyl N. This reaction was chosen for further refinement, the results of which are discussed at length in Part III. While the other reactions were not refined further, they do have some potential for relevance to astrophysical environments or planetary atmospheres.

$N_2 + HCCCHCHCHCH$ is the only pathway that is feasible solely as an N-heterocycle destruction pathway, but is still worth further investigation. The extremely high relative stability of N_2 makes it an unrealistic precursor, especially at low temperatures, but the N-heterocycle breakdown pathway is likely quite exothermic. The long hydrocarbon chain radical is structurally similar to the known astronomical molecule allenyl acetylene ($H_2CCCHCCH$)²³⁷. It is also a structural isomer of phenyl, a radical derivative of benzene, so further cyclization is another route that could be explored computationally.

$H + NCCHCHCHCHCN$, $HCCH + HCNCHCHCN$, and $CHCH_2 + HCNCNCCH$ all involve small species known (or inferred in the case of $CHCH_2$) to be present in the ISM^{238–240} that bond to a chain containing two nitrogen atoms, followed by a ring closure. There have been multiple acyclic hydrocarbons that include two nitrogen atoms detected in the ISM, including isocyanogen ($CNCN$),²⁴¹ protonated cyanogen ($NCCNH^+$, considered a proxy for cyanogen, $NCCN$),²⁴² cyanamide (NH_2CN),²⁴³ carbodiimide ($HNCNH$),²⁴⁴ E- and Z-cyanomethanimine ($HNCHCN$),^{245,246} and aminoacetonitrile (H_2NCH_2CN).²⁴⁷ Larger species like the ones seen in these simulations have likely not been detected due to a lack of laboratory spectroscopy and a decrease in abundance as the possible variety of such species increases with size. In the case of $NCCHCHCHCHCN$, only conformers with a net dipole moment can be observed in the radio frequencies. Future computational work on these reactions is quite promising. If any of these pathways are calculated to be barrierless, laboratory spectroscopy and astronomical searches for these nitrogen-containing species are highly worthwhile.

The final class of bimolecular pathways discovered were between HCN and $HCCHCHCHNC$, $H_2CCNCHCCH$, and $HCCCHCHCNH$. Very similar, albeit closed-shell, species have been detected in the ISM, most notably propargyl cyanide ($HCCCH_2CN$)²⁴⁸ and isomers cyanovinylacetylene ($HCCCHCHCN$) and vinylcyanoacetylene ($H_2CCHCCN$).²⁴⁹ Similar to the other trajectories that produced N-containing chains, any barrierless

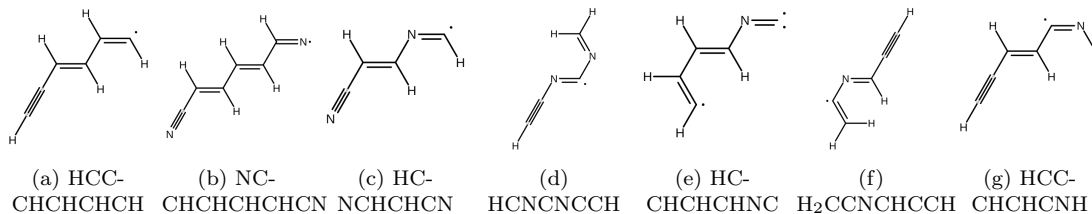


Figure 4.2: Structures of pyridine precursors discussed in the text.

pathways found can direct future experimental and observational work.

Hydrogen abstraction from the pyridine ring by the CN radical occurred in 9 of the 19 bimolecular trajectories. In four of these trajectories, the final products were HCN and either ortho-, meta-, or para-pyridyl, while ring breakage occurred in the remaining five. HNC appeared instead of HCN in only one of these simulations.

For the reactions discussed above, an important component of future computational work is to expand the potential energy surfaces beyond just the MEPs of the reactions identified in the nanoreactor simulations. There are many different potential isomers of these long chains, and ideally all should be explored as potential pyridine precursors. Pathways where the identity of the radical precursor is switched should be explored, as well. For example, when finding the MEP between HCCH and HCNCHCHCN, HCC and H₂CNCHCHCN should also be considered.

4.3.2 Pyrrole

Simulation Outcomes

In total, 156 nanoreactor simulations were run beginning with pyrrole, CN, and He. A number of trajectories involved three-body reactions and/or CN polymerization, and will not be discussed further.

In all of the R1 simulations, the initial minimization of the spheres resulted in CN bound to the ring. All were in the 2-cyanopyrrole position except for configuration 0, which was in the 3-cyanopyrrole position, and configuration 5, which was in the 2-isocyanopyrrole position. Of these 60 simulations, 31 resulted in three or more products (Table 4.7), 18 in two products (Table 4.8), and four in a single product (Table 4.9). Seven had either no reaction or only resulted in CN dissociating from pyrrole (Table 4.10). There were fewer parameters varied in these simulations than there were in the pyridine ones; only k_2 , t_2 , and temperature were varied, while the other parameters were held constant, as shown in Table 4.2. Similar trends appeared here as were noted above. The higher the k_2 value, the more fragmentation was seen. The simulations that

Table 4.3: Parameters of P1 trajectories that fragmented into 3 or more components.

config	T (K)	r_1 (Å)	r_2 (Å)	k_1 ($\frac{\text{kcal}}{\text{molÅ}^2}$)	k_2 ($\frac{\text{kcal}}{\text{molÅ}^2}$)	t_1 (0.5 fs)	t_2 (0.5 fs)	Products
0	1500	12.0	3.0	1.0	0.6	2000	1000	HNC + HCCCN + CCH + 2 H
0	1500	12.0	3.0	1.0	0.75	2000	200	CCCCH + HCN + HNC + 2 H
0	1500	12.0	3.0	1.0	0.75	2000	500	HCCHCN + CN + CCH + H
0	2000	12.0	3.0	1.0	0.75	2000	200	HCCHNC + HCN + CCH + H
0	2000	12.0	3.0	1.0	0.75	2000	500	H ₂ CNC + CCH + HCN + H
1	1500	12.0	3.0	1.0	0.6	2000	500	HCCH + 2 CH + HCN + CN
1	1500	12.0	3.0	1.0	0.75	1500	200	C ₃ N + HCCH + HCN + 2 H
1	1500	12.0	3.0	1.0	0.75	1500	500	C ₃ N + H ₂ CCH ₂ + HCN
1	1500	12.0	3.0	1.0	0.75	2000	200	2 HCCH + CH + CN + N
1	1500	12.0	3.0	1.0	0.75	2000	500	2 HCCH + HCN + CN
1	2000	12.0	3.0	1.0	0.75	2000	500	HCN + HCCN + C ₂ + 3 H
1	2500	12.0	3.0	1.0	0.5	2000	500	CN + HCN + c-C ₃ H ₂ CH ₂
1	2500	12.0	3.0	1.0	0.5	2000	500	HCCCN + HCCH + HNC + H
2	1500	12.0	3.0	1.0	0.6	2000	1000	CNCHCH + HCCH + HCN
2	1500	12.0	3.0	1.0	0.75	2000	200	CN + HCN + 2 HCCH
2	1500	12.0	3.0	1.0	0.75	2000	200	HCCH + CCH + HCN + HCN
2	1500	12.0	3.0	1.0	0.75	2000	500	2 HCN + HC ₄ H ₂
2	1500	12.0	3.0	1.0	0.75	2000	500	CN + HCN + 2 HCCH
2	2000	12.0	3.0	1.0	0.75	2000	200	HCCN + HCCH + CH + CN
2	2000	12.0	3.0	1.0	0.75	2000	500	HCCN + CCH + CH + CN + 2 H
2	2500	10.0	3.0	1.0	0.5	2000	500	HC(CH)CCH + HNC + HCN
2	2500	12.0	3.0	1.0	0.5	2000	500	HCCHCN + HCCCN + 2 H
2	2500	12.0	3.0	1.0	0.6	2000	500	HCN + CNCHCHCHC + H
3	1500	10.0	3.0	1.0	0.5	2000	500	CNCHCH + HCCH + HCN
3	1500	12.0	3.0	1.0	0.5	2000	1000	HCN + HCCCCHCN + 2 H
3	1500	12.0	3.0	1.0	0.6	2000	1000	HCN + HCCH + HCCNCH
3	1500	12.0	3.0	1.0	0.6	2000	500	HCN + C ₂ + C ₃ N + 2 H
3	1500	12.0	3.0	1.0	0.75	2000	200	HCCCHCHCN + HCN + H
3	2000	12.0	3.0	1.0	0.75	2000	500	HCCH + HCN + CCH + HNC
3	2500	12.0	3.0	1.0	0.6	2000	500	H ₂ CCH + CCNCH + HCN

Table 4.4: Parameters of P1 trajectories that resulted in two products.

config	T (K)	r_1 (Å)	r_2 (Å)	k_1 ($\frac{\text{kcal}}{\text{molÅ}^2}$)	k_2 ($\frac{\text{kcal}}{\text{molÅ}^2}$)	t_1 (0.5 fs)	t_2 (0.5 fs)	Products
0	1500	10.0	3.0	1.0	0.5	2000	500	HCCHCHCHNC + HCN
0	2500	8.0	5.0	1.0	0.5	2000	500	HCN + para-pyridyl
0	2500	8.0	3.0	1.0	0.5	2000	500	HCN + para-pyridyl
0	2500	10.0	5.0	1.0	0.5	2000	500	H + NCCHCHCHCHCN
1	1500	12.0	3.0	1.0	0.5	2000	1000	HNC + HCCCHCHCHN
1	1500	12.0	3.0	1.0	0.6	2000	1000	HCN + CNCHCHCCH ₂
1	2000	12.0	3.0	1.0	0.75	2000	200	H2CCNCHCCH + HCN
1	2500	8.0	3.0	1.0	0.5	2000	500	HCN + meta
1	2500	10.0	3.0	1.0	0.5	2000	500	N ₂ + HCCCHCHCHCH
1	2500	10.0	5.0	1.0	0.5	2000	500	HCCH + HCNCHCHCN
2	1500	10.0	3.0	1.0	0.5	2000	500	HCN + o-pyridyl
2	1500	12.0	3.0	1.0	0.5	2000	1000	HNC + HCCHCHCHCN
2	1500	12.0	3.0	1.0	0.6	2000	500	HCN + HCCCHNCCH ₂
3	1500	12.0	3.0	1.0	0.75	2000	500	HCCCHCHCNH + HCN
3	1500	12.0	3.0	1.0	0.75	2000	200	pyrrolyl + HCCN
3	1500	12.0	3.0	1.0	0.75	2000	500	pyrrolyl + HCCN
3	2000	12.0	3.0	1.0	0.75	2000	200	HCN + HCCHCCHCHN
3	2500	12.0	3.0	1.0	0.5	2000	500	HCNCNCCH + CHCH ₂
3	2500	10.0	3.0	1.0	0.5	2000	500	H + o-cyanopyridine

Table 4.5: Parameters of P1 trajectories that resulted in one product.

config	T (K)	r_1 (Å)	r_2 (Å)	k_1 ($\frac{\text{kcal}}{\text{molÅ}^2}$)	k_2 ($\frac{\text{kcal}}{\text{molÅ}^2}$)	t_1 (0.5 fs)	t_2 (0.5 fs)	Products
0	1500	12.0	3.0	1.0	0.5	2000	1000	CN + c-C3H3CHNH (unimolecular, CN doesn't participate)
0	1500	12.0	3.0	1.0	0.75	1500	200	CN + HCNCHCHCHCH (unimolecular, CN doesn't participate)
0	1500	12.0	3.0	1.0	0.75	1500	500	CN + HCNCHCHCHCH (unimolecular, CN doesn't participate)
1	1500	8.0	5.0	1.0	0.5	2000	500	CN bound to N
1	1500	10.0	3.0	1.0	0.5	2000	500	pyrrolyl-HCCN (HCCN bound to N)
2	1500	8.0	5.0	1.0	0.5	2000	500	CN bound to N
2	1500	8.0	3.0	1.0	0.5	2000	500	CN bound to N
2	1500	10.0	5.0	1.0	0.5	2000	500	CN bound to meta
2	2500	10.0	5.0	1.0	0.5	2000	500	CN bound to meta
3	1500	8.0	3.0	1.0	0.5	2000	500	CN bound to meta, migrates to ortho
3	1500	8.0	5.0	1.0	0.5	2000	500	CN bound to meta
3	1500	10.0	5.0	1.0	0.5	2000	500	CN bound to meta

Table 4.6: Parameters of P1 trajectories where no reactions occurred.

config	T (K)	r_1 (Å)	r_2 (Å)	k_1 ($\frac{\text{kcal}}{\text{molÅ}^2}$)	k_2 ($\frac{\text{kcal}}{\text{molÅ}^2}$)	t_1 (0.5 fs)	t_2 (0.5 fs)
0	1500	8.0	5.0	1.0	0.5	2000	500
0	1500	8.0	3.0	1.0	0.5	2000	500
0	1500	10.0	5.0	1.0	0.5	2000	500
0	1500	12.0	3.0	1.0	0.6	2000	500
0	2500	10.0	3.0	1.0	0.5	2000	500
0	2500	12.0	3.0	1.0	0.5	2000	500
0	2500	12.0	3.0	1.0	0.6	2000	500
1	1500	8.0	3.0	1.0	0.5	2000	500
1	1500	10.0	5.0	1.0	0.5	2000	500
1	2500	8.0	5.0	1.0	0.5	2000	500
2	2500	8.0	5.0	1.0	0.5	2000	500
2	2500	8.0	3.0	1.0	0.5	2000	500
3	2500	8.0	5.0	1.0	0.5	2000	500
3	2500	8.0	3.0	1.0	0.5	2000	500
3	2500	10.0	5.0	1.0	0.5	2000	500

had the highest value of $k_2 = 1.0 \text{ kcal mol}^{-1} \text{ Å}^{-2}$ all resulted in three or more products. The next highest value, $k_2 = 0.75 \text{ kcal mol}^{-1} \text{ Å}^{-2}$, had 66.6% of trajectories result in three or more products, while only 41.6% of trajectories with $k_2 = 0.5 \text{ kcal mol}^{-1} \text{ Å}^{-2}$ lead to three or more products.

In the pyridine simulations, variation in t_2 did not lead to an observable trend in the results. Here, however, the shorter the time, the higher the degree of fragmentation seen. 83.3% of trajectories run with $t_2 = 200$ frames (at 0.5 fs/frame) lead to three or more products, followed by 66.6% of those with 500 frames, and then only 27.7% of those with 1000 frames. Like the pyridine simulations, the lowest degree of fragmentation was seen when the temperature was set to 2500 K; however, that was the mid-range value for these simulations, not the highest as it was for pyridine. Again, more trajectories with other variables held constant are needed for further comparison.

Bimolecular Pathways

The nanoreactor trajectories that resulted in two products are shown in Table 4.8. Descriptions of the mechanisms seen in each trajectory are provided in Table 7.14. Perhaps the two most interesting reactions discovered were $\text{HCCHCN} + \text{H}_2\text{CCNH}$ and $\text{HCCN} + 1\text{-H-azete}$. $\text{HCCHCN} + \text{H}_2\text{CCNH}$ is quite similar to the barrierless pyridine formation pathway that has been studied previously.⁸⁸ Part II is devoted to the search for the MEP of this mechanism. $\text{HCCN} + 1\text{-H-azete}$ follows the same scheme as what was seen in the pyridine forming reaction of $\text{HCCN} + 1\text{-pyrrolyl}$. This suggests a possible broader trend of N-heterocycle

Table 4.7: Parameters of R1 trajectories where 3 or more products were formed.

config	T (K)	r_1 (Å)	r_2 (Å)	k_1 ($\frac{\text{kcal}}{\text{molÅ}^2}$)	k_2 ($\frac{\text{kcal}}{\text{molÅ}^2}$)	t_1 (0.5 fs)	t_2 (0.5 fs)	Products
0	1500	12.0	3.0	1.0	0.75	1500	200	CN + C ₃ H ₂ + CNH ₃
0	1500	12.0	3.0	1.0	0.75	1500	500	CN + CNH + C ₃ H + 3 H
0	1500	12.0	3.0	1.0	1.0	1500	200	NCCN + CH + HCCH + 2 H
0	1500	12.0	3.0	1.0	1.0	1500	500	CH ₂ + 2 CN + CH + 2 H
0	3500	12.0	3.0	1.0	0.5	1500	1000	HCCH + CNCHNCH + H
0	3500	12.0	3.0	1.0	0.5	1500	500	HCN + HCCHCNH + H
1	1500	12.0	3.0	1.0	0.75	1500	200	CNH + HNC ₂ H + CCH + H
1	1500	12.0	3.0	1.0	0.75	1500	500	CCNH + C ₃ NH ₂ + 2 H
1	1500	12.0	3.0	1.0	1.0	1500	200	C ₄ H ₃ N + CN + 2 H
1	1500	12.0	3.0	1.0	1.0	1500	500	CCCCN + HNC + 4 H
1	3500	12.0	3.0	1.0	0.5	1500	1000	NH + HCCH + HCCH + CN
1	3500	12.0	3.0	1.0	0.5	1500	500	HCCCN + HNH + HCCH
2	1500	12.0	3.0	1.0	0.75	1500	200	HCCH + NCCN + CH + 2 H
2	1500	12.0	3.0	1.0	0.75	1500	500	NCCHCCH + CN + 3 H
2	1500	12.0	3.0	1.0	1.0	1500	200	C ₃ H ₂ N ₂ + CCH + 2 H
2	1500	12.0	3.0	1.0	1.0	1500	500	C ₃ HN ₂ + HCCH + 2 H
2	2500	12.0	3.0	1.0	0.5	1500	500	HCCH + HCCH + HNCN
3	1500	12.0	3.0	1.0	0.5	1500	1000	HCN + CNCHCHCH + H
3	1500	12.0	3.0	1.0	1.0	1500	200	H ₂ + CCHN + C ₃ H ₂ N
3	1500	12.0	3.0	1.0	1.0	1500	500	HCCCN + HCN + 3 H
4	1500	12.0	3.0	1.0	0.5	1500	500	CN + HCNHCH + HCCH
4	1500	12.0	3.0	1.0	0.75	1500	200	HCCN + HNCH + HCCH
4	1500	12.0	3.0	1.0	0.75	1500	500	HCCN + HNCH + HCCH
4	1500	12.0	3.0	1.0	1.0	1500	200	HCCN + C ₃ H ₂ N + 2 H
4	1500	12.0	3.0	1.0	1.0	1500	500	HCCCN + HC ₂ NH ₂ + H
4	2500	12.0	3.0	1.0	0.5	1500	1000	HCCH + HNCCHCN + H
4	2500	12.0	3.0	1.0	0.5	1500	500	HCN + c-C ₃ HCHNH + H
4	3500	12.0	3.0	1.0	0.5	1500	500	HC ₃ N + c-C ₂ H ₃ N + H
5	1500	12.0	3.0	1.0	1.0	1500	200	c-C ₃ H + HCNH + HNC + H
5	1500	12.0	3.0	1.0	1.0	1500	500	c-C ₃ H + HCN + HNC + 2 H
5	3500	12.0	3.0	1.0	0.5	1500	500	HCN + HCCCH ₂ CN + H

Table 4.8: Parameters of R1 trajectories where two products were formed.

config	T (K)	r_1 (Å)	r_2 (Å)	k_1 ($\frac{\text{kcal}}{\text{molÅ}^2}$)	k_2 ($\frac{\text{kcal}}{\text{molÅ}^2}$)	t_1 (0.5 fs)	t_2 (0.5 fs)	Products
0	12.0	2500	3.0	1.0	0.5	1500	1000	HCN + HCHCH ₂ CCN
0	12.0	2500	3.0	1.0	0.5	1500	500	HCN + 1-pyrrolyl
0	12.0	1500	3.0	1.0	0.5	1500	1000	HCN + <i>c</i> -CHCHC(CHNH)
0	12.0	1500	3.0	1.0	0.5	1500	500	HCN + CCHNHCHCH
1	12.0	1500	3.0	1.0	0.5	1500	1000	HCCH + NCCHCHNH
2	12.0	1500	3.0	1.0	0.5	1500	1000	HCN + 2-pyrrolyl
3	12.0	1500	3.0	1.0	0.5	1500	500	HCCH + H ₂ CNCHCN
3	12.0	1500	3.0	1.0	0.75	1500	200	HCCHCN + H ₂ CCNH
3	12.0	1500	3.0	1.0	0.75	1500	500	HCCH + NCCHCHNH
3	12.0	2500	3.0	1.0	0.5	1500	1000	H + 3-cyanopyrrole
3	12.0	3500	3.0	1.0	0.5	1500	1000	H + <i>c</i> -CHC(H)(HCNC)C(CN)
4	12.0	3500	3.0	1.0	0.5	1500	1000	H + 2-cyanopyrrole
5	12.0	1500	3.0	1.0	0.5	1500	500	HCCN + 1-hydroazete
5	12.0	1500	3.0	1.0	0.75	1500	200	HNC + C ₄ H ₄ N
5	12.0	1500	3.0	1.0	0.75	1500	500	2-pyrrolyl + HNC
5	12.0	2500	3.0	1.0	0.5	1500	1000	HCN + 1-pyrrolyl
5	12.0	2500	3.0	1.0	0.5	1500	500	HCN + 1-pyrrolyl
5	12.0	3500	3.0	1.0	0.5	1500	1000	HCN + 1-pyrrolyl

Table 4.9: Parameters of R1 trajectories where one product was formed.

config	T (K)	r_1 (Å)	r_2 (Å)	k_1 ($\frac{\text{kcal}}{\text{molÅ}^2}$)	k_2 ($\frac{\text{kcal}}{\text{molÅ}^2}$)	t_1 (0.5 fs)	t_2 (0.5 fs)	Products
3	12.0	2500	3.0	1.0	0.5	1500	500	NCCHCHCHCHNH
3	12.0	3500	3.0	1.0	0.5	1500	500	<i>c</i> -NHCNHCHCHCHC
4	12.0	1500	3.0	1.0	0.5	1500	1000	CCHCH ₂ NHCHCN
5	12.0	1500	3.0	1.0	0.5	1500	1000	HCCHCH(CN)CHNH

Table 4.10: Parameters of R1 trajectories where either no reaction occurred or the only event was CN dissociation from pyrrole.

config	T (K)	r_1 (Å)	r_2 (Å)	k_1 ($\frac{\text{kcal}}{\text{molÅ}^2}$)	k_2 ($\frac{\text{kcal}}{\text{molÅ}^2}$)	t_1 (0.5 fs)	t_2 (0.5 fs)
1	12.0	1500	3.0	1.0	0.5	1500	500
2	12.0	2500	3.0	1.0	0.5	1500	1000
1	12.0	2500	3.0	1.0	0.5	1500	1000
1	12.0	2500	3.0	1.0	0.5	1500	500
2	12.0	1500	3.0	1.0	0.5	1500	500
2	12.0	3500	3.0	1.0	0.5	1500	1000
2	12.0	3500	3.0	1.0	0.5	1500	500

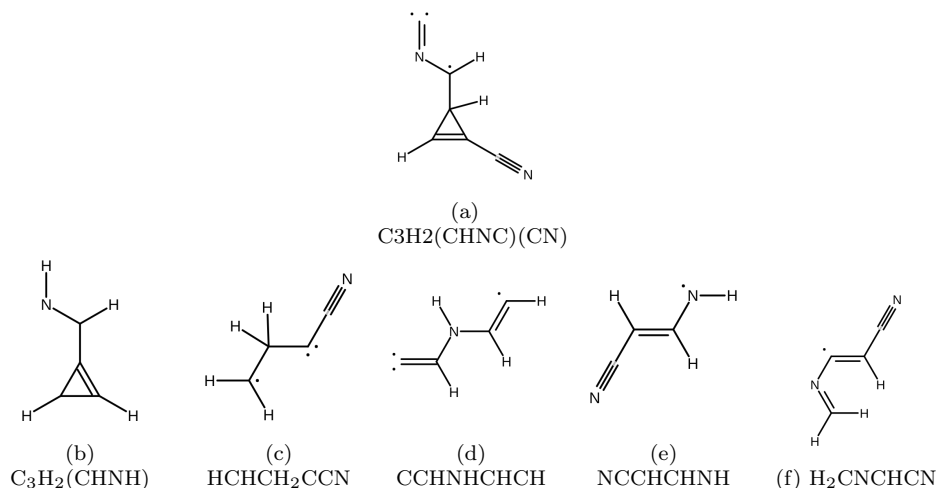


Figure 4.3: Structures of pyrrole precursors discussed in the text.

formation from smaller rings and is discussed in Part III.

Two trajectories produced functionalized cyclopropene, $\text{H} + \text{c-CHCH}(\text{HCNC})\text{C}(\text{CN})$ and $\text{HCN} + \text{c-CHCHC}(\text{CHNH})$. The latter is very similar to (cyanomethylene)cyclopropane, recently characterized by rotational spectroscopy and an excellent candidate for astronomical searches due to recent detections of other cyano-substituted species.²⁵⁰ C_3H_2 has been identified in the ISM²⁵¹ and more recently in Titan's atmosphere.¹⁴¹ Therefore, these reactions and others that start with 3-membered rings and lead to larger N-heterocycles are promising candidates for future studies. Additionally, joint cross molecular beam experiments and electronic structure calculations have shown the formation of C_5H_6 isomers that contain a cyclopropene group from the barrierless reaction of methyldiyne (CH) and 1,2-butadiene ($\text{CH}_3\text{CHCCH}_2$).²⁵² This suggests that a similar formation mechanism to N-containing cyclopropene species might also be barrierless.

The remaining reactions are $\text{HCN} + \text{HCHCHCHCN}$, $\text{HCN} + \text{CCHNHCHCH}$, $\text{HCCH} + \text{NCCHCHNH}$ (seen twice), and $\text{HCCH} + \text{H}_2\text{CNCHCN}$. As discussed above, these N-containing chains are very similar to known astrophysical species. Additionally, six pathways resulted in HCN/HNC and pyrrolyl; four in 1-pyrrolyl and two in 2-pyrrolyl. Two pathways resulted in H and either 2- or 3-cyanopyrrole. Future work should include refinement of these reactions, as well as HCCH with other $\text{C}_3\text{H}_3\text{N}_2$ isomers and HCN with other $\text{C}_4\text{H}_4\text{N}$ isomers.

4.4 Conclusion

These results demonstrate the usefulness of the *ab initio* nanoreactor for the discovery of formation mechanisms of a specific product, and have revealed multiple novel pathways to pyridine and pyrrole formation. Three of the pathways identified have been further studied and are discussed in the following chapters, but there remains a wealth of future directions to explore.

In total, 249 simulations with pyridine and 156 simulations with pyrrole were performed and analyzed. The optimal simulations for the discovery of bimolecular pathways start with only one N-heterocycle and one radical byproduct (in this case, CN) in a sphere of helium atoms. Searching for pathways in this reverse manner requires that a ring breakage occur, but fragmentation into three or more components is avoided. The results suggest that this is best achieved by tuning the parameters that most directly effect the velocity of the sphere contents as it moves into the center, notably r_1 and k_2 .

Of 19 pyridine and 18 pyrrole simulations that resulted in two products, a large number result in N-containing chains that are very similar to species that have been detected the ISM. Most of these chains are radicals and react with either HCN or HCCH to form their respective N-heterocycle. Further in-depth studies of all potential pathways that include an open-shell chain and either HCN or HCCH are necessary in order to determine the potential contribution these pathways might have to N-heterocycle formation in both the ISM and other low-temperature environments, like the atmosphere of Titan. These pathways, however, could have easily been intuited without employing this kind of simulation.

The true usefulness of this method is in the identification of less intuitive N-heterocycle precursors (or, in at least the case of the N_2 forming pyridine trajectory, destruction products). Both sets of simulations revealed acyclic precursors besides HCN and HCCH; $HCNCNCCH + CHCH_2$ for pyridine and $HCCHCN + H_2CCNH$ for pyrrole. The latter is a particularly intriguing reaction due to both the likely presence of the precursors in the ISM and the similarity of this reaction to a pyridine formation pathway previously identified,⁸⁸ and is the focus of Part II.

The insertion reactions discovered in both the pyrrole and pyridine simulations are additional excellent example of non-intuitive pathways. Such reactions are particularly relevant to the atmosphere of Titan, where there have already been tentative detections of N-heterocycles, although it is unclear if such pathways could be operative in the ISM because they rely on the existence of smaller N-heterocycles. These reactions are the focus of Part III.

Besides refinement of the pathways identified here, there is a large parameter space still to be explored with the goal of seeking new N-heterocycle formation pathways. Precursors to pyrimidine and purine would

be particularly interesting from an origin of life perspective, as would formation of imidazole, indole, and pyrrolidine, residues of histidine, tryptophan, and proline, respectively. Functionalized N-heterocycles and larger PANHs should also be explored. Other radical byproducts that are known to be common in the ISM, such as OH and H, should also be used in place of CN.

Chapter 5

Reaction Discovery Part II:

Gas-Phase N-heterocycle Formation

Pathways From Acyclic Precursors

The incorporation of nitrogen atoms into cyclic carbon rings is a prerequisite for terrestrial life; nitrogen-containing heterocycles make up DNA and RNA nucleobases, several amino acids, B vitamins, and the tetrapyrrole moiety essential to a variety of biological processes. The discovery of these and other biologically relevant molecules on meteorites with non-terrestrial isotopic abundances has given credence to the hypothesis of exogenous delivery of prebiotic material to early Earth. However, it is currently not understood where the N-heterocycles identified on meteorites are formed because there has been no detection of these species in interstellar environments. Furthermore, while it seems likely that these species play a role in the chemistry of Titan's atmosphere, a definitive identification has still not been made. The inclusion of many N-heterocycle formation pathways within the relevant predictive chemical kinetics models is needed to solve this puzzle. This work discusses a gas-phase pyrrole formation mechanism from two astrophysically relevant allylic precursors, discovered in simulations with an *ab initio* nanoreactor. This pathway begins with β -cyanovinyl radical and ketenimine and leads to pyrrole and a cyano radical, representing a promising avenue for continued investigations into low temperature N-heterocycle formation.

5.1 Introduction

A fundamental question in astrobiology is at what point in the processing of presolar material are nitrogen atoms incorporated into cyclic molecules. Such nitrogen-containing heterocycles are critical in biology, so understanding their formation has been linked to questions pertaining to the origin of life on earth, and the search for extraterrestrial life. Since the N-heterocyclic moiety has been detected on meteorites,^{6,7,115} but not elsewhere in space, it is clear that this chemistry does happen, but specific formation mechanisms are still uncertain. In order for molecules to be incorporated in meteorite parent bodies, they must be present in either the outer envelopes of protoplanetary disks or the parent cold molecular cloud. Conditions in these regions are extremely cold with very low densities; temperatures are as low as 10 K, and number densities are roughly 10^3 cm^{-3} for molecular clouds and 10^5 cm^{-3} for protoplanetary disks.^{13,15}

In order to improve our understanding of the chemistry that can lead to meteoritic N-heterocycle formation, it is necessary that chemical models incorporate reactions that can both form and destroy these species. Much of the existing work on N-heterocycle formation involves both experiment and theory of photochemistry occurring on icy grains (see Refs 111,115,116,230,232 for examples) while comparatively little considers the potential contribution of gas-phase reactions to meteoritic N-heterocycle abundance, although low-temperature gas-phase reactions have been shown experimentally to proceed efficiently, even between neutral species.^{177,253,254} Of the roughly 250 molecules that have been identified in the gas-phase in space, the vast majority are acyclic, so the inclusion of reactions that link N-heterocycles to acyclic molecules is important for the accuracy and completion of chemical models.

Furthermore, nitrogen-containing species are known to play a significant role in the atmospheric chemistry of Titan,¹²⁷ and have been identified through both radio astronomy^{128,129} and Cassini's Ion Neutral Mass Spectrometer (INMS).^{130,131} Such species are able to form after chemically available nitrogen, produced in the photodissociation or ionization of N_2 in the upper atmosphere, reacts with methane (CH_4) and other organic hydrocarbons. Cyclization is likely an important molecular weight growth process in the formation of Titan's distinctive orange haze,^{127,255–257} as well as a potential proxy for how prebiotic species could have formed on early Earth.^{133,136} N-containing aromatics have been detected on haze particle analogs (generally referred to as tholins) in numerous laboratory investigations,^{136–140} and the INMS detected species with mass to charge ratios that match those of N-heterocycles and N-heterocycle radicals.¹³⁰

There have been several previous studies that have proposed low temperature gas-phase chemical pathways that form or grow N-heterocycles from acyclic precursors. Pyridine formation has been calculated to occur barrierlessly through the radical-neutral reactions of vinyl cyanide and β -cyanovinyl⁸⁵ (Figure 1.3b)

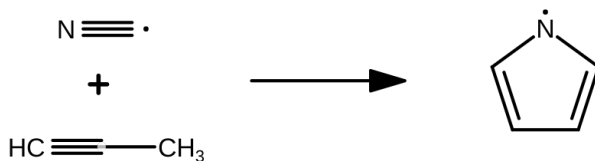


Figure 5.1: $\text{CH}_3\text{CCH} + \text{CN}$ barrierlessly forms 1-pyrrolyl¹⁷⁹

as well as through 1,3-butadiene and the cyano radical (Figure 1.3d).^{87,258} In the latter reaction, however, the pyridine branching fraction was relatively small, only 3-6%, with 1-cyano-1,3-butadiene being the dominant product. A suggested pathway to the formation of 1-pyrrolyl radical has been proposed to operate via $\text{CH}_3\text{CCH} + \text{CN}$ (Figure 5.1).¹⁷⁹ The CN bonds to the acetylene CH, making a new C – C bond, followed by a hydrogen migration and ring closure. This is a radiative association pathway, and is unlikely to contribute significantly to chemistry in the interstellar medium because the rate of dissociation will likely out-compete rate of radiative relaxation,⁸¹ but it could occur in Titan’s atmosphere where densities are higher and collisional relaxation is possible. Further low-temperature molecular weight growth pathways have been shown to occur between the pyridyl radical and both 1,3-butadiene⁹⁴ (Figure 1.3e) and vinylacetylene (Figure 1.3f).^{89,88}

Detailed gas-phase mechanisms to form pyrrole from acyclic precursors at low temperatures are, to the best of my knowledge, not currently available in the literature. Perhaps the most promising work has been the identification of pyrrole as a product of a high voltage electrical discharge of butadiene and ammonia, although a potential energy surface describing this reaction has not been published (Figure 1.3a).^{62,84} A theoretical gas-phase pathway forms pyrrole via the cycloaddition of H_2CCNH and HCCH ,²⁵⁹ but barriers of over 100 kJ/mol make this reaction highly unfavorable at conditions of cold molecular clouds. The other suggested pyrrole formation pathways have cyclic precursors. Gas-phase pyrrole formation has been suggested to occur through the reaction of $\text{N}(^2\text{D}) + \text{pyridine}$, (Figure 1.3g) leading to pyrrole and CN, although pyrrolyl + HCN and pyrrole-2-carbonitrile + H are expected to be the more dominant product channels.⁹⁰

One of the primary goals of the nanoreactor simulations described in the previous chapter was to find new mechanisms for gas-phase pyrrole formation that are feasible in the conditions of the ISM and Titan’s atmosphere. The rest of this chapter details a novel pathway beginning with acyclic precursors β -cyanovinyl

(HCCHCN) and ketenimine (H_2CCNH) that is potentially feasible in star-forming regions, specifically around hot cores, and in Titan’s atmosphere. Of the gas-phase pyrrole formation pathways with acyclic precursors described in the literature, this one is the most relevant to the chemistry in these environments.

5.2 Methods

The nanoreactor simulations¹²⁵ were described in Chapter 4. The trajectories containing interesting reaction events are subjected to a computational procedure called energy refinement, in which the reactive molecular dynamics trajectories are converted into minimum energy paths on the potential energy surface, facilitating comparison with experiment.¹⁰⁵ All of the refinement processes described below were performed with open source python scripts available on the nanoreactor GitHub repository^a unless otherwise specified.

Of the trajectories that started with pyrrole and CN, the trajectory that resulted in $\text{HCCHCN} + \text{H}_2\text{CCNH}$ had an equilibrium temperature of 1500 K, r_1 and r_2 values of 12.0 and 3.0 Å, k_1 and k_2 values of 1.0 and 0.75 kcal mol⁻¹ Å⁻², and t_1 and t_2 values of 750 and 100 fs and was calculated at the uB3LYP/6-31G*^{260–262} level of theory. The reactants were initially identified by visual inspection, followed by an extraction of individual reaction events from the nanoreactor trajectories using the LearnReactions code.

In order to find the minimum energy path (MEP) of this reaction coordinate, the first step after extraction is to optimize the structures found in individual frames of the simulation. Every tenth frame of the extracted trajectory is optimized, also at the uB3LYP/6-31G* level of theory. This provides estimates of the structures of the end points and intermediates. Nearly identical unoptimized nanoreactor geometries of sequential frames that minimized to two different structures are identified and used as an initial guess of the transition state structure. These minimizations, which include all steps from the original nanoreactor structures to the optimized ones, are then concatenated together to produce an initial series of coordinates describing the barrier between one minimum energy structure and the next.

This initial pathway guess is not yet sufficient for higher level transition state optimization methods due to kinks and high-frequency motions left over from the nanoreactor simulation, so a smoothing process is performed with the Nebterpolator program. A nudged elastic band (NEB) calculation is done on this smoothed pathway using a development version of the program TeraChem²³⁴ to find a discretized and energy minimized path where the highest energy structure is a transition state (TS) estimate. This is followed by a TS geometry optimization, where the TS structure is identified and verified to have one

^a<https://github.com/leeping/nanoreactor>

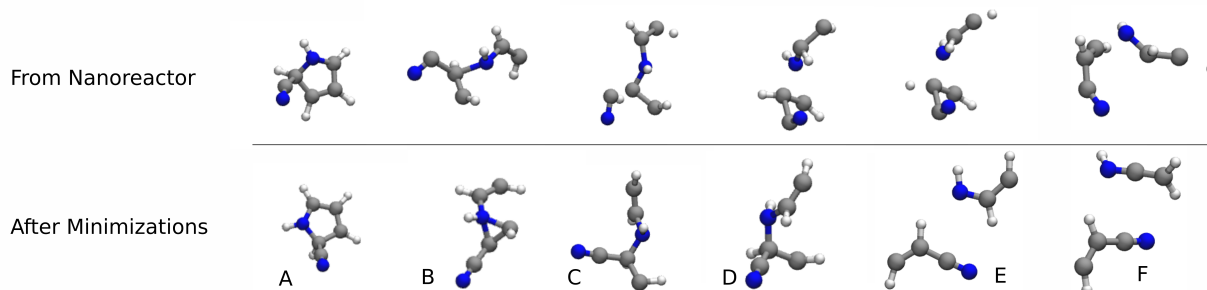


Figure 5.2: The five minimum energy structures that result from the nanoreactor trajectories, as they appear after each step of the refinement process, as noted on the left. All structures here were calculated at the uB3LYP/6-31G* level of theory.

imaginary frequency mode in the direction of the reaction coordinate using version 4.4 of the program Q-Chem.²⁶³ Intrinsic reaction coordinate (IRC) calculations are then performed to determine the full MEP. This specific nanoreactor simulation had multiple minimum energy structures along the path from pyrrole + CN to HCCHCN + H₂CCNH, so this process was repeated for each step.

In order to expand the potential energy surface beyond this single pathway with the goal of determining whether this reaction can proceed barrierlessly at low temperatures, first the intermediates in the nanoreactor pathway that were lower in energy than the reactants were identified. Starting with these structures, bonds were changed iteratively in order to connect the reactants and products. New structures were made using Avogadro.^{264b} These new intermediates were minimized at uB3LYP/6-31G*, and a Cartesian interpolation of the coordinates was used to generate initial path estimates. These paths were then refined with NEB and TS optimizations as discussed above using both uB3LYP/cc-pVTZ²⁰⁰ and u ω B97X-D3²⁶⁵/cc-pVTZ.

Finally, the potential energy curve of the collision and initial bond formation between HCCHCN and H₂CCNH was calculated using the constraint scan option in TeraChem at the u ω B97X-D3/aug-cc-pVTZ(-f)³⁵ level of theory, as the TS optimization program failed to find an appropriate transition state structure between the pre-reaction complex and the first intermediate. The distance between the bonding atoms was scanned from 15 Å apart to the appropriate equilibrium bond distance in 0.2 Å steps, with all other coordinates optimized. The same process was repeated for the exit channel to produce pyrrole + CN.

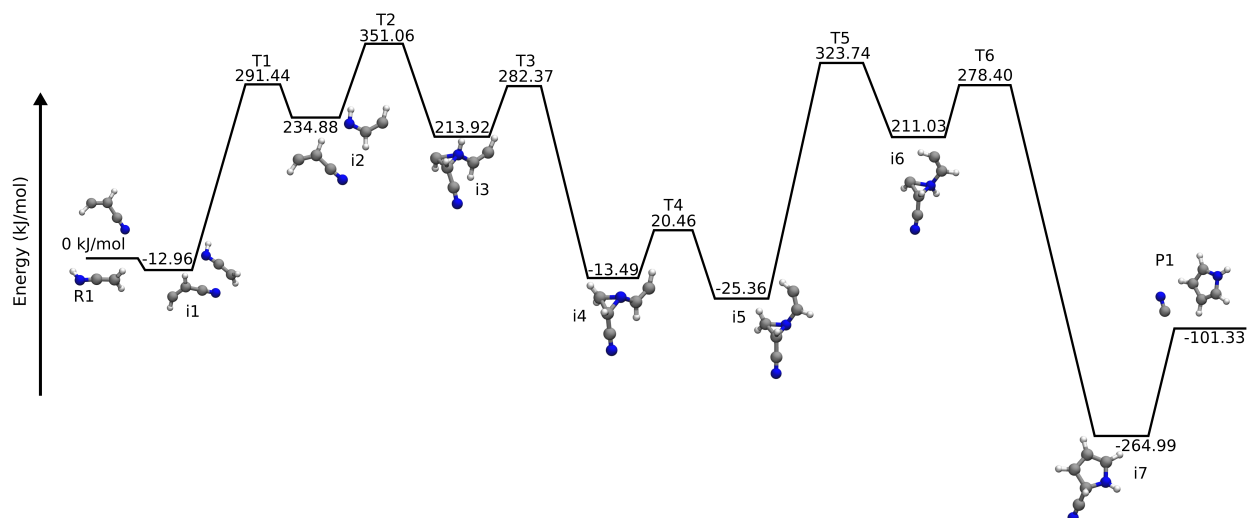


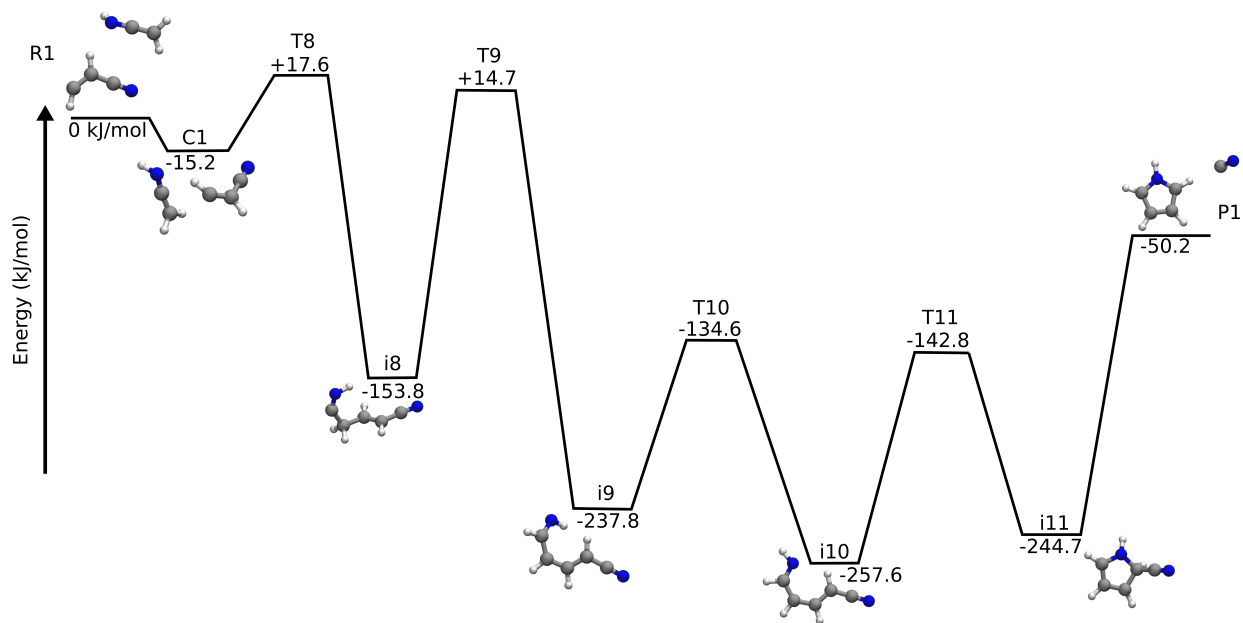
Figure 5.3: The uB3LYP/6-31G* reaction pathway found after refinement of the nanoreactor trajectory, augmented by the path from **i3** – **i6** that was calculated separately.

5.3 Results and Discussion

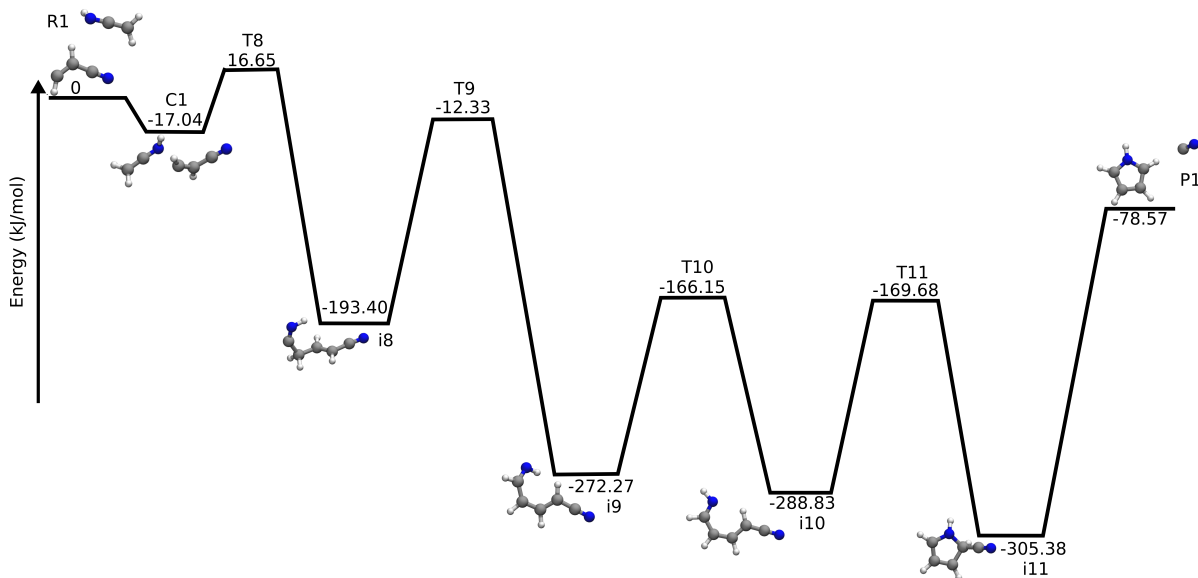
The nanoreactor trajectory that resulted in $\text{HCCHCN} + \text{H}_2\text{CCNH}$ minimized to 5 distinct intermediates and the reactants. Figure 5.2 shows these structures compared to their corresponding nanoreactor frames. (They are shown in the order they were produced in the nanoreactor; the astrophysical pathway of interest begins at structure **F** and proceeds backward to **A**.) After NEB, TS optimization, and IRC calculations were performed, minimized structures **C** and **D** were rendered redundant, as **C** barrierlessly fragmented to **E**. However, the IRC calculations on pathways from **A** to **B** and **B** to **E** resulted in two different conformers of **B**, shown in Figure 5.3 as **i3** and **i6**. In order to connect these intermediates, Cartesian interpolation of the **i3** and **i6** coordinates resulted in an initial pathway guess, followed by NEB calculations which found two distinct minima along this path (**i4** and **i5**). Additionally, the IRC calculation of the **E** to **F** step did not actually produce **F**, the H_2CCNH reactants, but rather just slightly shifted the geometry of **E**. For this reason, the **i1** to **i2** step in Figure 5.3 reflects the results of the NEB calculations only.

The full pathway shown in Figure 5.3 begins with the reactants first coming together to form a pre-reaction complex **i1** that is slightly lower in energy than the separated reactants. From this structure, H_2CCNH undergoes a hydrogen migration in order to form HCCHNH (**i2**), before the nitrogen bonds to both carbons in the vinyl group of HCCHCN (**i3**). In order to get all the carbon atoms close enough for the final pyrrole ring to form, the nitrogen-bound HCCH has to switch places with the nitrogen-bound hydrogen.

^bAvogadro: an open-source molecular builder and visualization tool. Version 1.93.0. <http://avogadro.cc/>



(a) The uB3LYP/cc-pVTZ reaction pathway found as part of the search for low energy pathways to pyrrole from HCCHCN + H₂CCNH.



(b) The ωB97X-D3/cc-pVTZ reaction pathway found as part of the search for low energy pathways to pyrrole from HCCHCN + H₂CCNH.

Figure 5.4: A comparison of the same pyrrole formation pathway calculated with uB3LYP/cc-pVTZ (a) and ωB97X-D3/cc-pVTZ (b).

Free rotation is prevented by the 3-membered ring, so this is accomplished by a hydrogen migration between **i3** and **i4**, followed by inversion of the nitrogen-bound HCCH between **i4** and **i5**. The hydrogen migration is reversed between **i5** and **i6**, before the final concerted unimolecular step where one C – N bond breaks and another forms. This transforms the 3-membered ring into a 5-membered pyrrole moiety. In the final step, CN dissociates from the ring.

This pathway represents only one of many possible routes to pyrrole formation along this potential energy surface. With the objective of discovering pathways that have only submerged barriers (i.e. having lower energy than the reactants), first all the intermediates that were formed as part of the initial TS optimizations were examined (including those that were part of redundant steps and not shown in Figure 5.3) in order to identify all the structures lower in energy than the reactants. There were three such intermediates found, the lowest energy of which was acyclic without branching (similar to **i8** in Figure 5.4), while the other two were **i4** and **i5** in Figure 5.3, both of which contain a three-membered ring. Further exploration into the cyclic intermediates showed that only when the nitrogen included in the ring does not have a H bound to it is the total electronic energy below that of the reactants. This limitation does not make intermediates with this structural moiety useful along the path to pyrrole formation, since that nitrogen begins bound to a hydrogen and must end bound to a hydrogen; this is why two hydrogen migrations occur between **i3** and **i6**. This moiety could be an intermediate in the path to 2-H pyrrole, though, and therefore represents a potentially promising route for future exploration.

The acyclic intermediate identified in one of the redundant nanoreactor steps, $\text{HC}_2\text{HNNHCHCHCN}$, is the result of a bond forming between the β carbon in HCCHCN and the nitrogen in HCCHNH , the triplet ketenimine isomer. Starting from this low-energy structure and the analogous one formed between HCCHCN and H_2CCNH , the singlet isomer, bond angles and hydrogen positions were changed iteratively using Avogadro in order to make the final intermediate, the doublet cyano-pyrrole species. A similar process was followed starting from $\text{HNC}_2\text{H}_2\text{CHCHCN}$, the result of a bond forming between terminal carbon atoms in both reactants. NEB and TS optimization calculations were then performed between sequential intermediates. 21 unique intermediates were identified, and 13 transition states were calculated at the uB3LYP/6-31G* level of theory. Energies, structures, and Cartesian coordinates for these intermediates and transition states are provided in Appendix E.

The steps for the C – C bond formation pathway, shown in Figure 5.4, were also calculated at uB3LYP/cc-pVTZ and ω B97X-D3/cc-pVTZ. The uB3LYP/cc-pVTZ combination was used so that a more direct comparison to the pyridine formation pathway in Parker et al.⁸⁵ could be made, while ω B97X-D3/cc-pVTZ

(with aug-cc-pVTZ-f used for the prereaction complex and following barrier) was selected for its reported accuracy at calculating reaction barriers and non-covalent interactions.²⁶⁵ This pathway had the fewest steps from start to finish and was the most promising low-temperature pathway identified due to the low barriers; the only barrier that is not submerged when calculated at ω B97X-D3/cc-pVTZ is **T8**, the transition state between **C1**, the pre-reaction complex, and **i8**, the first unimolecular intermediate. The relative simplicity of this path compared to ones that begin with C – N bond formation is due in part to the curved nature of **i8**. A hydrogen migration leads to **i9** and forces the structure to become planar and more ring-like. This is followed by a movement of the terminal hydrogen from a trans position with respect to the hydrogen on the adjacent carbon to a cis position in **i10**. The next step is a ring closure (**i11**), followed by the loss of the CN.

B3LYP, commonly used when calculating PESs, results in some notable differences when compared to the ω B97X-D3 path, despite being qualitatively similar. When calculated with uB3LYP/cc-pVTZ, **T9** is not submerged. **C1** and **T8** are similar in value between both reaction diagrams, but the structure of the pre-reaction complexes are different. Additionally, the relative energy ordering of the other intermediates and transition states varies between the two methods. The current literature on DFT strongly suggests that the range-separated hybrids with additional dispersion corrections, and ω B97X-D3 in particular, are significantly more accurate when it comes to calculating a wide range of molecular properties than the B3LYP hybrid functional.^{123,266} Since this pathway is similar to the pyridine formation mechanism in Parker et al.⁸⁵, which was calculated at the uB3LYP/cc-pVTZ//CCSD(T)/cc-pVTZ level of theory, it would be worthwhile to recalculate that pathway at ω B97x-D3/cc-pVTZ, particularly since the first transition state along the barrierless path is only 1 kJ/mol below the energy of the reactants. Like the pathway shown here, the radical precursor is β -cyanovinyl, the reaction is also initiated with the formation of a C – C bond, the intermediates are all acyclic and unbranched until the pyrrole ring forms, and the steps with the highest activation barriers involve a hydrogen migration.

As mentioned earlier, ketenimine has previously been investigated as a potential precursor to pyrrole, albeit not in a low-temperature pathway.²⁵⁹ This same group also investigated ketenimine as a precursor to other 5-membered N-heterocycles, specifically pyrazole, imidazole, and their methylated analogs. The reactions of ketenimine with HCN,²⁶⁷ CH₃CN,²⁶⁸ and H₂CNH²⁶⁹ were explored. Again, the highest barriers (>100 kJ/mol) along these reaction coordinates represent hydrogen transfer steps.

It is important to note, however, that when it comes to the relatively high barriers to hydrogen transfer, it is possible that quantum-mechanical tunneling could be significant, allowing for reactions to still be operative

at low temperatures. Hydrogen transfer has been shown to proceed efficiently at the temperatures of cold molecular clouds,^{75,254} so the existence of a non-submerged barrier at this step may not negate the pathway's astrophysical relevance. Future calculations of the rate constants and branching ratios of the HCCHCN + H₂CCNH reaction will have to correct for tunneling, as described by Shannon et al.²⁵⁴ for the reaction of CH₃OH + OH.

Finally, comparison of the nanoreactor reaction path shown in Figure 5.3 with the lower energy paths in Figure 5.4 illustrates an important principle of working with the *ab initio* nanoreactor in this way. The main purpose of the nanoreactor is to generate new mechanistic hypotheses, but there is no guarantee that the exact pathways found in the nanoreactor are the most plausible ones among all the possibilities. In this study, visual examination and modification of the initial mechanistic ideas from the nanoreactor prove vital in producing an astrochemically plausible mechanism. Time spent refining a complicated nanoreactor pathway could likely be better spent searching for lower energy intermediates and calculating transition states between them, unless the initial minimization steps show that most of the intermediates are lower in energy than the reactants. This strategy will make further investigations of the pathways of interest shown in Part I faster and easier than the study described here.

5.4 Implications for N-heterocycle Formation in the ISM and Planetary Atmospheres

Vinyl cyanide has been detected in multiple environments in the ISM,^{150,151} and as discussed in Chapter 2, the β -cyanovinyl radical is likely also present in these environments. Ketenimine has been detected near hot molecular cores (HMCs) in the giant molecular cloud Sagittarius B2 (Sgr B2), where it is believed to form from the tautomerization of methyl cyanide (CH₃CN) during shocks.¹²⁶ The barrier to tautomerization from ketenimine back to methyl cyanide is calculated by CCSD(T)/aug-cc-pVTZ to be 262 kJ/mol,²⁷⁰ preventing the reverse reaction from occurring spontaneously in the absence of a shock. An additional formation mechanism of ketenimine is H + cyanomethyl radical (CH₂CN), which has been calculated to be barrierless and exothermic.²⁷⁰ CH₂CN has also been detected in Sgr B2, as well as the Taurus Molecular Cloud 1.²⁷¹ The likely presence of both precursors in multiple interstellar environments, therefore, makes this pyrrole forming pathway an important one to include in chemical kinetics models.

When it comes to chemistry in Titan's atmosphere, reaction pathways are not limited exclusively to those with submerged barriers due to the relatively elevated temperature (up to 200 K, see Figure 1 in Ref 132),

although reactions with barriers of more than 1 to 2 kJ/mol rapidly become less favorable. Ketenimine has not been detected directly but seems likely to be present based on crossed molecular beam experiments of $\text{N}(^2\text{D}) + \text{C}_2\text{H}_2$ which saw ketenimine form with a branching ratio between 4 - 5%.²⁷⁰ Neutral vinyl cyanide was detected in 2017,¹²⁸ and the presence of the cyanovinyl radicals is likely because photodissociation processes are rapid in the upper atmosphere. Vuitton et al.¹²⁷ emphasized the need for more Titan-relevant reactions of nitrogen-bearing species, as well as a better understanding of processes leading to macromolecules, for which aromatics are believed to be key precursors. For these reasons, the mechanism described in this chapter is important for inclusion in models of interstellar environments and Titan’s atmosphere.

5.5 Conclusion

The formation of N-heterocycles from acyclic precursors that are known or likely to be present in the ISM and Titan’s atmosphere is an avenue worth pursuing further. The pyrrole forming pathway shown in Figure 5.4b is a promising starting point, and the first gas-phase, radical-neutral pyrrole-forming mechanism with acyclic precursors and potential low temperature feasibility proposed in the literature. Future work on this reaction should first calculate the vibrational zero-point energy for all stationary points and determine basis set superposition error for **C1** and the following transition state **T8**. Once these minor corrections have been made to the previously calculated PESs, pathways to other products should be developed and calculated. This should be followed by calculations of rate constants and branching ratios. The initial entrance channel can be calculated with microcanonical transition state theory,²⁷² and the unimolecular steps following with RRKM theory.²⁷³ Finally, experimental kinetics studies are warranted to determine the actual temperature dependence of this pathway.

Overall, the discovery of this new gas-phase route to pyrrole formation suggests that the nanoreactor can indeed be used to find astrophysically relevant precursors, despite the conditions of the nanoreactor simulations being drastically different than those of interstellar space or even planetary atmospheres. In future nanoreactor investigations, the emphasis should not be placed on refining the entire chemical pathway seen in the nanoreactor, but rather searching for low energy intermediates in the simulations that can serve as a starting point for expanding the potential energy surface to find low temperature pathways.

Chapter 6

Reaction Discovery Part III: Low-Temperature Gas-Phase Ring Insertion Reactions

Gas-phase reactions of nitrogen-containing heterocycles are thought to be important to chemistry of cold molecular clouds, Titan's atmosphere, and terrestrial combustion, however current kinetic models to describe chemistry in these environments contain little, if any, information on reactions that include N-heterocycles. Reactions that either increase or decrease the size of a N-heterocycle via insertion or elimination have been shown to occur experimentally with a variety of different species, but little is known about the potential importance of such reactions in these environments. Here, two novel ring-insertion pathways are discussed that form pyrrole and pyridine, prototypical N-heterocycles. These pathways were calculated at the ω B97X-D3/cc-pVTZ level of theory and are shown to be particularly promising for low-temperature environments.

6.1 Introduction

Nitrogen-containing heterocycles are a crucial molecular component of biological systems, making up DNA and RNA nucleobases as well as certain vitamins and amino acids. The presence of these biological molecules on meteorites has often been held up as evidence for exogenous delivery of prebiotic material to early Earth,^{7,8} leading to numerous studies of their potential formation mechanisms in cold molecular

clouds.^{86,110–112,114–116,230,274–277} In our present-day solar system, Titan is believed to have the most relevant conditions to those of early Earth,^{132,133,136} and the tentative detections of N-heterocyclic species in its atmosphere¹³⁰ have sparked additional interest in these molecules, particularly in their gas phase formation mechanisms.¹⁷⁹ Additionally, because of their presence in biological materials, the oxidation and thermal decomposition pathways of N-heterocycles must be taken into account when considering the combustion of biomass. Multiple investigations into these combustion pathways, particularly those of pyridine and pyrrole, have been performed.^{142–145,180–182,278}

Within all of these chemical environments, potentially important reactions that have often been overlooked are gas-phase insertion/elimination reactions involving N-heterocycles. For astrochemistry, these have generally been dismissed as improbable, likely due to the fact that no N-heterocycle has been detected in space, so the plausibility of one N-heterocycle acting as a precursor for another is highly uncertain. However, the inclusion of reactions with N-heterocycles into predictive chemical kinetics models is the best way we have to understand how and where meteoritic N-heterocycles form, making the study of these reactions at low temperatures still worth pursuing. In Titan’s atmosphere, the majority of the studies of ring growth have pertained to adding new rings, not to changing the size of an individual one. The addition of new rings (mono- to bicyclic species, for example) is believed to contribute to the aerosols, known as tholins, that make up Titan’s distinctive orange haze.^{148,255,257,279} Despite evidence that ring insertion/elimination reactions are feasible with small radicals/ions known to be abundant on Titan (as discussed below),²⁸⁰ current models do not include these types of pathways.^{127,178} In the chemical kinetics models of N-heterocycle combustion, the only such reaction path involves the elimination of CO from pyridine to pyrrolyl during pyridine oxidation.^{142,144,180,182}

Experimental work has provided strong evidence that these types of reactions can occur. Pyridine was observed as the main product of the reaction of CH with pyrrole (C_4H_5N) in a slow-flow reactor coupled with a VUV-photoionization mass spectrometer.⁸⁶ Their proposed ring-expansion mechanism was further confirmed with isotopic substitution. The elimination of CO from the peridoxo (C_5H_4NO) radical was shown to form 1-pyrrolyl, as detected by imaging photoion photoelectron (iPEPICO) spectroscopy. This iPEPICO technique was also used to study decomposition of the picolyl radical ($C_5H_4NCH_2$). Functionalized 5-membered rings pyrrole and cyclopentadiene were detected in this decomposition; accompanying theoretical calculations predicted that the reaction proceeds first by CH_2 insertion to produce a 7-membered ring, followed by isomerization to form a bicyclic 4-membered and 5-membered species, which further isomerizes to the observed products. Most recently, the reaction of pyridine with $N(^2D)$ was investigated with the

crossed molecular beam technique.⁹⁰ Insertion, elimination, and replacement reactions were all shown to occur, as the products included 5-, 6-, and 7-membered rings including pyrrole, imidazole (C₃H₄N₂), and pyrimidine (C₄N₂H₄). This work did not propose mechanisms for these pathways, but a similar theoretical study of benzene and N(²D)⁹¹ proposed a pathway similar to that of picolyl decomposition, whereby first a seven-membered ring is formed, followed by bicyclic 4- and 5-membered fused rings. The range of products studied in this theoretical investigation is similar to what was seen in the pyridine + N(²D) reaction.

Here, two novel ring-expansion mechanisms are described that were identified in *ab initio* nanoreactor simulations, detailed in Chapter 4. In the first, the cyanomethyl radical H₂CCN and the unsaturated 4-membered N-heterocycle, azete (C₃H₃N), react to form pyrrole and the CN radical. To the best of my knowledge, this is the only gas phase pathway proposed in the literature that includes a 4-membered N-heterocycle, and one of a very small number that forms pyrrole.^{62,90,91,259} The second reaction detailed here is that of cyanomethylene (HCCN) and pyrrolyl, which form pyridine and CN. Comparison of these mechanisms to those in the literature is presented, as well as a discussion of the implications for astrochemistry, planetary atmospheres, and combustion chemistry. Ultimately, these pathways further illustrate the promising trend of ring insertion/elimination reactions for gas-phase environments and motivate further exploration for additional N-heterocycle formation pathways.

6.2 Methods

The same methods as were described in the preceding chapter were used to identify the two reactions described here, with two main exceptions. Refinement steps were done solely at the $u\omega B97X-D3^{265}/cc-pVTZ^{200}$ level, and $u\omega B97X-D3/aug-cc-pVTZ-f$ was used to search for pre-reaction complexes and barriers along the entrance channel. Both pathways were derived directly from the nanoreactor trajectory, with redundant steps excluded, so searches for other low energy intermediates were unnecessary.

6.3 Results and Discussion

6.3.1 H₂CCN + Azete

As shown in Figure 6.1, azete and H₂CCN first form a pre-reaction complex (**C1**) that is 22.07 kJ/mol below **R1**. A small barrier of 4 kJ/mol relative to **R1**, must then be overcome as a bond forms between the terminal C of H₂CCN and the α C of azete (**i1**). A H-atom transfer then occurs between the bonded C of

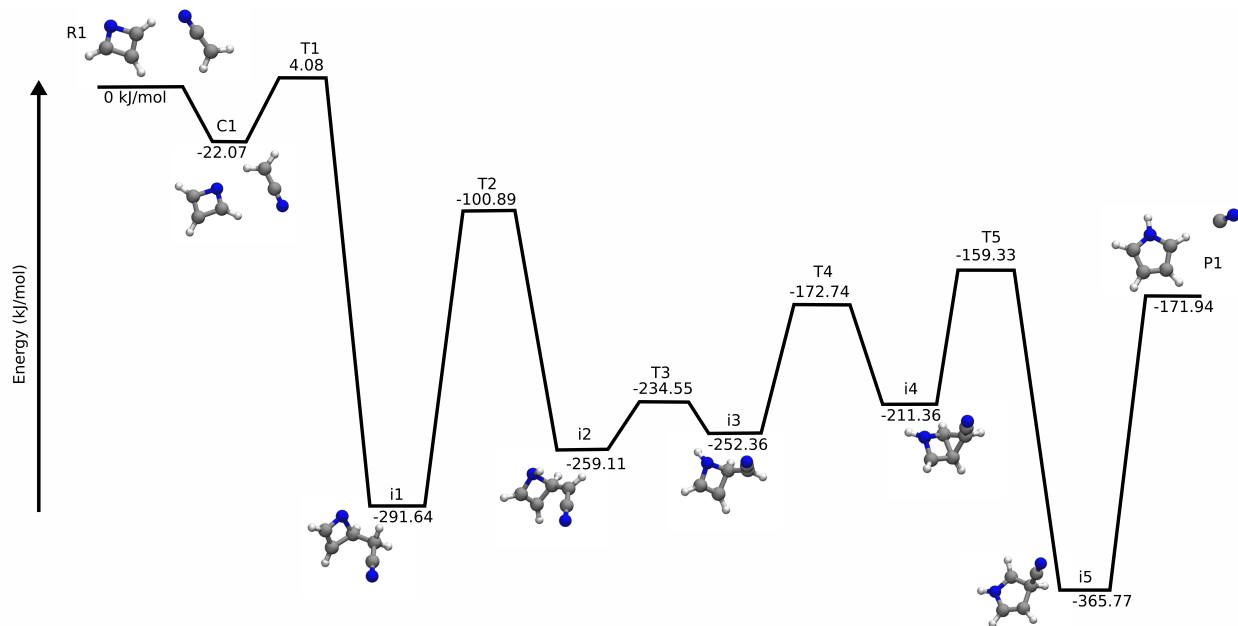


Figure 6.1: The PES detailing the reaction of azete ($c\text{-C}_3\text{H}_3\text{N}$) with the cyanomethyl radical (H_2CCN).

H_2CCN and the azete N to produce **i2**. This submerged barrier is the highest energy transition state after the initial entrance barrier, as was seen in the $\text{HCCHCN} + \text{H}_2\text{CCNH}$ reaction detailed in Chapter 5. In the next step to **i3** the N-H bond flips downward, away from the HCCN, which also rotates closer to the azete N. This is followed by the bonded C in HCCN forming a second bond to the adjacent azete C to make **i4**. Next, the azete bond breaks, and the ring opens and flattens into **i5**, the cyano-pyrrole radical. Lastly, the products are produced in the barrierless dissociation of pyrrole and CN.

This calculation was done on a doublet surface to reflect the spin multiplicity of the products. Azete was optimized as a singlet and cyanomethyl as a doublet. There is a potential discrepancy within the literature about the azete ground state wavefunction. Multireference configuration interaction calculations with a 4-31G basis set suggest that the ground electronic state of azete is well-described by a singlet closed-shell wavefunction with little diradical character.²⁸¹ A more recent theoretical study at the CCSD(T) level of theory with basis sets cc-pVTZ, cc-pVQZ, cc-pwCVTZ, and cc-pwcVQZ describe azete as a diradical, but only provide the equilibrium structure and do not specify if their calculations suggested a singlet or triplet ground state.²⁸² However, the provided azete structure is very similar to the one calculated here at $\omega\text{B97X-D3/cc-pVTZ}$, with bond lengths varying by no more than 0.01 Å. Future exploration of azete reactivity should include verification of the ground electronic state.

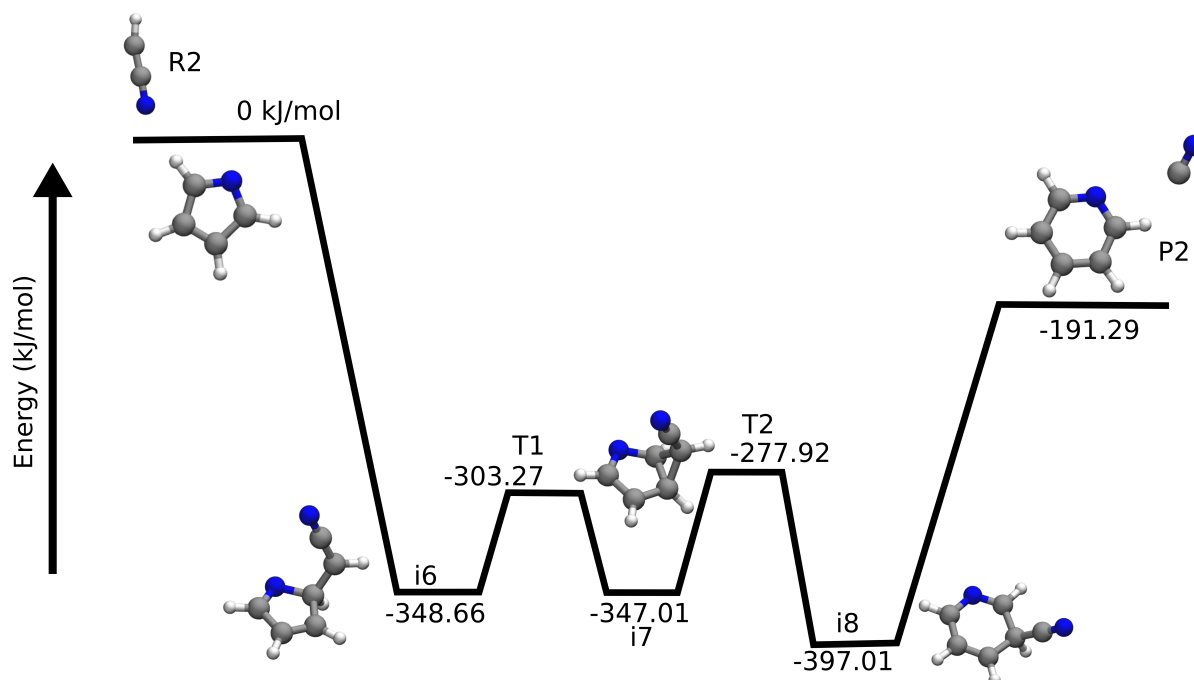


Figure 6.2: The PES detailing the reaction of 1-pyrrolyl ($c\text{-C}_4\text{H}_4\text{N}$) with the cyanomethylene radical (HCCN).

6.3.2 $\text{HCCN} + 1\text{-Pyrrolyl}$

This reaction, unlike the one described above, does not have an actual barrier along the entrance channel, making this reaction effectively barrierless. This path is very similar to the azete insertion from **i3** on. HCCN bonds to the α C in pyrrole via the terminal C. This C atom then forms a second bond to the adjacent pyrrole β C. The pyrrole bond breaks and the ring widens and flattens to produce the 3-cyanopyridine doublet, followed by loss of CN to form pyridine.

This pathway was also calculated on a doublet surface due to the spin multiplicity of the products. However, HCCN is a carbene which has been experimentally determined to have a triplet electronic ground state and quasi-linear structure,^{283,284} where the HCC bond angle is calculated by CCSD(T)/aug-cc-pVQZ to be 145.9° and the barrier to linearity only $0.67 - 0.86$ kcal/mol.²⁸⁵ In the $\omega\text{B97X-D3/cc-pVTZ-f}$ calculations presented here, with either a total spin multiplicity (including HCCN and pyrrolyl) of 4 or of 2, the HCC and CCN bond angles were 164.2° and 177.6° , respectively, at both spin multiplicities. Further investigations of electronic structure as well as contributions from zero point corrections are needed.

Overall, this reaction is very similar to the proposed mechanism of CH insertion into pyrrole.⁸⁶ CH first bonds concertedly to both the α and β C atoms, followed by that pyrrole bond breaking and the loss of the nitrogen-bonded H. This final step is unnecessary when the conversion begins with pyrrolyl. Converting from

a pyridine ring to pyrrolyl was seen in the pyrolysis of 3-methoxypyridine,²⁸⁶ where a CO elimination from the ring occurred after the loss of the methyl radical produced the pyridoxy radical (C₅H₄NO). Calculated activation barriers show that this reaction is not barrierless in either direction, but is driven by the cleavage of the O - CH₃ bond.

6.4 Implications for Astrochemistry, Planetary Science, and Combustion Chemistry

The question of “top-down” versus “bottom-up” chemistry as a means to form aromatic species in the ISM does not have a clear answer. Inclusion of insertion and elimination reactions with N-heterocycles and PANHs within chemical models could provide an avenue for the formation of variously sized heteroaromatics. The exothermic nature of the pyrrole and pyridine formation mechanisms as described here fit well into a “bottom-up” scheme, but the library of known reactions that involve size changes of individual rings is too small to know if this is generally common. Since current chemical models lack reactions that involve N-heterocycles,²⁶ much less that involve insertion or elimination from an N-heterocycle, significant additional work is required to characterize these types of pathways and determine their potential relevance to the ISM.

For Titan’s atmosphere, bottom-up pathways are how tholins form. HCCN has been suggested to be important in this process; chemical models²⁸⁷ predict HCCN to be the third most abundant open-shell species, and molecular dynamics simulations²⁵⁵ include reactions of HCCN with PAHs both in the gas-phase and on tholin surfaces as a means of promoting ring growth. The specific process of ring growth is not specified, however, so it is unclear if what is occurring in the simulations is insertion to increase ring size, polymerization to add additional rings, or a combination thereof. As is the case with interstellar chemistry, more work is needed to understand the role insertion reactions play in these environments.

To this end, future studies should take into account what other acyclic precursors might be more abundant than either HCCN or H₂CCN, for both the ISM and Titan’s atmosphere. CH was the co-reactant in the pyridine formation mechanism described by Soorkia et al.⁸⁶, and is certainly a promising precursor due to its ubiquity and relatively high abundance.²⁸⁸ Longer linear chains like those in the C_nH^{289–293} or HC_nN^{294–297} family, known to be present in dense clouds, could also reasonably react with a cyclic species in this way. To the best of my knowledge such a reaction has not been described in the literature.

The presence of both HCCN and H₂CCN has been confirmed in space.^{271,298} HCCN was detected definitively in IRC+10216, a circumstellar envelope, and tentatively in dense cloud Sgr B2, while H₂CCN has

been detected in dense clouds TMC-1 and Sgr B2. Both species are presumed to be present in Titan’s atmosphere based on data from the Cassini/Huygens INMS and current chemical models.^{127,130,287,299} Azete and pyrrolyl not only lack astronomical detections, but also the relevant laboratory spectroscopy required for their identification in both the ISM and Titan’s atmosphere. The computational work described in Chapter 3 and recently published Ref 300 provides high-level theoretical predictions of the rotational and vibrational spectra of 1-pyrrolyl, as well as the 2- and 3-pyrrolyl isomers. For all of these species, laboratory work in the millimeter-wave frequency range is particularly promising because the collapse of the hyperfine structure leads to significant improvement in intensity over the centimeter-wave region and transitions arising from the isomers are well-spaced and easy to tell apart. For azete, the theoretical structure determination by Csaszar et al.²⁸² provides an excellent starting point for further spectroscopic predictions. Both pyrrolyl and azete are excellent candidates for laboratory spectroscopy using a high-voltage discharge source, as described in Chapter 2. Pyrrolyl has been shown to form efficiently from methoxypyridine under pyrolytic conditions,²⁸⁶ mentioned above, although for both pyrrolyl and azete, the reversed reactions discussed in this chapter could be used as discharge precursors; pyridine and pyrrole, respectively, along with a source to produce CN radicals.

Finally, elimination of CO from oxidized pyridine to form pyrrolyl is thought to be an important pathway in pyridine combustion.^{142,144,180,182} However, this is the only change-of-ring-size reaction within the current kinetic models of N-heterocycle combustion. Many other small acyclic radicals are produced that could also bond to the aromatic ring, potentially leading to an elimination reaction, including CN, which could lead to pyrrolyl or azete formation in the reverse direction. This is particularly worth further investigation under conditions of incomplete combustion, where the amount of fuel exceeds the amount of oxygen available, and non-oxygen bearing radicals could out-compete oxygen for this elimination reaction.

6.5 Conclusion

Two novel gas-phase reactions have been identified in *ab initio* nanoreactor simulations. The first produces pyrrole + CN from the insertion of H₂CCN into the 4-membered N-heterocycle, azete, while the second produces pyridine + CN from the insertion of HCCN into the 1-pyrrolyl radical. As calculated, the azete pathway has a total barrier of 4 kJ/mol along the entrance channel, while the pyrrolyl pathway is effectively barrierless, making the latter pathway particularly promising for low-temperature N-heterocycle formation.

Further work on these specific pathways includes the incorporation of vibrational zero-point energies of

the stationary points, and calculation of the basis set super position error for the pre-reaction complexes. Additionally, there are other analogous reactions between N-heterocycles and small reactive species, such as CH or OH, that could be more relevant to the environments where gas-phase N-heterocycles are thought to be important. Finally, these reactions illustrate a potential trend in ring growth; that if a small N-heterocycle is present, it can be expanded repeatedly to form larger rings. Therefore, insertion into 3-membered rings should also be explored as a potential pathway to form azete.

Chapter 7

Conclusion and Future Work

The work presented in this dissertation is the start of a foundational research program to study astrophysical N-heterocycles. These species have gone undetected in space despite their presence on meteorites and the likely incorporation of nitrogen within instellar polycyclic aromatic hydrocarbons (PAHs). This has left our understanding of their formation highly uncertain, and no N-heterocycle-including pathway exists within the main databases of astrochemical reactions. The main goal of this research is to develop a fundamental knowledge base of for elucidating the role of N-heterocycles in astrophysical environments through spectroscopic characterization of relevant precursors and intermediates, *ab initio* molecular dynamics (AIMD) simulations, experimental determination of rate constants and branching ratios, and astronomical searches. The spectroscopic characterization of the radicals β -cyanovinyl and pyrrolyl were presented in Chapters 2 and 3, while Chapters 4 – 6 detailed the results of the AIMD simulations. Below is an overview of this work and the future directions for this research program.

7.1 Spectroscopic characterization

Chapter 2 details the rotational spectrum of the two β -cyanovinyl radicals between 5 and 75 GHz, as well as the theoretical study of all three cyanovinyl isomers at the CCSD(T) level of theory. This work marks the first experimental detection of cis- and trans- β -cyanovinyl and the first theoretical treatment of these species with coupled cluster methods. The observed spectra were in excellent agreement with the calculations, although the complex hyperfine structure could not be fully assigned without extension of the frequency coverage into the millimeter wave region, where hyperfine structure collapses and spin-rotation splitting increases.

The theoretical treatment of the pyrrolyl radicals is discussed in Chapter 3. The electronic ground state structures and full spectroscopic predictions of both the vibrational and rotational spectra were calculated at the CCSD(T) level for the first time. The anharmonic vibrational spectra included several combination bands with appreciable intensity that make distinguishing between the three isomers possible. The rotational spectra for the three isomers are particularly promising for millimeter wave spectroscopy. Similar to the cyanovinyl radicals, the pure rotational spectra are heavily split by the angular momentum coupling at low N , with the structure collapsing at higher frequency transitions.

Both cyanovinyl and pyrrolyl require further spectroscopic work, particularly in the vibrational regime and at millimeter wavelengths. Recently developed methods like cryogenic slow photoelectron velocity map imaging would be an excellent avenue to pursue for measuring vibrational transitions of both of these species, similar to work done on the pyridyl radicals.³⁰¹ For rotational spectra, long-pass millimeter-wave frequency modulation spectroscopy coupled with fluorine-abstraction to produce the radicals is likely to provide the capability necessary to measure transitions between higher N levels. Measuring rotational spectra in this frequency region is also important for future observations with ALMA, which has coverage currently from 84 GHz and higher.

Ultimately, the goal of this spectroscopic work is to detect these species in astronomical environments. With that in mind, there are other N-containing species of potential astrochemical relevance that do not have known rotational spectra. These include many cyano-functionalized species, similar to benzonitrile and other cyano-PAHs recently detected in TMC-1.⁶² Specifically, cyanoquinoline, cyanopyrimidine, cyanoindole, and cyanopurine. Additionally, no 4-membered N-heterocycle has been characterized spectroscopically. Other future spectroscopic targets should include other N-heterocyclic radicals. Computational and experimental characterization of pyridyl is currently underway in our laboratory. Radical derivatives of the 3-membered N-heterocycles azirine and aziridine and the bicyclic rings indole and quinoline should be characterized as well in order to have a well-developed catalog of prototypical N-heterocyclic radical spectra to be used for kinetics experiments and astronomical searches.

7.2 Reaction path discovery

In Chapter 4, details of the *ab initio* nanoreactor simulations of pyrrole and pyridine with the CN radical were presented with the goal of discovering novel formation pathways. Nineteen pyridine and eighteen pyrrole bimolecular pathways were found that warrant further study. One of the pyrrole formation paths

from two acyclic precursors, β -cyanovinyl and ketenimine, was further expanded upon in order to search for a barrierless formation pathway that differed from the nanoreactor-discovered mechanism. These efforts were covered in Chapter 5. In Chapter 6, two ring-insertion reactions that arose from the nanoreactor are discussed. The first converts azete into pyrrole through a reaction with H_2CCN , the cyanomethyl radical. The second converts pyrrole into pyridine through a reaction with cyanomethylene, HCCN . These reactions were found directly within the nanoreactor simulations; further expansion of their potential energy surfaces was not required. Thus far, only this final pathway with pyrrolyl and HCCN has been calculated to be barrierless, although zero-point vibrational corrections for all stationary points and basis set superposition error for the prereaction complex and following transition state still need to be taken into account.

There is a vast amount of parameter space still to explore with this component of the project. The work thus far demonstrates that a long list of potential astrophysical precursors can be generated with the nanoreactor. Additional refinement to search for barrierless pathways should begin by first searching for low energy intermediates within the nanoreactor simulations, as described in Chapter 5. Nudged elastic band calculations, followed by transition state optimizations, are then performed to connect the intermediates and develop full paths from precursors to the N-heterocycle of interest.

All the simulations thus far have used CN as a co-reactant. This limits the potential precursors to only contain carbon, nitrogen, and hydrogen. Future simulations should use OH instead to investigate the possible role of oxygen-containing species, particularly alcohols, in N-heterocycle formation. Other co-reactants should include H, CH, NH, and NH_2 . It could also be worthwhile to start simulations with N-heterocycle radicals and a neutral, closed-shell co-reactant, such as pyrrolyl and HCN. Future work with the analogous ion-neutral pathways should also be pursued.

An interesting question to explore with the nanoreactor is how N-heterocycle structure effects the types of trajectories. The next targets should perhaps be imidazole and pyrimidine, to explore how adding another nitrogen to the ring effects the reactivity and energetics. Bicyclic structures, as well, such as indole and quinoline, should be included in future work.

7.3 Experimental determination of rate constants and branching ratios

Once a reaction of interest is identified through the nanoreactor simulations, the next step is to determine the rate constants and branching ratios at astrophysically relevant temperatures. Preparation and building

of a laboratory experiment to do exactly this has been ongoing in conjunction with the other work described here. This instrument combines the CRESU molecular beam technique⁷⁷ with a broadband, chirped-pulse FTMW spectrometer and laser-induced fluorescence, similar to experiments described by Cooke and Sims⁷⁴. Reaction kinetics at temperatures down to 10 K can be probed this way.

To begin, kinetics of the reactions that have already been proposed within the literature should be studied. The first ones to study are the ones that form a single ring, such as $\text{NH}_2 + 1,3\text{-butadiene}$ to pyrrole or $\beta\text{-cyanovinyl} + \text{vinyl cyanide}$ to form pyridine. This will allow for the incorporation of these pathways into astrochemical databases. The same process should then be applied to reactions found within the nanoreactor simulations, starting with those detailed in Chapters 5 and 6. This should then be followed by reactions that form additional rings, such as the quinoline formation mechanisms of $\text{pyridyl} + 1,3\text{-butadiene}$ ⁹⁴ and $\text{pyridyl} + \text{vinyl acetylene}$.⁸⁹

7.4 Astronomical searches

Finally, molecules important to N-heterocycle formation must be included in future astronomical searches. Ideally these searches would be conducted with ALMA, where angular resolution is high enough to observe species within hot cores. Astronomical targets should include a variety of sources with a frequency range broad enough to include many species. Besides hot cores, observations should also include dark molecular clouds, protoplanetary disks, as well as circumstellar shells to constrain our understanding of the potential for top-down PANH synthesis. The publicly available data from previous observations with ALMA should be explored first, as actual observing time with ALMA is in high demand.

Particularly promising molecular targets are N-heterocycles with especially strong dipole moments. Cyano-substituted species are ideal for this, particularly cyanopyrrole and cyanopyridine, for which microwave spectra are known.^{63–67} After spectroscopic characterization of additional cyano-substituted species, transitions of these should be searched for as well.

Appendix A: Cyanovinyl

***cis*- β -CV rotational structure** As the *cis*- β -CV lines had a higher signal to noise ratio, we have focused on this species for fitting the hyperfine structure using a standard Watson A-reduced effective Hamiltonian with the coupling terms added. However, the magnitudes of the coupling terms are so similar that small changes in parameter values change the quantum numbers associated with some eigenvectors when performing a projection assignment onto the basis. In several cases, this causes two peaks separated by ~ 100 MHz to trade quantum number assignments. Standard fitting approaches which involve minimizing the squared differences between the calculated and observed frequencies for a particular set of quantum numbers fail when sudden discontinuities like this occur. This is illustrated in Figures 7.1 and 7.2.

We attempted to circumvent this by manually modeling the spectrum, done by individually altering parameters in order to reproduce the experimental data seen in the fundamental *a*-type transition and in a 2D plot of the fundamental *a*-type versus the fundamental *b*-type transitions (Figure 7.3). The latter method in particular revealed useful patterns that helped us develop a qualitative reproduction of the spectrum. Multiple experimental *a*-type transitions (the “probe” lines in the double resonance experiment) were linked to the same sets of *b*-type transitions, which is indicative of a shared ground state between these *a*-type lines. This would not have been determinable without the DR linkages. Figure 7.4 shows our best qualitative fit. Although attempts to manually reproduce the spectrum led to new insights, the 28 term parameter space is simply too large to make a thorough model by this method.

T_1 Diagnostics and MRCI calculations In coupled cluster calculations of open shell molecules, the T_1 diagnostic is used to denote the extent of the multireference character in the electronic wavefunction. The higher the diagnostic, the greater the multireference character. Using the definition of the T_1 diagnostic from¹⁶², the results are shown in Table 7.1 for our CCSD(T)/ANO1 calculations. T_1 should generally be under 0.02, and our values are roughly twice this. To verify that any multireference character in the wave-

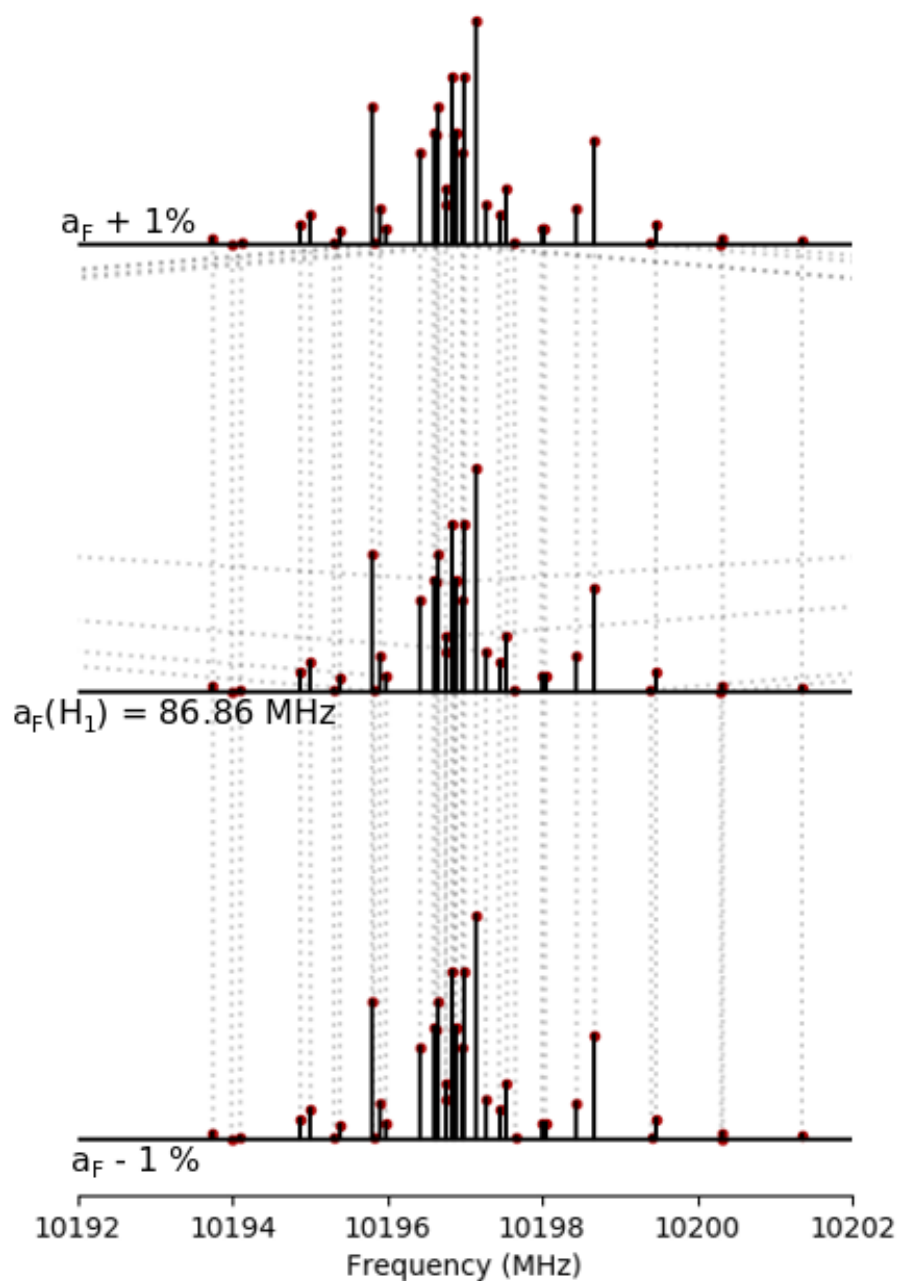


Figure 7.1: An illustration of the change in quantum number assignments with a small change in the value of a hydrogen Fermi contact parameter. The middle stick spectrum shows the most intense simulated lines in the $1_{01} - 0_{00}$ rotational transition of *cis*- β -CV. The top and bottom are the spectra with one of the hydrogen Fermi contact terms increased and decreased by 1%, respectively. Lines with identical quantum numbers are linked by dotted lines. Several lines that shift only slightly in frequency between the middle and top spectra are given different quantum number assignments, indicated by the dotted lines extending out of frame.

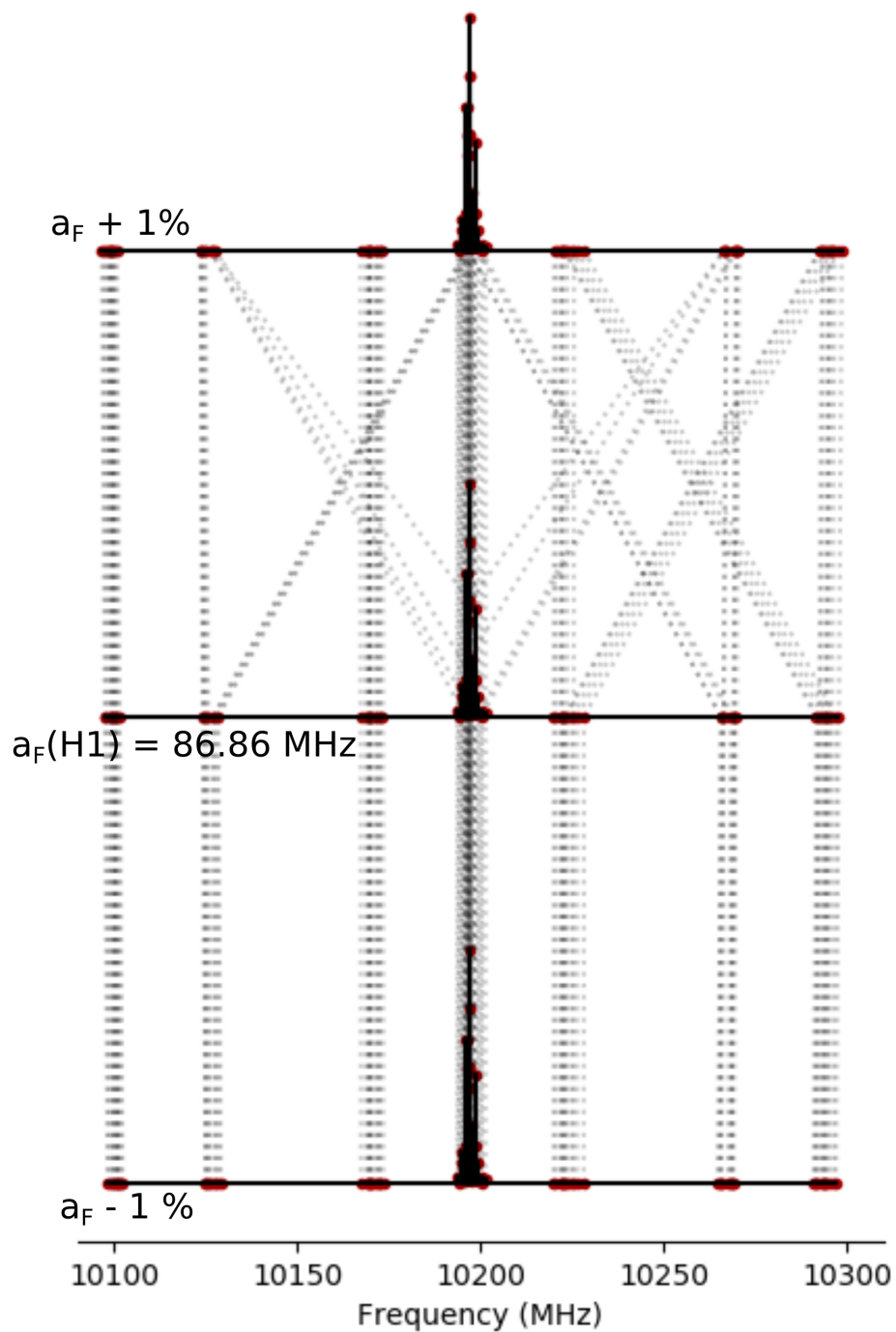


Figure 7.2: A zoomed-out version of Figure 7.1, to include every simulated component of the $1_{01} - 0_{00}$ transition in *cis*- β -CV. The changing quantum numbers between the middle and top spectra are represented by the diagonal lines.

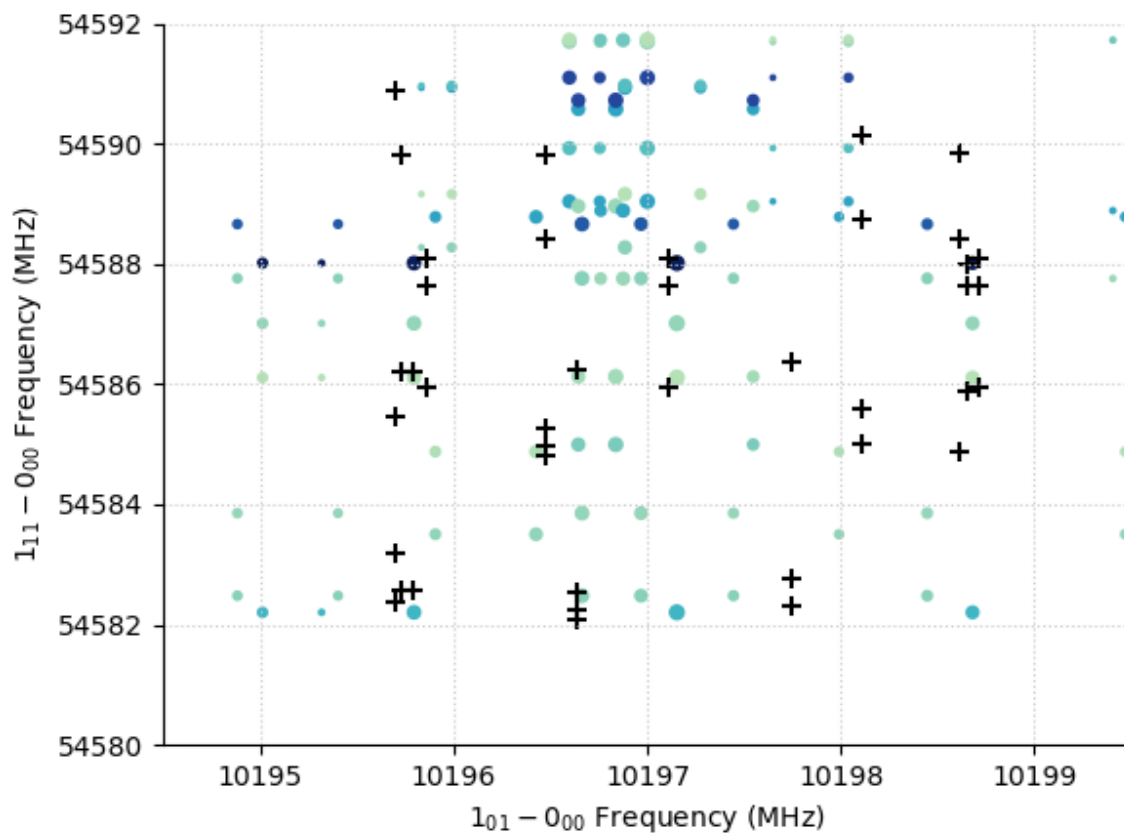


Figure 7.3: The 2D *cis*- β -CV spectrum, with experimental values labeled as black crosses and theoretical values labeled as colored dots. The frequencies of fundamental *b*-type transitions of *cis*- β -CV measured by DR are plotted along the vertical axis against their fundamental *a*-type monitor transition frequencies on the *x* axis. Sets of transition pairs that all share a common lower state are aligned vertically, while sets that share a common upper state (within $l_{11} - 0_{00}$) are aligned horizontally. The sizes of the dots are related to the calculated intensities of each $l_{01} - 0_{00}$ component, and the colors are related to the calculated intensities of each $l_{11} - 0_{00}$ component (darker colors represent stronger transitions). In an effort to fit the spectrum, parameters were varied in turn to make the simulated spectrum better match the experimental one.

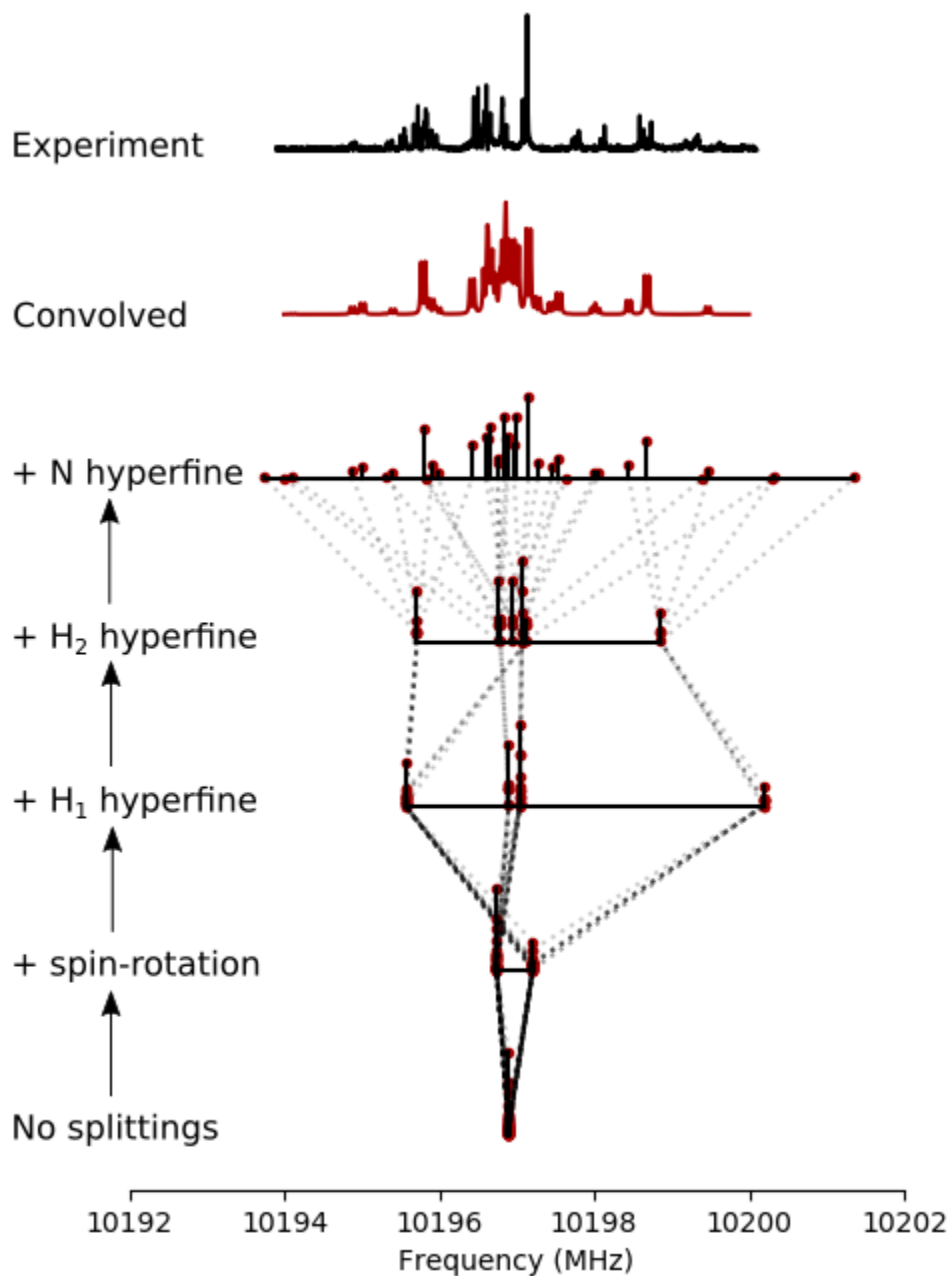


Figure 7.4: The *cis*- β -CV fundamental *a*-type transition, with each source of splitting added individually. From the bottom up: 1. Simple asymmetric top transition with CD terms. 2. Spin-rotation added. 3. Hydrogen 1 spin-spin added. 4. Hydrogen 2 spin-spin added. 5. Nitrogen spin-spin and quadrupole added. 6. Theoretical spectrum convolved with instrumental lineshape function. 7. Experimental spectrum. This simulated spectrum reflects one of the best qualitative fits we were able to produce.

Table 7.1: T_1 Diagnostics for all CV species

Isomer	T_1 (AA)	T_1 (BB)
α -CV	0.049	0.046
<i>cis</i> - β -CV	0.038	0.040
<i>trans</i> - β -CV	0.038	0.041

Table 7.2: Rotational constants (in MHz) for CV isomers calculated at MRCI+Q/aug-cc-pVTZ and CCSD(T)/ANO1.

Isomer	Constant	MRCI+Q	CCSD(T)	% Diff. ^a
α -CV	A_e	152167.27	175612.55	13.4
	B_e	4456.17	4451.72	-0.1
	C_e	4329.38	4341.66	0.3
<i>cis</i> - β -CV	A_e	49447.10	50602.68	2.3
	B_e	5352.24	5387.26	0.7
	C_e	4829.49	4868.91	0.8
<i>trans</i> - β -CV	A_e	63640.54	65002.95	2.1
	B_e	5074.10	5118.28	0.9
	C_e	4699.41	4744.68	1.0

$$^a[\text{CCSD(T)} - \text{MRCI+Q}]/\text{CCSD(T)}$$

function does not significantly affect the quality of our theoretical structures, we performed multireference configuration interaction with single and double excitations with Davidson’s correction^{302,303} using Dunning’s augmented correlation-consistent polarized valence triple-zeta basis set³⁵ (MRCI+Q/aug-cc-pVTZ) as implemented in MOLPRO³⁰⁴ (Table 7.2). All B_e and C_e values are within 1% between the two methods. The A_e values differ by about 2% for *cis*- β -CV and *trans*- β -CV, and 13.4% for α -CV. Given the smaller basis set used in the MRCI calculations, the structural agreement is satisfactory for rotational spectroscopy applications.

Table 7.3: *cis*- β -CV transitions measured using cavity FTMW spectroscopy, in MHz. Uncertainties on each transition are estimated to be 5 kHz.

$N'_{K'_a, K'_c} - N''_{K''_a, K''_c}$	Freq.	$N'_{K'_a, K'_c} - N''_{K''_a, K''_c}$	Freq.
1 ₀₁ - 0 ₀₀	10194.897	2 ₀₂ - 1 ₀₁	20389.337
1 ₀₁ - 0 ₀₀	10195.369	2 ₀₂ - 1 ₀₁	20389.453
1 ₀₁ - 0 ₀₀	10195.699	2 ₀₂ - 1 ₀₁	20389.617
1 ₀₁ - 0 ₀₀	10195.786	2 ₀₂ - 1 ₀₁	20389.706
1 ₀₁ - 0 ₀₀	10195.862	2 ₀₂ - 1 ₀₁	20389.741
1 ₀₁ - 0 ₀₀	10195.923	2 ₀₂ - 1 ₀₁	20389.946
1 ₀₁ - 0 ₀₀	10196.409	2 ₀₂ - 1 ₀₁	20390.230
1 ₀₁ - 0 ₀₀	10196.583	2 ₀₂ - 1 ₀₁	20390.530
1 ₀₁ - 0 ₀₀	10196.610	2 ₀₂ - 1 ₀₁	20390.829
1 ₀₁ - 0 ₀₀	10196.639	3 ₀₃ - 2 ₀₂	30569.243
1 ₀₁ - 0 ₀₀	10196.847	3 ₀₃ - 2 ₀₂	30569.913
1 ₀₁ - 0 ₀₀	10197.111	3 ₀₃ - 2 ₀₂	30570.505
1 ₀₁ - 0 ₀₀	10197.779	3 ₀₃ - 2 ₀₂	30570.566
1 ₀₁ - 0 ₀₀	10198.113	3 ₀₃ - 2 ₀₂	30570.662
1 ₀₁ - 0 ₀₀	10198.610	3 ₀₃ - 2 ₀₂	30571.028
1 ₀₁ - 0 ₀₀	10198.664	3 ₀₃ - 2 ₀₂	30571.278
1 ₀₁ - 0 ₀₀	10198.711	3 ₀₃ - 2 ₀₂	30571.737
1 ₀₁ - 0 ₀₀	10199.213	3 ₀₃ - 2 ₀₂	30571.927
1 ₀₁ - 0 ₀₀	10199.300	3 ₀₃ - 2 ₀₂	30572.262
1 ₀₁ - 0 ₀₀	10199.648	3 ₀₃ - 2 ₀₂	30572.496
2 ₁₂ - 1 ₁₁	19862.500	3 ₀₃ - 2 ₀₂	30572.972
2 ₀₂ - 1 ₀₁	20387.604	3 ₀₃ - 2 ₀₂	30573.741
2 ₀₂ - 1 ₀₁	20387.668	4 ₀₄ - 3 ₀₃	40738.248
2 ₀₂ - 1 ₀₁	20388.299	4 ₀₄ - 3 ₀₃	40738.766
2 ₀₂ - 1 ₀₁	20388.380	4 ₀₄ - 3 ₀₃	40738.847
2 ₀₂ - 1 ₀₁	20388.571	4 ₀₄ - 3 ₀₃	40739.072
2 ₀₂ - 1 ₀₁	20388.783	4 ₀₄ - 3 ₀₃	40739.115
2 ₀₂ - 1 ₀₁	20388.983	4 ₀₄ - 3 ₀₃	40739.234
2 ₀₂ - 1 ₀₁	20389.104	4 ₀₄ - 3 ₀₃	40739.320
2 ₀₂ - 1 ₀₁	20389.219	4 ₀₄ - 3 ₀₃	40742.880

Table 7.4: *cis*- β -CV transitions measured using DR, in MHz. Each transition is shown together with its linked transition measured using cavity FTMW spectroscopy. Uncertainties are in units of the last digit.

$N'_{K'_a, K'_c} - N''_{K''_a, K''_c}$ (DR)	DR Freq.	$N'_{K'_a, K'_c} - N''_{K''_a, K''_c}$ (Cavity)	Cavity Freq.
1 ₁₁ - 0 ₀₀	54585.962(2.9)	1 ₀₁ - 0 ₀₀	10197.111
1 ₁₁ - 0 ₀₀	54587.629(2.7)	1 ₀₁ - 0 ₀₀	10197.111
1 ₁₁ - 0 ₀₀	54588.082(3.3)	1 ₀₁ - 0 ₀₀	10197.111
1 ₁₁ - 0 ₀₀	54584.800(14.6)	1 ₀₁ - 0 ₀₀	10196.477
1 ₁₁ - 0 ₀₀	54584.966(10.3)	1 ₀₁ - 0 ₀₀	10196.477
1 ₁₁ - 0 ₀₀	54585.273(4.8)	1 ₀₁ - 0 ₀₀	10196.477
1 ₁₁ - 0 ₀₀	54588.403(9.3)	1 ₀₁ - 0 ₀₀	10196.477
1 ₁₁ - 0 ₀₀	54589.820(5.2)	1 ₀₁ - 0 ₀₀	10196.477
1 ₁₁ - 0 ₀₀	54582.095(16.6)	1 ₀₁ - 0 ₀₀	10196.639
1 ₁₁ - 0 ₀₀	54582.254(7.7)	1 ₀₁ - 0 ₀₀	10196.639
1 ₁₁ - 0 ₀₀	54582.548(6.7)	1 ₀₁ - 0 ₀₀	10196.639
1 ₁₁ - 0 ₀₀	54586.225(7.2)	1 ₀₁ - 0 ₀₀	10196.639
1 ₁₁ - 0 ₀₀	54582.312(13.8)	1 ₀₁ - 0 ₀₀	10197.773
1 ₁₁ - 0 ₀₀	54582.759(9.4)	1 ₀₁ - 0 ₀₀	10197.773
1 ₁₁ - 0 ₀₀	54586.379(16.9)	1 ₀₁ - 0 ₀₀	10197.773
1 ₁₁ - 0 ₀₀	54585.018(18.0)	1 ₀₁ - 0 ₀₀	10198.113
1 ₁₁ - 0 ₀₀	54585.600(21.7)	1 ₀₁ - 0 ₀₀	10198.113
1 ₁₁ - 0 ₀₀	54588.732(15.7)	1 ₀₁ - 0 ₀₀	10198.113
1 ₁₁ - 0 ₀₀	54590.129(13.3)	1 ₀₁ - 0 ₀₀	10198.113
1 ₁₁ - 0 ₀₀	54585.974(11.7)	1 ₀₁ - 0 ₀₀	10198.711
1 ₁₁ - 0 ₀₀	54587.605(12.4)	1 ₀₁ - 0 ₀₀	10198.711
1 ₁₁ - 0 ₀₀	54588.105(14.3)	1 ₀₁ - 0 ₀₀	10198.711
1 ₁₁ - 0 ₀₀	54585.875(16.7)	1 ₀₁ - 0 ₀₀	10198.653
1 ₁₁ - 0 ₀₀	54587.623(17.2)	1 ₀₁ - 0 ₀₀	10198.653
1 ₁₁ - 0 ₀₀	54588.004(17.7)	1 ₀₁ - 0 ₀₀	10198.653
1 ₁₁ - 0 ₀₀	54584.869(48.3)	1 ₀₁ - 0 ₀₀	10198.616
1 ₁₁ - 0 ₀₀	54588.408(23.8)	1 ₀₁ - 0 ₀₀	10198.616
1 ₁₁ - 0 ₀₀	54589.839(25.6)	1 ₀₁ - 0 ₀₀	10198.616
1 ₁₁ - 0 ₀₀	54585.944(8.1)	1 ₀₁ - 0 ₀₀	10195.862
1 ₁₁ - 0 ₀₀	54587.596(6.8)	1 ₀₁ - 0 ₀₀	10195.862
1 ₁₁ - 0 ₀₀	54588.081(8.6)	1 ₀₁ - 0 ₀₀	10195.862
1 ₁₁ - 0 ₀₀	54582.559(35.7)	1 ₀₁ - 0 ₀₀	10195.786
1 ₁₁ - 0 ₀₀	54586.211(17.2)	1 ₀₁ - 0 ₀₀	10195.786
1 ₁₁ - 0 ₀₀	54582.563(14.9)	1 ₀₁ - 0 ₀₀	10195.730
1 ₁₁ - 0 ₀₀	54586.209(18.8)	1 ₀₁ - 0 ₀₀	10195.730
1 ₁₁ - 0 ₀₀	54589.802(31.8)	1 ₀₁ - 0 ₀₀	10195.730
1 ₁₀ - 1 ₀₁	44921.452(9.9)	1 ₀₁ - 0 ₀₀	10197.111
1 ₁₀ - 1 ₀₁	44922.188(5.8)	1 ₀₁ - 0 ₀₀	10197.111
1 ₁₀ - 1 ₀₁	44922.321(3.3)	1 ₀₁ - 0 ₀₀	10197.111
1 ₁₀ - 1 ₀₁	44922.906(6.5)	1 ₀₁ - 0 ₀₀	10197.111
2 ₁₂ - 1 ₀₁	64253.183(8.3)	1 ₀₁ - 0 ₀₀	10197.111

Table 7.5: *trans*- β -CV transitions measured using cavity FTMW spectroscopy, in MHz. Uncertainties on each transition are estimated to be 5 kHz.

$N'_{K'_a, K'_c} - N''_{K''_a, K''_c}$	Freq.	$N'_{K'_a, K'_c} - N''_{K''_a, K''_c}$	Freq.
$1_{01} - 0_{00}$	9748.785	$2_{02} - 1_{01}$	19498.835
$1_{01} - 0_{00}$	9749.368	$2_{02} - 1_{01}$	19499.765
$1_{01} - 0_{00}$	9749.641	$2_{02} - 1_{01}$	19499.869
$1_{01} - 0_{00}$	9750.340	$2_{02} - 1_{01}$	19500.148
$1_{01} - 0_{00}$	9750.867	$2_{02} - 1_{01}$	19501.737
$1_{01} - 0_{00}$	9752.370	$2_{02} - 1_{01}$	19506.800
$1_{01} - 0_{00}$	9760.040	$2_{02} - 1_{01}$	19507.200
$1_{01} - 0_{00}$	9760.570	$3_{03} - 2_{02}$	29248.950

Table 7.6: *trans*- β -CV transitions measured using DR, in MHz. Each transition is shown together with its linked transition measured using cavity FTMW spectroscopy. Uncertainties are in units of the last digit.

$N'_{K'_a, K'_c} - N''_{K''_a, K''_c}$ (DR)	DR Freq.	$N'_{K'_a, K'_c} - N''_{K''_a, K''_c}$ (Cavity)	Cavity Freq.
$1_{10} - 1_{01}$	61161.701(16.4)	$2_{02} - 1_{01}$	19499.765
$1_{10} - 1_{01}$	61161.771(8.6)	$2_{02} - 1_{01}$	9750.867
$1_{10} - 1_{01}$	61161.849(26.6)	$2_{02} - 1_{01}$	19499.765
$1_{11} - 0_{00}$	70544.755(13.5)	$1_{01} - 0_{00}$	9750.867
$1_{11} - 0_{00}$	70545.547(28.5)	$1_{01} - 0_{00}$	9750.867
$1_{11} - 0_{00}$	70545.864(14.8)	$1_{01} - 0_{00}$	9750.867
$1_{11} - 0_{00}$	70699.630(6.1)	$1_{01} - 0_{00}$	9750.867
$2_{12} - 1_{01}$	79932.631(12.7)	$1_{01} - 0_{00}$	9750.867

Mode	<i>cis</i> - β -CV		<i>trans</i> - β -CV		α -CV	
	Harmonic	Anharmonic	Harmonic	Anharmonic	Harmonic	Anharmonic
7	223.2	223.3	235.0	235.0	176.8	163.5
8	371.1	367.5	360.5	357.7	281.2	273.3
9	529.1	524.2	550.0	545.1	468.8	452.3
10	710.9	700.8	699.3	690.5	586.1	573.4
11	855.5	819.7	797.5	773.3	853.4	830.9
12	888.5	864.7	836.6	819.9	921.8	901.9
13	984.4	948.4	1004.1	970.1	986.1	963.4
14	1263.1	1244.2	1256.4	1229.8	1426.6	1391.0
15	1643.2	1603.9	1656.4	1627.2	1764.9	1740.1
16	2371.8	2305.1	2380.1	2312.2	2172.9	2117.5
17	3197.5	3046.0	3136.7	2986.0	3122.0	2969.9
18	3274.9	3115.6	3280.1	3141.1	3227.9	3071.9
ZPVE	8156.7	8054.1	8096.4	7996.2	7994.3	7724.6

Table 7.7: CCSD(T)/ANO0 harmonic and anharmonic vibrational frequencies of the cyanovinyl isomers, in cm^{-1}

Table 7.8: Calculated parameters of *cis*- and *trans*- β -CV, in MHz

Parameter	<i>cis</i>	<i>trans</i>
A_0	51001.38	65143.77
B_0	5363.23	5107.83
C_0	4844.05	4728.75
$10^3 \Delta_N$	3.13	2.15
$10^1 \Delta_{NK}$	-41.10	-1.56
Δ_K	3.03	7.08
$10^4 \delta_N$	6.86	4.19
$10^2 \delta_K$	3.03	2.17
ϵ_{aa}	4.86	-99.04
ϵ_{bb}	5.82	-9.23
ϵ_{cc}	-4.77	1.66
χ_{aa}	-3.88	-4.00
χ_{bb}	1.81	1.87
χ_{cc}	2.08	2.13
χ_{ab}	1.78	1.63
$a_F(N)$	5.03	4.07
$T_{aa}(N)$	-1.41	-0.89
$T_{bb}(N)$	3.00	1.45
$T_{cc}(N)$	-1.59	-0.56
$T_{ab}(N)$	-0.13	0.59
$a_F(H1)$	86.86	150.96
$T_{aa}(H1)$	-0.54	0.05
$T_{bb}(H1)$	7.28	6.25
$T_{cc}(H1)$	-6.74	-6.29
$T_{ab}(H1)$	8.93	3.28
$a_F(H2)$	35.33	30.31
$T_{aa}(H2)$	-4.57	40.86
$T_{bb}(H2)$	39.36	-5.71
$T_{cc}(H2)$	-34.79	-35.15
$T_{ab}(H2)$	9.26	3.44

cis- β -CV SPFIT/SPCAT input files (no splittings)

cis_no_spin.par

```
8 8 50 0 0.0000E+00 1.0000E+06 -1.0000E+00 1.0000000000
'a' 1 1 1 0 10 0 1 1 1 0 0 1
10000 4.975753840412576E+04 1.000000000E+36
20000 5.364295487047583E+03 1.000000000E+36
30000 4.832548502995252E+03 1.000000000E+36
200 -3.129900000000000E-03 1.38789580E-37 /-Delta_N
2000 -3.025700000000001E+00 1.38789580E-37 /-Delta_K
1100 1.101800000000000E-01 1.38789580E-37 /-Delta_NK
40100 -6.863400000000001E-04 1.38789580E-37 /-delta_J
41000 -3.032420000000000E-02 1.38789580E-37 /-delta_K
```

cis_no_spin.lin

```
1 0 1 0 0 0 10196.6680 0.6000 2.481E-07
2 0 2 1 0 1 20389.1791 0.6000 1.648E-06
1 1 1 0 0 0 54586.1531 2.4000 1.517E-05
1 1 0 1 0 1 44922.1790 0.6000 1.500E-05
2 1 2 1 0 1 64253.1830 2.4000 1.500E-05
3 0 3 2 0 2 30571.4100 0.6000 1.500E-05
4 0 4 3 0 3 40738.8600 0.6000 1.500E-05
2 1 2 1 1 1 19862.5000 0.6000 1.000E-05
```

cis_no_spin.int

```
112 1 1314.0 0 10 -50. -50. 95.00
1 3.18
2 0.40
```

cis- β -CV SPFIT/SPCAT input (ab initio)

```
cis_theory.par
28 4 10 2 0.0000E+00 1.0000E+06 -1.0000E+00 1.0000000000
'a' 3222 1 0 9 0 1 1 1 1 -1 1
10000 5.1001378060000000E+04 1.00000000E-37
20000 5.3632341800000000E+03 1.00000000E-37
30000 4.8440502340000000E+03 1.00000000E-37
200 -3.1299000000000000E-03 1.38789580E-37 /-Delta_N
2000 -3.0257000000000001E+00 1.38789580E-37 /-Delta_K
1100 1.1018000000000000E-01 1.38789580E-37 /-Delta_NK
40100 -6.8634000000000001E-04 1.38789580E-37 /-delta_J
41000 -3.0324200000000000E-02 1.38789580E-37 /-delta_K
10010000 4.8601470000000000E+00 1.38789580E-36 /e_aa
10020000 5.8240450000000000E-00 1.59003886E-37 /e_bb
10030000 -4.7717220000000000E-00 1.00000000E-37 /e_cc
440010000 -5.8241156250000000E+00 5.69881433E-37 /3chi_aa/2
440040000 -6.7682780000000000E-02 1.38789580E-37 /chi(b-c)/4
440610000 1.7782921000000000E+00 1.00000000E-37 /chi.ab
140000000 5.032457602313510E+00 1.38789580E-37 /a_f
140010000 -2.116078535548397E+00 1.00000000E-37 /1.5 T_aa
140040000 1.147461860475000E+00 1.38789580E-37 /T_(bb-cc)/4
140610000 -1.3353859850000000E-01 1.00000000E-37 /T.ab
130000000 8.686288970506232E+01 1.38789580E-37 /a_f
130010000 -8.030599569565532E-01 1.00000000E-37 /1.5 T_aa
130040000 3.5053402758000000E+00 1.38789580E-37 /T_(bb-cc)/4
130610000 8.9289316140000000E+00 1.00000000E-37 /T.ab
120000000 3.532996519467918E+01 1.38789580E-37 /a_f
120010000 -6.860313681454295E+00 1.00000000E-37 /1.5 T_aa
120040000 1.853906216962000E+01 1.38789580E-37 /T_(bb-cc)/4
120610000 9.2596912310000000E+00 1.00000000E-37 /T.ab
```

trans- β -CV SPFIT/SPCAT input files (spin-rotation splitting only)

trans_spin_rot_only.par

```
11 9 10 2 0.0000E+00 1.0000E+06 -1.0000E+00 1.0000000000
'a' 2 1 0 9 0 1 1 1 1 -1 0
10000 6.591832899532368E+04 1.00000000E-37 /A
20000 5.068497891984823E+03 1.00000000E-37 /B
30000 4.684555696741106E+03 1.00000000E-37 /C
200 -2.150000000000000E-03 1.00000000E-37 /-Delta_N
1100 1.560000000000000E-01 1.00000000E-37 /-Delta_NK
2000 -7.080000000000000E+00 1.00000000E-37 /-Delta_K
40100 -4.190000000000000E-04 1.00000000E-37 /-delta_J
41000 -2.170000000000000E-02 1.00000000E-37 /-delta_K
10010000 -2.099057158368144E+02 1.00000000E-37 /e_aa
10020000 -1.736750179679782E+01 1.00000000E-37 /e_bb
-10030000 3.123516032793540E+00 1.00000000E-37 /e_cc
```

trans_spin_rot_only.lin

```
1 0 1 2 0 0 0 1 9750.2285 1.6500 6.494E-05
1 0 1 1 0 0 0 1 9760.1000 1.6500 4.195E-05
2 0 2 3 1 0 1 2 19500.0023 1.6500 3.000E-05
2 0 2 2 1 0 1 1 19507.0000 1.6500 1.000E-05
1 1 1 2 0 0 0 1 70545.3887 1.8050 2.874E-04
1 1 1 1 0 0 0 1 70699.6250 1.8050 2.874E-04
1 1 0 2 1 0 1 1 61161.9450 1.8050 1.200E-04
3 0 3 4 2 0 2 3 29248.9500 1.6500 1.500E-04
2 1 2 3 1 0 1 2 79932.6300 1.8050 1.500E-04
```

trans_spin_rot_only.int

```
0 1 13387.5632 0 9 -15.2 -9.0 4444.0 5
1 4.91
2 1.47
```

trans- β -CV SPFIT/SPCAT input (ab initio)

trans_theory.par

```
22 32 10 2 0.0000E+00 1.0000E+06 -1.0000E+00 1.0000000000
'a' 3222 1 0 9 0 1 1 1 1 -1 0
10000 6.514377270000000E+04 1.00000000E-37 /A
20000 5.107828700000000E+03 1.00000000E-37 /B
30000 4.728746500000000E+03 1.00000000E-37 /C
200 -2.150000000000000E-03 1.00000000E-37 /-Delta_N
1100 1.560000000000000E-01 1.00000000E-37 /-Delta_NK
2000 -7.080000000000000E+00 1.00000000E-37 /-Delta_K
40100 4.190000000000000E-04 1.00000000E-37 /-delta_J
41000 2.170000000000000E-02 1.00000000E-37 /-delta_K
10010000 -9.904328600000000E+01 1.00000000E-37 /e_aa
10020000 -9.231790000000000E+00 1.00000000E-37 /e_bb
10030000 1.664832000000000E+01 1.00000000E-37 /e_cc
440010000 -6.003917805000000E+00 1.00000000E-37 /3chi_aa/2
440040000 -6.395500000000000E-02 1.00000000E-37 /chi(b-c)/4
140000000 4.066270819300000E+00 1.00000000E-37 /a_f
140010000 -1.337030729250000E+00 1.00000000E-37 /1.5 T_aa
140061000 0.596329748200000E+00 1.00000000E-37 /T_ab
140040000 0.504208067675000E+00 1.00000000E-37 /T_(bb-cc)/4
130000000 1.509590309665000E+02 1.00000000E-37 /a_f
```

130010000	0.067890407550000E+00	1.00000000E-37	/1.5 T_aa
130061000	3.280351955100000E+00	1.00000000E-37	/T_ab
130040000	3.228982067820000E+00	1.00000000E-37	/T_(bb-cc)/4
120000000	3.031177531380000E+00	1.00000000E-37	/a_f
120010000	6.129684846575000E+00	1.00000000E-37	/1.5 T_aa
120061000	3.452001998000000E+00	1.00000000E-37	/T_ab
120040000	7.360324658000000E+00	1.00000000E-37	/T_(bb-cc)/4

Appendix B: Pyrrolyl

This file contains full electronic spin-rotation tensors for 1-pyrrolyl (Table 7.9), 2-pyrrolyl (Table 7.10), and 3-pyrrolyl (Table 7.11) evaluated at different levels of electronic structure theory and with different basis sets, as explained in the main text. Table 7.12 contains the ground state (vibrationally averaged) geometries, calculated by applying fc-CCSD(T)/ANO0 displacements to the ae-CCSD(T)/cc-pwCVTZ equilibrium geometries. In addition to the tables in this document, additional plain text files are provided for each isomer which contain:

- `normal_mode_coords.txt` - Displacement coordinates for each normal mode.
- `anharm_transitions.txt` - fc-CCSD(T)/ANO0 VPT2 frequencies and intensities of all anharmonic transitions from the ground vibrational state to modes with up to 3 quanta.
- `B_excited_vib_states.txt` - fc-CCSD(T)/ANO0 vibration-rotation corrections for single-quantum vibrationally excited states.
- `full_rot_HF.txt` - Complete ae-CCSD(T)/cc-pwCVTZ spin-spin and quadrupole tensors for all $I > 0$ nuclei, including rare isotopes.

1-Pyrrolyl Normal Coordinates

Normal Coordinates									
A2			B2			B1			
488.72			541.00			668.35			
VIBRATION			VIBRATION			VIBRATION			
N1	0.000	-0.0000	-0.0000	0.0000	0.5940	-0.0000	0.4636	0.0000	-0.0000
C2	0.000	0.2119	-0.0000	0.0000	-0.3321	-0.0000	0.0626	-0.0000	0.5163
C5	0.000	-0.2119	-0.0000	0.0000	-0.3321	-0.0000	0.0626	0.0000	-0.5163
C3	-0.000	-0.5130	-0.0000	0.0000	0.1128	-0.0000	-0.3013	-0.0000	0.1123
C4	-0.000	0.5130	-0.0000	0.0000	0.1128	-0.0000	-0.3013	-0.0000	-0.1123
H2	-0.000	0.3639	-0.0000	0.0000	-0.4390	-0.0000	0.0445	0.0000	0.0927

Table 7.9: 1-pyrrolyl electronic spin-rotation tensors (in MHz) calculated at the levels of theory indicated.

ae-CCSD(T)/cc-pVDZ			
	J_x	J_y	J_z
S_x	0.088603	-0.098048	0.050817
S_y	0.304697	-0.836035	-0.024457
S_z	0.357892	-0.000132	-9.600845
Eigenvalues of SR-Tensor	0.104204	-0.847304	-9.605177
ae-CCSD(T)/cc-pVTZ			
	J_x	J_y	J_z
S_x	0.299976	0.155850	0.034401
S_y	0.477591	-0.937775	-0.223365
S_z	-0.114570	0.008421	-10.041144
Eigenvalues of SR-Tensor	0.376707	-1.013110	-10.042541
ae-CCSD(T)/cc-pwCVDZ			
	J_x	J_y	J_z
S_x	0.265236	0.009594	-0.053036
S_y	-0.367954	-0.833982	0.049022
S_z	0.277206	-0.089034	-9.914846
Eigenvalues of SR-Tensor	0.294975	-0.862452	-9.916116
ae-CCSD/cc-pwCVDZ			
	J_x	J_y	J_z
S_x	2.254079	0.002020	0.024198
S_y	0.003960	-0.748761	-0.025190
S_z	0.058751	-0.000521	-9.684744
Eigenvalues of SR-Tensor	2.254226	-0.748745	-9.684906
ae-CCSD(T)/ANO0			
	J_x	J_y	J_z
S_x	0.106065	-0.080326	-0.023852
S_y	-7.480309	-1.054280	0.030292
S_z	2.551904	0.047884	-9.316110
Eigenvalues of SR-Tensor	3.419442	-4.160696	-9.523070
fc-CCSD/aug-cc-pVDZ			
	J_x	J_y	J_z
S_x	1.734249	-0.011434	0.417579
S_y	2.178671	-0.910171	-0.813762
S_z	0.974806	-0.089139	-8.296985
Eigenvalues of SR-Tensor	2.146147	-1.236546	-8.382508

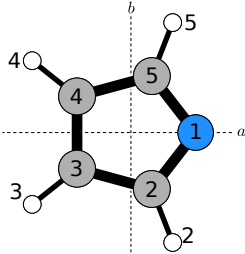
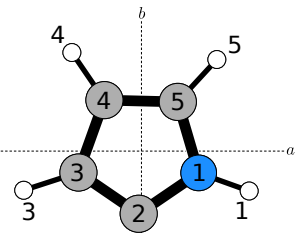
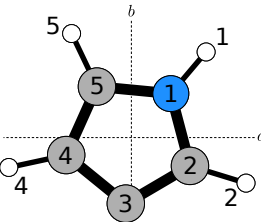
Table 7.10: 2-pyrrolyl electronic spin-rotation tensors (in MHz) calculated at the levels of theory indicated.

ae-CCSD(T)/cc-pVDZ			
	J_x	J_y	J_z
S_x	16.098629	1.501271	0.243691
S_y	0.276220	3.300084	-0.018566
S_z	-0.037671	-0.006967	-2.524297
Eigenvalues of SR-Tensor	16.160606	3.238731	-2.524921
ae-CCSD(T)/cc-pVTZ			
	J_x	J_y	J_z
S_x	17.837577	1.546325	-0.147103
S_y	-0.713352	3.789831	-0.069226
S_z	0.260788	0.006651	-2.953024
Eigenvalues of SR-Tensor	17.850064	3.777655	-2.953335
ae-CCSD(T)/cc-pwCVDZ			
	J_x	J_y	J_z
S_x	16.514029	1.567298	0.106053
S_y	0.272382	3.228755	0.041455
S_z	0.451221	0.239509	-2.652546
Eigenvalues of SR-Tensor	16.581716	3.167882	-2.659360
ae-CCSD/cc-pwCVDZ			
	J_x	J_y	J_z
S_x	17.571053	1.352201	-0.000934
S_y	-0.077742	3.345097	-0.003798
S_z	0.026547	-0.021089	-2.458374
Eigenvalues of SR-Tensor	17.599547	3.316640	-2.458410
ae-CCSD(T)/ANO0			
	J_x	J_y	J_z
S_x	16.959713	1.404095	-0.177957
S_y	-0.707999	3.851168	0.011100
S_z	-0.116581	-0.024475	-2.707020
Eigenvalues of SR-Tensor	16.970051	3.841934	-2.708125
fc-CCSD/aug-cc-pVDZ			
	J_x	J_y	J_z
S_x	18.187458	1.731717	0.492475
S_y	-0.931975	4.068492	0.214232
S_z	-1.294454	0.883629	-2.748182
Eigenvalues of SR-Tensor	18.205866	4.102889	-2.800987

Table 7.11: 3-pyrrolyl electronic spin-rotation tensors (in MHz) calculated at the levels of theory indicated.

ae-CCSD(T)/cc-pVDZ			
	J_x	J_y	J_z
S_x	9.185782	-2.786717	-0.078725
S_y	-1.380936	2.238769	0.088069
S_z	-0.258567	0.057089	-3.144017
Eigenvalues of SR-Tensor	9.765466	1.661777	-3.146709
ae-CCSD(T)/cc-pVTZ			
	J_x	J_y	J_z
S_x	10.591591	-3.178427	0.125607
S_y	-0.788966	3.083487	-0.013994
S_z	-0.207569	0.217152	-3.569744
Eigenvalues of SR-Tensor	11.083754	2.592882	-3.571303
ae-CCSD(T)/cc-pwCVDZ			
	J_x	J_y	J_z
S_x	9.284677	-2.965170	0.347361
S_y	-1.443033	2.224460	0.022291
S_z	0.073728	0.241005	-3.282334
Eigenvalues of SR-Tensor	9.918358	1.599842	-3.291397
ae-CCSD/cc-pwCVDZ			
	J_x	J_y	J_z
S_x	10.181291	-3.205765	-0.004494
S_y	-0.677538	2.583289	0.006572
S_z	-0.003932	-0.018510	-3.226816
Eigenvalues of SR-Tensor	10.648720	2.115870	-3.226826
ae-CCSD(T)/ANO0			
	J_x	J_y	J_z
S_x	9.562738	-2.840489	-0.098450
S_y	-0.779115	3.162065	-0.034175
S_z	0.030432	-0.443708	-3.373901
Eigenvalues of SR-Tensor	10.039080	2.695250	-3.383428
fc-CCSD/aug-cc-pVDZ			
	J_x	J_y	J_z
S_x	10.495251	-2.788957	0.331744
S_y	-0.805353	3.517603	-0.139486
S_z	0.136832	-1.753597	-3.273206
Eigenvalues of SR-Tensor	10.945304	3.197026	-3.402682

Table 7.12: Ground state bond lengths (in Ångstroms) and bond angles (in degrees) calculated by adding fc-CCSD(T)/ANO0 displacements to the ae-CCSD(T)/cc-pwCVTZ equilibrium geometries.

	1-Pyrrolyl	2-Pyrrolyl	3-Pyrrolyl
			
N1-C2	1.349	1.360	1.385
C2-C3	1.460	1.366	1.366
C3-C4	1.367	1.441	1.417
C4-C5	1.460	1.374	1.382
C5-N1	1.349	1.388	1.374
N1-H1	–	0.986	0.996
C2-H2	1.097	–	1.086
C3-H3	1.093	1.087	–
C4-H4	1.097	1.092	1.089
C5-H5	1.093	1.087	1.089
\angle C2-N1-C5	104.5	107.8	109.9
\angle N1-C2-C3	112.6	111.5	105.5
\angle N1-C5-C4	112.6	107.8	108.8
\angle C2-C3-C4	105.2	104.6	110.9
\angle C5-C4-C3	105.2	108.4	104.9
\angle C2-N1-H1	–	125.9	125.2
\angle N1-C2-H2	121.0	–	122.5
\angle N1-C5-H5	121.0	121.3	121.4
\angle C2-C3-H3	126.4	127.5	–
\angle C5-C4-H4	126.4	125.6	126.5

H5	0.000	-0.3639	-0.0000	0.0000	-0.4390	-0.0000	0.0445	0.0000	-0.0927
H3	-0.000	-0.2441	-0.0000	-0.0000	0.0886	-0.0000	-0.0848	0.0000	0.0294
H4	-0.000	0.2441	0.0000	-0.0000	0.0886	-0.0000	-0.0848	0.0000	-0.0294

B2	B2			A2					
700.92	814.95			815.62					
VIBRATION	VIBRATION			VIBRATION					
N1	-0.000	0.1509	0.0000	0.0000	0.2210	-0.0000	-0.0000	0.0000	-0.0000
C2	-0.000	-0.1229	-0.0000	0.0000	-0.4009	0.0000	0.0000	0.4167	0.0000
C5	0.000	-0.1229	0.0000	-0.0000	-0.4009	0.0000	-0.0000	-0.4167	-0.0000
C3	0.000	-0.2088	-0.0000	0.0000	0.2164	0.0000	-0.0000	-0.0538	-0.0000
C4	0.000	-0.2088	0.0000	-0.0000	0.2164	0.0000	-0.0000	0.0538	0.0000
H2	-0.000	0.2626	0.0000	0.0000	0.4608	0.0000	0.0000	-0.5001	0.0000
H5	-0.000	0.2626	-0.0000	-0.0000	0.4608	0.0000	-0.0000	0.5001	-0.0000
H3	0.000	0.6008	-0.0000	-0.0000	-0.2360	0.0000	-0.0000	-0.2708	-0.0000
H4	-0.000	0.6008	0.0000	0.0000	-0.2360	-0.0000	-0.0000	0.2708	0.0000

A1	A2			B1					
869.47	885.34			924.59					
VIBRATION	VIBRATION			VIBRATION					
N1	-0.000	0.0000	0.6401	0.0000	0.0000	0.0000	0.0779	0.0000	0.0000
C2	-0.380	-0.0000	-0.0352	-0.0000	0.1143	-0.0000	0.0278	-0.0000	-0.1812
C5	0.380	-0.0000	-0.0352	0.0000	-0.1143	0.0000	0.0278	0.0000	0.1812
C3	-0.017	0.0000	-0.2826	-0.0000	-0.3529	0.0000	-0.1471	0.0000	0.4828
C4	0.017	-0.0000	-0.2826	-0.0000	0.3529	-0.0000	-0.1471	-0.0000	-0.4828
H2	-0.050	0.0000	-0.1648	0.0000	-0.1783	-0.0000	0.0755	0.0000	-0.2349
H5	0.050	0.0000	-0.1648	0.0000	0.1783	0.0000	0.0755	-0.0000	0.2349
H3	0.187	-0.0000	0.0686	0.0000	0.5750	0.0000	0.1908	-0.0000	0.3336
H4	-0.187	0.0000	0.0686	0.0000	-0.5750	-0.0000	0.1908	0.0000	-0.3336

A1	B1			A1					
1039.12	1069.37			1084.25					
VIBRATION	VIBRATION			VIBRATION					
N1	-0.000	-0.0000	0.2774	0.5486	0.0000	-0.0000	0.0000	0.0000	0.2491
C2	0.159	0.0000	0.2309	-0.4755	0.0000	-0.0156	-0.0106	0.0000	-0.2212
C5	-0.159	0.0000	0.2309	-0.4755	0.0000	0.0156	0.0106	-0.0000	-0.2212
C3	-0.037	0.0000	-0.3411	0.1482	0.0000	-0.1508	-0.1822	-0.0000	0.2464
C4	0.037	-0.0000	-0.3411	0.1482	-0.0000	0.1508	0.1822	0.0000	0.2464
H2	-0.003	-0.0000	0.2133	-0.1167	-0.0000	-0.0708	0.1149	0.0000	-0.3789
H5	0.003	-0.0000	0.2133	-0.1167	0.0000	0.0708	-0.1149	0.0000	-0.3789
H3	-0.311	-0.0000	-0.3501	0.2234	0.0000	0.0996	-0.3736	0.0000	-0.1724
H4	0.311	0.0000	-0.3501	0.2234	0.0000	-0.0996	0.3736	0.0000	-0.1724

A1	B1			B1					
1188.60	1284.26			1348.99					
VIBRATION	VIBRATION			VIBRATION					
N1	0.000	-0.0000	0.2583	0.0835	-0.0000	-0.0000	0.2567	-0.0000	-0.0000
C2	0.496	-0.0000	0.0247	0.1302	-0.0000	-0.1982	-0.1332	-0.0000	-0.1724
C5	-0.496	0.0000	0.0247	0.1302	0.0000	0.1982	-0.1332	-0.0000	0.1724
C3	0.126	-0.0000	-0.1175	-0.1822	0.0000	-0.0749	0.1462	-0.0000	0.3852
C4	-0.126	-0.0000	-0.1175	-0.1822	-0.0000	0.0749	0.1462	0.0000	-0.3852

H2	0.262	0.0000	-0.2564	-0.1898	0.0000	0.5310	-0.1556	-0.0000	0.2200
H5	-0.262	-0.0000	-0.2564	-0.1898	0.0000	-0.5310	-0.1556	0.0000	-0.2200
H3	0.215	0.0000	0.0952	0.2136	-0.0000	0.1946	-0.3677	0.0000	-0.2050
H4	-0.215	0.0000	0.0952	0.2136	0.0000	-0.1946	-0.3677	-0.0000	0.2050

A1	A1			B1					
1447.28	1549.09			3226.20					
VIBRATION	VIBRATION			VIBRATION					
N1	0.000	-0.0000	0.3934	-0.0000	-0.0000	0.1330	0.0047	-0.0000	0.0000
C2	0.125	0.0000	-0.4324	0.1719	-0.0000	-0.1469	-0.1826	0.0000	-0.0732
C5	-0.125	0.0000	-0.4324	-0.1719	0.0000	-0.1469	-0.1826	-0.0000	0.0732
C3	0.284	-0.0000	0.1391	-0.5879	-0.0000	-0.0455	0.0344	-0.0000	-0.0338
C4	-0.284	-0.0000	0.1391	0.5879	0.0000	-0.0455	0.0344	0.0000	0.0338
H2	-0.135	-0.0000	0.3161	-0.0412	-0.0000	0.2060	0.6110	-0.0000	0.2383
H5	0.135	0.0000	0.3161	0.0412	-0.0000	0.2060	0.6110	-0.0000	-0.2383
H3	-0.008	0.0000	-0.0369	0.0649	-0.0000	0.2098	-0.1085	-0.0000	0.1306
H4	0.008	-0.0000	-0.0369	-0.0649	-0.0000	0.2098	-0.1085	0.0000	-0.1306

A1	B1			A1					
3230.74	3254.18			3275.14					
VIBRATION	VIBRATION			VIBRATION					
N1	-0.000	0.0000	0.0065	0.0020	-0.0000	0.0000	-0.0000	0.0000	0.0037
C2	0.192	-0.0000	0.0713	-0.0479	-0.0000	-0.0260	0.0373	0.0000	0.0226
C5	-0.192	0.0000	0.0713	-0.0479	0.0000	0.0260	-0.0373	-0.0000	0.0226
C3	-0.027	-0.0000	0.0220	-0.1165	0.0000	0.1578	0.1473	-0.0000	-0.1601
C4	0.027	0.0000	0.0220	-0.1165	0.0000	-0.1578	-0.1473	-0.0000	-0.1601
H2	-0.619	0.0000	-0.2414	0.1553	0.0000	0.0638	-0.1101	-0.0000	-0.0468
H5	0.619	-0.0000	-0.2414	0.1553	-0.0000	-0.0638	0.1101	0.0000	-0.0468
H3	0.079	0.0000	-0.0926	0.4080	-0.0000	-0.5137	-0.4144	0.0000	0.5145
H4	-0.079	0.0000	-0.0926	0.4080	0.0000	0.5137	0.4144	0.0000	0.5145

1-Pyrrolyl Rotational Constants for Vibrationally Excited States

 Be, B0 AND B-B0 SHIFTS FOR SINGLY EXCITED VIBRATIONAL STATES (CM-1)

VIBRATION	X AXIS	Y AXIS	Z AXIS
Be	0.28891755	0.15383849	0.32904165
B0	0.28762026	0.15262077	0.32557740
Be-B0	0.00129729	0.00121772	0.00346425
B'	0.28762050	0.15262042	0.32557763
Be-B'	0.00129706	0.00121807	0.00346402
B''	0.28762053	0.15262086	0.32557768
Be-B''	0.00129702	0.00121763	0.00346397
B^A	0.28762057	0.15262040	0.32557757
Be-B^A	0.00129698	0.00121809	0.00346408
B^S	0.28762030	0.15262054	0.32557773
Be-B^S	0.00129725	0.00121795	0.00346392
7	-0.00059898	0.00014678	-0.00038900
8	-0.00072081	0.00011749	-0.00039246
9	0.00097129	-0.00064002	-0.00185616

10	-0.00039934	0.00008481	-0.00045106
11	-0.00067135	0.00001444	-0.00062877
12	-0.00032746	0.00003744	-0.00153220
13	0.00046906	0.00017705	0.00052477
14	-0.00051739	0.00001318	-0.00028057
15	0.00013077	-0.00041704	0.00025649
16	-0.00037861	-0.00042706	0.00042564
17	0.00003143	-0.00143077	-0.00007137
18	0.00023635	0.00121691	0.00009757
19	-0.00005861	-0.00010399	-0.00028727
20	0.00042950	-0.00010280	0.00008688
21	-0.00010636	-0.00024258	0.00014486
22	-0.00017489	-0.00021796	-0.00057096
23	0.00001275	-0.00013758	-0.00068000
24	-0.00017582	-0.00011665	-0.00034041
25	-0.00017235	-0.00011956	-0.00035014
26	-0.00028563	-0.00014142	-0.00030384
27	-0.00028813	-0.00014612	-0.00033053

 Be, B0 AND B-B0 SHIFTS FOR SINGLY EXCITED VIBRATIONAL STATES (MHz)

VIBRATION	X AXIS	Y AXIS	Z AXIS
Be	8661.53029617	4611.96177519	9864.42047683
B0	8622.63847542	4575.45553612	9760.56480112
Be-B0	38.89182075	36.50623907	103.85567571
B'	8622.64551899	4575.44497078	9760.57184467
Be-B'	38.88477718	36.51680441	103.84863215
B''	8622.64667131	4575.45817803	9760.57335093
Be-B''	38.88362486	36.50359716	103.84712590
B^A	8622.64789092	4575.44442758	9760.57001594
Be-B^A	38.88240524	36.51734762	103.85046088
B^S	8622.63980271	4575.44865337	9760.57484397
Be-B^S	38.89049346	36.51312182	103.84563286
7	-17.95707119	4.40042570	-11.66181290
8	-21.60923024	3.52222624	-11.76579068
9	29.11860678	-19.18735653	-55.64640178
10	-11.97189843	2.54253490	-13.52243934
11	-20.12651872	0.43284670	-18.85000745
12	-9.81713352	1.12254317	-45.93428907
13	14.06200270	5.30780657	15.73227533
14	-15.51108236	0.39527032	-8.41121938
15	3.92042557	-12.50248447	7.68949180
16	-11.35053238	-12.80285127	12.76046532
17	0.94227122	-42.89339204	-2.13965901
18	7.08551297	36.48213533	2.92521076
19	-1.75705011	-3.11754479	-8.61200339
20	12.87611009	-3.08198626	2.60461928
21	-3.18861237	-7.27235876	4.34284503
22	-5.24295632	-6.53426031	-17.11693790
23	0.38210992	-4.12443786	-20.38592458

24	-5.27081015	-3.49712785	-10.20518623
25	-5.16689152	-3.58433056	-10.49686238
26	-8.56292274	-4.23953833	-9.10877519
27	-8.63797071	-4.38059805	-9.90894967

1-Pyrrolyl Z-Matrix for CCSD(T)/cc-pwCVTZ Optimized Geometry and CFOUR Inputs

1-Pyrrolyl

X

X 1 RX

N 2 RX1* 1 AX

C 2 RX2* 3 AN 1 DX1

C 2 RX2* 3 AN 1 DX

C 2 RX3* 4 AC1* 1 DX1

C 2 RX3* 5 AC1* 1 DX

H 4 RC4* 3 ACN* 6 DC5

H 5 RC4* 3 ACN* 7 DC51

H 6 RC5* 4 ACC* 7 DC6

H 7 RC5* 5 ACC* 4 DC61

```

RX   =      1.000001023287330
RX1  =      0.823557178701364
AX   =      90.000000000000000
RX2  =      1.061513996470007
AN   =      90.000000000000000
DX1  =     -90.000000000000000
DX   =      90.000000000000000
RX3  =      1.562508092561348
AC1  =      64.205240430228059
RC4  =      1.080123155294570
ACN  =     120.896512173812610
DC5  =    -180.000000000000000
DC51 =     180.000000000000000
RC5  =      1.077284354054957
ACC  =     126.300845446273215
DC6  =    -180.000000000000000
DC61 =     180.000000000000000

```

*CFOUR(CALC=CCSD(T),BASIS=PWCVTZ

SCF_CONV=9

CC_CONV=10

GEO_CONV=6

CC_PROGRAM=ECC

OCCUPATION=9-6-2-1/9-6-2-0

SCF_DAMPING=500

SCF_MAXCYC=500

MULTIPLICITY=2

MEMORY_SIZE=10, MEM_UNIT=GB)

1-Pyrrolyl Hyperfine Terms at CCSD(T)/cc-pwCVTZ

Dipole-dipole contributions to HFS at atomic centers

Z-matrix center 3:

Atomic charge is

7

XX = -0.1049918948 YY = 0.2090032860 ZZ = -0.1040113912

XY = 0.0000000000 XZ = 0.0000000000 YZ = 0.0000000000

In MHz, Mass number 14

aF = -8.2428719897

Txx = 4.0447043465

Tyy = -8.0516358045

Tzz = 4.0069314580

Txy = -0.0000000000

Txz = -0.0000000000

Tyz = -0.0000000000

In MHz, Mass number 15

aF = 11.5627283146

Txx = -5.6737284687

Tyy = 11.2944708364

Tzz = -5.6207423677

Txy = 0.0000000000

Txz = 0.0000000000

Tyz = 0.0000000000

Z-matrix center 4:

Atomic charge is

6

XX = 0.2914945879 YY = -0.5909796487 ZZ = 0.2994850608

XY = 0.0000000000 XZ = -0.0071932158 YZ = 0.0000000000

In MHz, Mass number 13

aF = 34.1360901122

Txx = -39.0713962232

Tyy = 79.2138206790

Tzz = -40.1424244559

Txy = -0.0000000000

Txz = 0.9641653646

Tyz = -0.0000000000

Z-matrix center 5:

Atomic charge is

6

XX = 0.2914945879 YY = -0.5909796487 ZZ = 0.2994850608

XY = 0.0000000000 XZ = 0.0071932158 YZ = 0.0000000000

In MHz, Mass number 13

aF = 34.1360901122

Txx = -39.0713962232

Tyy = 79.2138206790

Tzz = -40.1424244559

Txy = -0.0000000000

Txz = -0.9641653646

Tyz = -0.0000000000

Z-matrix center 6:

Atomic charge is

6

XX = 0.0599549253 YY = -0.1108421681 ZZ = 0.0508872428

XY = 0.0000000000 XZ = 0.0035638498 YZ = 0.0000000000

In MHz, Mass number 13

```

aF = -10.5630201368
Txx = -8.0362474611
Tyy = 14.8570795070
Tzz = -6.8208320460
Txy = -0.0000000000
Txz = -0.4776918390
Tyz = -0.0000000000
Z-matrix center 7:
Atomic charge is 6
XX = 0.0599549253 YY = -0.1108421681 ZZ = 0.0508872428
XY = 0.0000000000 XZ = -0.0035638498 YZ = 0.0000000000
In MHz, Mass number 13
aF = -10.5630201368
Txx = -8.0362474611
Tyy = 14.8570795070
Tzz = -6.8208320460
Txy = -0.0000000000
Txz = 0.4776918390
Tyz = -0.0000000000
Z-matrix center 8:
Atomic charge is 1
XX = -0.0271146424 YY = 0.0002675966 ZZ = 0.0268470458
XY = 0.0000000000 XZ = -0.0300585664 YZ = 0.0000000000
In MHz, Mass number 1
aF = -36.1970143350
Txx = 14.4506613066
Tyy = -0.1426147460
Tzz = -14.3080465606
Txy = -0.0000000000
Txz = 16.0196161173
Tyz = -0.0000000000
In MHz, Mass number 2
aF = -5.5564625655
Txx = 2.2182646848
Tyy = -0.0218922337
Tzz = -2.1963724511
Txy = -0.0000000000
Txz = 2.4591088216
Tyz = -0.0000000000
In MHz, Mass number 3
aF = -38.6091800420
Txx = 15.4136520473
Tyy = -0.1521185795
Tzz = -15.2615334677
Txy = -0.0000000000
Txz = 17.0871618623
Tyz = -0.0000000000
Z-matrix center 9:
Atomic charge is 1
XX = -0.0271146424 YY = 0.0002675966 ZZ = 0.0268470458
XY = 0.0000000000 XZ = 0.0300585664 YZ = 0.0000000000

```

```

In MHz, Mass number 1
aF = -36.1970143350
Txx = 14.4506613066
Tyy = -0.1426147460
Tzz = -14.3080465606
Txy = -0.0000000000
Txz = -16.0196161173
Tyz = -0.0000000000
In MHz, Mass number 2
aF = -5.5564625655
Txx = 2.2182646848
Tyy = -0.0218922337
Tzz = -2.1963724511
Txy = -0.0000000000
Txz = -2.4591088216
Tyz = -0.0000000000
In MHz, Mass number 3
aF = -38.6091800420
Txx = 15.4136520473
Tyy = -0.1521185795
Tzz = -15.2615334677
Txy = -0.0000000000
Txz = -17.0871618623
Tyz = -0.0000000000
Z-matrix center 10:
Atomic charge is 1
XX = 0.0077463521 YY = 0.0046634335 ZZ = -0.0124097856
XY = 0.0000000000 XZ = 0.0103050790 YZ = 0.0000000000
In MHz, Mass number 1
aF = -9.0978518520
Txx = -4.1283933946
Tyy = -2.4853618518
Tzz = 6.6137552465
Txy = -0.0000000000
Txz = -5.4920586757
Tyz = -0.0000000000
In MHz, Mass number 2
aF = -1.3965757721
Txx = -0.6337335765
Tyy = -0.3815182093
Tzz = 1.0152517858
Txy = -0.0000000000
Txz = -0.8430645179
Tyz = -0.0000000000
In MHz, Mass number 3
aF = -9.7041318629
Txx = -4.4035091508
Tyy = -2.6509861371
Tzz = 7.0544952879
Txy = -0.0000000000
Txz = -5.8580489609

```

```

Tyz = -0.0000000000
Z-matrix center 11:
Atomic charge is 1
XX = 0.0077463521 YY = 0.0046634335 ZZ = -0.0124097856
XY = 0.0000000000 XZ = -0.0103050790 YZ = 0.0000000000
In MHz, Mass number 1
aF = -9.0978518520
Txx = -4.1283933946
Tyy = -2.4853618518
Tzz = 6.6137552465
Txy = -0.0000000000
Txz = 5.4920586757
Tyz = -0.0000000000
In MHz, Mass number 2
aF = -1.3965757721
Txx = -0.6337335765
Tyy = -0.3815182093
Tzz = 1.0152517858
Txy = -0.0000000000
Txz = 0.8430645179
Tyz = -0.0000000000
In MHz, Mass number 3
aF = -9.7041318629
Txx = -4.4035091508
Tyy = -2.6509861371
Tzz = 7.0544952879
Txy = -0.0000000000
Txz = 5.8580489609
Tyz = -0.0000000000
Electric field gradient at atomic centers
Z-matrix center 3:
Atomic charge is 7
XX = 0.3695978459 YY = 0.4741163616 ZZ = -0.8437142075
XY = 0.0000000000 XZ = 0.0000000000 YZ = 0.0000000000
In kHz, Mass number 14
CHIxx = 1775.05992
CHIyy = 2277.02883
CHIzz = -4052.08875
CHIxy = 0.00000
CHIxz = 0.00000
CHIyz = 0.00000
Z-matrix center 4:
Atomic charge is 6
XX = -0.2196975116 YY = 0.3789602112 ZZ = -0.1592626996
XY = -0.0000000000 XZ = -0.0496374260 YZ = 0.0000000000
Z-matrix center 5:
Atomic charge is 6
XX = -0.2196975116 YY = 0.3789602112 ZZ = -0.1592626996
XY = 0.0000000000 XZ = 0.0496374260 YZ = 0.0000000000
Z-matrix center 6:
Atomic charge is 6

```

```

XX =  -0.1818444463  YY =   0.2476126047  ZZ =  -0.0657681583
XY =  -0.0000000000  XZ =   0.0102578295  YZ =   0.0000000000
Z-matrix center   7:
Atomic charge is                               6
XX =  -0.1818444463  YY =   0.2476126047  ZZ =  -0.0657681583
XY =   0.0000000000  XZ =  -0.0102578295  YZ =   0.0000000000
Z-matrix center   8:
Atomic charge is                               1
XX =   0.2456100490  YY =  -0.1576283392  ZZ =  -0.0879817097
XY =  -0.0000000000  XZ =   0.1497005963  YZ =   0.0000000000
In kHz, Mass number  2
CHIxx =    165.04975
CHIyy =   -105.92611
CHIzz =    -59.12363
CHIxy =    -0.00000
CHIxz =    100.59867
CHIyz =     0.00000
Z-matrix center   9:
Atomic charge is                               1
XX =   0.2456100490  YY =  -0.1576283392  ZZ =  -0.0879817097
XY =   0.0000000000  XZ =  -0.1497005963  YZ =   0.0000000000
In kHz, Mass number  2
CHIxx =    165.04975
CHIyy =   -105.92611
CHIzz =    -59.12363
CHIxy =     0.00000
CHIxz =   -100.59867
CHIyz =     0.00000
Z-matrix center  10:
Atomic charge is                               1
XX =   0.0309273997  YY =  -0.1636489090  ZZ =   0.1327215093
XY =  -0.0000000000  XZ =  -0.2250723583  YZ =   0.0000000000
In kHz, Mass number  2
CHIxx =     20.78319
CHIyy =   -109.97193
CHIzz =     89.18874
CHIxy =    -0.00000
CHIxz =   -151.24843
CHIyz =     0.00000
Z-matrix center  11:
Atomic charge is                               1
XX =   0.0309273997  YY =  -0.1636489090  ZZ =   0.1327215093
XY =   0.0000000000  XZ =   0.2250723583  YZ =   0.0000000000
In kHz, Mass number  2
CHIxx =     20.78319
CHIyy =   -109.97193
CHIzz =     89.18874
CHIxy =     0.00000
CHIxz =    151.24843
CHIyz =     0.00000

```

2-Pyrrolyl Normal Coordinates (fc/CCSD(T)/ANO0)

Normal Coordinates

A''			A''			A''			
325.83			499.35			610.56			
VIBRATION			VIBRATION			VIBRATION			
N1	-0.000	0.0000	0.5478	-0.0000	0.0000	0.1510	0.0000	0.0000	0.3218
C2	-0.000	0.0000	-0.2956	0.0000	0.0000	-0.5975	0.0000	0.0000	-0.0855
C3	-0.000	0.0000	0.0580	-0.0000	-0.0000	0.4451	-0.0000	-0.0000	-0.2226
C4	-0.000	0.0000	-0.0968	-0.0000	-0.0000	-0.1132	0.0000	-0.0000	0.5658
C5	-0.000	0.0000	-0.0594	-0.0000	0.0000	0.0787	0.0000	0.0000	-0.5408
H1	-0.000	-0.0000	-0.7389	0.0000	0.0000	0.4706	0.0000	-0.0000	0.2271
H3	-0.000	0.0000	0.1749	-0.0000	-0.0000	0.1636	-0.0000	0.0000	-0.2519
H4	-0.000	-0.0000	0.0195	0.0000	-0.0000	-0.3098	-0.0000	-0.0000	0.1155
H5	-0.000	-0.0000	-0.1389	-0.0000	0.0000	-0.2426	-0.0000	0.0000	-0.3140

A''			A''			A''			
695.67			750.04			841.99			
VIBRATION			VIBRATION			VIBRATION			
N1	-0.000	-0.0000	0.1722	0.0000	-0.0000	0.0437	0.0000	0.0000	0.0161
C2	-0.000	-0.0000	-0.1737	0.0000	0.0000	0.0120	-0.0000	0.0000	-0.0166
C3	0.000	0.0000	0.2127	-0.0000	-0.0000	-0.4011	-0.0000	-0.0000	0.1684
C4	-0.000	0.0000	-0.1722	-0.0000	0.0000	-0.0390	0.0000	-0.0000	-0.3494
C5	-0.000	-0.0000	-0.4276	0.0000	-0.0000	0.0297	0.0000	0.0000	0.1682
H1	-0.000	-0.0000	0.1562	0.0000	-0.0000	0.2271	-0.0000	-0.0000	0.0807
H3	0.000	0.0000	0.0429	0.0000	-0.0000	0.8048	-0.0000	-0.0000	-0.3427
H4	-0.000	0.0000	0.3775	0.0000	0.0000	0.3343	0.0000	-0.0000	0.7220
H5	0.000	-0.0000	0.7167	-0.0000	-0.0000	-0.1540	-0.0000	0.0000	-0.4188

A'			A'			A'			
845.99			878.92			1020.69			
VIBRATION			VIBRATION			VIBRATION			
N1	0.123	0.1472	-0.0000	0.5201	-0.2290	0.0000	0.2581	-0.0688	-0.0000
C2	-0.136	0.4049	0.0000	0.0808	0.4113	-0.0000	-0.0379	-0.0765	0.0000
C3	-0.495	-0.2248	-0.0000	-0.1783	0.1367	0.0000	0.0955	0.3560	0.0000
C4	0.242	-0.4610	0.0000	-0.2593	0.1198	0.0000	-0.0379	-0.3330	-0.0000
C5	0.290	0.1614	-0.0000	-0.2422	-0.3926	-0.0000	-0.1406	-0.0355	0.0000
H1	-0.036	-0.1557	-0.0000	0.1423	-0.0583	-0.0000	0.0847	0.0117	0.0000
H3	-0.154	-0.0364	0.0000	0.0272	-0.2097	-0.0000	-0.1380	0.6354	0.0000
H4	0.110	-0.1061	-0.0000	0.1416	0.1861	-0.0000	-0.2399	-0.2627	0.0000
H5	-0.040	0.1621	0.0000	-0.1826	-0.0142	0.0000	-0.2519	0.1791	-0.0000

A'			A'			A'			
1060.22			1103.77			1166.76			
VIBRATION			VIBRATION			VIBRATION			
N1	0.004	0.3478	0.0000	0.1372	-0.2827	0.0000	0.4433	-0.0380	0.0000
C2	-0.034	-0.3003	0.0000	-0.1194	-0.2827	-0.0000	-0.1074	-0.3123	0.0000
C3	-0.154	-0.0501	-0.0000	0.0332	-0.1195	-0.0000	-0.3947	-0.2206	0.0000
C4	0.218	-0.0445	0.0000	0.0886	0.2102	0.0000	-0.1430	0.3325	-0.0000
C5	-0.132	-0.2548	0.0000	-0.0819	0.4210	-0.0000	0.1540	0.1935	0.0000
H1	0.113	0.4187	-0.0000	-0.0365	-0.3040	-0.0000	0.2022	0.1919	-0.0000

H3	-0.112	0.1797	0.0000	0.0228	-0.0848	-0.0000	-0.1984	0.1413	-0.0000
H4	0.521	0.2962	-0.0000	0.1795	0.1731	-0.0000	-0.2433	-0.0252	0.0000
H5	-0.184	0.0508	0.0000	-0.4030	0.4792	0.0000	0.2818	-0.1422	0.0000

A'	A'			A'			A'		
1245.69	1373.79			1412.57			1412.57		
VIBRATION	VIBRATION			VIBRATION			VIBRATION		
N1	0.080	0.0557	0.0000	0.0848	-0.1429	-0.0000	0.1568	0.5315	-0.0000
C2	-0.400	-0.1158	-0.0000	0.0234	-0.2117	-0.0000	-0.0200	-0.3451	-0.0000
C3	0.014	0.2526	-0.0000	-0.0626	0.4501	0.0000	-0.0695	0.1955	0.0000
C4	0.190	-0.0244	0.0000	-0.2800	-0.4477	-0.0000	-0.2430	0.0135	-0.0000
C5	0.148	-0.1202	0.0000	0.0034	0.3981	-0.0000	0.2375	-0.2675	-0.0000
H1	0.152	0.3826	0.0000	0.0759	0.0801	-0.0000	-0.1956	-0.5369	-0.0000
H3	0.193	-0.5082	-0.0000	0.0952	-0.2096	0.0000	0.0250	-0.1043	0.0000
H4	-0.279	-0.2444	0.0000	0.3189	0.1392	0.0000	-0.0439	0.0289	0.0000
H5	-0.200	0.1894	0.0000	0.2837	-0.1282	0.0000	-0.0419	0.0240	-0.0000

A'	A'			A'			A'		
1460.84	1562.87			3259.05			3259.05		
VIBRATION	VIBRATION			VIBRATION			VIBRATION		
N1	0.298	0.1919	0.0000	0.0829	0.0658	0.0000	0.0004	-0.0012	0.0000
C2	-0.634	0.1088	-0.0000	0.2119	-0.1486	-0.0000	0.0023	0.0023	0.0000
C3	0.412	-0.2275	-0.0000	-0.2693	0.1894	-0.0000	0.0500	0.0088	-0.0000
C4	0.060	-0.0905	0.0000	0.5515	0.0436	-0.0000	-0.1510	0.2150	0.0000
C5	-0.283	0.0862	0.0000	-0.5562	0.0818	0.0000	-0.0631	-0.0816	0.0000
H1	0.012	-0.1478	0.0000	-0.0610	-0.2195	-0.0000	-0.0054	-0.0007	-0.0000
H3	0.100	0.0577	-0.0000	-0.0183	-0.1691	-0.0000	-0.1747	-0.0532	-0.0000
H4	0.117	0.0292	-0.0000	-0.0996	-0.1928	-0.0000	0.4911	-0.7132	-0.0000
H5	0.189	-0.2293	-0.0000	0.0839	-0.2374	0.0000	0.2455	0.2725	0.0000

A'	A'			A'			A'		
3286.90	3295.27			3695.35			3695.35		
VIBRATION	VIBRATION			VIBRATION			VIBRATION		
N1	0.001	0.0072	0.0000	0.0023	-0.0017	0.0000	0.2542	-0.0898	0.0000
C2	0.008	-0.0008	0.0000	0.0105	-0.0112	-0.0000	-0.0038	-0.0073	0.0000
C3	-0.111	-0.0274	0.0000	-0.2570	-0.0816	0.0000	-0.0036	0.0033	-0.0000
C4	0.068	-0.0649	0.0000	-0.0576	0.0861	-0.0000	-0.0053	-0.0007	0.0000
C5	-0.185	-0.1885	-0.0000	0.0710	0.0648	-0.0000	0.0031	0.0116	0.0000
H1	-0.014	-0.0004	-0.0000	0.0074	-0.0003	0.0000	-0.9078	0.3206	-0.0000
H3	0.359	0.1142	0.0000	0.8160	0.2633	-0.0000	0.0006	0.0004	-0.0000
H4	-0.156	0.2194	0.0000	0.1684	-0.2462	0.0000	0.0001	-0.0003	-0.0000
H5	0.564	0.6118	0.0000	-0.1959	-0.2108	-0.0000	-0.0070	-0.0098	-0.0000

2-Pyrrolyl Rotational Constants of Vibrationally Excited States (fc-CCSD(T)/ANO0)

 Be, B0 AND B-B0 SHIFTS FOR SINGLY EXCITED VIBRATIONAL STATES (CM-1)

VIBRATION	X AXIS	Y AXIS	Z AXIS
Be	0.33724422	0.29301694	0.15678940

B0	0.33450637	0.29086976	0.15558801
Be-B0	0.00273784	0.00214718	0.00120139
B'	0.33450651	0.29086990	0.15558780
Be-B'	0.00273771	0.00214704	0.00120160
B''	0.33450655	0.29086995	0.15558804
Be-B''	0.00273766	0.00214699	0.00120136
B^A	0.33450645	0.29086998	0.15558779
Be-B^A	0.00273776	0.00214697	0.00120162
B^S	0.33450653	0.29086984	0.15558786
Be-B^S	0.00273768	0.00214710	0.00120154
7	-0.00117010	-0.00022127	0.00003952
8	-0.00074573	-0.00032537	0.00011289
9	-0.00111857	-0.00046937	0.00007203
10	-0.00049431	-0.00046381	0.00009768
11	-0.00092513	-0.00042176	0.00006217
12	-0.00082277	-0.00110318	0.00003107
13	0.00056748	0.00045351	-0.00065802
14	0.00066760	0.00077356	0.00008627
15	0.00043099	0.00006428	-0.00063641
16	0.00041140	0.00014010	0.00017532
17	-0.00033626	0.00014522	-0.00000542
18	-0.00026621	-0.00020235	-0.00018419
19	0.00029850	-0.00000855	-0.00013085
20	-0.00036746	-0.00013836	-0.00045116
21	-0.00006373	-0.00046605	-0.00050911
22	-0.00039783	-0.00040674	0.00012091
23	-0.00000732	-0.00051725	-0.00008440
24	-0.00032294	-0.00025353	-0.00013744
25	-0.00031865	-0.00027533	-0.00014035
26	-0.00027450	-0.00030706	-0.00013960
27	-0.00022013	-0.00029106	-0.00012368

Be, B0 AND B-B0 SHIFTS FOR SINGLY EXCITED VIBRATIONAL STATES (MHz)

VIBRATION	X AXIS	Y AXIS	Z AXIS
Be	10110.32724078	8784.42698897	4700.42798130
B0	10028.24876190	8720.05613348	4664.41120843
Be-B0	82.07847888	64.37085549	36.01677286
B'	10028.25290102	8720.06027259	4664.40499976
Be-B'	82.07433977	64.36671637	36.02298153
B''	10028.25411292	8720.06172950	4664.41211671
Be-B''	82.07312787	64.36525947	36.01586459
B^A	10028.25122728	8720.06248972	4664.40445637
Be-B^A	82.07601350	64.36449925	36.02352492
B^S	10028.25357554	8720.05845201	4664.40661548
Be-B^S	82.07366525	64.36853696	36.02136582
7	-35.07869620	-6.63341408	1.18492614
8	-22.35627376	-9.75441766	3.38421109
9	-33.53401226	-14.07135598	2.15952299
10	-14.81914198	-13.90452449	2.92827729

11	-27.73482946	-12.64397044	1.86367675
12	-24.66617306	-33.07251269	0.93139863
13	17.01272262	13.59574140	-19.72697145
14	20.01416472	23.19062399	2.58620427
15	12.92069315	1.92720794	-19.07911688
16	12.33337378	4.20022236	5.25588422
17	-10.08068065	4.35362873	-0.16243430
18	-7.98070732	-6.06616149	-5.52200514
19	8.94868562	-0.25626582	-3.92268093
20	-11.01625759	-4.14805667	-13.52544179
21	-1.91053356	-13.97195203	-15.26267973
22	-11.92659921	-12.19367385	3.62469227
23	-0.21957106	-15.50679908	-2.53017121
24	-9.68151184	-7.60070963	-4.12041634
25	-9.55301114	-8.25403940	-4.20756190
26	-8.22939346	-9.20556016	-4.18515206
27	-6.59920509	-8.72572193	-3.70770766

2-Pyrrolyl Z-Matrix for CCSD(T)/cc-pwCVTZ Optimized Geometry and CFOUR Inputs

2-Pyrrolyl

X

X 1 RX

N 2 RX1* 1 AX

C 2 RX2* 3 AN* 1 DX

C 2 RX3* 3 AN1* 1 DX1

C 2 RX4* 4 AC1* 1 DX

C 2 RX5* 5 AC4* 1 DX1

H 3 RN* 4 ANC1* 5 DNC

H 5 RC4* 3 AC4N* 7 DC3

H 6 RC2* 4 ACC1* 7 DC31

H 7 RC3* 5 ACC2* 6 DC2

RX = 1.000000613972272
RX1 = 0.777437561268902
AX = 90.000000000000000
RX2 = 1.102135811041587
AN = 90.612790364636894
DX = 90.000000000000000
RX3 = 1.111418085509932
AN1 = 92.286997934649449
DX1 = -90.000000000000000
RX4 = 1.537560537728550
AC1 = 59.502329988798536
RX5 = 1.500433880347238
AC4 = 61.197953004619137
RN = 1.001394918994613
ANC1 = 125.995713305681249
DNC = -180.000000000000000
RC4 = 1.075524433198914

AC4N = 120.993268520813700
DC3 = -180.000000000000000
RC2 = 1.074352991065507
ACC1 = 127.652419940505766
DC31 = 180.000000000000000
RC3 = 1.076905058964320
ACC2 = 125.734050763996862
DC2 = 180.000000000000000

*CFOUR(CALC=CCSD(T),BASIS=PWCVTZ
SCF_CONV=9
CC_CONV=10
GEO_CONV=6
CC_PROGRAM=ECC
SCF_MAXCYC=500
MULTIPLICITY=2
MEMORY_SIZE=31, MEM_UNIT=GB)

2-Pyrrolyl Hyperfine Terms at CCSD(T)/cc-pwCVTZ

Dipole-dipole contributions to HFS at atomic centers

Z-matrix center 3:

Atomic charge is 7
XX = -0.0287370156 YY = -0.0624068562 ZZ = 0.0911438718
XY = -0.0781534791 XZ = 0.0000000000 YZ = 0.0000000000

In MHz, Mass number 14

aF = 16.0526569371
Txx = 1.1070638579
Tyy = 2.4041597019
Tzz = -3.5112235599
Txy = 3.0107820908
Txz = 0.0000000000
Tyz = 0.0000000000

In MHz, Mass number 15

aF = -22.5179416983
Txx = -1.5529391494
Tyy = -3.3724465809
Tzz = 4.9253857303
Txy = -4.2233890535
Txz = 0.0000000000
Tyz = 0.0000000000

Z-matrix center 4:

Atomic charge is 6
XX = 0.5015511030 YY = -0.9213982723 ZZ = 0.4198471693
XY = 0.1884788133 XZ = 0.0000000000 YZ = 0.0000000000

In MHz, Mass number 13

aF = 506.7592347848
Txx = -67.2269835672
Tyy = 123.5025227576
Tzz = -56.2755391904
Txy = -25.2633520483
Txz = 0.0000000000

```

Tyz = 0.0000000000
Z-matrix center 5:
Atomic charge is 6
XX = 0.0238640903 YY = -0.0493824603 ZZ = 0.0255183699
XY = 0.0046225508 XZ = 0.0000000000 YZ = 0.0000000000
In MHz, Mass number 13
aF = 43.0027360442
Txx = -3.1986985969
Tyy = 6.6191337725
Tzz = -3.4204351756
Txy = -0.6195981750
Txz = 0.0000000000
Tyz = 0.0000000000
Z-matrix center 6:
Atomic charge is 6
XX = -0.0439567768 YY = -0.0571231396 ZZ = 0.1010799164
XY = 0.0863048175 XZ = 0.0000000000 YZ = 0.0000000000
In MHz, Mass number 13
aF = 50.9288153362
Txx = 5.8918851823
Tyy = 7.6566801379
Tzz = -13.5485653203
Txy = -11.5681383456
Txz = 0.0000000000
Tyz = 0.0000000000
Z-matrix center 7:
Atomic charge is 6
XX = 0.0071883053 YY = -0.0660275450 ZZ = 0.0588392398
XY = -0.0136692489 XZ = 0.0000000000 YZ = 0.0000000000
In MHz, Mass number 13
aF = 39.3316162395
Txx = -0.9635071620
Tyy = 8.8502101966
Tzz = -7.8867030347
Txy = 1.8322008789
Txz = 0.0000000000
Tyz = 0.0000000000
Z-matrix center 8:
Atomic charge is 1
XX = -0.0237663500 YY = 0.0092947499 ZZ = 0.0144716001
XY = -0.0118338472 XZ = 0.0000000000 YZ = 0.0000000000
In MHz, Mass number 1
aF = 12.9168808422
Txx = 12.6661996634
Tyy = -4.9536069992
Tzz = -7.7125926641
Txy = 6.3068107354
Txz = 0.0000000000
Tyz = 0.0000000000
In MHz, Mass number 2
aF = 1.9828200248

```

```

Txx = 1.9443389343
Tyy = -0.7604089000
Tzz = -1.1839300342
Txy = 0.9681339305
Txz = 0.0000000000
Tyz = 0.0000000000
In MHz, Mass number 3
aF = 13.7776605939
Txx = 13.5102740443
Tyy = -5.2837149142
Tzz = -8.2265591301
Txy = 6.7270960229
Txz = 0.0000000000
Tyz = 0.0000000000
Z-matrix center 9:
Atomic charge is 1
XX = -0.0005871579 YY = -0.0056570034 ZZ = 0.0062441612
XY = -0.0057808449 XZ = 0.0000000000 YZ = 0.0000000000
In MHz, Mass number 1
aF = 6.0429698191
Txx = 0.3129238876
Tyy = 3.0148817116
Tzz = -3.3278055992
Txy = 3.0808826459
Txz = 0.0000000000
Tyz = 0.0000000000
In MHz, Mass number 2
aF = 0.9276327399
Txx = 0.0480357261
Tyy = 0.4628027388
Tzz = -0.5108384649
Txy = 0.4729342849
Txz = 0.0000000000
Tyz = 0.0000000000
In MHz, Mass number 3
aF = 6.4456727722
Txx = 0.3337771067
Tyy = 3.2157931516
Tzz = -3.5495702583
Txy = 3.2861923821
Txz = 0.0000000000
Tyz = 0.0000000000
Z-matrix center 10:
Atomic charge is 1
XX = -0.0212487255 YY = 0.0079768143 ZZ = 0.0132719112
XY = 0.0092796587 XZ = 0.0000000000 YZ = 0.0000000000
In MHz, Mass number 1
aF = 8.2393344043
Txx = 11.3244398025
Tyy = -4.2512174866
Tzz = -7.0732223158

```

```

Txy = -4.9455641946
Txz = 0.0000000000
Tyz = 0.0000000000
In MHz, Mass number 2
aF = 1.2647881054
Txx = 1.7383706086
Tyy = -0.6525878241
Tzz = -1.0857827845
Txy = -0.7591742804
Txz = 0.0000000000
Tyz = 0.0000000000
In MHz, Mass number 3
aF = 8.7884028914
Txx = 12.0790994296
Tyy = -4.5345182290
Tzz = -7.5445812006
Txy = -5.2751361377
Txz = 0.0000000000
Tyz = 0.0000000000
Z-matrix center 11:
Atomic charge is 1
XX = -0.0011792246 YY = -0.0049595432 ZZ = 0.0061387678
XY = 0.0029821876 XZ = 0.0000000000 YZ = 0.0000000000
In MHz, Mass number 1
aF = 18.9070817047
Txx = 0.6284639503
Tyy = 2.6431725683
Tzz = -3.2716365186
Txy = -1.5893472653
Txz = 0.0000000000
Tyz = 0.0000000000
In MHz, Mass number 2
aF = 2.9023524079
Txx = 0.0964730511
Tyy = 0.4057431172
Tzz = -0.5022161683
Txy = -0.2439745030
Txz = 0.0000000000
Tyz = 0.0000000000
In MHz, Mass number 3
aF = 20.1670478910
Txx = 0.6703447301
Tyy = 2.8193133452
Tzz = -3.4896580754
Txy = -1.6952612209
Txz = 0.0000000000
Tyz = 0.0000000000
Electric field gradient at atomic centers
Z-matrix center 3:
Atomic charge is 7
XX = 0.3057192487 YY = 0.3289245660 ZZ = -0.6346438146

```

XY = 0.0026757266 XZ = 0.0000000000 YZ = -0.0000000000
 In kHz, Mass number 14
 CHIxx = 1468.27150
 CHIyy = 1579.71920
 CHIzz = -3047.99070
 CHIxy = 12.85066
 CHIxz = 0.00000
 CHIyz = -0.00000
 Z-matrix center 4:
 Atomic charge is 6
 XX = -0.1164155825 YY = 0.1486976832 ZZ = -0.0322821007
 XY = 0.1182328798 XZ = 0.0000000000 YZ = -0.0000000000
 Z-matrix center 5:
 Atomic charge is 6
 XX = -0.2032650703 YY = 0.1861673437 ZZ = 0.0170977267
 XY = -0.1096700425 XZ = -0.0000000000 YZ = -0.0000000000
 Z-matrix center 6:
 Atomic charge is 6
 XX = -0.0885174174 YY = -0.0015954010 ZZ = 0.0901128185
 XY = -0.0196131970 XZ = 0.0000000000 YZ = 0.0000000000
 Z-matrix center 7:
 Atomic charge is 6
 XX = -0.1058008457 YY = -0.0370606982 ZZ = 0.1428615440
 XY = 0.0201429084 XZ = -0.0000000000 YZ = 0.0000000000
 Z-matrix center 8:
 Atomic charge is 1
 XX = 0.3509219509 YY = -0.1128463260 ZZ = -0.2380756249
 XY = -0.1881931336 XZ = 0.0000000000 YZ = -0.0000000000
 In kHz, Mass number 2
 CHIxx = 235.81925
 CHIyy = -75.83264
 CHIzz = -159.98662
 CHIxy = -126.46563
 CHIxz = 0.00000
 CHIyz = -0.00000
 Z-matrix center 9:
 Atomic charge is 1
 XX = 0.0692838294 YY = 0.1058238552 ZZ = -0.1751076847
 XY = 0.2275225941 XZ = -0.0000000000 YZ = -0.0000000000
 In kHz, Mass number 2
 CHIxx = 46.55867
 CHIyy = 71.11354
 CHIzz = -117.67222
 CHIxy = 152.89499
 CHIxz = -0.00000
 CHIyz = -0.00000
 Z-matrix center 10:
 Atomic charge is 1
 XX = 0.2772559371 YY = -0.1052305127 ZZ = -0.1720254244
 XY = 0.1359048876 XZ = 0.0000000000 YZ = 0.0000000000
 In kHz, Mass number 2

CHIxx = 186.31576
 CHIyy = -70.71482
 CHIzz = -115.60094
 CHIxy = 91.32797
 CHIxz = 0.00000
 CHIyz = 0.00000
 Z-matrix center 11:
 Atomic charge is 1
 XX = 0.0015697553 YY = 0.1676717224 ZZ = -0.1692414777
 XY = -0.2163412971 XZ = -0.0000000000 YZ = 0.0000000000
 In kHz, Mass number 2
 CHIxx = 1.05487
 CHIyy = 112.67526
 CHIzz = -113.73013
 CHIxy = -145.38117
 CHIxz = -0.00000
 CHIyz = 0.00000
 Electrostatic potential at atomic centers
 Z-matrix Potential
 center [$\langle 1/r \rangle$]
 3 -18.3230171555
 4 -14.7252507197
 5 -14.7416701559
 6 -14.7768560148
 7 -14.7764489965
 8 -0.9882727495
 9 -1.0833397718
 10 -1.1012614124
 11 -1.1041288641

3-Pyrrolyl Normal Coordinates (fc/CCSD(T)/ANO0)

Normal Coordinates

A''	A''		A''		A''		A''		A''	
402.98	543.39		632.88		664.95		747.26		828.25	
VIBRATION	VIBRATION		VIBRATION		VIBRATION		VIBRATION		VIBRATION	
N1	-0.000	0.0000	0.5099	-0.0000	0.0000	0.2291	-0.0000	0.0000	0.3883	
C2	0.000	0.0000	-0.0656	0.0000	0.0000	-0.3978	-0.0000	-0.0000	-0.3092	
C5	-0.000	-0.0000	-0.1634	-0.0000	-0.0000	0.0104	-0.0000	0.0000	-0.4975	
C3	0.000	-0.0000	-0.1083	0.0000	0.0000	0.6457	-0.0000	-0.0000	-0.0464	
C4	0.000	-0.0000	0.0373	0.0000	-0.0000	-0.4177	0.0000	0.0000	0.4197	
H1	-0.000	0.0000	-0.8133	0.0000	0.0000	0.0463	-0.0000	0.0000	0.4549	
H5	-0.000	-0.0000	-0.1243	-0.0000	0.0000	0.1716	-0.0000	-0.0000	-0.3325	
H2	0.000	0.0000	-0.0544	0.0000	-0.0000	-0.3834	-0.0000	-0.0000	-0.0986	
H4	-0.000	0.0000	0.1265	-0.0000	0.0000	-0.1387	0.0000	0.0000	0.0242	
N1	-0.000	-0.0000	0.0145	0.0000	-0.0000	0.0766	-0.0000	0.0000	0.0025	

C2	-0.000	0.0000	0.3598	0.0000	0.0000	-0.3366	-0.0000	-0.0000	0.0527
C5	-0.000	0.0000	-0.3887	0.0000	-0.0000	-0.1471	-0.0000	0.0000	0.2654
C3	-0.000	-0.0000	-0.1257	0.0000	0.0000	0.0972	-0.0000	-0.0000	0.0015
C4	0.000	-0.0000	-0.0383	-0.0000	-0.0000	-0.1495	0.0000	0.0000	-0.3320
H1	0.000	0.0000	0.0929	0.0000	0.0000	0.0608	0.0000	-0.0000	0.1310
H5	-0.000	0.0000	0.5293	0.0000	0.0000	0.3298	0.0000	0.0000	-0.5866
H2	0.000	-0.0000	-0.4596	0.0000	-0.0000	0.7020	0.0000	0.0000	-0.1652
H4	0.000	0.0000	0.4494	0.0000	-0.0000	0.4713	0.0000	-0.0000	0.6542

A'			A'			A'			
852.80			877.87			1032.52			
VIBRATION			VIBRATION			VIBRATION			
N1	0.171	-0.0547	0.0000	0.3717	0.4732	0.0000	0.2195	0.1897	-0.0000
C2	0.332	0.0033	0.0000	-0.3656	0.2207	0.0000	-0.0888	-0.2342	0.0000
C5	0.064	-0.3688	-0.0000	0.2710	-0.3288	-0.0000	-0.2680	0.2043	-0.0000
C3	-0.032	0.5763	0.0000	-0.1821	-0.1955	0.0000	-0.0321	0.2293	0.0000
C4	-0.526	-0.0973	0.0000	-0.0493	-0.2118	-0.0000	0.1778	-0.1031	0.0000
H1	-0.106	0.1140	0.0000	0.0939	0.1338	0.0000	0.1448	-0.0121	-0.0000
H5	0.119	-0.0574	-0.0000	-0.1274	-0.1994	-0.0000	-0.2467	-0.0165	-0.0000
H2	0.048	-0.1598	-0.0000	-0.1581	-0.1005	0.0000	-0.1518	-0.4868	0.0000
H4	-0.141	-0.0843	0.0000	-0.0691	0.1808	0.0000	0.1642	-0.5239	-0.0000

A'			A'			A'			
1065.79			1149.36			1168.24			
VIBRATION			VIBRATION			VIBRATION			
N1	0.077	-0.1905	0.0000	0.2989	-0.1983	0.0000	0.2445	0.3007	0.0000
C2	-0.300	0.3716	-0.0000	0.0333	0.1362	-0.0000	0.2064	-0.1289	-0.0000
C3	-0.099	0.0795	0.0000	0.0521	0.0796	-0.0000	0.1591	-0.4974	-0.0000
C4	-0.049	-0.2544	0.0000	-0.1718	0.0252	0.0000	-0.4993	-0.0222	0.0000
C5	0.186	0.0721	-0.0000	-0.2559	0.0156	0.0000	-0.2036	0.2651	-0.0000
H1	0.165	-0.1764	0.0000	0.4901	-0.3940	0.0000	0.0840	0.0791	0.0000
H2	-0.053	0.2516	-0.0000	0.0951	0.3173	-0.0000	0.0905	0.0195	-0.0000
H4	0.078	-0.4978	-0.0000	-0.0769	0.1037	0.0000	-0.1375	-0.1261	-0.0000
H5	0.430	0.2050	-0.0000	-0.4415	-0.1732	0.0000	0.2161	0.2301	-0.0000

A'			A'			A'			
1232.04			1386.18			1440.97			
VIBRATION			VIBRATION			VIBRATION			
N1	0.046	0.1586	0.0000	0.0524	-0.2234	0.0000	0.4272	-0.3695	-0.0000
C2	0.134	-0.2939	0.0000	-0.2045	0.2033	-0.0000	0.1625	0.3779	0.0000
C3	-0.399	-0.0315	0.0000	0.3668	-0.2108	0.0000	-0.3399	-0.1434	0.0000
C4	0.012	0.1168	0.0000	-0.2122	0.5847	0.0000	0.1456	-0.0710	-0.0000
C5	0.219	-0.0107	-0.0000	0.1172	-0.1776	-0.0000	-0.3117	0.1294	-0.0000
H1	-0.150	0.1850	0.0000	-0.1789	0.0866	-0.0000	-0.3576	0.3008	-0.0000
H2	0.233	0.5321	-0.0000	-0.1223	-0.1148	0.0000	0.0019	-0.0583	0.0000
H4	0.102	-0.3935	-0.0000	0.0530	-0.3489	-0.0000	0.0228	0.0682	0.0000
H5	-0.246	-0.1579	-0.0000	-0.1795	-0.1691	-0.0000	-0.0742	0.0559	-0.0000

A'			A'			A'			
1489.36			1537.23			3269.92			
VIBRATION			VIBRATION			VIBRATION			

N1	0.279	0.0945	-0.0000	0.1819	-0.1634	-0.0000	0.0041	-0.0033	-0.0000
C2	-0.272	-0.2534	-0.0000	-0.3975	-0.2588	0.0000	-0.0078	-0.0031	0.0000
C3	0.119	0.1448	-0.0000	0.3911	0.2170	0.0000	-0.0005	0.0033	0.0000
C4	0.209	0.2445	-0.0000	-0.1392	-0.3142	0.0000	0.1417	0.0222	0.0000
C5	-0.485	-0.4022	0.0000	0.1312	0.3561	-0.0000	-0.1120	0.2230	-0.0000
H1	-0.009	0.1034	0.0000	-0.2844	0.2349	0.0000	0.0044	0.0142	0.0000
H2	0.020	0.2858	-0.0000	-0.0502	0.2215	0.0000	0.0258	-0.0074	-0.0000
H4	0.080	0.0617	0.0000	-0.1062	0.1368	-0.0000	-0.4818	-0.1054	-0.0000
H5	0.349	0.1154	-0.0000	-0.1877	0.0158	-0.0000	0.3625	-0.7358	-0.0000

A'	A'			A'			A'		
3291.82	3299.65			3676.28					
VIBRATION	VIBRATION			VIBRATION			VIBRATION		
N1	0.007	-0.0035	0.0000	0.0039	-0.0046	0.0000	0.1739	0.2065	0.0000
C2	-0.034	0.0090	-0.0000	-0.2855	0.0798	0.0000	0.0091	-0.0086	-0.0000
C3	0.010	-0.0060	0.0000	0.0133	0.0114	0.0000	-0.0051	-0.0012	0.0000
C4	-0.250	-0.0678	-0.0000	0.0307	0.0057	-0.0000	-0.0011	-0.0055	0.0000
C5	-0.058	0.1497	0.0000	0.0162	-0.0264	0.0000	-0.0106	0.0078	-0.0000
H1	0.002	0.0085	-0.0000	-0.0159	-0.0110	-0.0000	-0.6177	-0.7381	-0.0000
H2	0.119	-0.0357	0.0000	0.9058	-0.2708	-0.0000	-0.0123	0.0057	0.0000
H4	0.791	0.1799	-0.0000	-0.0899	-0.0205	0.0000	0.0004	0.0002	-0.0000
H5	0.208	-0.4324	0.0000	-0.0369	0.0762	0.0000	0.0077	-0.0114	-0.0000

3-Pyrrolyl Rotational Constants of Vibrationally Excited States (fc-CCSD(T)/ANO0)

 Be, B0 AND B-B0 SHIFTS FOR SINGLY EXCITED VIBRATIONAL STATES (CM-1)

VIBRATION	X AXIS	Y AXIS	Z AXIS
Be	0.33770117	0.29484792	0.15741148
B0	0.33532483	0.29246470	0.15619482
Be-B0	0.00237635	0.00238322	0.00121666
B'	0.33532496	0.29246483	0.15619462
Be-B'	0.00237622	0.00238309	0.00121686
B''	0.33532500	0.29246488	0.15619484
Be-B''	0.00237617	0.00238304	0.00121664
B^A	0.33532490	0.29246491	0.15619460
Be-B^A	0.00237628	0.00238301	0.00121688
B^S	0.33532497	0.29246479	0.15619467
Be-B^S	0.00237620	0.00238313	0.00121681
7	-0.00063762	-0.00065441	-0.00001401
8	-0.00091908	-0.00033053	0.00009732
9	-0.00082556	-0.00081118	0.00006082
10	-0.00067135	-0.00024991	0.00011150
11	-0.00072458	-0.00026800	0.00008326
12	-0.00141890	-0.00051701	0.00005219
13	0.00059728	0.00038890	-0.00077330
14	0.00115047	0.00041294	0.00022057
15	0.00088960	-0.00017544	-0.00079682
16	0.00016395	0.00009284	0.00041491

17	0.00004087	0.00005457	-0.00005508
18	-0.00036664	-0.00033702	-0.00027918
19	0.00026757	0.00005254	-0.00007980
20	-0.00019597	-0.00036818	-0.00053180
21	-0.00037765	-0.00047666	-0.00038360
22	-0.00033506	-0.00023206	-0.00003648
23	-0.00022831	-0.00022904	0.00001887
24	-0.00034510	-0.00024343	-0.00013862
25	-0.00029650	-0.00028771	-0.00013843
26	-0.00021860	-0.00034104	-0.00013748
27	-0.00030153	-0.00024661	-0.00012815

Be, B0 AND B-B0 SHIFTS FOR SINGLY EXCITED VIBRATIONAL STATES (MHz)

VIBRATION	X AXIS	Y AXIS	Z AXIS
Be	10124.02648507	8839.31833771	4719.07745164
B0	10052.78538896	8767.87118124	4682.60291244
Be-B0	71.24109611	71.44715647	36.47453920
B'	10052.78932194	8767.87511422	4682.59701297
Be-B'	71.23716313	71.44322348	36.48043867
B''	10052.79058795	8767.87649632	4682.60355095
Be-B''	71.23589712	71.44184139	36.47390069
B^A	10052.78753031	8767.87746449	4682.59645433
Be-B^A	71.23895476	71.44087322	36.48099731
B^S	10052.78971229	8767.87375756	4682.59841568
Be-B^S	71.23677278	71.44458015	36.47903596
7	-19.11532848	-19.61879898	-0.42002312
8	-27.55329428	-9.90902640	2.91746123
9	-24.74972386	-24.31852845	1.82323500
10	-20.12642602	-7.49218535	3.34273238
11	-21.72238597	-8.03439261	2.49598727
12	-42.53764122	-15.49966463	1.56468743
13	17.90608471	11.65903009	-23.18308615
14	34.49021212	12.37973187	6.61255032
15	26.66953554	-5.25967329	-23.88813602
16	4.91516714	2.78324345	12.43872405
17	1.22531078	1.63590514	-1.65126149
18	-10.99153463	-10.10345560	-8.36954104
19	8.02166869	1.57503825	-2.39228118
20	-5.87509759	-11.03786105	-15.94302662
21	-11.32167828	-14.28985376	-11.50009873
22	-10.04484338	-6.95689286	-1.09371902
23	-6.84450941	-6.86634221	0.56564249
24	-10.34582815	-7.29787140	-4.15566923
25	-8.88875171	-8.62542217	-4.14994249
26	-6.55360408	-10.22417285	-4.12144012
27	-9.03952416	-7.39312012	-3.84187339

3-Pyrrolyl Z-Matrix for CCSD(T)/cc-pwCVTZ Optimized Geometry and CFOUR Inputs

3-Pyrrolyl

X

X 1 RX

N 2 RX1* 1 AX

C 2 RX2* 3 AN* 1 DX

C 2 RX3* 3 AN1* 1 DX1

C 2 RX4* 4 AC1* 1 DX

C 2 RX5* 5 AC4* 1 DX1

H 3 RN* 4 ANC1* 5 DNC

H 5 RC4* 3 AC4N* 7 DC3

H 4 RC1* 3 AC1N* 6 DC21

H 7 RC3* 5 ACC2* 6 DC2

RX = 1.000000613972272
RX1 = 0.768262996409491
AX = 90.000000000000000
RX2 = 1.138503957487006
AN = 90.482597821676521
DX = 90.000000000000000
RX3 = 1.113342034113988
AN1 = 91.420391627112778
DX1 = -90.000000000000000
RX4 = 1.475977636352398
AC1 = 61.301618921921346
RX5 = 1.524840969618970
AC4 = 60.675770145784817
RN = 1.002523759193760
ANC1 = 125.022401059476437
DNC = -180.000000000000000
RC4 = 1.076181095459977
AC4N = 121.050445531093757
DC3 = -180.000000000000000
RC1 = 1.074017662974611
AC1N = 121.971372379077522
DC21 = -180.000000000000000
RC3 = 1.074967903505180
ACC2 = 126.407603189002970
DC2 = 180.000000000000000

*ACES2(CALC=CCSD(T),BASIS=PWCVTZ

SCF_CONV=9

CC_CONV=10

GEO_CONV=6

CC_PROGRAM=ECC

SCF_MAXCYC=500

SCF_DAMPING=500

MULTIPLICITY=2

MEMORY_SIZE=31, MEM_UNIT=GB)

3-Pyrrolyl Hyperfine Terms at CCSD(T)/cc-pwCVTZ

Dipole-dipole contributions to HFS at atomic centers

Z-matrix center 3:

Atomic charge is

7

XX = 0.0154434825 YY = -0.0768817576 ZZ = 0.0614382751

XY = 0.0034623644 XZ = 0.0000000000 YZ = 0.0000000000

In MHz, Mass number 14

aF = 23.5987790937

Txx = -0.5949442180

Tyy = 2.9617903353

Tzz = -2.3668461173

Txy = -0.1333840147

Txz = -0.0000000000

Tyz = -0.0000000000

In MHz, Mass number 15

aF = -33.1033008347

Txx = 0.8345608623

Tyy = -4.1546656330

Tzz = 3.3201047706

Txy = 0.1871050679

Txz = 0.0000000000

Tyz = 0.0000000000

Z-matrix center 4:

Atomic charge is

6

XX = -0.0735961560 YY = 0.0040216225 ZZ = 0.0695745334

XY = -0.0519268643 XZ = 0.0000000000 YZ = 0.0000000000

In MHz, Mass number 13

aF = 69.2989428161

Txx = 9.8646928260

Tyy = -0.5390508555

Tzz = -9.3256419705

Txy = 6.9601809867

Txz = -0.0000000000

Tyz = -0.0000000000

Z-matrix center 5:

Atomic charge is

6

XX = -0.0068967166 YY = -0.0558088455 ZZ = 0.0627055621

XY = -0.0179557184 XZ = 0.0000000000 YZ = 0.0000000000

In MHz, Mass number 13

aF = 39.6457226898

Txx = 0.9244231521

Tyy = 7.4805145805

Tzz = -8.4049377326

Txy = 2.4067513295

Txz = -0.0000000000

Tyz = -0.0000000000

Z-matrix center 6:

Atomic charge is

6

XX = 0.5155171046 YY = -0.9614089087 ZZ = 0.4458918041

XY = -0.0919894375 XZ = 0.0000000000 YZ = 0.0000000000

In MHz, Mass number 13

```

aF = 460.0493489560
Txx = -69.0989606279
Tyy = 128.8654745711
Tzz = -59.7665139433
Txy = 12.3300943136
Txz = -0.0000000000
Tyz = -0.0000000000
Z-matrix center 7:
Atomic charge is 6
XX = -0.0069806152 YY = -0.0343173105 ZZ = 0.0412979258
XY = 0.0629879704 XZ = 0.0000000000 YZ = 0.0000000000
In MHz, Mass number 13
aF = 37.9193394450
Txx = 0.9356687749
Tyy = 4.5998289251
Tzz = -5.5354977000
Txy = -8.4427912260
Txz = -0.0000000000
Tyz = -0.0000000000
Z-matrix center 8:
Atomic charge is 1
XX = -0.0009388001 YY = -0.0054064623 ZZ = 0.0063452624
XY = -0.0044158442 XZ = 0.0000000000 YZ = 0.0000000000
In MHz, Mass number 1
aF = 14.9300196942
Txx = 0.5003304847
Tyy = 2.8813566842
Tzz = -3.3816871689
Txy = 2.3534099455
Txz = -0.0000000000
Tyz = -0.0000000000
In MHz, Mass number 2
aF = 2.2918491223
Txx = 0.0768037823
Tyy = 0.4423058323
Tzz = -0.5191096146
Txy = 0.3612627865
Txz = -0.0000000000
Tyz = -0.0000000000
In MHz, Mass number 3
aF = 15.9249548338
Txx = 0.5336724622
Tyy = 3.0733700287
Tzz = -3.6070424909
Txy = 2.5102409679
Txz = -0.0000000000
Tyz = -0.0000000000
Z-matrix center 9:
Atomic charge is 1
XX = -0.0005265306 YY = -0.0053299407 ZZ = 0.0058564713
XY = 0.0015119972 XZ = 0.0000000000 YZ = 0.0000000000

```

```

In MHz, Mass number 1
aF = 18.1472905772
Txx = 0.2806127674
Tyy = 2.8405747314
Tzz = -3.1211874988
Txy = -0.8058140371
Txz = -0.0000000000
Tyz = -0.0000000000
In MHz, Mass number 2
aF = 2.7857198338
Txx = 0.0430757720
Tyy = 0.4360455537
Tzz = -0.4791213258
Txy = -0.1236973716
Txz = -0.0000000000
Tyz = -0.0000000000
In MHz, Mass number 3
aF = 19.3566243526
Txx = 0.2993127764
Tyy = 3.0298703703
Tzz = -3.3291831468
Txy = -0.8595134104
Txz = -0.0000000000
Tyz = -0.0000000000
Z-matrix center 10:
Atomic charge is 1
XX = -0.0181765232 YY = 0.0072560735 ZZ = 0.0109204497
XY = -0.0084045686 XZ = 0.0000000000 YZ = 0.0000000000
In MHz, Mass number 1
aF = 6.9576651463
Txx = 9.6871195006
Tyy = -3.8671010161
Tzz = -5.8200184845
Txy = 4.4791877317
Txz = -0.0000000000
Tyz = -0.0000000000
In MHz, Mass number 2
aF = 1.0680440539
Txx = 1.4870319517
Tyy = -0.5936236020
Tzz = -0.8934083497
Txy = 0.6875826477
Txz = -0.0000000000
Tyz = -0.0000000000
In MHz, Mass number 3
aF = 7.4213233119
Txx = 10.3326682534
Tyy = -4.1248042722
Tzz = -6.2078639812
Txy = 4.7776803903
Txz = -0.0000000000

```

Tyz = -0.0000000000
 Z-matrix center 11:
 Atomic charge is 1
 XX = -0.0197611556 YY = 0.0083167641 ZZ = 0.0114443915
 XY = 0.0105045031 XZ = 0.0000000000 YZ = 0.0000000000
 In MHz, Mass number 1
 aF = 10.8214869312
 Txx = 10.5316442311
 Tyy = -4.4323926331
 Tzz = -6.0992515981
 Txy = -5.5983410758
 Txz = -0.0000000000
 Tyz = -0.0000000000
 In MHz, Mass number 2
 aF = 1.6611642739
 Txx = 1.6166716509
 Tyy = -0.6803993145
 Tzz = -0.9362723364
 Txy = -0.8593795148
 Txz = -0.0000000000
 Tyz = -0.0000000000
 In MHz, Mass number 3
 aF = 11.5426298253
 Txx = 11.2334720343
 Tyy = -4.7277668706
 Tzz = -6.5057051637
 Txy = -5.9714140103
 Txz = -0.0000000000
 Tyz = -0.0000000000
 Electric field gradient at atomic centers
 Z-matrix center 3:
 Atomic charge is 7
 XX = 0.2803354067 YY = 0.3245806394 ZZ = -0.6049160461
 XY = 0.0209578957 XZ = 0.0000000000 YZ = 0.0000000000
 In kHz, Mass number 14
 CHIxx = 1346.36105
 CHIyy = 1558.85671
 CHIzz = -2905.21776
 CHIxxy = 100.65405
 CHIxzy = 0.00000
 CHIyyz = 0.00000
 Z-matrix center 4:
 Atomic charge is 6
 XX = -0.1892414997 YY = 0.1845351847 ZZ = 0.0047063150
 XY = -0.0864108016 XZ = -0.0000000000 YZ = 0.0000000000
 Z-matrix center 5:
 Atomic charge is 6
 XX = 0.1496424693 YY = -0.2015747071 ZZ = 0.0519322379
 XY = -0.0402114979 XZ = 0.0000000000 YZ = -0.0000000000
 Z-matrix center 6:
 Atomic charge is 6


```

XX =  -0.2227960588  YY =   0.1753214510  ZZ =   0.0474746079
XY =  -0.0029303257  XZ =   0.0000000000  YZ =   0.0000000000
Z-matrix center   7:
Atomic charge is                               6
XX =  -0.0842065425  YY =  -0.0360295293  ZZ =   0.1202360718
XY =  -0.0259477734  XZ =  -0.0000000000  YZ =  -0.0000000000
Z-matrix center   8:
Atomic charge is                               1
XX =   0.0653066664  YY =   0.1719881087  ZZ =  -0.2372947750
XY =   0.2918679022  XZ =   0.0000000000  YZ =   0.0000000000
In kHz, Mass number  2
CHIxx =    43.88602
CHIyy =   115.57586
CHIzz =  -159.46189
CHIxy =   196.13498
CHIxz =    0.00000
CHIyz =    0.00000
Z-matrix center   9:
Atomic charge is                               1
XX =  -0.0520567148  YY =   0.2255141909  ZZ =  -0.1734574761
XY =  -0.1803754502  XZ =   0.0000000000  YZ =  -0.0000000000
In kHz, Mass number  2
CHIxx =   -34.98207
CHIyy =   151.54535
CHIzz =  -116.56328
CHIxy =  -121.21215
CHIxz =    0.00000
CHIyz =   -0.00000
Z-matrix center  10:
Atomic charge is                               1
XX =   0.2805999065  YY =  -0.1046217865  ZZ =  -0.1759781200
XY =  -0.1259315586  XZ =  -0.0000000000  YZ =   0.0000000000
In kHz, Mass number  2
CHIxx =   188.56290
CHIyy =   -70.30575
CHIzz =  -118.25715
CHIxy =   -84.62590
CHIxz =   -0.00000
CHIyz =    0.00000
Z-matrix center  11:
Atomic charge is                               1
XX =   0.2967090764  YY =  -0.1258772517  ZZ =  -0.1708318248
XY =   0.1005015549  XZ =  -0.0000000000  YZ =  -0.0000000000
In kHz, Mass number  2
CHIxx =   199.38825
CHIyy =   -84.58941
CHIzz =  -114.79884
CHIxy =    67.53696
CHIxz =   -0.00000
CHIyz =   -0.00000
Electrostatic potential at atomic centers

```

Z-matrix center	Potential [<1/r>]
3	-18.3255791254
4	-14.7414977453
5	-14.7386767150
6	-14.7639497813
7	-14.7766381854
8	-0.9935302072
9	-1.0828821062
10	-1.0816627204
11	-1.1012781705

Appendix C: Reaction Discovery Part I

Table 7.13: Parameters of trajectories of 1 pyridine, 1 CN, and 50 He atoms that resulted in two products with mechanism description.

config	temp (Å)	r1 (K)	r2 (Å)	k1 (kcal mol ⁻¹ Å ⁻²)	k2 (kcal mol ⁻¹ Å ⁻²)	t1 (0.5 fs)	t2 (0.5 fs)	Products	Mechanism
0	1500	10.0	3.0	1.0	0.5	2000	500	HCCHCHCHNC + HCN	CN to N, ring breaks, HCN leaves
0	2500	8.0	5.0	1.0	0.5	2000	500	HCN + para-pyridyl	abstraction
0	2500	8.0	3.0	1.0	0.5	2000	500	HCN + para-pyridyl	abstraction
0	2500	10.0	5.0	1.0	0.5	2000	500	H + NCCHCHCHCHCN	CN to ortho, ring breaks, H leaves
1	1500	12.0	3.0	1.0	0.5	2000	1000	HNC + HCCCHCHCHCN	abstraction
1	1500	12.0	3.0	1.0	0.6	2000	1000	HCN + CNCHCHCCH ₂	abstraction
1	2000	12.0	3.0	1.0	0.75	2000	200	H ₂ CCNCHCCH + HCN	meta-isocyanopyridyl forms, concerted ring breakage and HCN leaving
1	2500	8.0	3.0	1.0	0.5	2000	500	HCN + meta	abstraction
1	2500	10.0	3.0	1.0	0.5	2000	500	N ₂ + HCCCHCHCHCH	CN to meta, cyano C bridges to meta and pyr N, cyano N binds to pyr N, ring breaks
1	2500	10.0	5.0	1.0	0.5	2000	500	HCCH + HCNCHCHCN	CN to meta, bond to ortho breaks, HCCH leaves
2	1500	10.0	3.0	1.0	0.5	2000	500	HCN + o-pyridyl	abstraction from meta, H migration to form o-pyridyl
2	1500	12.0	3.0	1.0	0.5	2000	1000	HNC + HCCHCHCHCN	abstraction to form o-pyridyl, then ring breaks
2	1500	12.0	3.0	1.0	0.6	2000	500	HCN + HCCCHNCCH ₂	abstraction to form m-pyridyl, then ring breaks
3	1500	12.0	3.0	1.0	0.75	2000	500	HCCCHCHCHCNH + HCN	CN bonds to meta, ring breaks, HCN leaves
3	1500	12.0	3.0	1.0	0.75	2000	200	pyrrolyl + HCCN	CN bonds to ortho, removes CH from ring
3	1500	12.0	3.0	1.0	0.75	2000	500	pyrrolyl + HCCN	CN bonds to ortho, removes CH from ring
3	2000	12.0	3.0	1.0	0.75	2000	200	HCN + HCCHCHCHCN	abstraction from ortho, ring breaks
3	2500	12.0	3.0	1.0	0.5	2000	500	HCNCNCC + CHCH ₂	CN inserts between N and ortho, ring opens then breaks apart
3	2500	10.0	3.0	1.0	0.5	2000	500	H + o-cyanopyridine	first forms o-isocyanopyridine

Table 7.14: Parameters of trajectories of 1 pyrrole, 1 CN, and 50 He atoms where two products were formed with mechanism description.

config	temp (Å)	r1 (K)	r2 (Å)	k1 (kcal mol ⁻¹ Å ⁻²)	k2 (kcal mol ⁻¹ Å ⁻²)	t1 (0.5 fs)	t2 (0.5 fs)	Products	Mechanism
0	12.0	2500	3.0	1.0	0.5	1500	1000	HCN + HCHCH ₂ CCN	CN starts on 3, migrates to 2, N-2 toward CN breaks, N-H migrates to 2-C toward CN, 3-2 opposite from CN breaks
0	12.0	2500	3.0	1.0	0.5	1500	500	HCN + 1-pyrrolyl	abstraction
0	12.0	1500	3.0	1.0	0.5	1500	1000	HCN + c-CHCHC(CHNH)	3-CN leaves w/ 3-H, N-2 breaks, 2- and opposite 3- bond
0	12.0	1500	3.0	1.0	0.5	1500	500	HCN + CCHNHCHCH	H on 3-C w/CN migrates to CN carbon, HCN leaves, 3-C bond breaks
1	12.0	1500	3.0	1.0	0.5	1500	1000	HCCH + NCCHCHNH	breaks 3-3 bond, N-2 bonds breaks away from CN
2	12.0	1500	3.0	1.0	0.5	1500	1000	HCN + 2-pyrrolyl	HCN leaves from 2-H-cyanopyrrole
3	12.0	1500	3.0	1.0	0.5	1500	500	HCCH + H ₂ CNCHCN	2-, 3- bond breaks toward CN, opposite 2-,3- breaks
3	12.0	1500	3.0	1.0	0.75	1500	200	HCCHCN + H ₂ CCNH	CN on 2-, ring breaks opposite of N, pyrrolyl N-C bond breaks toward CN
3	12.0	1500	3.0	1.0	0.75	1500	500	HCCH + NCCHCHNH	CN on 2-, ring breaks opposite of N, pyrrole N-C bond breaks
3	12.0	2500	3.0	1.0	0.5	1500	1000	H + 3-cyanopyrrole	H leaves
3	12.0	3500	3.0	1.0	0.5	1500	1000	H, c-CHC(H)(HCNC)C(CN)	N to 2- breaks, 3 membered ring forms between 2-,3-,3-
4	12.0	3500	3.0	1.0	0.5	1500	1000	H + 2-cyanopyrrole	H leaves
5	12.0	1500	3.0	1.0	0.5	1500	500	HCCN + 1-hydroazete	2-NC to 3-CN, 3-CH extraced from ring
5	12.0	1500	3.0	1.0	0.75	1500	200	HNC + C ₄ H ₄ N	CN leaves from 2, abstracts H from 3-, N to 2- bond breaks
5	12.0	1500	3.0	1.0	0.75	1500	500	2-pyrrolyl + HNC	ring breaks then reforms, HNC leaves
5	12.0	2500	3.0	1.0	0.5	1500	1000	HCN + 1-pyrrolyl, abstraction	abstraction
5	12.0	2500	3.0	1.0	0.5	1500	500	HCN + 1-pyrrolyl, abstraction	abstraction
5	12.0	3500	3.0	1.0	0.5	1500	1000	HCN + 1-pyrrolyl, abstraction	abstraction

Bibliography

- [1] Seiki, K.; Sumiyoshi, Y.; Oshima, Y.; Endo, Y.; Tang, J. Detection of the H₂CCCN radical by FTMW spectroscopy and observation of the tunneling inversion motion. *Bunshi Kozo Sogo Toronkai Koen Yoshishu* **2000**, *2000*, 11.
- [2] Spencer, M. The stereochemistry of deoxyribonucleic acid. II. Hydrogen-bonded pairs of bases. *Acta Crystallographica* **1959**, *12*, 66–71.
- [3] Wu, F.; Chamchoumis, C. M.; Thummel, R. P. Bidentate Ligands That Contain Pyrrole in Place of Pyridine. *Inorganic Chemistry* **2000**, *39*, 584–590.
- [4] Wiebeler, C.; Rao, A. G.; Gärtner, W.; Schapiro, I. The Effective Conjugation Length Is Responsible for the Red/Green Spectral Tuning in the Cyanobacteriochrome Slr1393g3. *Angewandte Chemie - International Edition* **2019**, *58*, 1934–1938.
- [5] Callahan, M. P.; Smith, K. E.; Cleaves, H. J.; Ruzicka, J.; Stern, J. C.; Glavin, D. P.; House, C. H.; Dworkin, J. P. Carbonaceous meteorites contain a wide range of extraterrestrial nucleobases. *Proceedings of the National Academy of Sciences* **2011**, *108*, 13995–13998.
- [6] Martins, Z.; Botta, O.; Fogel, M. L.; Sephton, M. A.; Glavin, D. P.; Watson, J. S.; Dworkin, J. P.; Schwartz, A. W.; Ehrenfreund, P. Extraterrestrial nucleobases in the Murchison meteorite. *Earth and Planetary Science Letters* **2008**, *270*, 130–136.
- [7] Martins, Z. The Nitrogen Heterocycle Content of Meteorites and Their Significance for the Origin of Life. *Life* **2018**, *8*, 28.
- [8] Chyba, C.; Sagan, C. *Endogenous production, exogenous delivery and impact-shock synthesis of organic molecules: an inventory for the origins of life*; 1992.
- [9] Tielens, A. Interstellar Polycyclic Aromatic Hydrocarbon Molecules. *Annual Review of Astronomy and Astrophysics* **2008**, *46*, 289–337.

- [10] Hudgins, D. M.; Bauschlicher, Jr., C. W.; Allamandola, L. J. Variations in the Peak Position of the 6.2 μm Interstellar Emission Feature: A Tracer of N in the Interstellar Polycyclic Aromatic Hydrocarbon Population. *The Astrophysical Journal* **2005**, *632*, 316–332.
- [11] Ziurys, L. M. The chemistry in circumstellar envelopes of evolved stars: Following the origin of the elements to the origin of life. *Proceedings of the National Academy of Sciences* **2006**, *103*, 12274–12279.
- [12] Snow, T. P.; McCall, B. J. Diffuse atomic and molecular clouds. *Annual Review of Astronomy and Astrophysics* **2006**, *44*, 367–414.
- [13] Bergin, E. A.; Tafalla, M. Cold Dark Clouds: The Initial Conditions for Star Formation. *Annual Review of Astronomy and Astrophysics* **2007**, *45*, 339–396.
- [14] Garrod, R. T.; Widicus Weaver, S. L. Simulations of Hot-Core Chemistry. *Chemical Reviews* **2013**, *113*, 8939–8960.
- [15] Henning, T.; Semenov, D. Chemistry in Protoplanetary Disks. *Chemical Reviews* **2013**, *113*, 9016–9042.
- [16] Kenyon, S. J.; Dobrzycka, D.; Hartmann, L. A new optical extinction law and distance estimate for the Taurus-Auriga molecular cloud. *The Astronomical Journal* **1994**, *108*, 1872.
- [17] van Dishoeck, E. F. Astrochemistry of dust, ice and gas: introduction and overview. *Faraday Discuss.* **2014**, *168*, 9–47.
- [18] Latter, W. B. Large molecule production by mass-losing carbon stars - The primary source of interstellar polycyclic aromatic hydrocarbons? *The Astrophysical Journal* **1991**, *377*, 187.
- [19] Berné, O.; Montillaud, J.; Joblin, C. Top-down formation of fullerenes in the interstellar medium (Corrigendum). *Astronomy & Astrophysics* **2016**, *588*, C1.
- [20] Kroto, H. W.; McKay, K. The formation of quasi-icosahedral spiral shell carbon particles. *Nature* **1988**, *331*, 328–331.
- [21] Peeters, Z.; Botta, O.; Charnley, S. B.; Kisiel, Z.; Kuan, Y.-J.; Ehrenfreund, P. Formation and photostability of N-heterocycles in space. *Astronomy & Astrophysics* **2005**, *433*, 583–590.

- [22] McGuire, B. A.; Burkhardt, A. M.; Kalenskii, S.; Shingledecker, C. N.; Remijan, A. J.; Herbst, E.; McCarthy, M. C. Detection of the aromatic molecule benzonitrile ($c\text{-C}_6\text{H}_5\text{CN}$) in the interstellar medium. *Science* **2018**, *359*, 202–205.
- [23] McGuire, B. A.; Loomis, R. A.; Burkhardt, A. M.; Lee, K. L. K.; Shingledecker, C. N.; Charnley, S. B.; Cooke, I. R.; Cordiner, M. A.; Herbst, E.; Kalenskii, S.; Siebert, M. A.; Willis, E. R.; Xue, C.; Remijan, A. J.; McCarthy, M. C. Detection of two interstellar polycyclic aromatic hydrocarbons via spectral matched filtering. *Science* **2021**, *371*, 1265–1269.
- [24] Cernicharo, J.; Agúndez, M.; Cabezas, C.; Tercero, B.; Marcelino, N.; Pardo, J. R.; de Vicente, P. Pure hydrocarbon cycles in TMC-1: Discovery of ethynyl cyclopropenylidene, cyclopentadiene, and indene. *Astronomy & Astrophysics* **2021**, *649*, L15.
- [25] Burkhardt, A. M.; Long Kelvin Lee, K.; Bryan Changala, P.; Shingledecker, C. N.; Cooke, I. R.; Loomis, R. A.; Wei, H.; Charnley, S. B.; Herbst, E.; McCarthy, M. C.; McGuire, B. A. Discovery of the Pure Polycyclic Aromatic Hydrocarbon Indene ($c\text{-C}_9\text{H}_8$) with GOTHAM Observations of TMC-1. *The Astrophysical Journal Letters* **2021**, *913*, L18.
- [26] Wakelam, V. et al. The 2014 kida network for interstellar chemistry. *Astrophysical Journal, Supplement Series* **2015**, *217*, 20.
- [27] McElroy, D.; Walsh, C.; Markwick, A.; Cordiner, M.; Smith, K.; Millar, T. The UMIST database for astrochemistry 2012. *Astronomy & Astrophysics* **2013**, *550*.
- [28] Bernath, P. F. *Spectra of Atoms and Molecules*, 2nd ed.; Oxford University Press: Oxford, 2005.
- [29] Mangum, J. G.; Shirley, Y. L. How to Calculate Molecular Column Density. *Publications of the Astronomical Society of the Pacific* **2015**, *127*, 266–298.
- [30] McCarthy, M. C.; Lee, K. L. K.; Carroll, P. B.; Porterfield, J. P.; Changala, P. B.; Thorpe, J. H.; Stanton, J. F. Exhaustive Product Analysis of Three Benzene Discharges by Microwave Spectroscopy. *Journal of Physical Chemistry A* **2020**, *124*, 5170–5181.
- [31] McCarthy, M. C.; Chen, W.; Travers, M. J.; Thaddeus, P. Microwave Spectra of 11 Polyne Carbon Chains. *The Astrophysical Journal Supplement Series* **2000**, *129*, 611–623.
- [32] Saito, S.; Yamamoto, S. The microwave spectrum of the cyanomethyl radical $\text{CH}_2\text{CN}(\text{B}^2_1)$. *The Journal of Chemical Physics* **1997**, *107*, 1732.

- [33] Bartlett, R. J. Many-Body Perturbation Theory and Coupled Cluster Theory for Electron Correlation in Molecules. *Annual Review of Physical Chemistry* **1981**, *32*, 359–401.
- [34] Raghavachari, K.; Trucks, G. W.; Pople, J. A.; Head-Gordon, M. A fifth-order perturbation comparison of electron correlation theories. *Chemical Physics Letters* **1989**, *157*, 479–483.
- [35] Kendall, R. A.; Dunning, T. H.; Harrison, R. J. Electron affinities of the first-row atoms revisited. Systematic basis sets and wave functions. *The Journal of Chemical Physics* **1992**, *96*, 6796–6806.
- [36] Peterson, K. A.; Dunning, T. H. Accurate correlation consistent basis sets for molecular core–valence correlation effects: The second row atoms Al–Ar, and the first row atoms B–Ne revisited. *The Journal of Chemical Physics* **2002**, *117*, 10548–10560.
- [37] Mills, I. M. *Molecular Spectroscopy*; Elsevier, 1972; pp 115–140.
- [38] Boogert, A. A.; Gerakines, P. A.; Whittet, D. C. Observations of the Icy Universe. *Annual Review of Astronomy and Astrophysics* **2015**, *53*, 541–581.
- [39] Öberg, K. I. Photochemistry and Astrochemistry: Photochemical Pathways to Interstellar Complex Organic Molecules. *Chemical Reviews* **2016**, *116*, 9631–9663.
- [40] Gillett, F. C.; Forrest, W. J. Spectra of the Becklin-Neugebauer point source and the Kleinmann-low nebula from 2.8 to 13.5 microns. *The Astrophysical Journal* **1973**, *179*, 483.
- [41] Soifer, B. T.; Puetter, R. C.; Russell, R. W.; Willner, S. P.; Harvey, P. M.; Gillett, F. C. The 4–8 micron spectrum of the infrared source W33 A. *The Astrophysical Journal* **1979**, *232*, L53.
- [42] D’Hendecourt, L. B.; Jourdain de Muizon, M. The discovery of interstellar carbon dioxide. *Astronomy & Astrophysics* **1989**, *223*, L5–L8.
- [43] Lacy, J. H.; Carr, J. S.; Evans, Neal J., I.; Baas, F.; Achtermann, J. M.; Arens, J. F. Discovery of interstellar methane - Observations of gaseous and solid CH₄ absorption toward young stars in molecular clouds. *The Astrophysical Journal* **1991**, *376*, 556.
- [44] Grim, R. J. A.; Baas, F.; Geballe, T. R.; Greenberg, J. M.; Schutte, W. A. Detection of solid methanol toward W 33A. *Astronomy & Astrophysics* **1991**, *243*, 473–477.

- [45] Lacy, J. H.; Faraji, H.; Sandford, S. A.; Allamandola, L. J. Unraveling the 10 Micron “Silicate” Feature of Protostars: The Detection of Frozen Interstellar Ammonia. *The Astrophysical Journal* **1998**, *501*, L105–L109.
- [46] Dickens, J.; Irvine, W.; Nummelin, A.; Møllendal, H.; Saito, S.; Thorwirth, S.; Hjalmarsen, Å.; Ohishi, M. Searches for new interstellar molecules, including a tentative detection of aziridine and a possible detection of propenal. *Spectrochimica Acta Part A: Molecular and Biomolecular Spectroscopy* **2001**, *57*, 643–660.
- [47] Kuan, Y. J.; Charnley, S. B.; Huang, H. C.; Kisiel, Z.; Ehrenfreund, P.; Tseng, W. L.; Yan, C. H. Searches for interstellar molecules of potential prebiotic importance. *Advances in Space Research* **2004**, *33*, 31–39.
- [48] Kutner, M. L.; Machnik, D. E.; Tucker, K. D.; Dickman, R. L. Search for interstellar pyrrole and furan. *The Astrophysical Journal* **1980**, *242*, 541.
- [49] Myers, P. C.; Thaddeus, P.; Linke, R. A. A search for interstellar pyrrole - Evidence that rings are less abundant than chains. *The Astrophysical Journal* **1980**, *241*, 155.
- [50] Dickens, J. E.; Langer, W. D.; Velusamy, T. Small-Scale Abundance Variations in TMC-1: Dynamics and Hydrocarbon Chemistry. *The Astrophysical Journal* **2001**, *558*, 693–701.
- [51] McCarthy, M. C.; Lee, K. L. K.; Loomis, R. A.; Burkhardt, A. M.; Shingledecker, C. N.; Charnley, S. B.; Cordiner, M. A.; Herbst, E.; Kalenskii, S.; Willis, E. R.; Xue, C.; Remijan, A. J.; McGuire, B. A. Interstellar detection of the highly polar five-membered ring cyanocyclopentadiene. *Nature Astronomy* **2020**,
- [52] Simon, M. N.; Simon, M. *A SEARCH FOR INTERSTELLAR ACRYLONITRILE, PYRIMIDINE, AND PYRIDINE*; 1973; Vol. 184; pp 757–761.
- [53] Charnley, S. B.; Kuan, Y.-J.; Huang, H.-C.; Botta, O.; Butner, H. M.; Cox, N.; Despois, D.; Ehrenfreund, P.; Kisiel, Z.; Lee, Y.-Y.; Markwick, A. J.; Peeters, Z.; Rodgers, S. D. Astronomical searches for nitrogen heterocycles. *Advances in Space Research* **2005**, *36*, 137–145.
- [54] Kuan, Y.-J.; Yan, C.-H.; Charnley, S. B.; Kisiel, Z.; Ehrenfreund, P.; Huang, H.-C. A search for interstellar pyrimidine. *Monthly Notices of the Royal Astronomical Society* **2003**, *345*, 650–656.

- [55] Cordiner, M. A.; Charnley, S. B.; Kisiel, Z.; McGuire, B. A.; Kuan, Y.-J. Deep K-band Observations of TMC-1 with the Green Bank Telescope: Detection of HC 7 O, Nondetection of HC 11 N, and a Search for New Organic Molecules. *The Astrophysical Journal* **2017**, *850*, 187.
- [56] Irvine, W. M.; Elder, J.; Hjalmarsen, A.; Kollberg, E.; Rydbeck, O. E. H.; Sorensen, G. O.; Bak, B.; Svanholt, H. Searches for Interstellar Imidazole and Cyanoforn. *Astronomy & Astrophysics* **1981**, *97*, 192–194.
- [57] Brünken, S.; McCarthy, M. C.; Thaddeus, P.; Godfrey, P. D.; Brown, R. D. Improved line frequencies for the nucleic acid base uracil for a radioastronomical search. *Astronomy & Astrophysics* **2006**, *459*, 317–320.
- [58] Dickens, J. E.; Irvine, W. M.; Ohishi, M.; Ikeda, M.; Ishikawa, S.; Nummelin, A.; Hjalmarsen, A. Detection of Interstellar Ethylene Oxide. *The Astrophysical Journal* **1997**, *489*, 753–757.
- [59] Nummelin, A.; Dickens, J. E.; Bergman, P.; Hjalmarsen, A.; Irvine, W. M.; Ikeda, M.; Ohishi, M. Abundances of ethylene oxide and acetaldehyde in hot molecular cloud cores. *Astronomy & Astrophysics* **1998**, *286*, 275–286.
- [60] McGuire, B. A.; Carroll, P. B.; Loomis, R. A.; Finneran, I. A.; Jewell, P. R.; Remijan, A. J.; Blake, G. A. Discovery of the interstellar chiral molecule propylene oxide (CH₃CHCH₂O). *Science* **2016**, *352*, 1449–1452.
- [61] Burkhardt, A. M.; Loomis, R. A.; Shingledecker, C. N.; Lee, K. L. K.; Remijan, A. J.; McCarthy, M. C.; McGuire, B. A. Ubiquitous aromatic carbon chemistry at the earliest stages of star formation. *Nature Astronomy* **2021**, *5*, 181–187.
- [62] McCarthy, M. C.; McGuire, B. A. Aromatics and Cyclic Molecules in Molecular Clouds: A New Dimension of Interstellar Organic Chemistry. *J. Phys. Chem. A* **2021**, *125*, 3243.
- [63] Vogt, N.; Khaikin, L. S.; Rykov, A. N.; Grikin, O. E.; Batiukov, A. A.; Vogt, J.; Kochikov, I. V.; Shishkov, I. F. The equilibrium molecular structure of 2-cyanopyridine from combined analysis of gas-phase electron diffraction and microwave data and results of ab initio calculations. *Structural Chemistry* **2019**, *30*, 1699–1706.
- [64] Dorman, P. M.; Esselman, B. J.; Woods, R. C.; McMahan, R. J. An analysis of the rotational ground state and lowest-energy vibrationally excited dyad of 3-cyanopyridine: Low symmetry reveals rich

- complexity of perturbations, couplings, and interstate transitions. *Journal of Molecular Spectroscopy* **2020**, *373*, 111373.
- [65] Dorman, P. M.; Esselman, B. J.; Park, J. E.; Woods, R. C.; McMahon, R. J. Millimeter-wave spectrum of 4-cyanopyridine in its ground state and lowest-energy vibrationally excited states, ν_{20} and ν_{30} . *Journal of Molecular Spectroscopy* **2020**, *369*, 111274.
- [66] Davis, R. W.; Gerry, M. C. L. Microwave spectrum and structure of pyrrole-2-carbonitrile. *The Journal of Physical Chemistry* **1980**, *84*, 1767–1771.
- [67] Sakaizumi, T.; Oka, M.; Miyake, S.; Ohashi, O.; Yamaguchi, I. The microwave spectra of pyrrole-3-carbonitrile and pyrrole-2-carbonitrile. *Journal of Molecular Spectroscopy* **1991**, *147*, 229–242.
- [68] Loomis, R. A.; Burkhardt, A. M.; Shingledecker, C. N.; Charnley, S. B.; Cordiner, M. A.; Herbst, E.; Kalenskii, S.; Lee, K. L. K.; Willis, E. R.; Xue, C.; Remijan, A. J.; McCarthy, M. C.; McGuire, B. A. An investigation of spectral line stacking techniques and application to the detection of HC11N. *Nature Astronomy* **2021**, *5*, 188–196.
- [69] Nesvadba, R.; Studecký, T.; Uhlíková, T.; Urban, Š. Microwave spectrum and molecular constants of indole. *Journal of Molecular Spectroscopy* **2017**, *339*, 6–11.
- [70] Vávra, K.; Luková, K.; Kania, P.; Koucký, J.; Urban, Rotational spectra of indole in the lowest vibrational states. *Journal of Molecular Spectroscopy* **2019**, *363*, 28–32.
- [71] Peeters, Z.; Botta, O.; Charnley, S. B.; Ruiterkamp, R.; Ehrenfreund, P. *THE ASTROBIOLOGY OF NUCLEOBASES*; 2003; Vol. 593; pp 129–132.
- [72] Alexander, C. M. O.; Nittler, L. R.; Davidson, J.; Ciesla, F. J. Measuring the level of interstellar inheritance in the solar protoplanetary disk. *Meteoritics & Planetary Science* **2017**, *52*, 1797–1821.
- [73] Smith, I. W. M.; Barnes, P. W. Advances in low temperature gas-phase kinetics. *Annual Reports Section "C" (Physical Chemistry)* **2013**, *109*, 140.
- [74] Cooke, I. R.; Sims, I. R. Experimental Studies of Gas-Phase Reactivity in Relation to Complex Organic Molecules in Star-Forming Regions. *ACS Earth and Space Chemistry* **2019**, *3*, 1109–1134.
- [75] Tizniti, M.; Le Picard, S. D.; Lique, F.; Berteloite, C.; Canosa, A.; Alexander, M. H.; Sims, I. R. The rate of the F + H₂ reaction at very low temperatures. *Nature Chemistry* **2014**, *6*, 141–145.

- [76] Marcus, R. A. Unimolecular Dissociations and Free Radical Recombination Reactions. *The Journal of Chemical Physics* **1952**, *20*, 359–364.
- [77] Rowe, B. R.; Dupeyrat, G.; Marquette, J. B.; Gaucherel, P. Study of the reactions $N+2+2N_2 \rightarrow N+4+N_2$ and $O+2+2O_2 \rightarrow O+4+O_2$ from 20 to 160 K by the CRESU technique. *The Journal of Chemical Physics* **1984**, *80*, 4915.
- [78] Yu, A. A mini review of the crossed molecular beam apparatus in molecular reaction dynamics. *Journal of Saudi Chemical Society* **2019**, *23*, 1–6.
- [79] Casavecchia, P. Chemical reaction dynamics with molecular beams. *Reports on Progress in Physics* **2000**, *63*, 355–414.
- [80] Öberg, K. I. Photochemistry and Astrochemistry: Photochemical Pathways to Interstellar Complex Organic Molecules. *Chemical Reviews* **2016**, *116*, 9631–9663.
- [81] Smith, I. W. Laboratory astrochemistry: Gas-phase processes. *Annual Review of Astronomy and Astrophysics* **2011**, *49*, 29–66.
- [82] Gupta, V.; Tandon, P.; Mishra, P. Some new reaction pathways for the formation of cytosine in interstellar space – A quantum chemical study. *Advances in Space Research* **2013**, *51*, 797–811.
- [83] Majumdar, L.; Gorai, P.; Das, A.; Chakrabarti, S. K. Potential formation of three pyrimidine bases in interstellar regions. *Astrophysics and Space Science* **2015**, *360*, 1–14.
- [84] Lee, K. L. K. Interstellar Aromatic Chemistry: A Combined Laboratory, Observational, and Theoretical Perspective. IAU S350 Laboratory Astrophysics: From Observations to Interpretation. Cambridge, UK, 2019.
- [85] Parker, D. S. N.; Kaiser, R. I.; Kostko, O.; Troy, T. P.; Ahmed, M.; Sun, B.-J.; Chen, S.-H.; Chang, A. H. H. On the formation of pyridine in the interstellar medium. *Physical Chemistry Chemical Physics* **2015**, *17*, 32000–32008.
- [86] Soorkia, S.; Taatjes, C. a.; Osborn, D. L.; Selby, T. M.; Trevitt, A. J.; Wilson, K. R.; Leone, S. R. Direct detection of pyridine formation by the reaction of CH (CD) with pyrrole: a ring expansion reaction. *Physical chemistry chemical physics : PCCP* **2010**, *12*, 8750–8.

- [87] Morales, S. B.; Bennett, C. J.; Le Picard, S. D.; Canosa, A.; Sims, I. R.; Sun, B. J.; Chen, P. H.; Chang, A. H.; Kislov, V. V.; Mebel, A. M.; Gu, X.; Zhang, F.; Maksyutenko, P.; Kaiser, R. I. A crossed molecular beam, low-temperature kinetics, and theoretical investigation of the reaction of the cyano radical (CN) with 1,3-butadiene (C₄H₆). A route to complex nitrogen-bearing molecules in low-temperature extraterrestrial environments. *Astrophysical Journal* **2011**, *742*.
- [88] Parker, D. S.; Kaiser, R. I.; Kostko, O.; Troy, T. P.; Ahmed, M.; Mebel, A. M.; Tielens, A. G. Gas phase synthesis of (ISO)quinoline and its role in the formation of nucleobases in the interstellar medium. *Astrophysical Journal* **2015**, *803*, 53.
- [89] Zhao, L.; Prendergast, M.; Kaiser, R. I.; Xu, B.; Lu, W.; Ahmed, M.; Howlader, A. H.; Wnuk, S. F. F.; Korotchenko, A. S.; Evseev, M. M.; Bashkurov, E. K.; Azyazov, V. N.; Mebel, A. A Molecular Beams and Computational Study on the Barrierless Gas Phase Formation of (Iso)Quinoline in Low Temperature Extraterrestrial Environments. *Physical Chemistry Chemical Physics* **2021**, *19*.
- [90] Recio, P.; Marchione, D.; Caracciolo, A.; Murray, V. J.; Mancini, L.; Rosi, M.; Casavecchia, P.; Balucani, N. A crossed molecular beam investigation of the N(2D) + pyridine reaction and implications for prebiotic chemistry. *Chemical Physics Letters* **2021**, *779*, 138852.
- [91] Chin, C.-H.; Zhu, T.; Zhang, J. Z. H. Cyclopentadienyl radical formation from the reaction of excited nitrogen atoms with benzene: a theoretical study. *Physical Chemistry Chemical Physics* **2021**, *23*, 12408–12420.
- [92] Johnson, D. G.; Blitz, M. A.; Seakins, P. W. The reaction of methyldiene (CH) with methanol isotopomers. *Physical Chemistry Chemical Physics* **2000**, *2*, 2549–2553.
- [93] Thiesemann, H.; MacNamara, J.; Taatjes, C. A. Deuterium kinetic isotope effect and temperature dependence in the reactions of CH[2II] with methane and acetylene. *Journal of Physical Chemistry A* **1997**, *101*, 1881–1886.
- [94] Parker, D. S.; Yang, T.; Dangi, B. B.; Kaiser, R. I.; Bera, P. P.; Lee, T. J. LOW TEMPERATURE FORMATION of NITROGEN-SUBSTITUTED POLYCYCLIC AROMATIC HYDROCARBONS (PANHS) - BARRIERLESS ROUTES to DIHYDRO(iso)QUINOLINES. *Astrophysical Journal* **2015**, *815*, 115.

- [95] Hamid, A. M.; Bera, P. P.; Lee, T. J.; Aziz, S. G.; Alyoubi, A. O.; Samy El-Shall, M.; El-Shall, M. S. Evidence for the formation of pyrimidine cations from the sequential reactions of hydrogen cyanide with the acetylene radical cation. *Journal of Physical Chemistry Letters* **2014**, *5*, 3392–3398.
- [96] Soliman, A.-R.; Hamid, A. M.; Attah, I.; Momoh, P.; El-Shall, M. S. Formation of Nitrogen-Containing Polycyclic Cations by Gas-Phase and Intracluster Reactions of Acetylene with the Pyridinium and Pyrimidinium Ions. *Journal of the American Chemical Society* **2013**, *135*, 155–166.
- [97] Wang, Z.-C.; Cole, C. A.; Snow, T. P.; Bierbaum, V. M. EXPERIMENTAL AND COMPUTATIONAL STUDIES OF THE FORMATION MECHANISM OF PROTONATED INTERSTELLAR DIAZINES. *The Astrophysical Journal* **2015**, *798*, 102.
- [98] Cole, C. A.; Wang, Z. C.; Snow, T. P.; Bierbaum, V. M. Anionic derivatives of uracil: Fragmentation and reactivity. *Physical Chemistry Chemical Physics* **2014**, *16*, 17835–17844.
- [99] Cole, C. A.; Wang, Z. C.; Snow, T. P.; Bierbaum, V. M. Deprotonated Purine Dissociation: Experiments, Computations, and Astrobiological Implications. *Journal of Physical Chemistry A* **2015**, *119*, 334–343.
- [100] Fondren, L. D.; Adams, N. G.; Stavish, L. Gas phase reactions of CH₃⁺ with a series of homo- and heterocyclic molecules. *Journal of Physical Chemistry A* **2009**, *113*, 592–598.
- [101] Wang, Z.-C.; Cole, C. A.; Demarais, N. J.; Snow, T. P.; Bierbaum, V. M. Reactions of Azine Anions with Nitrogen and Oxygen Atoms: Implications for Titan’s Upper Atmosphere and Interstellar Chemistry. *Journal of the American Chemical Society* **2015**, *137*, 10700–10709.
- [102] Wang, Z.-C.; Bierbaum, V. M. Experimental and Computational Studies of the Reactions of N and O Atoms with Small Heterocyclic Anions. *The Journal of Physical Chemistry A* **2017**, *121*, 3655–3661.
- [103] Nichols, C. M.; Wang, Z. C.; Lineberger, W. C.; Bierbaum, V. M. Gas-phase reactions of deprotonated nucleobases with H, N, and O Atoms. *Journal of Physical Chemistry Letters* **2019**, *10*, 4863–4867.
- [104] Cole, C. A.; Demarais, N. J.; Yang, Z.; Snow, T. P.; Bierbaum, V. M. HETEROCYCLIC ANIONS OF ASTROBIOLOGICAL INTEREST. *The Astrophysical Journal* **2013**, *779*, 181.
- [105] Wang, L. P.; McGibbon, R. T.; Pande, V. S.; Martinez, T. J. Automated Discovery and Refinement of Reactive Molecular Dynamics Pathways. *Journal of Chemical Theory and Computation* **2016**, *12*, 638–649.

- [106] Fondren, L. D.; McLain, J.; Jackson, D. M.; Adams, N. G.; Babcock, L. M. Studies of reactions of a series of ions with nitrogen containing heterocyclic molecules using a selected ion flow tube. *International Journal of Mass Spectrometry* **2007**, *265*, 60–67.
- [107] Wren, S. W.; Vogelhuber, K. M.; Garver, J. M.; Kato, S.; Sheps, L.; Bierbaum, V. M.; Lineberger, W. C. C–H Bond Strengths and Acidities in Aromatic Systems: Effects of Nitrogen Incorporation in Mono-, Di-, and Triazines. **2012**,
- [108] Stein, T.; Bera, P. P.; Lee, T. J.; Head-Gordon, M. Molecular growth upon ionization of van der Waals clusters containing HCCH and HCN is a pathway to prebiotic molecules. *Physical Chemistry Chemical Physics* **2020**, *22*, 20337–20348.
- [109] Smoluchowski, R. Adsorption and mobility on amorphous surfaces. Application to astrophysical problems. *The Journal of Physical Chemistry* **1983**, *87*, 4229–4233.
- [110] Nuevo, M.; Milam, S. N.; Sandford, S. A. Nucleobases and Prebiotic Molecules in Organic Residues Produced from the Ultraviolet Photo-Irradiation of Pyrimidine in NH₃ and H₂O+NH₃ Ices. *Astrobiology* **2012**, *12*, 295–314.
- [111] Materese, C. K.; Nuevo, M.; Bera, P. P.; Lee, T. J.; Sandford, S. a. Thymine and Other Prebiotic Molecules Produced from the Ultraviolet Photo-Irradiation of Pyrimidine in Simple Astrophysical Ice Analogs. *Astrobiology* **2013**, *13*, 948–962.
- [112] Materese, C. K.; Nuevo, M.; McDowell, B. L.; Buffo, C. E.; Sandford, S. A. The Photochemistry of Purine in Ice Analogs Relevant to Dense Interstellar Clouds. *The Astrophysical Journal* **2018**, *864*, 44.
- [113] Bera, P. P.; Nuevo, M.; Materese, C. K.; Sandford, S. A.; Lee, T. J. Mechanisms for the formation of thymine under astrophysical conditions and implications for the origin of life. *The Journal of Chemical Physics* **2016**, *144*, 144308.
- [114] Nuevo, M.; Materese, C. K.; Sandford, S. A. THE PHOTOCHEMISTRY OF PYRIMIDINE IN REALISTIC ASTROPHYSICAL ICES AND THE PRODUCTION OF NUCLEOBASES. *The Astrophysical Journal* **2014**, *793*, 125.
- [115] Smith, K. E.; Callahan, M. P.; Gerakines, P. A.; Dworkin, J. P.; House, C. H. Investigation of pyridine carboxylic acids in CM2 carbonaceous chondrites: Potential precursor molecules for ancient coenzymes. *Geochimica et Cosmochimica Acta* **2014**, *136*, 1–12.

- [116] Materese, C. K.; Nuevo, M.; Sandford, S. A. N- and O-heterocycles produced from the irradiation of benzene and naphthalene in H₂ONH₃-containing ices. *Astrophysical Journal* **2015**, *800*, 116.
- [117] Oba, Y.; Takano, Y.; Naraoka, H.; Watanabe, N.; Kouchi, A. Nucleobase synthesis in interstellar ices. *Nature Communications* **2019**, *10*, 8–15.
- [118] Carrascosa, H.; Gonz, C.; Mu, G. M.; Sanz, M. L. Synthesis of the first nitrogen-heterocycles in interstellar ice analogues containing methylamine (CH₃NH₂) exposed to UV radiation : formation of trimethylenetriamine (TMT, C₃H₇N) and hexamethylenetetramine (HMT, C₆H₁₂N₄). *2021*, *805*, 791–805.
- [119] Naraoka, H.; Yamashita, Y.; Yamaguchi, M.; Orthous-Daunay, F. R. Molecular Evolution of N-Containing Cyclic Compounds in the Parent Body of the Murchison Meteorite. *ACS Earth and Space Chemistry* **2017**, *1*, 540–550.
- [120] Frank, R. L.; Seven, R. P. Pyridines. IV. A Study of the Chichibabin Synthesis. *Journal of the American Chemical Society* **1949**, *71*, 2629–2635.
- [121] Munoz, J.; Junior, J.; Silva, F. Radziszewski Reaction: An Elegant, Easy, Simple and Efficient Method to Synthesise Imidazoles. *Current Organic Synthesis* **2014**, *11*, 824–834.
- [122] Vinogradoff, V.; Bernard, S.; Le Guillou, C.; Remusat, L. Evolution of interstellar organic compounds under asteroidal hydrothermal conditions. *Icarus* **2018**, *305*, 358–370.
- [123] Goerigk, L.; Hansen, A.; Bauer, C.; Ehrlich, S.; Najibi, A.; Grimme, S. A look at the density functional theory zoo with the advanced GMTKN55 database for general main group thermochemistry, kinetics and noncovalent interactions. *Physical Chemistry Chemical Physics* **2017**, *19*, 32184–32215.
- [124] Etim, E. E.; Adelagun, R.; Andrew, C.; Enock Oluwole, O. Optimizing the searches for interstellar heterocycles. *Advances in Space Research* **2021**,
- [125] Wang, L.-P.; Titov, A.; McGibbon, R.; Liu, F.; Pande, V. S.; Martínez, T. J. Discovering chemistry with an ab initio nanoreactor. *Nature Chemistry* **2014**, *6*, 1044–1048.
- [126] Lovas, F. J.; Hollis, J. M.; Remijan, A. J.; Jewell, P. R. Detection of Ketenimine (CH₂CNH) in Sagittarius B2(N) Hot Cores. *The Astrophysical Journal* **2006**, *645*, L137–L140.

- [127] Vuitton, V.; Yelle, R.; Klippenstein, S.; Hörst, S.; Lavvas, P. Simulating the density of organic species in the atmosphere of Titan with a coupled ion-neutral photochemical model. *Icarus* **2019**, *324*, 120–197.
- [128] Palmer, M. Y.; Cordiner, M. A.; Nixon, C. A.; Charnley, S. B.; Teanby, N. A.; Kisiel, Z.; Irwin, P. G. J.; Mumma, M. J. ALMA detection and astrobiological potential of vinyl cyanide on Titan. *Science Advances* **2017**, *3*, e1700022.
- [129] Cordiner, M. A.; Palmer, M. Y.; Nixon, C. A.; Irwin, P. G. J.; Teanby, N. A.; Charnley, S. B.; Mumma, M. J.; Kisiel, Z.; Serigano, J.; Kuan, Y.-J.; Chuang, Y.-L.; Wang, K.-S. Ethyl Cyanide on Titan: Spectroscopic Detection and Mapping Using Alma. *The Astrophysical Journal* **2015**, *800*, L14.
- [130] Waite, J. H. et al. Ion Neutral Mass Spectrometer results from the first flyby of Titan. *Science* **2005**, *308*, 982–986.
- [131] Cravens, T. E. et al. Composition of Titan’s ionosphere. *Geophysical Research Letters* **2006**, *33*, L07105.
- [132] Hörst, S. M. Titan’s atmosphere and climate. *Journal of Geophysical Research: Planets* **2017**, *122*, 432–482.
- [133] Trainer, M. G.; Pavlov, A. A.; DeWitt, H. L.; Jimenez, J. L.; McKay, C. P.; Toon, O. B.; Tolbert, M. A. Organic haze on Titan and the early Earth. *Proceedings of the National Academy of Sciences* **2006**, *103*, 18035–18042.
- [134] Coustenis, A. TITANS ATMOSPHERE AND SURFACE - PARALLELS AND DIFFERENCES WITH THE PRIMITIVE EARTH. **1995**, *67*, 95–100.
- [135] Lunine, J. I. Saturn ’ s Titan : A Strict Test for Life ’ s Cosmic Ubiquity. *American Philosophical Society* **2009**, *153*, 403–418.
- [136] Hörst, S.; Yelle, R.; Buch, A.; Carrasco, N.; Cernogora, G.; Dutuit, O.; Quirico, E.; Sciamma-O’Brien, E.; Smith, M.; Somogyi, Á.; Szopa, C.; Thissen, R.; Vuitton, V. Formation of Amino Acids and Nucleotide Bases in a Titan Atmosphere Simulation Experiment. *Astrobiology* **2012**, *12*, 809–817.
- [137] Morisson, M.; Szopa, C.; Carrasco, N.; Buch, A.; Gautier, T. Titan’s organic aerosols: Molecular composition and structure of laboratory analogues inferred from pyrolysis gas chromatography mass spectrometry analysis. *Icarus* **2016**, *277*, 442–454.

- [138] McGuigan, M.; Waite, J. H.; Imanaka, H.; Sacks, R. D. Analysis of Titan tholin pyrolysis products by comprehensive two-dimensional gas chromatography–time-of-flight mass spectrometry. *Journal of Chromatography A* **2006**, *1132*, 280–288.
- [139] Mahjoub, A.; Schwell, M.; Carrasco, N.; Benilan, Y.; Cernogora, G.; Szopa, C.; Gazeau, M.-C. Characterization of aromaticity in analogues of titan’s atmospheric aerosols with two-step laser desorption ionization mass spectrometry. *Planetary and Space Science* **2016**, *131*, 1–13.
- [140] Derenne, S.; Coelho, C.; Anquetil, C.; Szopa, C.; Rahman, A.; McMillan, P.; Corà, F.; Pickard, C.; Quirico, E.; Bonhomme, C. New insights into the structure and chemistry of Titan’s tholins via ¹³C and ¹⁵N solid state nuclear magnetic resonance spectroscopy. *Icarus* **2012**, *221*, 844–853.
- [141] Nixon, C. A.; Thelen, A. E.; Cordiner, M. A.; Kisiel, Z.; Charnley, S. B.; Molter, E. M.; Serigano, J.; Irwin, P. G. J.; Teanby, N. A.; Kuan, Y.-J. Detection of Cyclopropenyldiene on Titan with ALMA. *The Astronomical Journal* **2020**, *160*, 205.
- [142] Alzueta, M. U.; Tena, A.; Bilbao, R. Pyridine conversion in a flow reactor and its interaction with nitric oxide. *Combustion Science and Technology* **2002**, *174*, 151–169.
- [143] LUMBRERAS, M.; ALZUETA, M.; MILLERA, A.; BILBAO, R. A STUDY OF PYRROLE OXIDATION UNDER FLOW REACTOR CONDITIONS. *Combustion Science and Technology* **2001**, *172*, 123–139.
- [144] Wu, L.-N.; Tian, Z.-Y.; Weng, J.-J.; Yu, D.; Liu, Y.-X.; Tian, D.-X.; Cao, C.-C.; Zou, J.-B.; Zhang, Y.; Yang, J.-Z. Experimental and kinetic study on the low-temperature oxidation of pyridine as a representative of fuel-N compounds. *Combustion and Flame* **2019**, *202*, 394–404.
- [145] Yamamoto, T.; Kuwahara, T.; Nakaso, K.; Yamamoto, T. Kinetic study of fuel NO formation from pyrrole type nitrogen. *Fuel* **2012**, *93*, 213–220.
- [146] Oluwoye, I.; Altarawneh, M.; Gore, J.; Dlugogorski, B. Z. Products of incomplete combustion from biomass reburning. *Fuel* **2020**, *274*, 117805.
- [147] Pizzarello, S.; Huang, Y. The deuterium enrichment of individual amino acids in carbonaceous meteorites: A case for the presolar distribution of biomolecule precursors. *Geochimica et Cosmochimica Acta* **2005**, *69*, 599–605.

- [148] Ricca, A. A Computational Study of the Mechanisms for the Incorporation of a Nitrogen Atom into Polycyclic Aromatic Hydrocarbons in the Titan Haze. *Icarus* **2001**, *154*, 516–521.
- [149] Costain, C. C.; Stoicheff, B. P. Microwave Spectrum, Molecular Structure of Vinyl Cyanide and a Summary of CC, CH Bond Lengths in Simple Molecules. *The Journal of Chemical Physics* **1959**, *30*, 777.
- [150] Gardner, F. F.; Winnewisser, G. The detection of interstellar vinyl cyanide (acrylonitrile). *The Astrophysical Journal* **1975**, *195*, L127.
- [151] Matthews, H. E.; Sears, T. J. The detection of vinyl cyanide in TMC-1. *The Astrophysical Journal* **1983**, *272*, 149.
- [152] Prozument, K.; Shaver, R. G.; Ciuba, M. A.; Muentner, J. S.; Park, G. B.; Stanton, J. F.; Guo, H.; Wong, B. M.; Perry, D. S.; Field, R. W. A new approach toward transition state spectroscopy. *Faraday Discussions* **2013**, *163*, 33.
- [153] Letendre, L.; Dai, H.-L. Structure and vibrational modes of the cyanovinyl radical: A study by time-resolved Fourier transform IR emission spectroscopy. *The Journal of Physical Chemistry A* **2002**, *106*, 12035–12040.
- [154] Letendre, L. T.; McNavage, W.; Pibel, C.; Liu, D.-K.; Dai, H.-L. Time-resolved FTIR emission spectroscopy of transient radicals. *Journal of the Chinese Chemical Society* **2005**, *52*, 677–686.
- [155] Guo, J.; Carrington, T.; Filseth, S. V. Energy disposal in CN ($X^2\Sigma^+$) produced in the 157 nm photodissociation of acrylonitrile. *The Journal of Chemical Physics* **2001**, *115*, 8411–8417.
- [156] Sun, J.; Wang, R.; Wang, B. Theoretical study on the gas phase reaction of acrylonitrile with a hydroxyl radical. *Physical Chemistry Chemical Physics* **2011**, *13*, 16585–16595.
- [157] Yung, Y. L.; Allen, M.; Pinto, J. P. Photochemistry of the atmosphere of Titan - Comparison between model and observations. *The Astrophysical Journal Supplement Series* **1984**, *55*, 465.
- [158] Levin, B. C. A summary of the NBS literature reviews on the chemical nature and toxicity of the pyrolysis and combustion products from seven plastics: Acrylonitrile-butadiene-styrenes (ABS), nylons, polyesters, polyethylenes, polystyrenes, poly(vinyl chlorides) and rigid polyurethane foams. *Fire and Materials* **1987**, *11*, 143–157.

- [159] Liu, N.; Yuan, X.; Zhang, R.; Xu, R.; Li, Y. Mechanistic insight into selective catalytic combustion of acrylonitrile (C_2H_3CN): NCO formation and its further transformation towards N_2 . *Physical Chemistry Chemical Physics* **2017**, *19*, 7971–7979.
- [160] Stanton, J. F.; Gauss, J.; Cheng, L.; Harding, M. E.; Matthews, D. A.; Szalay, P. G. CFOUR, Coupled-Cluster techniques for Computational Chemistry, a quantum-chemical program package. With contributions from A.A. Auer, R.J. Bartlett, U. Benedikt, C. Berger, D.E. Bernholdt, Y.J. Bomble, O. Christiansen, F. Engel, R. Faber, M. Heckert, O. Heun, M. Hilgenberg, C. Huber, T.-C. Jagau, D. Jonsson, J. Jusélius, T. Kirsch, K. Klein, W.J. Lauderdale, F. Lipparini, T. Metzroth, L.A. Mück, D.P. O'Neill, D.R. Price, E. Prochnow, C. Puzzarini, K. Ruud, F. Schiffmann, W. Schwalbach, C. Simmons, S. Stopkowitz, A. Tajti, J. Vázquez, F. Wang, J.D. Watts and the integral packages MOLECULE (J. Almlöf and P.R. Taylor), PROPS (P.R. Taylor), ABACUS (T. Helgaker, H.J. Aa. Jensen, P. Jørgensen, and J. Olsen), and ECP routines by A. V. Mitin and C. van Wüllen. For the current version, see <http://www.cfour.de>.
- [161] Almlöf, J.; Taylor, P. R. General contraction of Gaussian basis sets. I. Atomic natural orbitals for first- and second-row atoms. *The Journal of Chemical Physics* **1987**, *86*, 4070–4077.
- [162] Jayatilaka, D.; Lee, T. J. Open-shell coupled-cluster theory. *The Journal of Chemical Physics* **1993**, *98*, 9734–9747.
- [163] McCarthy, M. C.; Travers, M. J.; Kovacs, A.; Gottlieb, C. A.; Thaddeus, P. Eight new carbon chain molecules. *The Astrophysical Journal Supplement Series* **1997**, *113*, 105–120.
- [164] McCarthy, M. C.; Martinez, O.; McGuire, B. A.; Crabtree, K. N.; Martin-Drumel, M.-A.; Stanton, J. F. Isotopic studies of *trans*- and *cis*-HOCO using rotational spectroscopy: Formation, chemical bonding, and molecular structures. *The Journal of Chemical Physics* **2016**, *144*, 124304.
- [165] Balle, T. J.; Flygare, W. H. Fabry–Perot cavity pulsed Fourier transform microwave spectrometer with a pulsed nozzle particle source. *Review of Scientific Instruments* **1981**, *52*, 33–45.
- [166] Crabtree, K. N.; Martin-Drumel, M.-A.; Brown, G. G.; Gaster, S. A.; Hall, T. M.; McCarthy, M. C. Microwave spectral taxonomy: A semi-automated combination of chirped-pulse and cavity Fourier-transform microwave spectroscopy. *The Journal of Chemical Physics* **2016**, *144*, 124201.
- [167] Pickett, H. M. The fitting and prediction of vibration-rotation spectra with spin interactions. *Journal of Molecular Spectroscopy* **1991**, *148*, 371–377.

- [168] Markov, V. N.; Xu, Y.; Jäger, W. Microwave-submillimeter wave double-resonance spectrometer for the investigation of van der Waals complexes. *Review of Scientific Instruments* **1998**, *69*, 4061–4067.
- [169] Watson, J. K. G. Determination of centrifugal distortion coefficients of asymmetric-top molecules. *The Journal of Chemical Physics* **1967**, *46*, 1935–1949.
- [170] Glarborg, P. Fuel nitrogen conversion in solid fuel fired systems. *Progress in Energy and Combustion Science* **2003**, *29*, 89–113.
- [171] Sheng, L.; Wang, X.; Yang, X. Prediction model of biocrude yield and nitrogen heterocyclic compounds analysis by hydrothermal liquefaction of microalgae with model compounds. *Bioresource Technology* **2018**, *247*, 14–20.
- [172] Pershing, D. W.; Wendt, J. O. Relative Contributions of Volatile Nitrogen and Char Nitrogen to NO_x Emissions from Pulverized Coal Flames. *Industrial and Engineering Chemistry Process Design and Development* **1979**, *18*, 60–67.
- [173] Moller, L.; Lax, I.; Eriksson, L. C. Nitrated polycyclic aromatic hydrocarbons: A risk assessment for the urban citizen. *Environmental Health Perspectives* **1993**, *101*, 309–315.
- [174] Bünger, J.; Krahl, J.; Schröder, O.; Schmidt, L.; Westphal, G. A. Potential hazards associated with combustion of bio-derived versus petroleum-derived diesel fuel. *Crit. Rev. Toxicol.* **2012**, *42*, 732–750.
- [175] McGuire, B. A. 2018 census of interstellar, circumstellar, extragalactic, protoplanetary disk, and exoplanetary molecules. *Astrophys. J., Suppl. Ser.* **2018**, *239*, 17.
- [176] Vuitton, V.; Yelle, R.; McEwan, M. Ion chemistry and N-containing molecules in Titan’s upper atmosphere. *Icarus* **2007**, *191*, 722–742.
- [177] Cooke, I. R.; Gupta, D.; Messinger, J. P.; Sims, I. R. Benzonitrile as a Proxy for Benzene in the Cold ISM: Low-temperature Rate Coefficients for CN + C₆H₆. *The Astrophysical Journal* **2020**, *891*, L41.
- [178] Krasnopolsky, V. A. A photochemical model of Titan’s atmosphere and ionosphere. *Icarus* **2009**, *201*, 226–256.
- [179] Hendrix, J.; Bera, P. P.; Lee, T. J.; Head-Gordon, M. Cation, Anion, and Radical Isomers of C₄H₄N: Computational Characterization and Implications for Astrophysical and Planetary Environments. *The Journal of Physical Chemistry A* **2020**, *124*, 2001–2013.

- [180] Ikeda, E.; Nicholls, P.; Mackie, J. C. A kinetic study of the oxidation of pyridine. *Proceedings of the Combustion Institute* **2000**, *28*, 1709–1716.
- [181] Tian, Z.; Li, Y.; Zhang, T.; Zhu, A.; Cui, Z.; Qi, F. An experimental study of low-pressure premixed pyrrole/oxygen/argon flames with tunable synchrotron photoionization. *Combustion and Flame* **2007**, *151*, 347–365.
- [182] Luo, J.; Zou, C.; He, Y.; Jing, H.; Cheng, S. The characteristics and mechanism of NO formation during pyridine oxidation in O₂/N₂ and O₂/CO₂ atmospheres. *Energy* **2019**, *187*, 115954.
- [183] Blank, D. A.; North, S. W.; Lee, Y. T. The ultraviolet photodissociation dynamics of pyrrole. *Chemical Physics* **1994**, *187*, 35–47.
- [184] Cronin, B.; Nix, M. G. D.; Qadiri, R. H.; Ashfold, M. N. R. High resolution photofragment translational spectroscopy studies of the near ultraviolet photolysis of pyrrole. *Physical Chemistry Chemical Physics* **2004**, *6*, 5031.
- [185] Lippert, H.; Ritze, H.-H.; Hertel, I. V.; Radloff, W. Femtosecond Time-Resolved Hydrogen-Atom Elimination from Photoexcited Pyrrole Molecules. *ChemPhysChem* **2004**, *5*, 1423–1427.
- [186] Roberts, G. M.; Williams, C. A.; Yu, H.; Chatterley, A. S.; Young, J. D.; Ullrich, S.; Stavros, V. G. Probing ultrafast dynamics in photoexcited pyrrole: timescales for $1\pi\sigma^*$ mediated H-atom elimination. *Faraday Discussions* **2013**, *163*, 95.
- [187] Wei, J.; Kuczmann, A.; Riedel, J.; Renth, F.; Temps, F. Photofragment velocity map imaging of H atom elimination in the first excited state of pyrrole. *Physical Chemistry Chemical Physics* **2003**, *5*, 315–320.
- [188] Rubio-Lago, L.; Zaouris, D.; Sakellariou, Y.; Sofikitis, D.; Kitsopoulos, T. N.; Wang, F.; Yang, X.; Cronin, B.; Devine, A. L.; King, G. A.; Nix, M. G. D.; Ashfold, M. N. R.; Xantheas, S. S. Photofragment slice imaging studies of pyrrole and the Xe-pyrrole cluster. *The Journal of Chemical Physics* **2007**, *127*, 064306.
- [189] Vallet, V.; Lan, Z.; Mahapatra, S.; Sobolewski, A. L.; Domcke, W. Photochemistry of pyrrole: Time-dependent quantum wave-packet description of the dynamics at the $\pi 1\sigma^*$ -S₀ conical intersections. *The Journal of Chemical Physics* **2005**, *123*, 144307.

- [190] Saita, K.; Nix, M. G. D.; Shalashilin, D. V. Simulation of ultrafast photodynamics of pyrrole with a multiconfigurational Ehrenfest method. *Physical Chemistry Chemical Physics* **2013**, *15*, 16227.
- [191] Grebenschikov, S. Y.; Picconi, D. Fano resonances in the photoinduced H-atom elimination dynamics in the $\pi\sigma^*$ states of pyrrole. *Physical Chemistry Chemical Physics* **2017**, *19*, 14902–14906.
- [192] Picconi, D.; Grebenschikov, S. Y. Photodissociation dynamics in the first absorption band of pyrrole. I. Molecular Hamiltonian and the Herzberg-Teller absorption spectrum for the $A_{21}(\pi\sigma^*) \leftarrow X_{11} A_1(\pi\pi)$ transition. *The Journal of Chemical Physics* **2018**, *148*, 104103.
- [193] Nandipati, K. R.; Kanakati, A. K.; Singh, H.; Lan, Z.; Mahapatra, S. Initial state-specific photodissociation dynamics of pyrrole via $1 \pi \sigma^* / S_0$ conical intersection initiated with optimally controlled UV-laser pulses. *The European Physical Journal D* **2017**, *71*, 222.
- [194] Bacskay, G. B.; Martoprawiro, M.; Mackie, J. C. An ab initio quantum chemical study of the electronic structure and stability of the pyrrolyl radical: Comparison with the isoelectronic cyclopentadienyl radical. *Chemical Physics Letters* **1998**, *290*, 391–398.
- [195] Gianola, A. J.; Ichino, T.; Hoenigman, R. L.; Kato, S.; Bierbaum, V. M.; Carllineberger, W. Thermochemistry and electronic structure of the pyrrolyl radical. *Journal of Physical Chemistry A* **2004**, *108*, 10326–10335.
- [196] Samuni, A.; Neta, P. Electron spin resonance study of the reaction of hydroxyl radicals with pyrrole, imidazole, and related compounds. *Journal of Physical Chemistry* **1973**, *77*, 1629–1635.
- [197] Sah, C.; Yadav, A. K.; Venkataramani, S. Deciphering Stability of Five-Membered Heterocyclic Radicals: Balancing Act Between Delocalization and Ring Strain. *The Journal of Physical Chemistry A* **2018**, *122*, 5464–5476.
- [198] Matthews, D. A.; Cheng, L.; Harding, M. E.; Lipparini, F.; Stopkowicz, S.; Jagau, T.-C.; Szalay, P. G.; Gauss, J.; Stanton, J. F. Coupled-cluster techniques for computational chemistry: The CFOUR program package. *J. Chem. Phys* **2020**, *152*, 214108.
- [199] Tarczay, G.; Szalay, P. G.; Gauss, J. First-principles calculation of electron spin-rotation tensors. *Journal of Physical Chemistry A* **2010**, *114*, 9246–9252.
- [200] Dunning, T. H. Gaussian basis sets for use in correlated molecular calculations. I. The atoms boron through neon and hydrogen. *The Journal of Chemical Physics* **1989**, *90*, 1007–1023.

- [201] Nygaard, L.; Nielsen, J. T.; Kirchheiner, J.; Maltesen, G.; Rastrup-Andersen, J.; Sørensen, G. O. Microwave spectra of isotopic pyrroles. Molecular structure, dipole moment, and ^{14}N quadrupole coupling constants of pyrrole. *Journal of Molecular Structure* **1969**, *3*, 491–506.
- [202] Martinez, O.; Crabtree, K. N.; Gottlieb, C. A.; Stanton, J. F.; McCarthy, M. C. An Accurate Molecular Structure of Phenyl, the Simplest Aryl Radical. *Angewandte Chemie International Edition* **2015**, *54*, 1808–1811.
- [203] da Silva, G.; Moore, E. E.; Bozzelli, J. W. Quantum Chemical Study of the Structure and Thermochemistry of the Five-Membered Nitrogen-Containing Heterocycles and Their Anions and Radicals. *The Journal of Physical Chemistry A* **2006**, *110*, 13979–13988.
- [204] Zhang, X.; Sander, S. P.; Stanton, J. F. Detection of the Far-IR ν_{12} Bending Level in Propargyl: A Complete Set of Fundamentals for an Important Radical. *J. Phys. Chem. A* **2012**, *116*, 10338–10343.
- [205] Pullen, G. T.; Franke, P. R.; Haupa, K. A.; Lee, Y.-P.; Douberly, G. E. Infrared spectroscopy of the n-propyl and i-propyl radicals in solid para-hydrogen. *Journal of Molecular Spectroscopy* **2019**, *363*, 111170.
- [206] Abeysekera, C.; Hernandez-Castillo, A. O.; Stanton, J. F.; Zwier, T. S. Broadband Microwave Spectroscopy of 2-Furanyloxy Radical: Primary Pyrolysis Product of the Second-Generation Biofuel 2-Methoxyfuran. **2018**,
- [207] Johansen, S. L.; Martin-Drumel, M.-A.; Crabtree, K. N. Rotational Spectrum of the β -Cyanovinyl Radical: A Possible Astrophysical N-Heterocycle Precursor. *The Journal of Physical Chemistry A* **2019**, *123*, 5171–5177.
- [208] Szalay, P. G.; Vázquez, J.; Simmons, C.; Stanton, J. F. Triplet instability in doublet systems. *The Journal of Chemical Physics* **2004**, *121*, 7624.
- [209] Motzke, A.; Lan, Z.; Woywod, C.; Domcke, W. Simulation of the photodetachment spectrum of the pyrrolide anion. *Chemical Physics* **2006**, *329*, 50–64.
- [210] Watson, J. K. G. Determination of centrifugal distortion coefficients of asymmetric-top molecules. *J. Chem. Phys.* **1967**, *46*, 1935.
- [211] Bunker, P. R.; Jensen, P. *NRC Research Press*, 2nd ed.; Elsevier, 1979; p 752.

- [212] Bermudez, C.; Bailleux, S.; Cernicharo, J. Laboratory detection of the rotational-tunnelling spectrum of the hydroxymethyl radical, CH₂OH. *A&A* **2017**, *598*, 9.
- [213] DeVine, J. A.; Babin, M. C.; Blackford, K.; Neumark, D. M. High-resolution photoelectron spectroscopy of the pyridinide isomers. *The Journal of Chemical Physics* **2019**, *151*, 064302.
- [214] Korte, A.; Mardyukov, A.; Sander, W. Pyridyl- and Pyridylperoxy Radicals – A Matrix Isolation Study. *Aust. J. Chem.* **2014**, *67*, 1324.
- [215] Tokaryk, D. W.; Van, W. A. Fourier transform spectra of the ν_{16} , $2\nu_{16}$, and $2\nu_{16}-\nu_{16}$ bands of pyrrole taken with synchrotron radiation. *Canadian Journal of Physics* **2009**, *87*, 443–448.
- [216] Tokaryk, D.; Culligan, S.; Billingham, B.; van Wijngaarden, J. Synchrotron-based far-infrared spectroscopy of furan: Rotational analysis of the ν_{14} , ν_{11} , ν_{18} and ν_{19} vibrational levels. *Journal of Molecular Spectroscopy* **2011**, *270*, 56–60.
- [217] van Wijngaarden, J.; Van Nest, S. J.; van Dijk, C. W.; Tokaryk, D. W. Rovibrational spectrum and analysis of the ν_8 band of thiophene using infrared synchrotron radiation. *Journal of Molecular Spectroscopy* **2010**, *259*, 56–59.
- [218] Hrodmarsson, H. R.; Garcia, G. A.; Nahon, L.; Gans, B.; Loison, J.-C. Threshold Photoelectron Spectrum of the Anilino Radical. *The Journal of Physical Chemistry A* **2019**, *123*, 9193–9198.
- [219] Mellouki, A.; Liévin, J.; Herman, M. The vibrational spectrum of pyrrole (C₄H₅N) and furan (C₄H₄O) in the gas phase. *Chem. Phys.* **2001**, *271*, 239 – 266.
- [220] Nixon, C. A.; Achterberg, R. K.; Ádámkovics, M.; Bézard, B.; Bjoraker, G. L.; Cornet, T.; Hayes, A. G.; Lellouch, E.; Lemmon, M. T.; López-Puertas, M.; Rodriguez, S.; Sotin, C.; Teanby, N. A.; Turtle, E. P.; West, R. A. Titan Science with the James Webb Space Telescope. *Publications of the Astronomical Society of the Pacific* **2016**, *128*, 018007.
- [221] McMahon, R. J.; McCarthy, M. C.; Gottlieb, C. A.; Dudek, J. B.; Stanton, J. F.; Thaddeus, P. The radio spectrum of the phenyl radical. *Astrophys. J.* **2003**, *590*, L61–L64.
- [222] Oyama, T.; Funato, W.; Sumiyoshi, Y.; Endo, Y. Observation of the pure rotational spectra of trans- and cis-HOCO. *J. Chem. Phys.* **2011**, *134*, 174303.

- [223] Hernandez-Castillo, A. O.; Abeysekera, C.; Stanton, J. F.; Zwieter, T. S. Structural Characterization of Phenoxy Radical with Mass-Correlated Broadband Microwave Spectroscopy. *J. Phys. Chem. Lett.* **2019**, *10*, 2919–2923.
- [224] Patterson, D.; Doyle, J. M. Cooling molecules in a cell for FTMW spectroscopy. *Mol. Phys.* **2012**, *110*, 1757–1766.
- [225] Porterfield, J. P.; Satterthwaite, L.; Eibenberger, S.; Patterson, D.; McCarthy, M. C. High sensitivity microwave spectroscopy in a cryogenic buffer gas cell. *Rev. Sci. Instrum.* **2019**, *90*, 053104.
- [226] Gottlieb, C. A.; Gottlieb, E. W.; Thaddeus, P. Laboratory and astronomical measurement of the millimeter wave spectrum of the ethynyl radical CCH. *Astrophys. J.* **1983**, *264*, 740–745.
- [227] Bailleux, S.; Dréan, P.; Godon, M.; Zelinger, Z.; Duan, C. First observation of the rotational spectrum of the bromomethyl radical, CH₂Br. *Phys. Chem. Chem. Phys.* **2004**, *6*, 3049–3051.
- [228] Bailleux, S.; Dréan, P.; Zelinger, Z.; Civiš, S.; Ozeki, H.; Saito, S. Millimeter wave spectrum of bromomethyl radical, CH₂Br. *J. Chem. Phys.* **2005**, *122*, 134302.
- [229] Kwok, S. Complex organics in space from Solar System to distant galaxies. *The Astronomy and Astrophysics Review* **2016**, *24*, 8.
- [230] Materese, C. K.; Nuevo, M.; Sandford, S. A. The Formation of Nucleobases from the Ultraviolet Photoirradiation of Purine in Simple Astrophysical Ice Analogues. *Astrobiology* **2017**, *17*, 761–770.
- [231] Bera, P. P.; Stein, T.; Head-Gordon, M.; Lee, T. J. Mechanisms of the Formation of Adenine, Guanine, and Their Analogues in UV-Irradiated Mixed NH₃:H₂O Molecular Ices Containing Purine. *Astrobiology* **2017**, *17*, 771–785.
- [232] Smith, K. E.; Gerakines, P. A.; Callahan, M. P. Metabolic precursors in astrophysical ice analogs: Implications for meteorites and comets. *Chemical Communications* **2015**, *51*, 11787–11790.
- [233] Lattalais, M.; Ellinger, Y.; Matrane, a.; Guillemin, J.-C. Looking for heteroaromatic rings and related isomers as interstellar candidates. *Physical chemistry chemical physics : PCCP* **2010**, *12*, 4165–71.
- [234] Ufimtsev, I. S.; Martinez, T. J. Quantum Chemistry on Graphical Processing Units. 3. Analytical Energy Gradients, Geometry Optimization, and First Principles Molecular Dynamics. *Journal of Chemical Theory and Computation* **2009**, *5*, 2619–2628.

- [235] Martínez, L.; Andrade, R.; Birgin, E. G.; Martínez, J. M. PACKMOL: A package for building initial configurations for molecular dynamics simulations. *Journal of Computational Chemistry* **2009**, *30*, 2157–2164.
- [236] Humphrey, W.; Dalke, A.; Schulten, K. VMD – Visual Molecular Dynamics. *Journal of Molecular Graphics* **1996**, *14*, 33–38.
- [237] Cernicharo, J.; Cabezas, C.; Agúndez, M.; Tercero, B.; Marcelino, N.; Pardo, J. R.; Tercero, F.; Gallego, J. D.; López-Pérez, J. A.; DeVicente, P. Discovery of allenyl acetylene, H₂CCCHCCH, in TMC-1. *Astronomy & Astrophysics* **2021**, *647*, L3.
- [238] Ewen, H. I.; Purcell, E. M. Observation of a Line in the Galactic Radio Spectrum: Radiation from Galactic Hydrogen at 1,420 Mc./sec. *Nature* **1951**, *168*, 356–356.
- [239] RIDGWAY, S. T.; HALL, D. N. B.; KLEINMANN, S. G.; WEINBERGER, D. A.; WOJSLAW, R. S. Circumstellar acetylene in the infrared spectrum of IRC +10° 216. *Nature* **1976**, *264*, 345–346.
- [240] Betz, A. L. Ethylene in IRC +10216. *The Astrophysical Journal* **1981**, *244*, L103.
- [241] Agúndez, M.; Marcelino, N.; Cernicharo, J. Discovery of Interstellar Isocyanogen (CNCN): Further Evidence that Dicyanopolynes Are Abundant in Space. *The Astrophysical Journal* **2018**, *861*, L22.
- [242] Agúndez, M. et al. Probing non-polar interstellar molecules through their protonated form: Detection of protonated cyanogen (NCCNH⁺). *Astronomy and Astrophysics* **2015**, *579*, 1–4.
- [243] Turner, B. E.; Liszt, H. S.; Kaifu, N.; Kisliakov, A. G. Microwave detection of interstellar cyanamide. *The Astrophysical Journal* **1975**, *201*, L149.
- [244] McGuire, B. A.; Loomis, R. A.; Charness, C. M.; Corby, J. F.; Blake, G. A.; Hollis, J. M.; Lovas, F. J.; Jewell, P. R.; Remijan, A. J. Interstellar carbodiimide (HNCNH): A new astronomical detection from the gbt PRIMOS survey via maser emission features. *Astrophysical Journal Letters* **2012**, *758*.
- [245] Martinez, O. et al. Detection of E-cyanomethanimine toward sagittarius B2(N) in the green bank telescope primos survey. *Astrophysical Journal Letters* **2013**, *765*.
- [246] Rivilla, V. M.; Martín-Pintado, J.; Jiménez-Serra, I.; Zeng, S.; Martín, S.; Armijos-Abendaño, J.; Requena-Torres, M. A.; Aladro, R.; Riquelme, D. Abundant Z-cyanomethanimine in the interstellar medium: Paving the way to the synthesis of adenine. *Monthly Notices of the Royal Astronomical Society: Letters* **2019**, *483*, L114–L119.

- [247] Belloche, A.; Menten, K. M.; Comito, C.; Müller, H. S. P.; Schilke, P.; Ott, J.; Thorwirth, S.; Hieret, C. Detection of amino acetonitrile in Sgr B2(N). *Astronomy & Astrophysics* **2008**, *492*, 769–773.
- [248] McGuire, B. A.; Burkhardt, A. M.; Loomis, R. A.; Shingledecker, C. N.; Kelvin Lee, K. L.; Charnley, S. B.; Cordiner, M. A.; Herbst, E.; Kalenskii, S.; Momjian, E.; Willis, E. R.; Xue, C.; Remijan, A. J.; McCarthy, M. C. Early Science from GOTHAM: Project Overview, Methods, and the Detection of Interstellar Propargyl Cyanide (HCCCH 2 CN) in TMC-1. *The Astrophysical Journal* **2020**, *900*, L10.
- [249] Kelvin Lee, K. L.; Loomis, R. A.; Burkhardt, A. M.; Cooke, I. R.; Xue, C.; Siebert, M. A.; Shingledecker, C. N.; Remijan, A.; Charnley, S. B.; McCarthy, M. C.; McGuire, B. A. Discovery of Interstellar trans -cyanovinylacetylene (HCCCHCHCN) and vinylcyanoacetylene (H 2 CCHC 3 N) in GOTHAM Observations of TMC-1. *The Astrophysical Journal* **2021**, *908*, L11.
- [250] Esselman, B. J.; Kougias, S. M.; Zdanovskaia, M. A.; Woods, R. C.; McMahan, R. J. Synthesis, Purification, and Rotational Spectroscopy of (Cyanomethylene)Cyclopropane—An Isomer of Pyridine. *The Journal of Physical Chemistry A* **2021**, *125*, 5601–5614.
- [251] Vrtilek, J. M.; Gottlieb, C. A.; Thaddeus, P. *LABORATORY AND ASTRONOMICAL SPECTROSCOPY OF C 3 H 2 , THE FIRST INTERSTELLAR ORGANIC RING*; 1987; Vol. 314; pp 716–725.
- [252] He, C.; Nikolayev, A.; Zhao, L.; M. Thomas, A.; Doddipatla, S.; R. Galimova, G.; N. Azyazov, V.; M. Mebel, A.; I. Kaiser, R. Gas-Phase Formation of C₅H₆ Isomers via the Crossed Molecular Beam Reaction of the Methylidyne Radical (CH; X₂π) with 1,2-Butadiene (CH₃CHCCH₂; X₁A'). *The Journal of Physical Chemistry A* **2021**, *0*.
- [253] Gupta, D.; Cheikh Sid Ely, S.; Cooke, I. R.; Guillaume, T.; Abdelkader Khedaoui, O.; Hearne, T. S.; Hays, B. M.; Sims, I. R. Low Temperature Kinetics of the Reaction Between Methanol and the CN Radical. *The Journal of Physical Chemistry A* **2019**, *123*, 9995–10003.
- [254] Shannon, R. J.; Blitz, M. A.; Goddard, A.; Heard, D. E. Accelerated chemistry in the reaction between the hydroxyl radical and methanol at interstellar temperatures facilitated by tunnelling. **2013**,
- [255] Lavvas, P.; Sander, M.; Kraft, M.; Imanaka, H. SURFACE CHEMISTRY AND PARTICLE SHAPE: PROCESSES FOR THE EVOLUTION OF AEROSOLS IN TITAN'S ATMOSPHERE. *The Astrophysical Journal* **2011**, *728*, 80.

- [256] Delitsky, M. L.; McKay, C. P. The photochemical products of benzene in Titan's upper atmosphere. *Icarus* **2010**, *207*, 477–484.
- [257] Lebonnois, S.; Bakes, E.; McKay, C. P. Transition from Gaseous Compounds to Aerosols in Titan's Atmosphere. *Icarus* **2002**, *159*, 505–517.
- [258] Sun, B. J.; Huang, C. H.; Chen, S. Y.; Chen, S. H.; Kaiser, R. I.; Chang, A. H. H. Theoretical Study on Reaction Mechanism of Ground-State Cyano Radical with 1,3-Butadiene: Prospect of Pyridine Formation. *The Journal of Physical Chemistry A* **2014**, *118*, 7715–7724.
- [259] He, W.; Zhang, H.; Wang, N.; Tan, X.; Wang, W.; Li, P. Insights into the cycloaddition reaction mechanism between ketenimine and unsaturated hydrocarbon: A theoretical study. *Russian Journal of Physical Chemistry A* **2016**, *90*, 1027–1033.
- [260] Becke, A. D. Density-functional thermochemistry. III. The role of exact exchange. *The Journal of Chemical Physics* **1993**, *98*, 5648–5652.
- [261] Lee, C.; Yang, W.; Parr, R. G. Development of the Colle-Salvetti correlation-energy formula into a functional of the electron density. *Phys. Rev. B* **1988**, *37*, 785–789.
- [262] Hehre, W. J.; Ditchfield, R.; Pople, J. A. Self-Consistent Molecular Orbital Methods. XII. Further Extensions of Gaussian-Type Basis Sets for Use in Molecular Orbital Studies of Organic Molecules. *The Journal of Chemical Physics* **1972**, *56*, 2257–2261.
- [263] Shao, Y. et al. Advances in molecular quantum chemistry contained in the Q-Chem 4 program package. *Molecular Physics* **2015**, *113*, 184–215.
- [264] Hanwell, M. D.; Curtis, D. E.; Lonie, D. C.; Vandermeersch, T.; Zurek, E.; Hutchison, G. R. Avogadro: an advanced semantic chemical editor, visualization, and analysis platform. *Journal of Cheminformatics* **2012**, *4*, 17.
- [265] Lin, Y.-S.; Li, G.-D.; Mao, S.-P.; Chai, J.-D. Long-Range Corrected Hybrid Density Functionals with Improved Dispersion Corrections. *Journal of Chemical Theory and Computation* **2013**, *9*, 263–272.
- [266] Mardirossian, N.; Head-Gordon, M. Exploring the limit of accuracy for density functionals based on the generalized gradient approximation: Local, global hybrid, and range-separated hybrid functionals with and without dispersion corrections. *The Journal of Chemical Physics* **2014**, *140*, 18A527.

- [267] He, W.; Tan, X.; Wang, N.; Zhang, H. Theoretical study on the mechanism of the cycloaddition reaction between ketenimine and hydrogen cyanide. *Journal of the Serbian Chemical Society* **2016**, *81*, 187–195.
- [268] He, W.; Wang, W.; Tan, X.; Li, P. Theoretical study on the cycloaddition reaction mechanism between ketenimine and acetonitrile. *Main Group Chemistry* **2016**, *15*, 221–230.
- [269] WANG, N.; TAN, X.; WANG, W.; WANG, F.; LI, P. Theoretical insights into the cycloaddition reaction mechanism between ketenimine and methyleneimine: An alternative approach to the formation of pyrazole and imidazole. *Journal of Chemical Sciences* **2016**, *128*, 279–285.
- [270] Balucani, N.; Skouteris, D.; Leonori, F.; Petrucci, R.; Hamberg, M.; Geppert, W. D.; Casavecchia, P.; Rosi, M. Combined Crossed Beam and Theoretical Studies of the $N(2D) + C_2H_4$ Reaction and Implications for Atmospheric Models of Titan. *The Journal of Physical Chemistry A* **2012**, *116*, 10467–10479.
- [271] Irvine, W. M.; Friberg, P.; Hjalmarsen, A.; Ishikawa, S.; Kaifu, N.; Kawaguchi, K.; Madden, S. C.; Matthews, H. E.; Ohishi, M.; Saito, S.; Suzuki, H.; Thaddeus, P.; Turner, B. E.; Yamamoto, S.; Ziurys, L. M. Identification of the interstellar cyanomethyl radical (CH_2CN) in the molecular clouds TMC-1 and Sagittarius B2. *The Astrophysical Journal* **1988**, *334*, L107.
- [272] Sabbah, H.; Biennier, L.; Sims, I. R.; Georgievskii, Y.; Klippenstein, S. J.; Smith, I. W. Understanding reactivity at very low temperatures: The reactions of oxygen atoms with alkenes. *Science* **2007**, *317*, 102–105.
- [273] Baer, T.; Hase, W. L. *Unimolecular Reaction Dynamics: Theory and Experiments*; Oxford University Press, 1996.
- [274] Nuevo, M.; Chen, Y.-J.; Hu, W.-J.; Qiu, J.-M.; Wu, S.-R.; Fung, H.-S.; Chu, C.-C.; Yih, T.-S.; Ip, W.-H.; Wu, C.-Y. R. Irradiation of Pyrimidine in Pure H_2O Ice with High-Energy Ultraviolet Photons.
- [275] Nuevo, M.; Milam, S. N.; Sandford, S. A.; Elsila, J. E.; Dworkin, J. P. Formation of uracil from the ultraviolet photo-irradiation of pyrimidine in pure H_2O ices. *Astrobiology* **2009**, *9*, 683–695.
- [276] Nuevo, M.; Bredehöft, J. H.; Meierhenrich, U. J.; D’hendecourt, L.; Thiemann, W. H. Urea, glycolic acid, and glycerol in an organic residue produced by ultraviolet irradiation of interstellar/pre-cometary ice analogs. *Astrobiology* **2010**, *10*, 245–256.

- [277] Parker, D. S. N.; Kaiser, R. I. On the formation of nitrogen-substituted polycyclic aromatic hydrocarbons (NPAHs) in circumstellar and interstellar environments. *Chem. Soc. Rev.* **2017**, *452*, 452–463.
- [278] Tian, Z.; Li, Y.; Zhang, T.; Zhu, A.; Qi, F. Identification of combustion intermediates in low-pressure premixed pyridine/oxygen/argon flames. *Journal of Physical Chemistry A* **2008**, *112*, 13549–13555.
- [279] Gautier, T.; Sebree, J. A.; Li, X.; Pinnick, V. T.; Grubisic, A.; Loeffler, M. J.; Getty, S. A.; Trainer, M. G.; Brinckerhoff, W. B. Influence of trace aromatics on the chemical growth mechanisms of Titan aerosol analogues. *Planetary and Space Science* **2017**, *140*, 27–34.
- [280] Vuitton, V.; Yelle, R. V.; Anicich (Retired), V. G. The Nitrogen Chemistry of Titan’s Upper Atmosphere Revealed. *The Astrophysical Journal* **2006**, *647*, L175–L178.
- [281] Bonačić-Koutecký, V.; Schöffel, K.; Michl, J. Electronic States of Cyclobutadiene Heteroanalogues. Critical Biradicaloids. *Journal of the American Chemical Society* **1989**, *111*, 6140–6146.
- [282] Csaszar, A. G.; Demaison, J.; Dieter Rudolph, H. Equilibrium Structures of Three-, Four-, Five-, Six-, and Seven-Membered Unsaturated N-Containing Heterocycles. **2014**,
- [283] Brown, F. X.; Saito, S.; Yamamoto, S. Microwave spectroscopy of isotopically substituted HCCN and its molecular structure. *Journal of Molecular Spectroscopy* **1990**, *143*, 203–208.
- [284] Bernheim, R. A.; Kempf, R. J.; Gramas, J. V.; Skell, P. S. Electron paramagnetic resonance of triplet alternant methylenes. Propargylene and homologs. *The Journal of Chemical Physics* **1965**, *43*, 196–200.
- [285] Abbott, B. Z.; Hoobler, P. R.; Schaefer, H. F. Relatives of cyanomethylene: Replacement of the divalent carbon by B-, N+, Al-, Si, P+, Ga-, Ge, and As+. *Physical Chemistry Chemical Physics* **2019**, *21*, 26438–26452.
- [286] Holzmeier, F.; Wagner, I.; Fischer, I.; Bodi, A.; Hemberger, P. Pyrolysis of 3-Methoxypyridine. Detection and Characterization of the Pyrrolyl Radical by Threshold Photoelectron Spectroscopy. *The Journal of Physical Chemistry A* **2016**, *120*, 4702–4710.
- [287] Lavvas, P. P.; Coustenis, A.; Vardavas, I. M. Coupling photochemistry with haze formation in Titan’s atmosphere, Part II: Results and validation with Cassini/Huygens data. *Planetary and Space Science* **2008**, *56*, 67–99.

- [288] Wiesemeyer, H.; Güsten, R.; Menten, K. M.; Durán, C. A.; Csengeri, T.; Jacob, A. M.; Simon, R.; Stutzki, J.; Wyrowski, F. Unveiling the chemistry of interstellar CH Spectroscopy of the 2 THz $N = 2 \leftarrow 1$ ground state line. *Astronomy and Astrophysics* **2018**, *612*, 1–14.
- [289] Araki, M.; Takano, S.; Sakai, N.; Yamamoto, S.; Oyama, T.; Kuze, N.; Tsukiyama, K. Long Carbon Chains in the Warm Carbon-chain-chemistry Source L1527: First Detection of C_7H in Molecular Clouds. *The Astrophysical Journal* **2017**, *847*, 51.
- [290] BELL, M. B.; FELDMAN, P. A.; WATSON, J. K. G.; MCCARTHY, M. C.; TRAVERS, M. J.; GOTTLIEB, C. A.; THADDEUS, P. OBSERVATIONS OF LONG MOLECULES IN THE DUST CLOUD TMC-1. *The Astrophysical Journal* **1999**, *518*, 740–747.
- [291] Cernicharo, J.; Guelin, M.; Walmsley, C. M. Detection of the hyperfine structure of the C_5H radical. *Astronomy and Astrophysics* **1987**, *172*, L5,L6.
- [292] Suzuki, H.; Ohishi, M.; Kaifu, N.; Ishikawa, S.-I.; Kasuga, T. Detection of the interstellar C_6H radical. *Astronomical Society of Japan, Publications* **1986**, *38*, 911–917.
- [293] Guelin, M.; Green, S.; Thaddeus, P. Detection of the C_4H radical toward IRC plus 10216. *The Astrophysical Journal* **1978**, *224*, L27.
- [294] Kroto, H. W.; Kirby, C.; Walton, D. R. M.; Avery, L. W.; Broten, N. W.; MacLeod, J. M.; Oka, T. The detection of cyanohexatriyne in Heiles’s cloud 2. *The Astrophysical Journal* **1978**, *219*, L133.
- [295] Little, L. T.; Macdonald, G. H.; Riley, P. W.; Matheson, D. N. Observations of interstellar HC_5N and HC_7N in dark dust clouds. *Monthly Notices of the Royal Astronomical Society* **1978**, *183*, 45P–50P.
- [296] Avery, L. W.; Broten, N. W.; MacLeod, J. M.; Oka, T.; Kroto, H. W. Detection of the heavy interstellar molecule cyanodiacetylene. *The Astrophysical Journal* **1976**, *205*, L173.
- [297] Turner, B. E. Detection of Interstellar Cyanoacetylene. *The Astrophysical Journal* **1971**, *163*, L35.
- [298] Guelin, M.; Cernicharo, J. Astronomical detection of the $HCCN$ radical. Toward a new family of carbon-chain molecules? *Astronomy & Astrophysics* **1991**, L21–L24.
- [299] Waite, J. H.; Young, D. T.; Cravens, T. E.; Coates, A. J.; Crary, F. J.; Magee, B.; Westlake, J. The Process of Tholin Formation in Titan’s Upper Atmosphere. *Science* **2007**, *316*, 870–875.

- [300] Johansen, S. L.; Xu, Z.; Westerfield, J. H.; Wannemacher, A. C.; Crabtree, K. N. Coupled Cluster Characterization of 1-, 2-, and 3-Pyrrolyl: Parameters for Vibrational and Rotational Spectroscopy. *The Journal of Physical Chemistry A* **2021**, *125*, 1257–1268.
- [301] Devine, A. L.; Cronin, B.; Nix, M. G. D.; Ashfold, M. N. R. High resolution photofragment translational spectroscopy studies of the near ultraviolet photolysis of imidazole. *The Journal of Chemical Physics* **2006**, *125*.
- [302] Werner, H.; Knowles, P. J. An efficient internally contracted multiconfiguration–reference configuration interaction method. *The Journal of Chemical Physics* **1988**, *89*, 5803–5814.
- [303] Langhoff, S. R.; Davidson, E. R. Configuration interaction calculations on the nitrogen molecule. *International Journal of Quantum Chemistry* **1974**, *8*, 61–72.
- [304] Werner, H.; Knowles, P.; Knizia, G.; Manby, F.; Schütz, M.; Celani, P.; Györffy, W.; Kats, D.; Korona, T.; Lindh, R.; et al., MOLPRO, version 2015.1, a package of ab initio programs. *University of Cardiff Chemistry Consultants (UC3): Cardiff, Wales, UK* **2015**,